

# Conformable neural interfaces : from engineering stretchability at the micro-scale to translational applications

Présentée le 8 juillet 2022

Faculté des sciences et techniques de l'ingénieur  
Chaire Fondation Bertarelli de technologie neuroprosthétique  
Programme doctoral en microsystemes et microélectronique

pour l'obtention du grade de Docteur ès Sciences

par

## Florent-Valéry COEN

Acceptée sur proposition du jury

Prof. H. Shea, président du jury  
Prof. S. Lacour, directrice de thèse  
Prof. M. Asplund, rapporteuse  
Prof. F. Vitale, rapporteuse  
Prof. C. Guiducci, rapporteuse





The story is not in the words; it's in the struggle.  
Paul Auster, *The New York Trilogy*

To my grandparents, Rose and Pierre...



# Acknowledgements

I would like to take this opportunity to thank all the people that helped me during these years as PhD student and made this journey possible.

First, I want to warmly thank Prof. Stéphanie Lacour for giving the opportunity to work in the Laboratory for Soft Bioelectronic Interfaces. None of the work presented here would have been possible without the exceptional work environment she provided. She has always been a tremendous source of human and scientific support and gave me the freedom to pursue my own research interests.

I would also like to thank Prof. Herbert Shea, Prof. Maria Asplund, Prof. Carlotta Guiducci and Prof. Flavia Vitale for accepting to join my jury committee and for reviewing my work.

Next, I would like to give my warmest thanks to Dr. Alix Trouillet, Dr. Florian Fallegger and Noaf Alwahab for their unwavering support over the years. They are all exceptional scientists and even better friends. Through innumerable discussions and debates - over the lab bench, a delicious meal from Ottolenghi or a cold IPA - they have helped shape who I am as an engineer and as a person. Over the years, they were an infinite source of inspiration, joy and motivation and they helped me all the way until the very the end.

Next, I would like to give a very special thank you to Laurine Kolly and Emilie Revol, who both contributed a tremendous amount of work and helped "complete the picture". In particular, I would like to thank Laurine for her exceptional assiduity and sharp scientific mind which proved invaluable at the last hour.

Next, I would like to acknowledge the help of the rest of my colleagues at the LSBI, who all provided scientific and intellectual support during these five years. In particular, I would like to thank: Dr. Nicolas Vachicouras for answering my questions on electrochemistry at all hours of the day or the night; Ivan Furfaro for building instrumentation and measurement systems so advanced they belong on a space mission; Yashwanth Vyza for his selflessness and unwavering friendship; Outman Akouassi for his admirable "sens pratique" and for helping clean up my experiments gone wrong and

## Acknowledgements

---

finally Valentina Paggi for helping me keep the lab in a somewhat acceptable state of chaos. I would also like to acknowledge all the semester and master students who I supervised: Alix Nepveux, Pauline Treyvaud, Cédric Portmann and Laurine Kolly.

I want to thank the staff of the numerous platform I worked in: the neural microsystem platform cleanroom of the Wyss Center in Geneva; the staff of the Center for Microfabrication at EPFL in Lausanne; the staff at the Translational Neuroscience Platform at the University of Fribourg; the staff of the non-human primate facility at the University of Washington.

Next, I would like to give a very special thank you to Damien Maillard and Matthias Neuen-schwader who have been by my side all the way from the beginning of my scientific career in high school and without whom I would have not made it this far. Cleanroom work is not quite the same if you do not have someone to share your pain (and successes) with! I would also like to thank the rest of "c'équipe" for all our adventures during these past 15 years: Gabriel, Stéphane, Jibé, Yoram, Cédric and Arnaud.

Last but not least, I would like to warmly thank my family for their unconditional support during these five years, in particular parents and my siblings, Marie-Céline, Violaine-Ophélie et Charles-Théophile. Your encouragements made it possible!

*Lausanne, le 31 mars 2022*

FVC

# Abstract

Neural interfaces have been used in recent years to interrogate or modify the behaviour of the nervous system. On a fundamental level this enables the study of basic functions of the central (CNS) and peripheral nervous system (PNS), as well as treat neurological illnesses in patients. For example, using cochlear implants to stimulate dysfunctional hair cells can restore hearing precepts in deaf patients, stimulating the subthalamic nucleus in the deep brain removes essential tremors of Parkinson's disease or recording on the surface of the brain can inform about oncoming seizures in epilepsy. To achieve this, electrode arrays are implanted to increase the proximity to the signal source and enable better recordings or more efficient stimulation. However the nervous system is constituted of curved soft tissues moving microscopically with the respiration and heartbeat, and stretching macroscopically with bodily movement. In opposition, current clinical devices are made of stiff metal electrodes embedded in a thick polymeric shell. Implanting these rigid devices in this soft environment can lead to inflammatory responses due to the mechanical mismatch leading to scarring tissue and device degradation.

Recently, flexible and soft bioelectronic interfaces have been proposed as a solution to this challenge. These are devices fabricated with thin polymeric or elastomeric backbones to enable an optimal contact to the target tissue as well as reduced mechanical mismatch. For this the electrical interconnects that carry the electrical information from the tissue or deliver the stimulation charges need to be elastic to accommodate the stresses and remain conductive. Several strategies for creating stretchable tracks have been proposed in the past but are not compatible with high-density low-profile electrode arrays for chronic implantation in vivo.

A method of patterning thin material stacks of flexible polymers and platinum layers embedded in silicone membranes was proposed in the Laboratory for Soft Bioelectronic Interfaces at EPFL. By creating specific microscopic cuts in the materials permits the out-of-plane deformation of the film and enables stretchability above 50% strain while remaining conductive. However, the previous fabrication method was not optimal, was not hermetically encapsulated and not reliable. In this thesis, novel soft electrode arrays were designed and fabricated using an improved manufacturing process named core-shell micropatterning. This enables fully encapsulated electrical tracks that can be micropatterned with superior electromechanical performances and notable increase in

## Abstract

---

hermetic barrier lifetimes. Additionally, this method was applied to other material systems enabling new functions such as completely transparent devices to enable concurrent optical stimulation and microscopy through the implanted electrodes.

These fabricated devices were applied to several device concepts in multiple animal models. First, microelectrode arrays for electrocorticography (ECoG) recordings were designed to be implanted over the auditory cortex of rat and non-human primate (NHP) models to capture evoked potentials from acoustic stimulation. This enabled the precise tonotopic mapping and the spatial representation of the auditory cortex. Next, auditory brainstem implants (ABI), targeting the cochlear nucleus (CN) after the auditory nerve were designed. This implant needs to conform to the curved surface of the CN and stimulate the auditory pathway. In non-human primates, the placement of this device is challenging and new tools were developed for the insertion of the device. Finally, the combination of soft ABI and ECoG was implanted in chronic settings in a NHP to evoke auditory percepts from brainstem stimulation that could be monitored using the cortical evoked potentials. This will enable the fine-tuning of stimulation protocols for hearing restoration and verify the stability of the implants over time. Overall, this work represents a framework to design and fabricate soft electrode arrays that can be applied for recording and stimulation in small to large animal models in a reliable way. The careful design of the system around the implant such as fine-tuning of microfabrication parameters, the characterization in vitro, device geometry, connection scheme, experimental setup and tracking of the device properties in vivo enables reliable long-term implantations in new experimental paradigms.

## Résumée

Récemment, les interfaces neuronales ont été utilisées pour interroger ou modifier le comportement du système nerveux. À un niveau fondamental, cela permet d'étudier les fonctions de base du système nerveux central (SNC) et périphérique (SNP), ainsi que de traiter les maladies neurologiques des patients. Par exemple, l'utilisation d'implants cochléaires pour stimuler les cellules ciliées dysfonctionnelles permet de rétablir la perception auditive chez les patients sourds, la stimulation du noyau sous-thalamique en profondeur du cerveau supprime les tremblements de la maladie de Parkinson ou l'enregistrement à la surface du cerveau peut informer sur les crises épileptiques avant qu'elles ne surviennent. A cet effet, des champs d'électrodes sont implantés à la surface du tissu pour augmenter la proximité au signal, et ainsi permettre de meilleurs enregistrements ou une stimulation plus efficace. Cependant, le système nerveux est un tissu mou et circonvolé présentant des mouvements microscopiques qui suivent la respiration et les battements du coeur, et des mouvements macroscopiques d'étirement qui suivent les mouvements du corps. Les interfaces neuronales cliniques actuelles sont constituées d'électrodes métalliques rigides enveloppées dans une coque polymérique épaisse. L'implantation de ces dispositifs rigides dans cet environnement mou et dynamique entraîne des frottements mécaniques ce qui peut engendrer des réactions inflammatoires et de la fibrose et au final réduire l'efficacité du dispositif et compromettre l'intégrité du système nerveux du patient.

Depuis peu, des interfaces bioélectroniques souples et flexibles ont été proposées comme solution à ce problème. Il s'agit de matrices d'électrodes à encapsulations polymériques ou élastomériques ultrafines permettant un contact optimal avec le tissu cible et réduisant fortement les différences mécaniques et les frottements. Pour assurer la flexibilité et l'élasticité du dispositif, les interconnexions électriques qui transportent l'information électrique du tissu ou délivrent les charges de stimulation doivent être elles-mêmes élastiques pour s'adapter aux contraintes tout en restant conductrices. Plusieurs stratégies de fabrication de pistes extensibles ont été proposées dans le passé, mais elles ne sont pas compatibles avec les champs d'électrodes de haute densité ni pour une implantation chronique in vivo.

Le laboratoire des interfaces bioélectroniques souples de l'EPFL a développé une méthode permettant de micro-structurer des couches successives de films minces compo-

sés de polymères souples et de couches de platine incorporées dans des membranes de silicone. La création de découpes microscopiques spécifiques dans le plan du matériau permet la déformation hors plan du film permettant une déformation finale supérieure à 50% tout en restant conducteur. Cependant, la première itération de cette méthode de fabrication présentait des limitations, l'encapsulation n'était pas hermétique et le procédé peu robuste et sous-optimal. Dans cette thèse, de nouveaux champs d'électrodes souples ont été conçus et fabriqués à l'aide d'un procédé de fabrication optimisé appelé "core-shell micropatterning". Cela permet d'obtenir des pistes électriques entièrement encapsulées qui peuvent être micro-structurées et présentant des performances électromécaniques supérieures et une augmentation notable de la durée de vie de la barrière hermétique. De plus, cette méthode a été appliquée à d'autres systèmes de matériaux permettant de nouvelles fonctionnalités telles que des dispositifs complètement transparents permettant une stimulation optique et une microscopie simultanées à travers les électrodes implantées.

Cette méthode de microfabrication a été appliquée à plusieurs concepts d'interfaces neuronales dans plusieurs modèles animaux. Tout d'abord, des champs de microélectrodes pour les enregistrements d'électrocorticographie (ECoG) ont été conçus pour être implantés sur le cortex auditif de modèles de rats et de primates non humains afin de capturer les potentiels évoqués auditifs. Cela a permis d'établir une cartographie tonotopique précise et une représentation spatiale du cortex auditif. En parallèle, des implants auditifs du tronc cérébral (ABI) ciblant le noyau cochléaire (CN) ont été conçus. Cet implant doit se conformer à la surface incurvée du CN et stimuler efficacement la voie auditive afférente. Chez les primates non humains, l'implantation de l'ABI souple est difficile et de nouveaux outils ont été développés pour l'insertion de cet implant. Enfin, l'ABI souple et l'ECoG ont été implantés de manière chronique chez un macaque rhesus afin d'évoquer des perceptions auditives (monitorées à travers l'ECoG via l'enregistrement des potentiels évoqués corticaux) à partir de la stimulation électrique du tronc cérébral. Cette étape permet de vérifier la stabilité des implants dans le temps, d'affiner les protocoles de stimulation pour la restauration de l'audition et représente une étape importante vers la translation clinique de ces nouveaux implants. Dans l'ensemble, ce travail représente un système pour concevoir et fabriquer des champs d'électrodes souples qui peuvent être utilisés pour l'enregistrement et la stimulation dans des modèles animaux de petite à grande taille de manière fiable et reproductible. La conception minutieuse du système autour de l'implant, comme le réglage fin des paramètres de microfabrication, la caractérisation in vitro, la géométrie du dispositif, le schéma de connexion, le montage expérimental et le suivi des propriétés des implants in vivo, permet des implantations fiables à long terme et l'élaboration de nouveaux paradigmes expérimentaux.



# Contents

<b>Acknowledgements</b>	<b>i</b>
<b>Abstract (English/Français)</b>	<b>iii</b>
<b>1 Introduction</b>	<b>1</b>
1.1 Clinical Neural Interfaces . . . . .	1
1.2 Soft Neural Interfaces . . . . .	5
1.2.1 Characteristics of neural tissue . . . . .	5
1.2.2 Structure of soft neural interfaces . . . . .	7
1.2.3 Advantages of soft neural interfaces . . . . .	9
1.2.4 Potential for clinical translation . . . . .	10
1.3 Aims of this Thesis . . . . .	11
<b>2 Technologies for Conformable Neural Interfaces</b>	<b>13</b>
2.1 State of the Art . . . . .	14
2.1.1 Intrinsically stretchable conductors . . . . .	15
2.1.2 Stretchability by design . . . . .	16
2.2 Micropatterned Thin Films for Engineered Stretchability . . . . .	18
2.2.1 Introduction . . . . .	18
2.2.2 Methods . . . . .	20
2.2.3 Results . . . . .	28
2.2.4 Summary and Discussion . . . . .	32
2.3 Core-shell Micropatterns for Improved Stretchable Interconnects . . . . .	36
2.3.1 Introduction . . . . .	36
2.3.2 Methods . . . . .	37
2.3.3 Results . . . . .	42
2.3.4 Summary and Discussion . . . . .	46
2.4 Comparative electromechanical study . . . . .	54
2.4.1 Sheet resistance . . . . .	54
2.4.2 Electromechanical characterization . . . . .	55
2.4.3 Hermeticity characterization . . . . .	62
2.5 Variation on a Theme: Fabricating a Soft and Optically Transparent Neural Interface . . . . .	64
	vii

## Contents

---

2.5.1	Introduction . . . . .	64
2.5.2	Methods . . . . .	68
2.5.3	Results . . . . .	72
2.5.4	Summary and Discussion . . . . .	80
2.6	Conclusion . . . . .	82
<b>3</b>	<b>Application: ECoG</b>	<b>85</b>
3.1	Introduction . . . . .	86
3.2	Acute Study in Rodents . . . . .	88
3.2.1	Methods . . . . .	89
3.2.2	Results & Discussion . . . . .	91
3.3	Chronic Study in Non-human Primate . . . . .	93
3.3.1	Methods . . . . .	94
3.3.2	Results . . . . .	98
3.3.3	Conclusion . . . . .	103
<b>4</b>	<b>Application: Auditory Brainstem Implant</b>	<b>107</b>
4.1	Introduction . . . . .	108
4.2	Methods . . . . .	111
4.2.1	Experimental design . . . . .	111
4.2.2	Surgical approach . . . . .	113
4.2.3	ABI design & design validation . . . . .	117
4.2.4	Stimulation & recording protocols . . . . .	124
4.3	Results and Discussion . . . . .	125
4.3.1	Conclusion . . . . .	126
<b>5</b>	<b>Application: Spinal Cord Stimulation</b>	<b>129</b>
5.1	Introduction . . . . .	130
5.2	Methods . . . . .	131
5.3	Results & Discussion . . . . .	135
5.4	Conclusion . . . . .	141
<b>6</b>	<b>General Discussion and Outlook</b>	<b>143</b>
6.1	Discussion . . . . .	143
6.2	Outlook . . . . .	145
	<b>Bibliography</b>	<b>147</b>
	<b>Curriculum Vitae</b>	<b>163</b>

# 1 Introduction

## 1.1 Clinical Neural Interfaces

**Definition** Neural interfaces are a class of implantable medical devices designed to interact with the central or peripheral nervous system in order to repair a broken connection or disrupt abnormal activity (Fig. 1.1). They can act as a control input by injecting current into the underlying tissue or, alternatively, as a recording output in order to measure the biopotential of the surrounding neuron population. The act of interacting with the the nervous system in order to trigger or inhibit its activity is referred to as neuromodulation. The most common form of neuromodulation is electrical stimulation, which is currently used in a wide array of clinical applications including chronic pain management [1] (spinal cord stimulation), tremor alleviation [2] (deep brain stimulation), hearing [3] and vision [4] restoration (cochlear and retinal stimulation). In terms of recording, electrocorticography (ECoG) grids are most often used to locate foci of abnormal activity in drug-resistant, epileptic patients [5]. The collected data can then be used to guide the surgeon during the resection of the affected area. In recent years, so-called brain-machine interfaces (BMIs) have been a notable development in this category. These devices rely on the detection of cortical activity in order to provide patients with the control of an external assistive device such as a computer or a robotic arm. Although few and far between, bidirectional applications have also been proposed with, for instance, the close-loop management of epileptic seizures [6]. In this particular case, cortical readings from an ECoG are used to flag incoming seizure and to trigger inhibitory electrical stimulation through a deep brain implant.

**Clinical system components** Conceptually speaking, current clinical implants can be thought of as being composed of three interconnected parts (Fig. 1.2): (1) an implantable pulse generator (IPG), (2) an array of electrodes that interface with the tissue and (3) an insulated lead which carries electrical signals between the two. The IPG contains all the electronic components necessary to generate the stimuli and, in some cases, to com-

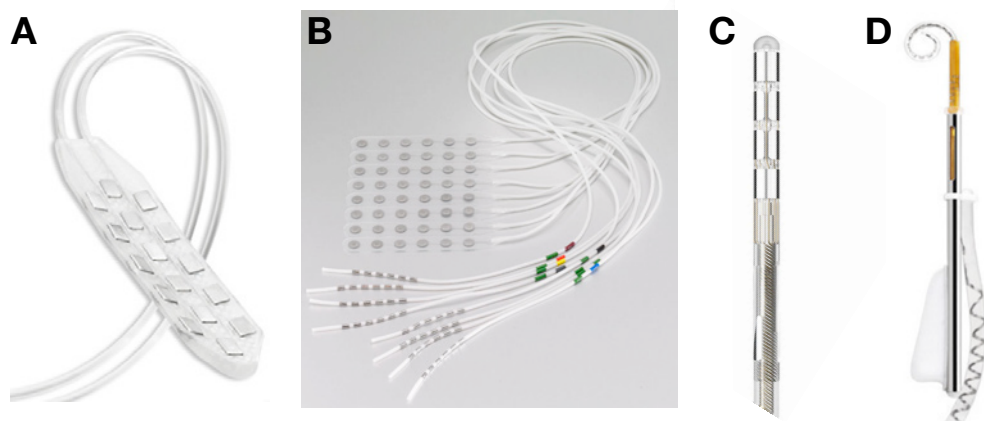


Figure 1.1: Examples of clinical neural interfaces: spinal cord implant from Medtronic (A), electrocorticography grid from Dixi Medical (B), a deep brain stimulation lead from Medtronic (C) and a cochlear implant from Cochlear (D).

municate with the outside world. It is powered by a non-rechargeable battery, enclosed along the rest of the electronic circuitry inside an hermetically sealed titanium case. Due to its large footprint, the IPG is most commonly placed under the skin, away from the stimulation target in locations such the chest (deep brain stimulation), the lower back (spinal cord stimulation) or the skull (seizure inhibition [7]). Clinical electrode arrays are composed of a multitude of electrically conductive disks or blocks, themselves made of alloys such as stainless steel or platinum-iridium. The contact sites are millimeter-size (1-5mm) and most often spatially separated by a constant pitch in a grid-like pattern. The actual paddle is formed by embedding the electrodes in a thick (1-3mm) and rigid (10-50MPa) elastomeric matrix, after having welded them to individually insulated wires. The electrical connection between the IPG and the leads is achieved either through a standardized connector or by soldering the wires directly into the titanium casing.

Electrode paddles can adopt many different geometries, depending on the application requirements. While planar devices such as ECoGs and spinal cord implants are built to interface with the tissue surface, alternative designs offer the possibility to penetrate the tissue in order to interact with deeper structures. This is the case of the DBS implant for instance, which is inserted through the cortex in order to reach the subthalamic nucleus and globus pallidus, where it is used to relieve tremors in Parkinson's disease patients. Electrode arrays can also be preformed in order to better match the anatomical target, for example in the cases of the cochlear implant (fig. 1.1) or the peripheral nerve cuffs.

Overall, clinical implants are very simple devices made of few components assembled using well-established manufacturing processes. This inherent simplicity in design makes it easier - and more economical - to integrate their production in a quality management system, a mandatory tool used for the controlled manufacturing of medical devices.

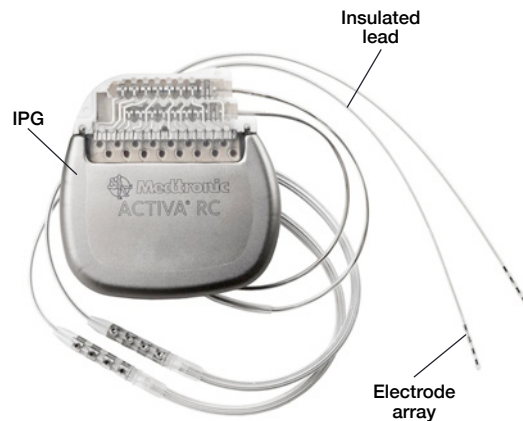


Figure 1.2: Picture of clinical implantable system for deep-brain stimulation from Medtronic.

This approach also proves to be an advantage in terms of reliability, as fewer parts naturally implicate fewer potential failure points. The robustness of clinical arrays originates in most part from the macroscopic nature of its components which tend to minimize surface-driven phenomenon. For instance, the integration of bulky metallic electrodes reduces the potential adverse effects of metal corrosion, which helps guarantee low impedance contacts over extended period of time. Similarly, the use of individual metal wires decreases the risk of an interconnect breaking through the sheer amount of material present. The added advantage of using large components is that they can be assembled mostly by hand, avoiding the need of complex machinery which, in the world of medical devices, necessitate regular calibration and maintenance. Another contributing factor to the reliability of clinical array is the intrinsic rigidity of the devices. Indeed, the stiffness of the silicone matrix helps minimize the stresses applied to the electrical interconnects, in particular at the level of the solder joints. Furthermore, the mechanical signature of the device also facilitates handling, offering less opportunity for the device to break while being hand manipulated by the factory worker or medical personnel. In fact, surgeons often use this property to their advantage in order to insert an implant by simply pushing it from its distal end.

**Limitations** Although contemporary clinical implants constitute a reliable tool to interact with the nervous system, they remain rather rudimentary interfaces. As such, they lack various important features required for the development of the next generation of neurotherapeutic applications including brain-machine interfaces or the restoration of motor functions. Current efforts on new therapies are being held back by three key limitations:

- **Electrode density** The combined use of macroscopic components and manual

manufacturing processes greatly limit the potential for miniaturization in conventional neural implants. High-density array of microelectrodes hold the promise to substantially increase spatial resolution of both stimulating and recording devices [8]. In the context of BMI for example, such an improvement can translate in a finer understanding of the patient's motor intents. On the stimulation side, a denser electrode array could be combined with multipolar stimulation in order to enable a more granular control over the applied stimuli.

- **Stiffness** Because of the thickness and rigidity of both the electrodes and the silicone paddle, clinical implant exhibit a high bending stiffness. As a result, they tend to maintain their shape once implanted and are thus unable to conform to the complex topology characteristic of most of the CNS. The potential consequences for this lack of mechanical compliance are two-fold. (1) It can lead to subpar contact between the electrode sites and the underlying tissue which, in the context of recording devices, translates into a decrease in signal quality. In stimulating implants, lack of conformability can lead to a less specific activation and in some case like the auditory brainstem implant, to the triggering of side effects. (2) Due to its rigidity, the implant can end up compressing the surrounding tissue, potentially leading to neurophysiological impairments. This is especially true of highly dynamic environment, such as the spinal cord.
- **Personalization** In the age of personalized healthcare, neural implants are still very much built following a "one size fits all" mentality. Indeed, the current manufacturing techniques and regulatory roadblocks make it cost prohibitive to develop implants tailored for a particular individual. Customizing the geometry of an electrode paddle for instance, would necessitate the production of a different injection mold for every single design, a financially unsound proposition. The inability to optimize electrode positioning based on imaging data is a significant limitations, especially in application such as spinal cord stimulation, where tailor-made devices have shown to significantly improve outcomes.

These limitations have motivated the development of soft bioelectronics, a term used to describe mechanically compliant electronic microsystems designed to interact with biological tissues. This new category of devices associate automated microfabrication techniques with novel materials in order to better address the biomechanical characteristics of the nervous system [9, 10].

## 1.2 Soft Neural Interfaces

### 1.2.1 Characteristics of neural tissue

In order to design neural interfaces that are more adapted to their environment, it is critical to understand what are the important characteristics of the CNS. Although numerous biochemical phenomena contribute to the relationship between living tissues and implantable devices, this section will touch upon the CNS/implant interactions from a purely mechanical standpoint. This admittedly simplistic approach will nevertheless highlight the major motivations behind the development of soft bioelectronic interfaces.

**Elastic modulus** In the context of neural interface, the most critical property of the CNS is certainly its elastic modulus. While it is qualitatively evident that the tissues comprising the CNS are soft, their precise characterization has proven to be a challenge. In the past six decades, numerous attempts have been made, with studies reporting values ranging from 100Pa in the brain to 100kPa in the spinal cord [11, 12, 13]. The significant spread in reported values can be attributed to several factors. First of all, the measurement techniques can change from one study to the next, with the most common ones being oscillatory shear rheology and atomic force microscopy. Within each specific approach, the selected measurement parameters can also strongly influence the results. In the case of rheological measurements for instance, variations in shear rate across studies make it difficult to compare the reported numbers on a one-to-one basis. Finally, accurate and reproducible measurements are made difficult by the fact that the CNS is, inherently, a very heterogeneous structure. Indeed, the proportion of grey matter (which mainly includes cell bodies) and white matter (which mainly contains axons) differs significantly from one CNS location to the next, with contradictory report on which type of tissue is stiffer than the other [14, 15, 16].

**Topology** The brain is an excessively complex surface defined by a multitude of ridges (gyri) and fissures (sulci). These structures (fig.1.3), formed by folds in the tissue at the surface of the brain, exhibit a wide range of geometries with some of them reaching millimeter-sized radii of curvature [18, 19]. They are the driving force behind the need for more compliant neural interfaces, as many areas of interest in the brain are located near, across or even inside a sulcus. Similarly, the spinal cord also possesses an intricate shape, with the particularity that it can dramatically change over time based on the subject's posture and movements.

**Dynamics** In addition to the static constraints discussed above, it should be mentioned that the CNS is also a very dynamic mechanical system. The spinal cord is the best example in that regard, as it can experience not only periodic ( $\sim 0.01\text{Hz}$ ) tensile

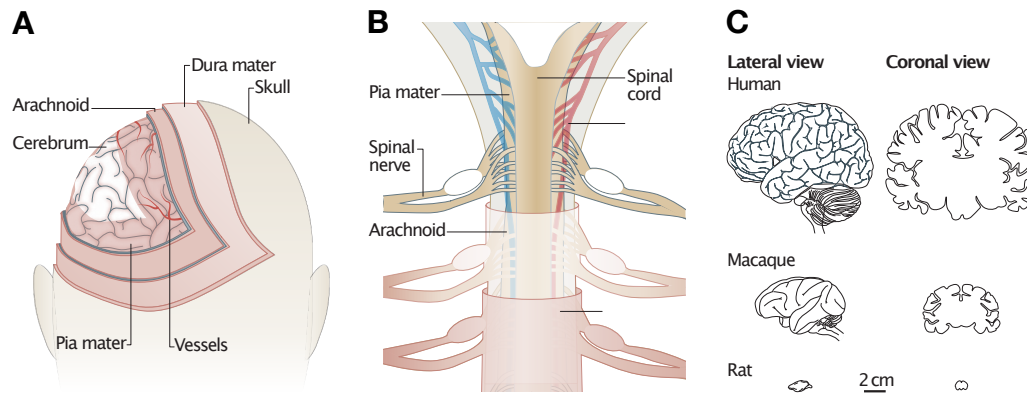


Figure 1.3: Structure and anatomy of the central nervous system. Adapted from [17]. **A-B** Illustrations of the anatomy of the human brain (A) and spinal cord (B). **C** Illustration of the topology of the brain across species.

and compressive deformation but also shear strain of up to 10-20% [13]. The brain also experiences strain but to a much lesser extent. Volumetric changes caused by blood flow, respiration and cerebrospinal fluid circulation will also caused periodic deformation ( $\sim 1$ -2Hz) in the range of 0.01 to 0.03% [20].

In light of these observations, it is evident that there exists a significant gap between the properties of the CNS and those of clinical implants. These differences are grouped under the term biomechanical mismatch.

**Biomechanical mismatch** The main consequence of the biomechanical mismatch that exists between clinical implants and the surrounding tissue is the inflammatory response of the body. Indeed, once the presence of a foreign object has been detected, the immune system will attempt to isolate and destroy it [21, 22]. The immune response is composed of many concurring phenomenons including the recruitment of microglia and macrophages, neuronal death and the buildup of fibrous tissue around the device. Because the stiff, bulky clinical implants are unable to comply with the natural dynamics of the CNS, they become a source of constant strain on the tissue. As such, their presence pushes the immune system into overdrive, leading to a worsening of the fibrosis and inflammatory response. The potential consequences of this immune reactions cascade are four-fold. (1) Driven by the growth of the fibrotic layer, the access resistance might increase so much that the voltage compliance of the stimulator is exceeded, leading to the inability to stimulate. (2) The distance between the electrodes and target tissue might increase so much that neuronal activity can no longer be triggered or recorded [23]. (3) The surrounding biochemical reactions and subsequent buildup



of adverse species might lead to a degradation of the device (e.g.  $\text{H}_2\text{O}_2$ ). (4) The extraneous tissue buildup might compress the rest of the anatomy, potentially leading to adverse side-effects (e.g. gait deficit in the case of the spinal cord [24]).

The concept of biomechanical mismatch - and how to reduce it - is at the core of the soft bioelectronics field. Broadly speaking, two approaches have been proposed in order to achieve biomechanical stealth: via the use of softer materials (silicone [24], hydrogels [25]) or via the reduction of the device footprint [26].

### 1.2.2 Structure of soft neural interfaces

Soft neural interfaces refer to a class of devices that establish a physical interface between the nervous tissue and an electronic circuit in order to measure or trigger physiological activity. Conceptually, neural interfaces can be divided into three functional blocks:

1. The carrier, which forms the physical body of the device. It supports and protects the other components.
2. The interconnects which establish the link between the electrodes and the computing and communication modules, further up in the system hierarchy.
3. The electrode arrays which constitute the physical interface through which the neuron population and the rest of the system interact.

**Carrier** The carrier material constitutes the backbone of the device: it supports the other components mechanically, allowing the device to maintain its shape and to be manipulated. As such, it determines the mechanical signature of the system, a notion which can be quantified through the bending stiffness  $D$ :

$$D = \frac{Eh^3}{12(1 - \nu^2)}$$

where  $E$  is the elastic modulus,  $h$  the thickness and  $\nu$  the Poisson's ratio of the material. The bending stiffness governs the ability of the device to conform to surfaces with a zero Gaussian curvature, i.e. shapes that can be flattened into a plane without distortion. This is not the case of the brain however, whose surface is characterized by two non-zero radii of curvature. This specificity is one of the motivations for using stretchable carriers, since they can accommodate non-developable surfaces through mechanical deformation [27].

In addition to its mechanical contribution, the carrier is also typically responsible to iso-

late the tracks electrically. In that regard, it is critical for the material to be as hermetic as possible. Indeed, not only can the diffusion of ionic species through the encapsulation generate electrical cross-talk [28], it can also potentially lead to mechanical failure by enabling adverse electrochemical reactions to occur at the interface between the materials [29]. In clinical implants, the issue of ionic diffusion is mitigated through the sheer amount of material (millimeter-thick silicone) used to isolate the electrical components [30]. In contrast, thin film devices are much more likely to suffer from adverse surface-driven phenomena such as corrosion. As a result, significant research efforts are being made towards the fabrication and integration of high-performance encapsulation layers.

**Interconnects** The interconnects carry the electrical signals to and from the biological tissue. Low track resistance is generally desirable because it will prolong the usable lifetime of the device. Indeed, since the electrical impedance faced by the device in-vivo is expected to increase over time, more conductive interconnects will lower the initial system impedance, allowing to stimulate longer before reaching the voltage compliance of the stimulator. In other words, low resistance interconnects give the system more headroom by minimizing the voltage draw imposed on the stimulator.

Mechanically speaking, the interconnects need to accommodate the bending or stretching of the device without an excessive increase in resistance ( $<10\times$ ). The range over which the tracks should be able to sustain deformation ranges from few percents when complying with the brain surface [31] to tens of percents on the spinal cord [13].

Finally, the interconnect technology should enable the patterning of high density electrical layout (critical dimension  $< 100\mu\text{m}$ ) using microfabrication techniques that are compatible with the selected carrier. Patterning methods include standard processes such as reactive ion etching and lift-off as well as transfer and ink-jet printing. The ability to manufacture increasingly small electrical circuits is the driving factor behind the development of neural interfaces with higher electrode densities and smaller footprints.

**Electrodes** The electrode coating constitute the physical interface through which the biological tissue and the rest of the system interact. Since the requirements of the coating differ from those of the interconnects, it is often made of a different material and/or deposited during a separate fabrication step. In stimulation applications, the coating should permit the safe and efficient injection of charges into the target tissue. For recording, it should aim to transduce surrounding biosignals without distorting them.

Generally speaking, the electrode coating impedance should be minimized in order to reduce the burden on the stimulator (stimulation) and minimize thermal noise (recording) [32]. The most common strategy to achieve this effect consists of increasing the effective electrode area either by roughening an existing surface or by depositing new

materials with rough topography. Biointegration is another crucial aspect of electrode coating. Clever surface engineering can be used to promote cell health and reduce astrocytes and microglia activation [33], effectively ensuring a close proximity between the neurons and the electrode.

Finally, since the electrode site is the main point of physical contact between the device and the target tissue, it is critical for the interface to be mechanically robust. In that regard, strong adhesion between the coating, carrier and interconnects is critical in order to prevent the diffusion of ionic species at the interface to cause delamination [34, 35]. From an electrochemical standpoint, the properties of the electrode should remain stable even with intensive stimulation paradigms [36].

### 1.2.3 Advantages of soft neural interfaces

Soft bioelectronics propose to address the limitations of the current clinical implants by combining the manufacturing techniques of the semiconductor industry with novel, polymeric materials. This new category of devices can bring numerous benefits with regard to the surgical procedure, diagnostic capability and therapeutic outcomes. Some of these advantages include:

**Reduction in footprint** Soft bioelectronic interfaces are fabricated using micro- and nanometric layers (thin films) of various materials including polymers (PDMS, polyimide, parylene), metals (Pt, Au), and other inorganic compounds (SiO<sub>2</sub>, SiC, ITO). Most of the manufacturing techniques employed to build these devices are directly inherited or adapted from processes established in the semiconductor industry. Methods such as sputtering, evaporation and spin-coating enable the deposition of layers with thicknesses ranging from tens of nanometers to hundreds of microns with extreme accuracy and repeatability. Using photolithography, these films can then be selectively patterned into structures as small as a few nanometers. The intrinsic size of the components, as well as the techniques used to fabricate/assemble them, permits an overall reduction in the thickness and lateral dimensions of the resulting device [37, 38]. In turn, this smaller footprint translates into a decrease in invasiveness, which will help the biointegration of the implant.

**Reduction in biomechanical mismatch** The manufacturing techniques described above can also be leveraged in order to incorporate materials with lower elastic moduli. The integration of soft materials entails a decrease of the biomechanical mismatch between the tissue and the device which, itself, leads to a reduction of the inflammatory response [17].

**Improved conformability** By virtue of their low elastic modulus and/or thinness, the bending stiffness of bioelectronic interfaces is inherently lower. As a result, these devices are able to better conform to complex topologies, leading to a more intimate contact between the electrode and the target tissue [27]. By reducing the distance between the electrode and the area of interest, one can achieve a more precise stimulation or higher quality recording, depending on the application at hand.

**Increased precision and sensitivity** At a device level, the miniaturization of the interconnect and contact sites brings three improvements: the fabrication of smaller electrodes, an increase in the number of these electrodes and a densification of their spatial distribution. Echoing the advantages cited above, these changes permit a more purposeful stimulation of the tissue or, conversely, a more nuanced recording of its activity. The increase in spatial resolution is particularly interesting in applications such as brain-machine interfaces, where the increase in information density can be leveraged to offer better understanding of the subject's intents [39].

**Multimodal interactions** Since soft bioelectronic interfaces are built using extremely versatile manufacturing techniques, they can be designed to integrate more than passive electrodes. Thin films can be engineered to form interfaces for other types of interactions such as capturing fluids [40], dispensing drugs [24], emitting/recording light [41, 42] and many more. The ability to simultaneously interrogate/modulate neural tissue through various modalities is extremely powerful and has been an instrumental tool in modern neuroscientific research.

### 1.2.4 Potential for clinical translation

The clinical translation of soft bioelectronics is an arduous process, requiring expertise in the domains of materials science, electronics, microfabrication, bioengineering and medical sciences. While new electrode coatings and interconnect technologies have been the focus of much of the academic research, the successful translation of soft implants will likely depend instead on often overlooked aspects such as connectors, system integration, power management and wireless capabilities.

On a fundamental level, the translation of radically new types of devices is challenging because the standards and norms currently in use in the industry are often inadequate [43]. For example, the techniques used to assess the mechanical robustness of conformable bioelectronic systems differ significantly from those established for conventional, more rigid devices. As a result, it is essential for standardized testing procedures to be developed and adopted in conjunction with the introduction of new materials and form factors. This is, in itself, not a trivial task, especially in academic settings where the establishment of standardized benchmarks is not managed through a cen-

tralized, officially sanctioned organization. Furthermore, the question of standards is especially challenging in the field of bioelectronics because the properties of the devices vary greatly from one technology to another, making it difficult to define a global set of requirements.

Besides standardized testing, pre-clinical in-vivo validation remains one of best tool to assess the biocompatibility, long-term functionality and efficacy of a device [44, 45, 46]. This approach, however, requires designing and optimizing a complete system, not just a single component. This represents a significant technological undertaking, in particular with regard to hermeticity. While the question of reliability is often discussed on a component level, a system can only be as good as its weakest link. In that regard, the interfaces between the different elements of the system (connectors, solder joints, etc) will always represent the most probable points of failure [47]. This is especially true of the transdermal access ports present in wired, in-vivo systems. This particular interface, which often takes the form of a transdermal feedthrough, connector or cable, is, by nature, more prone to infection and mechanical damage than any other. In fact, these ports will often fail before the technology being investigated [48, 49]. Nevertheless, there is no systematic study or recommended approach with regard to designing a robust, implantable system for in-vivo validation. Part of the issue is that, once again, the devices under investigation are very different from each other (size, anatomical target, connection scheme), making it difficult to come up with a one-size-fit-all solution.

With this in mind, it is clear that developing a soft neural interface in a clinically relevant fashion is a challenging endeavor. The framework required to characterize, analyze and compare these new devices is only starting to get established.

## 1.3 Aims of this Thesis

**General objective** The global objective of this thesis is to fabricate and characterize neural interfaces that conform intimately with the surface of the central nervous system. The starting point of this work is the technology presented by Vachicouras et al. in 2019 which consists of a soft microelectrode array and microstructured interconnects embedded in an ultrathin silicone matrix. Here, this proof of concept is improved upon in order to increase the reliability and performances of the fabricated implants. The technological developments presented in this thesis also enable the manufacturing of more complex and fully-featured devices, as well as the integration of new functionalities. This developmental work is undertaken as part of a translational study in non-human primates which aims to demonstrate the benefits of soft neural interfaces in the context of auditory brainstem stimulation.

**Aims** This work is subdivided into four aims:

## Chapter 1. Introduction

---

1. Implement manufacturing and technological improvements in order to produce microstructured, stretchable interconnects with superior electromechanical properties and extended barrier lifetimes.
2. Apply the kirigami-inspired approach to new materials in order to implement additional functionalities such as transparency.
3. Establish the versatility of the technological approach by demonstrating its use across various in-vivo applications.
4. Investigate the potential for clinical translation in the context of chronic experiments in non-human primates.

**Outline** This thesis is divided into five chapters:

1. Introduction to neural interfaces in the clinic and in research together with the associated challenges.
2. State of the art in the field of stretchable interconnects and extensive description of the technological novelties proposed in this thesis to manufacture microstructured interconnects with superior electromechanical properties.
3. Application of the technology to neural recordings of the auditory cortex in both rodents (acute) and non-human primates (chronic).
4. Application of the technology to an auditory brainstem implant (ABI) devised for the chronic stimulation of the auditory brainstem in non-human primates.
5. Application of the technology to spinal cord stimulation in the context of a study on the rehabilitation of upper-limb motor functions in rodents.

## 2 Technologies for Conformable Neural Interfaces

**Outline** This chapter describes the development of a stretchable interconnects technology for soft neural interfaces. It is organized in 5 sections:

1. **State of the art** on technologies for stretchable interconnects in the context of bioelectronic devices.
2. **Micropatterned thin films for engineered stretchability** introduces the basic process for engineering stretchability in thin films via micropatterning and explores the limitations of this initial approach.
3. **Core-shell micropatterns for improved stretchable interconnects** presents a new micropatterning strategy that addresses the shortcomings identified in the previous section.
4. **Comparative electromechanical study** contains a thorough characterization of the electromechanical performances of both generations of stretchable interconnects.
5. **Variation on theme, fabricating a soft and optically transparent neural interface** demonstrates the versatility of the core-shell strategy by applying it to a new stack of materials in order to produce transparent, stretchable interconnects.

**Acknowledgments** The results presented in this chapter were made possible thanks to the work of Nicolas Vachicouras, Laurine Kolly, Florian Fallegger and the staff of the center for Micro- and Nanotechnology (CMi) at EPFL. NVA developed the original Y-shaped micropatterns technology. LKO co-developed the ITO process and helped with the comparative electromechanical study. FFA developed the original FlexComb connector and manufactured the Pt-PDMS composite.

**Scientific contributions** The content of this chapter is being integrated into a scientific article:

- **Florent-Valéry Coen**, Laurine Kolly, Stéphanie P. Lacour. "Core-shell micropatterns for kirigami-inspired stretchable interconnects in soft neural interfaces", *in preparation*.

### 2.1 State of the Art

**Requirements** The fabrication of soft and conformable neural interfaces requires the development of interconnects able to maintain their electro-mechanical properties under both static and dynamic strain. The conductive tracks should be able to stretch and bend in order to conform to the topology of the target tissue and to accommodate bodily motion. The range over which the interconnects should stretch elastically is of course application dependent, ranging from 0.01-0.03% strain in the brain to 10% in the spinal cord [20, 13]. Additionally, the device needs be able to sustain a larger, one-time tensile strain (20-40%), which is likely to take place during implantation due to surgical manipulations. In terms of electrical properties, the interconnects conductivity has to be high enough to allow for the use of conventional implantable neurostimulators whose compliance typically ranges from 10 to 15V. Assuming a current pulse of 3mA, which is within the range used in deep brain stimulation, this translates into a track resistance limit of 5k $\Omega$ . Finally, the manufacturing process should allow to pattern narrow tracks (width and pitch <100 $\mu$ m) in order to be able to produce dense and large-scale arrays of microelectrodes (8 to 256 channels).

**Strategies** Conventional conductors used in neural interfaces include noble metals (platinum, gold) and conductive oxides such as Indium Tin Oxide (ITO). When considered in their simple form, these materials can unfortunately not fulfill the requirements for stretchable interconnects listed above [50]. Indeed, while metals are ductile (30-40% elongation at break) and could easily sustain a one-time, large deformation, they start to deform plastically at strains around 1-5% which means mechanical fatigue will quickly set in. As for oxide materials, their brittle nature is likely to lead to fractures at strains beyond a few percents. Moreover, both categories of material are characterized by high elastic moduli (10-500GPa) which, once integrated, translate into devices with a high bending stiffness and thus, low conformability. In order to address these issues, new strategies were developed to manufacture conductors suitable for conformable neural interfaces. These approaches can be broadly divided into two categories: (1) the integration of intrinsically stretchable materials and (2) the integration of conventional, rigid materials in unconventional ways (stretchability by design) [9, 51, 52].



### 2.1.1 Intrinsically stretchable conductors

**Definition** Intrinsically stretchable conductors refer to a class of materials whose electro-mechanical properties originate from the conservation of percolating pathways under elongation. It is the organization of these materials at the micro- or nano-scale, under the form of a 2D or 3D network of conductive elements, that enables conduction via a combination of ballistic transport and tunneling [53].

**2D and 3D percolating network** Percolating composites are constituted of a polymeric matrix in which conductive structures or particles are embedded. It is the nature of these elements, as well their concentration inside the matrix, that will determine the electro-mechanical performance of the conductor. Examples of these materials include composites based on nanostructures, such as graphene [54] and carbon nanotubes [55], as well as metallic macro- and nanoparticles (fig. 2.1A) [56, 57]. The interconnects fabricated using these materials have been reported to stretch up to 30% [57], 95% [54] or even 300% [56]. Alternatively, composites using conductive polymers (fig. 2.1B) have shown promising results, with some PEDOT:PSS blend reaching 200% elongation [58]. With regard to synthesis, conductive composites are most commonly formed by mixing the filler particles with the uncured polymeric matrix (fig. 2.1D) but alternative processes have been reported, such as direct ionic implantation of metals inside a polymerized elastomer [59].

A different approach to percolating networks consists of forming a 2D-like nanomesh at the surface of a stretchable material. The resulting structure is able to comply with the deformation of the substrate via in- and out-of-plane deformations. Nanowires (fig. 2.1C) are classical examples of this strategy but thin films of gold on PDMS (fig. 2.1E) have been demonstrated to exhibit a similar behavior [60, 61], sustaining strain of up to 40% [62].

**Liquid conductors** Pushing the definition of percolating network to its limit, conductive liquids have also been used in combination with microfluidic channels in order to form stretchable interconnects [63, 64]. While conductors based on ionic liquids have been demonstrated, they typically exhibit low conductivity (1-100mS/cm). Alternatively, liquid metals (fig. 2.1F), such as eutectic gallium-indium, have been shown to combine extreme stretchability (>700%) with high conductivity (50kS/cm) [65, 66]. Often integrated in wearable systems, these exceptional alloys have been challenging to interface with conventional electrical circuits due to corrosion.

**Advantages and downsides** The main advantage of intrinsically stretchable conductors resides in their ability to sustain very large, isotropic strain. Under displacement, the network will naturally reorganize, maintaining numerous parallel percolating pathways along the elongation axis. As a result, point defects in the material have little to no

effect on the conductivity of the material, since they can effectively be "bypassed". The conductivity of the network will only cease once the local concentration falls below the percolating threshold due to the physical distance between the filler particles. On the other hand, the patterning of these materials is often challenging, relying on processes such as transfer printing, additive printing or screen printing. The resulting interconnects are therefore often well above 100 $\mu\text{m}$  in size, exhibiting significant line-width roughness (Fig. 2.1D).

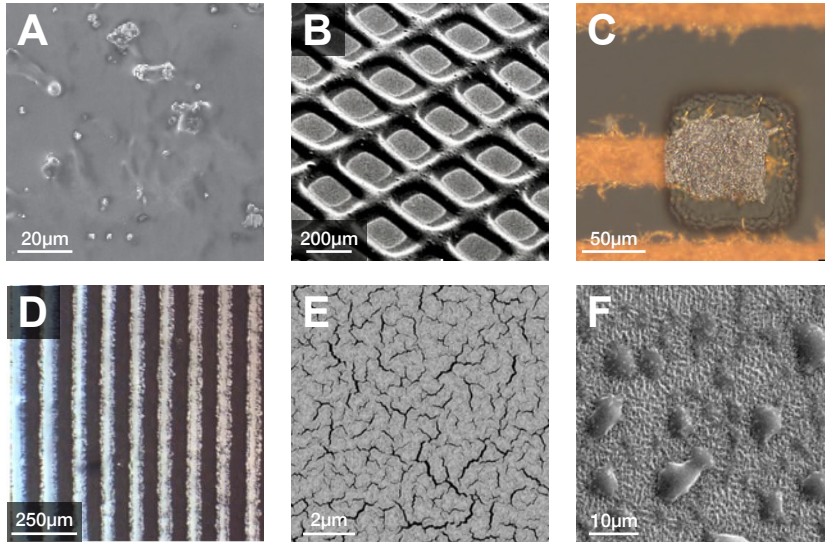


Figure 2.1: Examples of intrinsically stretchable conductors. **A** SEM image of nickel microparticles distributed in a supramolecular polymeric network. The resulting composite demonstrates self-healing properties upon tearing. Adapted from [57]. **B** SEM image of conducting polymer ink based on PEDOT:PSS. The mesh was constructed via 3D printing on PETE, allowing high throughput manufacturing [67]. **C** Stretchable interconnects composed of a percolating network of TiO<sub>2</sub> nanowires on PDMS. Following the patterning of the tracks via transfer printing, the electrode site is electroplated with a platinum layer. Adapted from [68]. **D** Parallel lines of Ag-PDMS composite screen-printed through a copper stencil mask [56]. **E** SEM image of a micro-cracked gold film formed via direct thermal evaporation on PDMS [62]. **F** SEM image of a biphase AuGa<sub>2</sub> film deposited on PDMS [69].

### 2.1.2 Stretchability by design

**Definition** Engineered stretchability refers to an approach in which conventional, stiff materials are rendered stretchable through their patterning into specific geometries. These structures are designed to prevent the concentration of local strain, enabling the conductors to elongate well beyond the ultimate tensile strength of the bulk material [70]. This effect is obtained in one of two ways: (1) by fabricating the tracks on top of a pre-stained substrate or (2) by patterning the interconnects in such a way that they can

deform out-of-plane.

**Wavy surfaces** The fundamental idea behind this category of interconnects consists of depositing the conductive layer on top of a pre-strained substrate such that it forms wrinkles once the assembly is relaxed. As a result, the conductive film is able to sustain elongation through the unfolding of its wavy surface. This strategy has been successfully employed to create Si nanomembranes which can be stretched up to 37%, well beyond the intrinsic properties of the bulk material (fig 2.2A). With regard to metals, the formation of wavy layers (fig 2.2B) has been demonstrated via direct thermal evaporation on pre-strained elastomeric substrate [71, 72]. Alternatively, metallic films on plastic foil can be laminated on pre-stretched PDMS membranes to achieve the same effect. Such structures have shown the ability to survive large tensile strains (>275%) as well as prolonged cyclic stretching (>1000 cycles at 50% strain) [73].

**Serpentine interconnects** The most common design strategy to obtain a stretchable interconnects consists of patterning the tracks into tortuous meanders instead of straight lines (fig 2.2C). As a result of their shape, these structures are able to unfold in a spring-like fashion upon tensile loading. Basic serpentine interconnects have been reported to accommodate strains up to 50% before mechanical failure [74], while more advanced designs, such as the horse-shoe pattern shown in figure 2.2D, have been able to push that limit to 100% elongation [75, 76, 77]. Increasingly sophisticated geometries have been developed, often taking the form of fractal patterns (fig. 2.2E), with some FEA analysis predicting a maximum elongation of 1200% for a three order fractal design [78].

**Kirigami interconnects** Named after the Japanese art of cutting paper, kirigami interconnects (fig. 2.2F) rely on presence of periodic cuts in the conductive film in order to deform in- and out-of-plane [79, 80]. It is the shape, orientation and density of the patterns etched inside the film that will define the final electro-mechanical properties of the structure, with some strategy reaching a maximum elongation of 370% [81].

**Advantages and downsides** Engineered stretchability is a particularly relevant concept in the context of implantable devices because the designs principles are independent of the materials themselves, allowing the integration of biocompatible or even medical grade compounds into soft neural interfaces. Furthermore, since these geometries are deterministic, their electromechanical performances can more easily be predicted, controlled and optimized in order to reach a trade-off suitable for each application. While these strategies do not allow to reach the level of strain sustained by intrinsically stretchable material, they do fulfill the requirements for use in the nervous system (see subsection 2.1). One notable drawback to engineered stretchability is that most geometries have one, or sometimes two, preferential directions in terms of defor-

mation. As a results of their anisotropic stretchability, they are unable to conform perfectly to non-developable surfaces such as the brain [78]. Furthermore, meander-based approaches also require the electrical layout to be designed in such a way that they can accommodate the serpentine patterns which are often in the same range of dimensions as the interconnects themselves. This effectively places additional constraints in terms of miniaturization of the stretchable tracks. This limitation is the driving force behind the development of some advanced kirigami designs [82], such as the one being used in this work.

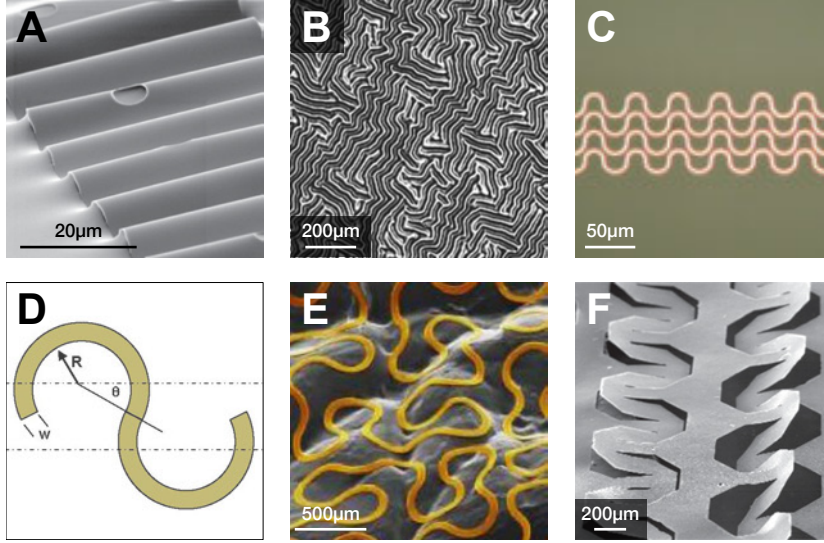


Figure 2.2: Examples of stretchability by design. **A** SEM image of wavy, single-crystal Si ribbons following release of the pre-strained PDMS substrate [83]. **B** Optical micrograph of a wavy gold surface formed via direct thermal evaporation of the metal on a PDMS substrate. Adapted from [71]. **C** Optical micrograph of a gold serpentine interconnect. The meanders were patterned via evaporation through a photoresist shadow mask. Scale bar 100µm. [74] **D** The horseshoe patterns are created by joining a series of circular arcs at varying intersection angles  $\theta$ . The case of  $\theta=0$  corresponds to the basic serpentine design shown in C. Adapted from [75] **E** SEM image of a third-order fractal design based on the horseshow motif [84]. Scale bar 500µm. **F** Example of a microscale kirigami pattern etched periodically into a GO-PVA nanocomposite layer [81].

## 2.2 Micropatterned Thin Films for Engineered Stretchability

### 2.2.1 Introduction

The basis of the technology discussed in this thesis was presented by Vachicouras et al in 2019. The proposed neural interface is represented schematically in figure 2.3A and is composed of three key elements: (1) a series of stretchable electrical interconnects, (2) a thin and elastic silicone encapsulation and (3) a grid of electrodes coated with a

## 2.2 Micropatterned Thin Films for Engineered Stretchability

platinum-silicone composite.

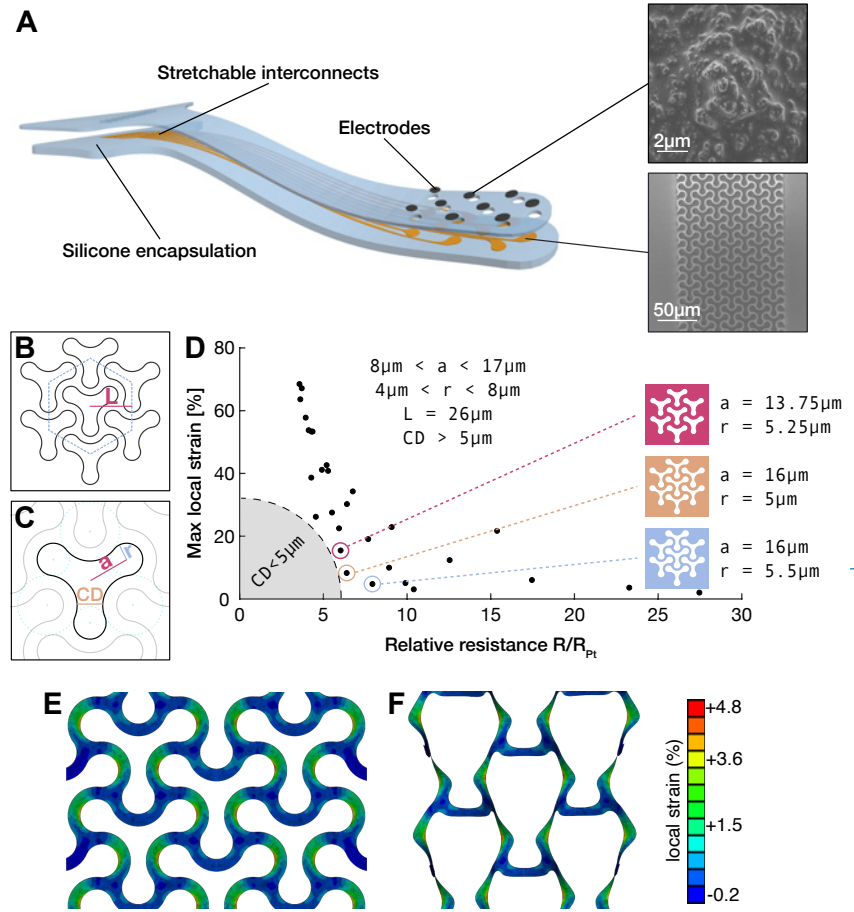


Figure 2.3: Original concept for a micropattern-based soft neural interface. Adapted from [85]. **A** Schematic representation of the kirigami-based neural interface. The stretchable interconnects are composed of a micropatterned stack of polyimide/platinum/polyimide (bottom inset) and encapsulated between two layers of silicone. The electrodes are coated with a Pt-PDMS composite to decrease their impedance (top inset). **B** The pattern is built using an hexagonal structure, enabling isotropic deformation. The period is fixed by design parameter  $L$ . **C** The Y-shaped motif is the atomic cut repeated inside the pattern. It can be described using three parameters only: the branch length  $a$ , the circle radius  $r$  and the critical dimension  $CD$ . **D** Finite element analysis was used to simulate the mechanical and electrical behavior of varying Y-shaped geometries. The parameter space was defined such that the critical dimension  $CD$  is kept above  $5\mu\text{m}$ , to maintain the ability to create the pattern via standard photolithographic techniques. **E** The selected Y-shaped motif is shown here, corresponding to design parameters  $a = 16\mu\text{m}$  and  $r = 5.5\mu\text{m}$ . The computed local strain at 20% elongation is projected onto the structure in order to highlight the location of the strain concentration. **F** The simulated behavior is shown here for the same 20% elongation value, highlighting the out-of-plane deflection mechanism responsible for the stretchability of the structure.

**Interconnects** The stretchable interconnects are based on the kirigami approach discussed in subsection 2.1.2. The fundamental idea consists of creating reversibly stretchable structures by performing periodic cuts into normally inelastic films. This strategy effectively enables the resulting patterned layers to stretch reversibly through a combination of in- and out-of-plane deformations. In Vachicouras et al 2019, this principle is leveraged to manufacture stretchable interconnects consisting of a multilayer stack of polyimide, platinum and polyimide (1/0.1/1 $\mu$ m). The polyimide (PI) layers serve as electrical insulators, while the platinum (Pt) acts as the electrical conductor. The pattern itself is the key factor determining the trade-off between the electrical and mechanical performances of the interconnects. In this case, the Y-shaped motif was inspired by the microcracks observable in the gold track created using the e-Dura process [24]. The pattern is defined by 3 parameters, shown in figure 2.3B-C: the period  $L$ , the branch length  $a$  and the circle radius  $r$ . These parameters were optimized using a combination of macroscale characterization and finite element analysis (fig. 2.3D). The final motif, used throughout the entirety of this work, is shown at rest in figure 2.3E and under tensile strain in figure 2.3F.

**Encapsulation** The top and bottom silicone layers serve not only as a second layer of electrical insulation but more importantly as a mechanical support allowing the device to maintain its shape and to be more easily manipulated. The device outline as well as the openings for the connector and electrode sites are cut via femtolaser machining.

**Electrode coating** The electrode sites are coated with a soft platinum-silicone composite previously developed by Minev et al. in 2015. The coating is applied via screen-printing, through a polyethylene terephthalate (PET) shadow mask. The role of conductive composite is to improve the electrical properties of the device and to provide a soft interface with the tissue.

The work of Vachicouras et al is selected as the technological starting point for this thesis. In this first subsection, the original process flow for manufacturing mouse auditory brainstem implants (ABIs) is described. The resulting devices are then characterized (subsection 2.2.3.2) and a set of technological limitations are identified (subsection 2.2.4). These limitations will be addressed in the revised version of the process flow, detailed in section 2.3.

## 2.2.2 Methods

### 2.2.2.1 Process flow gen 1

The first version of the process flow can be divided into 6 phases: (1) mask design, (2) multilayer stack deposition, (3) interconnects patterning, (4) top silicone encapsulation,

(5) bottom silicone encapsulation and (6) electrode coating and connector assembly.

**Design - Figure 2.4** The design procedure begins with the definition of the electrical layout in a computer-assisted drawing software (AutoCAD, Autodesk). At this stage, the devices are designed completely independently of the Y-shaped patterns, which greatly simplifies the process. Next, the design is transferred in another software (Klayout) where it is inverted and overlaid on top of the Y-shaped motifs. The layer containing the patterns is built using two arrays of Y-shapes, shifted by 26 and 15.011 microns in the horizontal and vertical direction respectively (fig. 2.4 step 3). With this approach, the motif is conveniently instanced only once by the software, which significantly reduces the size of the file. It is the superposition of the layer containing the electrical layout and the one containing the Y-shapes that forms the micropatterned interconnects. The union of the two layers (boolean OR) is performed when the design file is converted into the proprietary format (.LIC) of the lithography system. This operation is computationally quite expensive and the procedure can take up to several hours. Afterwards, the design can be written onto a 5-inch chromium (Cr) mask via direct laser writing (VPG200, Heidelberg Instruments). The Cr plate is then developed and etched in an automatic mask processor (HMR900, Hamatech). The resulting mask can be used for numerous UV exposures on 4-inch wafers.

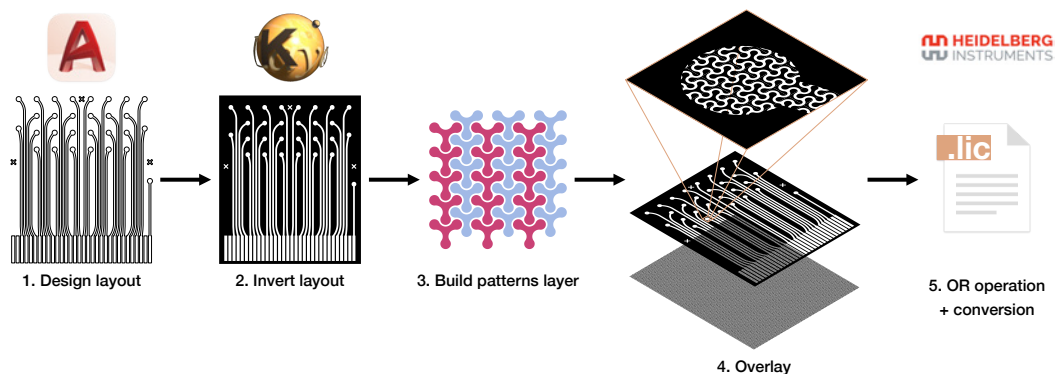


Figure 2.4: Phase 1 of the process flow - design.

**Multilayer stack deposition - Figure 2.5** First, a layer of titanium (Ti 25nm) and a layer of aluminum (Al 100nm) are deposited on a 4-inch silicon (Si) wafer via electron beam evaporation (EVA760, Alliance Concept) at a rate of 5Å/s. Next, the wafer surface is dehydrated in a convection oven at 150°C for 15min (UM100, Memmert) and cleaned via oxygen (O<sub>2</sub>) plasma at 600W, 0.8mbar, 400sccm O<sub>2</sub> for 1min (GiGAbatch, Tepla). Immediately after, a 25nm layer of silicon dioxide (SiO<sub>2</sub>) and a 5nm layer Ti are sputtered (SPIDER600, Pfeiffer) at rate of 11.9nm/min and 120nm/min respectively. Following dehydration on a hotplate (135°C, 3min) and O<sub>2</sub> plasma activation (600W, 0.8mbar, 400sccm,



1min), the surface of the wafer is covered with a 0.1% solution of 3-aminopropyl triethoxysilane (APTES) in isopropanol (VM652, HD MicroSystems) for 30 seconds before being spin-dried. After another dehydration step on a hotplate (110°C, 3min), a 1-micron thick layer of polyimide (PI2611, HD MicroSystems) is spin-coated at 5000rpm (LSM200, Sawatec). The curing of the polyimide (PI) is performed in the following sequence: first, a soft bake on a hotplate at 70°C for 3min, then a second soft bake on another hotplate at 110°C for 3min and finally a hard bake at 200°C under nitrogen (N<sub>2</sub>) atmosphere in a convection oven (Heraeus T6060). The APTES silanization ensures good adhesion between the metallic and organic layers by forming silanols groups with the TiO<sub>2</sub> and amide bonds with the PI. After another round of dehydration at 150°C for 15min (UM100, Memmert) and plasma activation (600W, 0.8mbar, 400sccm O<sub>2</sub>, 1min), the titanium, platinum, titanium layers (Ti/Pt/Ti 25/100/25nm) are deposited via sputtering (SPIDER600, Pfeiffer). All metals are deposited with the DC source power set to 1000W which corresponds to a rate of 120nm/min for the Ti and 230nm/min for the Pt. The APTES silanization steps are then performed again and a second layer of PI (1µm) is spin-coated at 5000rpm (LSM200, Sawatec). Next, the wafer surface is dehydrated (hotplate 110°C 3min) and plasma activated (600W, 0.8mbar, 400sccm O<sub>2</sub>, 1min) one last time. Immediately after, a layer of Ti and a layer SiO<sub>2</sub> (5/25nm) are deposited via sputtering (SPIDER600, Pfeiffer) with identical parameters to the first two layers. This effectively concludes the build up of the multilayer stack.

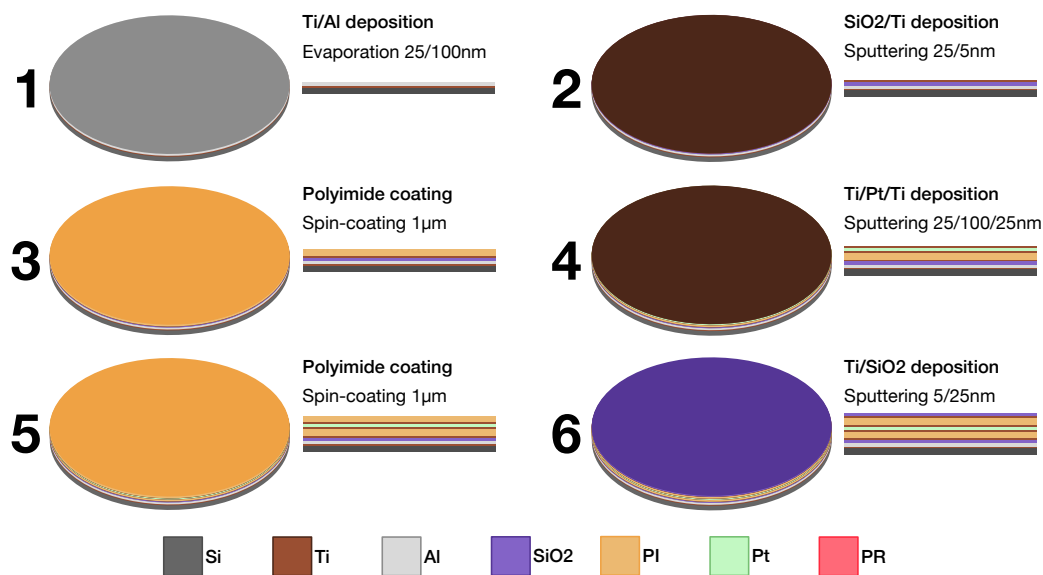


Figure 2.5: Phase 2 of the process flow - multilayer stack deposition.

**Interconnects patterning - Figure 2.6** First, the SiO<sub>2</sub> layer is primed using hexamethyl-disilazane (HMDS) in order to improve the adhesion of the subsequent photoresist (PR) film. Next, a PR layer of 5µm (AZ ECI 3027, MicroChemicals) is spin-coated at 1000rpm



## 2.2 Micropatterned Thin Films for Engineered Stretchability

(Series 88, RiteTrack) and baked on a hotplate at 115°C for 3min 25s. The exposure is performed on a mask aligner (MA6gen3, Süss) using a chromium mask previously patterned via direct-write laser lithography (VPG200, Heidelberg Instruments). The mask is designed such that the interconnects and Y-shaped motifs are defined at once, in a single lithographic step. The illumination dose is set to 430mJ/cm<sup>2</sup> (i-line) and the mask is placed in hard contact with the wafer. Following a post-exposure bake at 110°C for 2min, the PR is developed on the RiteTrack Series 88 using a TMAH-based solution (MF CD 26, Shipley Microposit) for 83s. The SiO<sub>2</sub>/Ti and PI layers are then dry etched using a CHF<sub>3</sub>/He and O<sub>2</sub> chemistry respectively (Advanced Plasma System, SPTS). The Ti/Pt/Ti metal stack is subsequently removed via ion beam etching (Nexus IBE350, Veeco). During this step, the wafer is tilted by a -10° angle with respect to the incoming argon (Ar) ions flux. Afterwards, the bottom PI and Ti/SiO<sub>2</sub> layers are etched using the same chemistry as before. The remaining PR is stripped using a 70°C solvent bath (Microposit Remover 1165, Dow Chemicals) combined with sonication. Next, the wafer is dehydrated and a 3-micron thick layer of PR is deposited (2800rpm, soft bake at 115°C for 3min). The openings for the contacts and electrode sites are then defined using a second chromium mask on the Süss MA6gen3 (260mJ/cm<sup>2</sup>, hard contact). The development is performed identically as before, except for the fact that the total contact time with the developer is reduced to 59s. Three etching steps are then performed sequentially: a CHF<sub>3</sub>/He etch to remove the top SiO<sub>2</sub>/Ti, an O<sub>2</sub> etch to remove the PI and finally, an Ar ion etch to clear the 25-nanometer thick layer of Ti (-10° tilt). This last step is performed to provide direct access to the Pt layer, as the Ti film could cause an increase in electrode impedance once it oxidizes. Finally, the left-over PR is stripped using the same method as described before, effectively concluding the fabrication of the micropatterned interconnects.

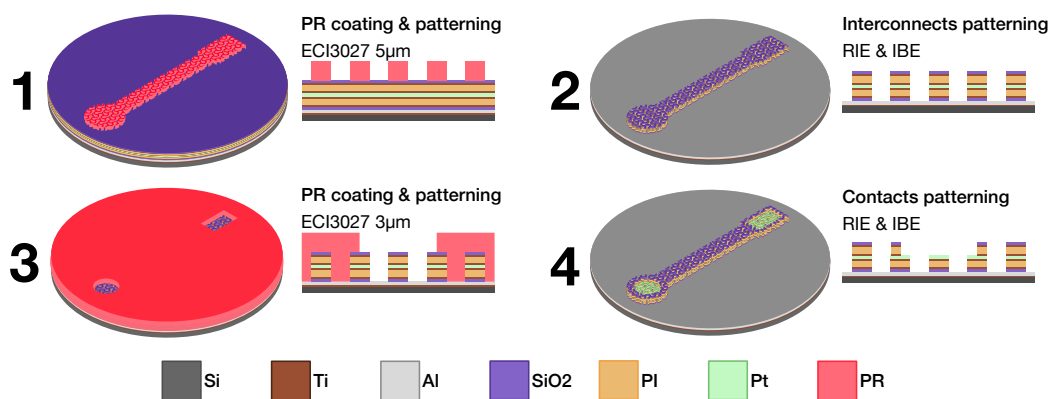


Figure 2.6: Phase 3 of the process flow - interconnects patterning.

**Top silicone encapsulation - Figure 2.7** The fabrication of the silicone encapsulation starts with the manufacturing of a carrier for the top polydimethylsiloxane (PDMS) membrane. The process begins by adding the silicone monomer (Sylgard 184 part A, Dow

Corning) to the cross-linker (Sylgard 184 part B, Dow Corning) following a 10-to-1 weight ratio between the two. The blend is mixed together and degassed (ARE-250, Thinky) before being spin-coated (EL S 200, Obducat) on a 4-inch silicon wafer at 3200rpm. Following a 10min reflow period on a flat surface, the PDMS layer is cured in a convection oven () at 75°C for 2h. Next, the manufacturing of the top encapsulation itself can begin. A first polyethylene terephthalate (PET) sheet of 23 $\mu$ m (DuPont Mylar 23A, Lohmann Technologies) is manually laminated onto the carrier wafer and cut to shape with a razor blade before being wiped with isopropanol (IPA). A new batch of PDMS is prepared following the same process as before and a 75-micron thick layer is spin-coated directly onto the PET. Just as before, the fresh PDMS layer is cured at 75°C for 2h after a 10-minute reflow. Afterwards, a second 23-micron thick PET sheet is laminated and cut to shape with a razor blade. The PET/PDMS/PET stack is then peeled off the carrier (Si/PDMS), which can now be reused for the creation of additional encapsulation stacks. Next, femtolaser machining (WS-TURRET 200, Optec) is used to cut the openings for the contacts and electrode sites in the newly fabricated encapsulation stack. In order to be bonded on top of the wafer containing the micropatterned interconnects, the PET/PDMS/PET stack is first mounted onto an acrylic disk using a thick PDMS slab as a weak adhesive between the two. The top PET sheet is then carefully peeled off, revealing the PDMS layer underneath. Both the interconnects wafer and the mounted encapsulation stack are then placed in a plasma oven (PCCE Nano, Diener) where an O<sub>2</sub> treatment is performed (100W, 0.2mbar, 30s) in order to activate the SiO<sub>2</sub> and PDMS layers respectively. The Si wafer and the acrylic disk are then mounted onto a custom alignment tool consisting of a vacuum holder attached to a z-axis micromanipulator atop of a x-y- $\theta$  stage. Using the pair of overhanging CCD cameras, the PET/PDMS encapsulation can be aligned with the structures present on the interconnects wafer before being lowered and pressed against it. Next, the stack is unloaded from the aligner, allowing for the acrylic disk and PDMS slab to be removed. the top PET film is kept in place, as it will later be used as a screen-printing mask. To complete the bonding process of the top PDMS membrane, the assembled stack is placed under a weight of 2kg and kept in an oven at 75°C for 12h.

**Bottom silicone encapsulation - Figure 2.8** Following the top bonding sequence, the wafer surface is divided into multiple parts by laser-cutting (WS-TURRET 200, Optec) the PET/PDMS layer. This step is performed to facilitate the assembly of the bottom PDMS membrane. Next, the individual pieces of the PET/PDMS/PI/Pt/PI stack are released from the carrier Si wafer via anodic dissolution of the Al layer. To do so, the wafer is placed in a sodium chloride solution (NaCl in H<sub>2</sub>O, 15g/L) alongside a Pt counter electrode and a potential of 1.5V is applied between the two for about 8h. The released samples are washed in deionized water and dried at room temperature. Next, the manufacturing of the bottom PDMS membrane can begin. Following an oxygen plasma treatment (200W, 0.2mbar, 5min), a 4-inch silicon wafer is covered with a sacrificial layer of

## 2.2 Micropatterned Thin Films for Engineered Stretchability

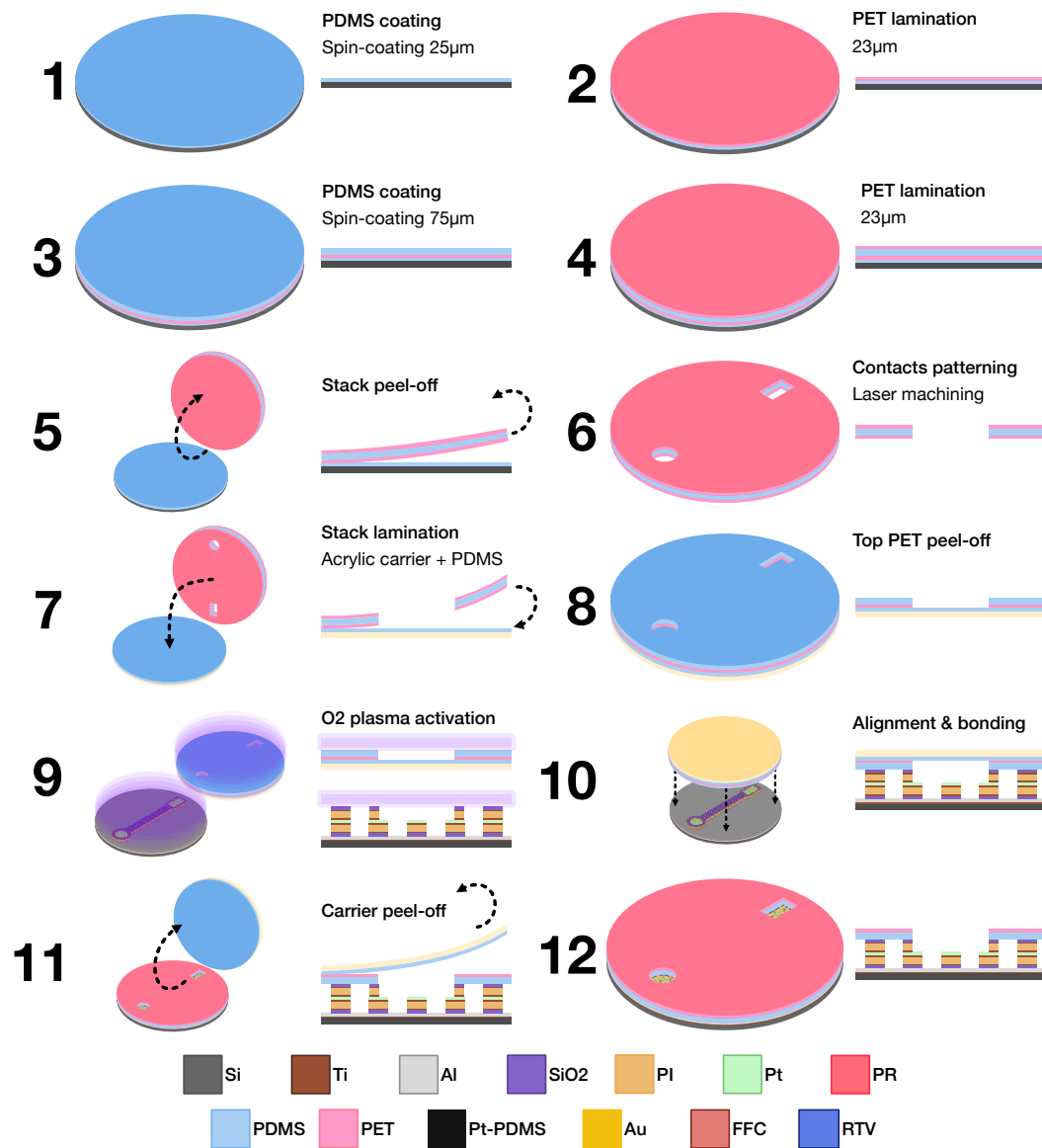


Figure 2.7: Phase 4 of the process flow - top silicone encapsulation.

Poly(sodium 4-styrenesulfonate) (PSS, Sigma Aldrich) by spin-coating the solution at 3200rpm. A 50-micron layer of PDMS (Sylgard 184, Dow Corning, 10:1 ratio) is then spin-coated on top and cured in an oven at 75°C for 2h. Next, a second PDMS layer of 20µm is spin-coated on top of the first one but this time the curing process is interrupted as soon as the gel point is reached (approximately after 15min at 75°C). Immediately after, the wafer and the pieces of the PET/PDMS/PI/Pt/PI stack then placed in a plasma oven (, Diener) where an O<sub>2</sub> treatment is performed (100W, 0.2mbar, 30s) in order to activate the SiO<sub>2</sub> and PDMS. The bottom bonding sequence is performed manually by carefully laying down the individual stack parts on the PDMS, with the PET side facing up. Finally, the curing of the PDMS is completed by placing the wafer back in an oven at 75°C for 2h.

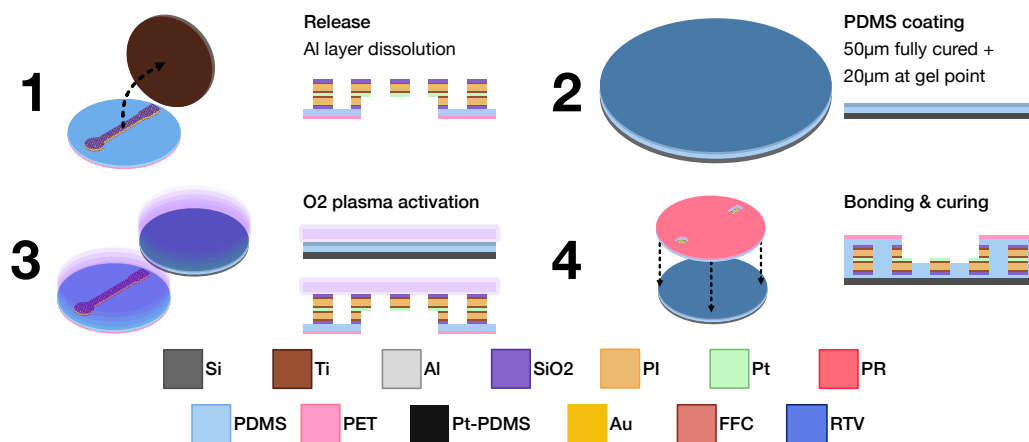


Figure 2.8: Phase 5 of the process flow - bottom silicone encapsulation.

**Electrodes coating and connector assembly - Figure 2.9** The process begins with the preparation of the Pt-PDMS composite for the coating of the electrode sites. First, a fresh batch of PDMS (Sylgard 184, Dow Corning) is prepared, following a 2-to-1 weight ratio between the monomer and the cross-linker. Next, an organic solvent (Cyclohexane, Sigma Aldrich) is added in order to obtain a 2:1 cyclohexane:PDMS blend. 742µL of the obtained solution are then pipetted in a glass Petri dish and mixed with 500mg of Pt particules (diameter 0.27-0.47µm, Strem Chemicals) using a spatula. Once the mixture is homogenous, the cyclohexane is evaporated under vacuum, resulting in a conductive composite with a PDMS-to-Pt ratio of 30%wt and a working time of 2 to 3 hours. Next, the surface of the wafer prepared previously is activated via an O<sub>2</sub> plasma treatment (20W, 0.2mbar, 30s). Immediately after, the Pt-PDMS composite is screen-printed onto the electrode sites, using the top PET film as a stencil mask. For the contact pads, a conductive silver paste (H27D Part A, Epotek) is used in lieu of the Pt-PDMS composite. Once this is done, the PET layer is carefully peeled off, exposing the top PDMS encapsulation. The connectors are then placed manually with a pair of precision tweezers or with a custom pick-and-place platform, depending on the selected parts. A layer of

## 2.2 Micropatterned Thin Films for Engineered Stretchability

silicone (RTV 734, Dow Corning) is applied on top and around the connectors to secure them in place. Afterwards, the whole assembly is left to rest overnight at room temperature before a last curing step in a convection oven (55°C, 3h). Finally, the outline of the individual devices is defined by laser-cutting (WS-TURRET 200, Optec) the PDMS encapsulation and the structures are released from the carrier wafer by dissolving the sacrificial PSS layer in a bath of deionized water.

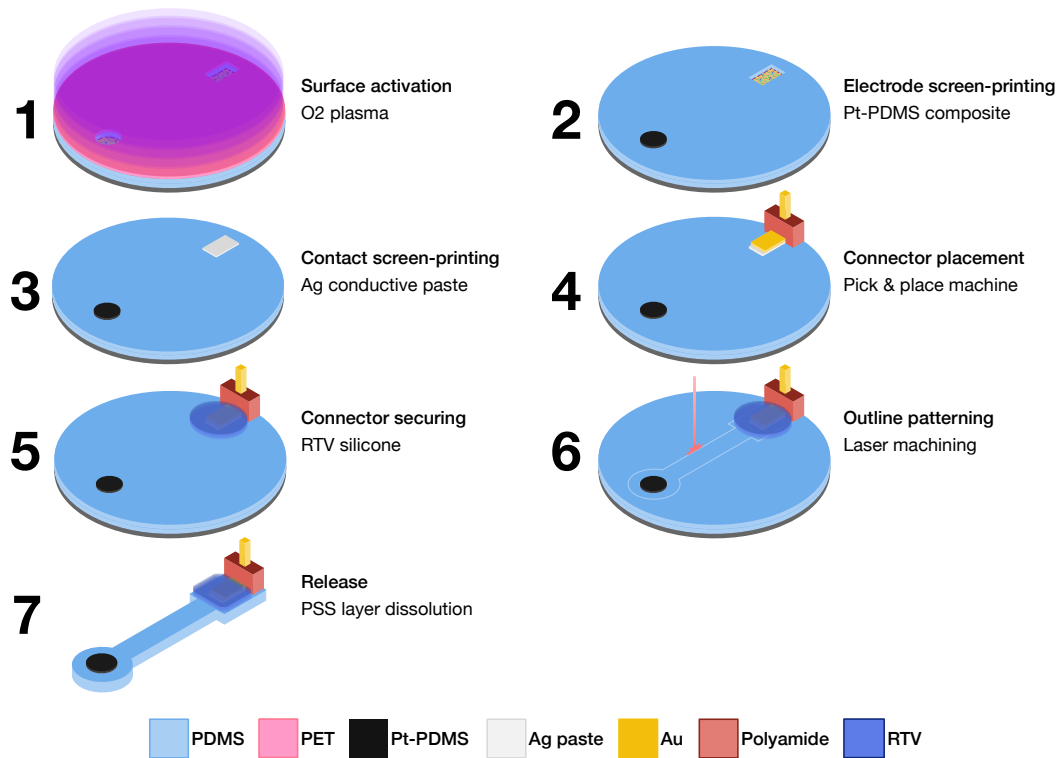


Figure 2.9: Phase 6 of the process flow - electrodes coating and connector assembly

### 2.2.2.2 Electromechanical characterization

**Impedance spectroscopy** In-vitro electrochemical impedance spectroscopy (EIS) is performed using a potentiostat (Reference 600, Gamry Instruments or Autolab PGSTAT128N, Metrohm) in a 3-electrode configuration. The Ag/AgCl reference electrode, platinum counter electrode and implant under test (working electrode) are immersed in PBS (1x) and the impedance spectrum is measured between 0.1Hz and 1MHz (or 500kHz, in the case of the Autolab) using an input signal amplitude of 100mV (root-mean-square).

**Chronopotentiometry** Voltage transients (VTs) are measured in PBS (1x) upon the application of symmetric, biphasic, cathodic-first, current pulses between the electrode under test and a platinum counter electrode. The pulses amplitude is set to 100μA and

their duration to 600 $\mu$ s (300 $\mu$ s/phase), with an inter-pulse period of 10ms. The resulting VTs are collected via an oscilloscope (MDO3014, Tektronix) connected across the two poles of the current pulse generator (ISP2100, A-M Systems). For each device, the access voltage, i.e. the purely resistive drop occurring at the onset of a current pulse, is estimated by averaging the voltage values over the first  $\mu$ s of each phase.

### 2.2.3 Results

#### 2.2.3.1 Microfabrication

A processed wafer is shown in figure 2.10A, prior to the bonding of the top PDMS encapsulation. SEM images reveal that the Y-shaped motifs were etched through the entire multilayer stack and that the top PI layer was properly removed from the contacts and electrodes area (Fig. 2.10B-E). The dimensions of the patterns are found to be within a  $\pm 400$ nm range of the target features. Two phenomena are likely responsible for these differences: (1) imperfect transfer of the pattern during photolithography, either on the Cr mask itself or on the wafer and (2) non-fully vertical etching of the polyimide layers.

A tilted view of a contact pad reveals the absence of aluminium at this location (Fig. 2.10D-E). The removal of the sacrificial layer is a byproduct of the etching of the top Ti layer at the very end of the contacts opening sequence. Indeed, during the IBE process both metals are exposed and etched, albeit at a much faster rate for the aluminium. As a result, the Al layer is completely removed except underneath the meanders. While the undesirable etching of the aluminium doesn't prevent the proper release of the structure, it does generate vertical redeposition along the periphery of the contacts.

A similar type of redeposition can be observed on the transectional view in figure 2.10F. The fence, a byproduct of the removal of the Ti/Pt/Ti via IBE, runs all along the sides of the micropatterns. Figure 2.10F also reveals the stepped profile of the multilayer stack: the top PI film is found to be receded by somewhere between 400 and 500nm compared to the bottom layer. Nevertheless, the remaining surface area is sufficiently large to allow for the proper bonding of the top PDMS encapsulation.

#### 2.2.3.2 Neural interfaces gen 1

Using the process described in section 2.2.2.1, two models of auditory brainstem implants (ABIs) were manufactured, one designed for use in mice (track length 12.5mm, electrode diameter 150 $\mu$ m) and the other in non-human primates (track length 40mm, electrode diameter 100 $\mu$ m).

## 2.2 Micropatterned Thin Films for Engineered Stretchability

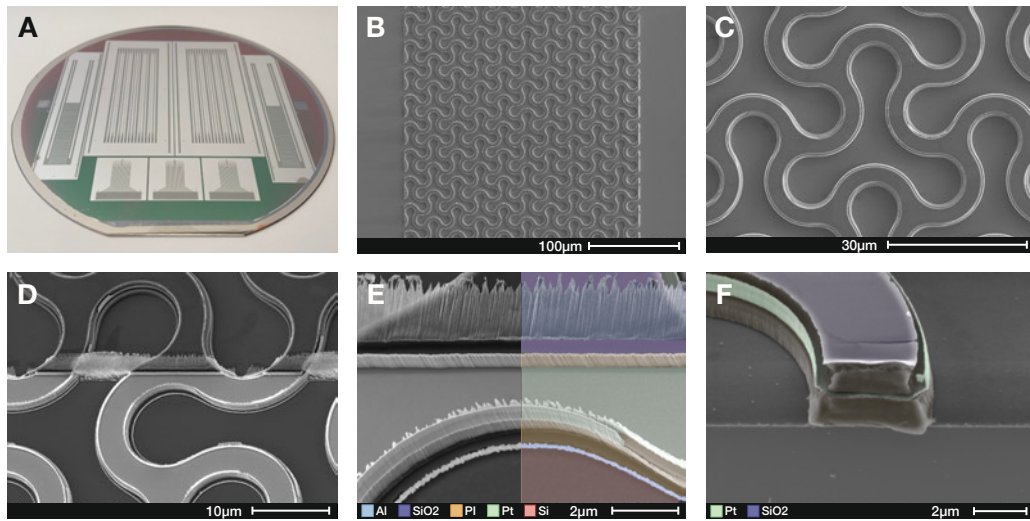


Figure 2.10: Microfabrication results following the completion of phase 3. **A** Picture of a wafer featuring four devices for electromechanical and hermeticity characterization as well as 3 electrode paddles at the front. **B** SEM image of a micropatterned interconnect. **C** Close-up view of the Y-shape motif etched into the multilayer stack. **D** Tilted view (30°) of a contact pad. **E** Close-up view of the transition between covered and exposed platinum. The right side of the image has been colorized to show SiO<sub>2</sub> in purple, PI in orange, platinum in green, Si in red and Al in blue. Note the absence of Al at the bottom and the presence of fence, fallen over the SiO<sub>2</sub>. **F** Transectional view of a micropatterned interconnect.

**Mouse ABIs** The mouse ABIs (Fig. 2.11A) were devised to investigate the differences, and potential interactions, between electrical and optical stimulation of the auditory brainstem in genetically modified animals. The implants feature 2 electrodes of 150 $\mu$ m diameter, addressable individually via a surface mount pin header (Molex), and an optical window through which light can be shined using an optic fiber connected to an external laser source (Fig. 2.11C). The third and fourth pins of the header were left unconnected and kept solely to provide additional mechanical stability during the placement of the connector. Figure 2.11B illustrates how precisely the PDMS outline can be defined via femto-laser machining, with a track-to-edge distance of only 200 $\mu$ m. The impedance spectrum (Fig. 2.11D) shows that the ABI behaves the closest to a purely resistive system at a frequency of 10kHz (phase  $-2.97^\circ \pm 1.23^\circ$ ). The impedance at this frequency is similar to the one seen by the generator when injecting current pulses. Indeed, imposing a sudden change in current (e.g. from 0 to 100 $\mu$ A) corresponds to the application of a very high frequency voltage, a situation in which the double layer capacitance at the interface is effectively short-circuited. As a result, the impedance at maximum phase (closest to  $0^\circ$ ) provides the most adequate value to assess the current injection capabilities of the ABI. Here, the average impedance at 10kHz is found to be  $6.5 \pm 1.4$  k $\Omega$ , a value which indeed corresponds closely to the access voltage of  $-6.07 \pm 1.15$  V and  $5.86 \pm 1.15$  V measured upon the injection of a current pulse of -1mA and +1mA respectively.

**NHP ABIs** The NHP ABIs (Fig. 2.11F) were designed to investigate the potential benefits of a compliant neural interface when attempting to restore auditory percepts via brainstem stimulation. A flexible flat cable (FFC) allows to address each one of the 11 electrodes (Fig. 2.11G, diameter 100 $\mu$ m) constituting the paddle. The transition between the FFC and the micropatterned interconnects is realized using a surface mounted, zero insertion force (ZIF) connector. The ZIF connector is isolated using a layer of RTV silicone applied manually with a syringe. As shown in Fig. 2.11I, poor execution of this step can lead to the presence of voids inside the seal, which are likely to lead to early device failure. The EIS reveals the maximum phase impedance to be located at a frequency of 30kHz (phase  $-9.64^\circ \pm 2.48^\circ$ ) with a value of  $23.23 \pm 11.49$  k $\Omega$ . The larger standard deviation compared to mouse ABI is likely driven by the longer interconnects (12.5mm vs 40mm) which are more prone to fabrication defects and mechanical damages during handling. The voltage transients measurements yield an access voltage of  $-4.66 \pm 1.72$  V and  $4.05 \pm 1.24$  V for a biphasic current pulse of  $\pm 200\mu$ A. Again, these values are within range of to the ones predicted by EIS ( $23\text{k}\Omega \times 200\mu\text{A} = 4.6\text{V}$ ), a demonstration that the maximum phase impedance does allow to assess accurately the performance of the electrodes when stimulating.



## 2.2 Micropatterned Thin Films for Engineered Stretchability

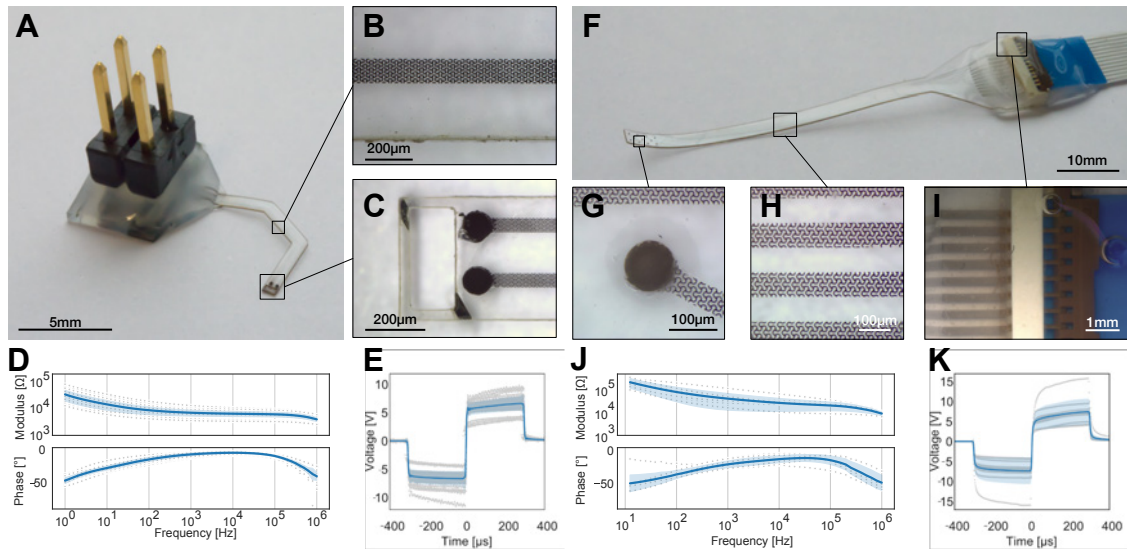


Figure 2.11: First generation of soft neural interfaces. **A** Picture of a 2-channel mouse ABI connected to a surface mounted pin header. **B** Microscope picture of the 100-micron-wide interconnect running alongside the laser-cut edge of the device. **C** Microscope picture of the two coated electrodes next to the optical window. The diagonal stripe across the window serves as a visual identifier for the top and bottom side of the implant. **D** Impedance modulus (top) and phase (bottom) typical of the mouse ABI electrodes (n=22 devices, 2 electrodes each). The shaded area corresponds to the standard deviation. **E** Voltage transients of the mouse ABI upon biphasic current stimulation in PBS at 1mA (n=22 devices, 2 electrodes each). The shaded area corresponds to the standard deviation. **F** Picture of a 11-channel primate ABI connected to a flexible flat cable via a zero-insertion force (ZIF) connector. **G** Microscope picture of an electrode coating with the Pt-PDMS composite. **H** Microscope picture of four 80-micron-wide interconnects running parallel to each other. **I** Microscope picture of the connector revealing the presence of voids inside the RTV overmolding. **J** Impedance modulus (top) and phase (bottom) typical of the primate ABI electrodes (n=1 device, 11 electrodes each). The shaded area corresponds to the standard deviation. **K** Voltage transients of the primate ABI upon biphasic current stimulation in PBS at 200μA (n=1 device, 11 electrodes). The shaded area corresponds to the standard deviation.

### 2.2.4 Summary and Discussion

**Summary** In this section, the ability to fabricate stretchable, conductive tracks via microscale patterning was demonstrated. These interconnects are composed of a 2-micron thick, multilayer stack of SiO<sub>2</sub>/PI/Ti/Pt/Ti/PI/SiO<sub>2</sub>, through which a Y-shaped motif is periodically etched. The resulting electrical layout is encapsulated between two PDMS membranes by means of plasma bonding in order to form a device that can be manipulated by hand. The screen-printing of a Pt-PDMS composite and a conductive silver paste allows for the creation of soft electrodes and contact pads respectively. The fabrication of a complete device is achieved with the addition of a surface-mounted connector on top of the latter. Two designs were introduced:

1. A small-scale ABI devised to stimulate the auditory brainstem of genetically modified mouse. The implant featured two electrodes of 150 $\mu$ m in diameter, addressable individually via a surface mount pin header (Molex). EIS in PBS showed an impedance value of 6.5k $\Omega$  at 10kHz. The devices were able to deliver 1mA current pulses with 6V.
2. A large-scale ABI devised to stimulate the auditory brainstem of non-human primate. The implant featured 11 electrodes of 150 $\mu$ m in diameter whose impedance in PBS at 30kHz was found to be 23k $\Omega$ . The VTs curves showed a drop of about 4V when injecting current pulses of 200 $\mu$ A.

The fabrication and characterization of the devices listed above highlighted a set of shortcomings that needed to be addressed before the technology could be deployed chronically in large animal models. More specifically, key technological improvements needed to be made with regard to the encapsulation, the connection scheme and the patterning strategy.

**Polyimide encapsulation** The main concern with the first generation of devices is the lack of complete encapsulation of the interconnects. Indeed, due to the fact that the PI and metal layers are etched using a single mask, the Pt and Ti films are left uncovered along the sides of the patterned structures (Fig. 2.10F). While the exposed area should theoretically be limited to the thickness of the metal layers (150nm total), SEM imaging reveals a significantly larger proportion of bare metal. Two undesirable metal surfaces can be identified: a vertical one, formed by redeposition of Ti/Pt/Ti on the PI sidewalls and a horizontal one, caused by the narrowing of the top PI film (Fig. 2.12A in red and green respectively). These surfaces both originate from the removal of the metal layers via ion-beam etching.

Because IBE is a purely physical process, the Ti and Pt species do not recombine into a gas to be evacuated away from the wafer surface and have thus a strong tendency

## 2.2 Micropatterned Thin Films for Engineered Stretchability

to redeposit on the sides of the nearby structures (Fig. 2.12B). This effect is further exacerbated in high aspect-ratio patterns, such as the ones being considered here, because they present more surface area on which the metal atoms can reattach. The redeposited materials eventually aggregate into the continuous vertical structures observed in figure 2.12A and often referred to as fences. A common strategy to mitigate the fencing effect is to tilt the wafer during the etching process. By doing so, the sidewalls are exposed to the incoming Ar ions and part of the materials that is being redeposited there can be removed (Fig. 2.12C step 1-2). A drawback of this technique however is the tapering of the layers above the one being etched. It is this change in profile that is responsible for narrowing of the top PI film. Indeed, during the removal of the second PI layer, the angled profile is also etched by the oxygen plasma, leading to the exposure of the metal underneath (Fig. 2.12C step 3).

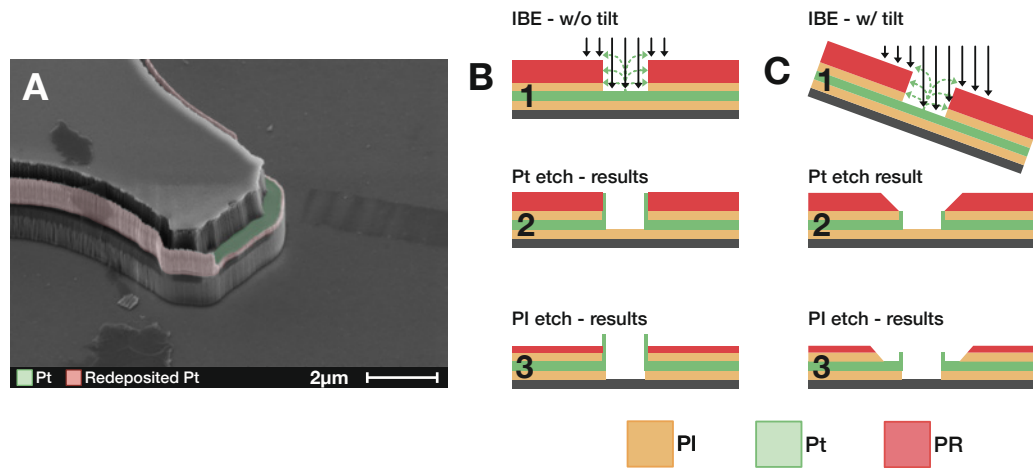


Figure 2.12: IBE fence formation. **A** SEM image of the micropatterned stack. The IBE process creates two bare metal surfaces, highlighted in red and green. **B** Illustration of fencing effect during IBE without tilt. **C** Schematic drawing of the stepped profile formation following IBE with tilt.

Without the PI layer, the PDMS encapsulation is the only barrier shielding these exposed metal surfaces from their environment. This raises concerns in terms of hermeticity, as elastomers have shown a significantly larger ions diffusivity compared to stiff polymer such as PI [86]. The primary adverse effect of ions diffusion arises when the reactive species reach the metal layers. There, the ions will begin to corrode the titanium and platinum [87, 36], leading to the progressive delamination of the encapsulation layers and, ultimately, device failure [34, 35]. With the absence of a polyimide barrier over a large part of the metal film, this diffusion-related failure mechanism is bound to develop at an accelerated rate.

**Connection scheme** The first generation of micropattern devices featured exclusively off-the-shelf connectors. Two categories of surface-mounted devices (SMD) were routinely used: (1) right angle pin header and (2) zero insertion force (ZIF) connector. Pin headers are the most convenient connector to interface with however they have a very large footprint and their significant height above board make them primed to being ripped off, causing the destruction of the implant. This makes them unsuitable for applications requiring a large number of channels or for chronic deployment in highly dextrous animal model, such as non-human primate. While ZIF connectors are significantly more compact in comparison, with contact pitch of 0.5mm and a height above board of only 2mm, they still create a stiff region at the interface of which mechanical stresses will concentrate. Furthermore, they must be combined with a flexible flat cable (FFC), which presents two challenges. Firstly, commercial FFC are single layer, resulting in a wide and stiff cable that can quickly interfere with the proper placement and securing of the implant. Secondly the FFC requires to be sealed inside the ZIF connector in order to avoid biological liquid from entering and shorting the interconnects. Since in this case the silicone sealant is simply applied on top of the connector using a syringe, the encapsulation is bound to be imperfect, containing many voids. Air pockets are always a concern in implantable devices as they offer favorable ground for water to condensate. The presence of liquid water will itself accelerate ions diffusion through osmosis, precipitating the corrosion process and, eventually, the failure of the device.

Another drawback with the connection scheme is the use of silver conductive paste. This compound was implemented because it allows to form both highly conductive and mechanically compliant electrical contacts, which prevents stresses building up at the interface with the connector to cause device failure. In the process flow presented in section 2.2.2.1, the conductive paste is screen-printed over the entire contact area, which means it is mostly only encapsulated by the 75-micron thick PDMS membrane on the bottom side. As discussed previously, ionic body fluid will inevitably diffuse through the silicone layer and begin the corrosion process of the silver particles, eventually leading to failure of the contacts (Fig. 2.13).

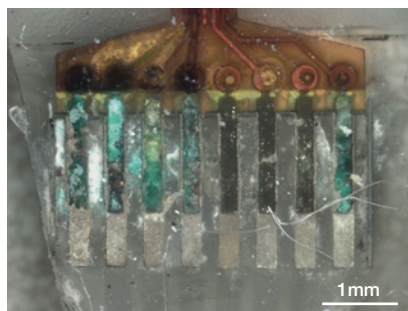


Figure 2.13: Micrograph of catastrophic failure caused by silver particles corrosion following accelerated ageing at 67° C for 24 months.

## 2.2 Micropatterned Thin Films for Engineered Stretchability

**Patterning strategy** In the first iteration of the process flow, the entire materials stack (SiO<sub>2</sub>/PI/Ti/Pt/Ti/PI/SiO<sub>2</sub>) is etched at once, using a single photoresist (PR) mask. While this approach avoids the need for inter-layer alignment, it also requires extremely accurate timing of each of 5 consecutive etching processes. Although some of these risks can be mitigated by using a thicker mask, the height of PR cannot be increased arbitrarily. Indeed, the thickness of the resist also needs to be chosen in order to: (1) prevent fences buildup during the IBE process and (2) keep the aspect ratio of the PR mask below 1:1. Concretely, if the PR layer is too thick, the IBE fencing effect will worsen and the accuracy of the lithography will decrease. On the other hand, if the PR layer is too thin, the top SiO<sub>2</sub>/PI will be attacked during the second O<sub>2</sub>/CHF<sub>3</sub> etching sequence, making it impossible to bond the top silicone membrane. While the appropriate PR thickness can be found via trials and errors, this single mask approach leaves very little leeway for adding new materials to the stack. Furthermore, the extensive processing undergone by the PR mask make it extremely hard to strip. In fact, the complete removal of the resin requires a sonication procedure so extensive that it can sometimes lead to delamination or even shattering of the Si carrier.

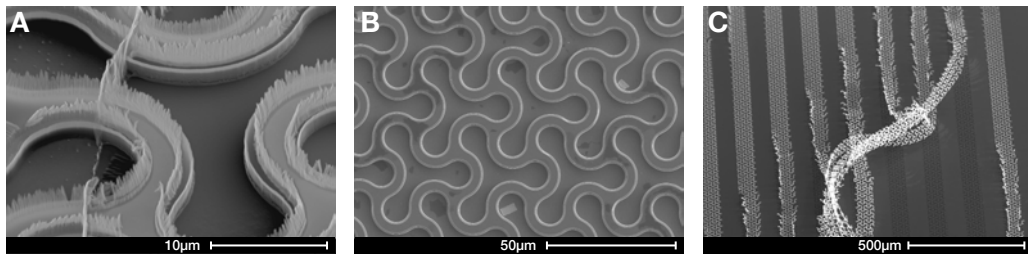


Figure 2.14: Technical challenges related to the patterning strategy. **A** Excessive etching during the first CHF<sub>3</sub>/O<sub>2</sub> sequence lead to increased recessing of the top SiO<sub>2</sub>/PI and to catastrophic fence buildup during the subsequent IBE step. **B** SEM image of a wafer surface following 80min in a heated solvent bath, 40 of which were spent with sonication at maximum power. Despite it all, patches of PR are still visible. **C** Track delamination following prolonged sonication.

**Outlook** The first generation of kirigami-inspired neural interfaces highlighted several challenges that needs to be addressed in a revised version of the fabrication process:

1. The encapsulation of the interconnects needs to be improved such that the metal layers are completely enclosed inside both the polyimide and the silicone.
2. The patterning strategy needs to be revisited in order not only to avoid the IBE fencing effect but also to provide more leeway in terms of the materials that can be integrated in the stack. This new approach should also seek to facilitate the stripping of the photoresist masks.

3. The connection scheme has to be overhauled. The use of large-size, stiff connectors and conductive silver paste has to be abandoned in favor of a low-profile, mechanically compliant connector.
4. The mask fabrication process should be optimized in order to avoid long computation time when the design file is converted by the lithography system.

### 2.3 Core-shell Micropatterns for Improved Stretchable Interconnects

#### 2.3.1 Introduction

The method to manufacture micropattern-based neural interfaces presented in section 2.2 suffered from several key limitations that prevented not only its scaling to chronic experiments in large animal models but also the potential transition to new materials. In order to address these shortcomings, a new patterning strategy needed to be developed. The fundamental idea consists of etching the conductive and dielectric layers in two separate steps. The key innovation is that the Ti/Pt/Ti films are patterned with a slightly scaled up version of the Y-shaped motif used for the PI. This effectively allows the conductive and dielectric layers to perfectly interlock inside each other, providing full encapsulation of the Ti/Pt/Ti. The improved kirigami motifs are dubbed core-shell micropatterns, as way to convey the fact that, with this new approach, the conductive core is fully contained inside an insulating sheath.

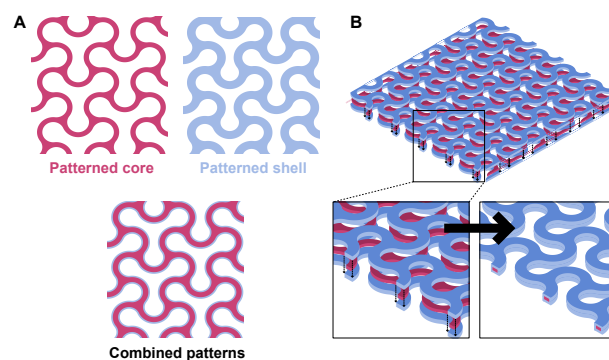


Figure 2.15: Illustration of the core-shell micropatterning strategy. **A** The core layer is patterned using a slightly scaled up version of the Y-shaped motif, resulting in a narrower meandering track that fits inside the shell layer. **B** The conductive core is sandwiched inside the insulating shell, such that it is completely encapsulated.

In order to implement this idea, a series of changes needed to be made in the fabrication process - it is the main subject of the methods subsection 2.3.2. The resulting structures are shown and discussed in part 2.3.3 in which the two generations of interconnects are then compared in terms of mechanical fatigue, ultimate tensile strength and hermeticity. With regard to functional devices, the new core-shell strategy was used to fabricate a large assortment of neural interfaces targeted at both neural stimulation (ABI, spinal cord implant) and recording (ECoG). This particular section will focus on the updated versions of the mouse and NHP ABIs, presented here as a mean of comparison between the two generations of implants. The remaining limitations of the core-shell process are discussed in the final part of this section.

### 2.3.2 Methods

#### 2.3.2.1 Process flow gen 2

**Design - Figure 2.16** The process begins with the definition of the electrical layout in a computer-assisted drawing software (AutoCAD, Autodesk). Next, the outline is transferred in another software (KLayout) and converted to the Graphic Design System II file format (.GDS) in order to enable instantiation of the different design elements. There, the electrical layout is inverted and overlaid on top of an array of Y-shapes. In the second iteration of the process flow, the base motif forming the patterned layer is redefined such that a single array is needed instead of two. Furthermore, the pattern is built such that it contains two nested Y-shapes, one for the patterning of the core layers and one for the patterning of the shell layers. The offset between the two motifs is set to 1µm, which defines the alignment accuracy required between the core and shell layers in order to achieve full encapsulation. The union of the core-shell patterns and the inverted outline (boolean OR) is performed in KLayout, resulting in a separate file for each of the two layers. Performing this operation destroys the software-defined instances which significantly increases the file size (from 10MB to >1GB). Nevertheless, this trade-off is beneficial as the conversion time on the lithography system (X-convert) is shortened to 30 minutes instead of 3 hours. Finally, the design can be written onto a 5-inch Cr mask via direct laser writing (VPG200, Heidelberg Instruments). The mask is then developed and etched in an automatic mask processor (HMR900, Hamatech).

**Core layers patterning - Figure 2.17** The fabrication process begins with the sputtering (SPIDER600, Pfeiffer) of a tungsten-titanium alloy film (TiW, 50nm) followed by aluminium (Al, 100nm) on a 4-inch silicon wafer. The increased conductivity of the TiW alloy compared to bare Ti will result in a faster anodic dissolution of the Al sacrificial layer at the end of the process. Next, the wafer surface is dehydrated at 150°C for 15min (UM100, Memmert) and cleaned from organic contaminants with an oxygen plasma treatment (GiGAbatch, Tepla at 600W, 0.8mbar, 400sccm, 2min). Soon after, a 25nm layer of SiO<sub>2</sub>



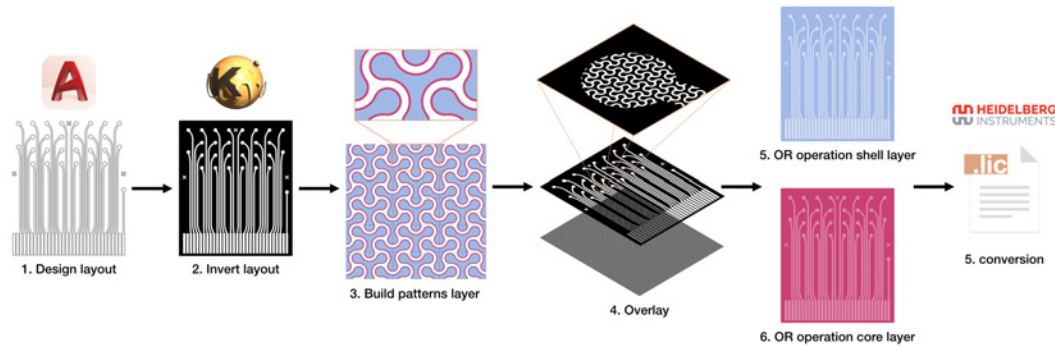


Figure 2.16: Phase 1 of the process flow - design.

and a 5nm layer of Ti are deposited via sputtering. Following another dehydration step in a convection oven and O<sub>2</sub> plasma activation (600W, 0.8mbar, 400sccm, 1min), the wafer surface is covered for 30 seconds with a 0.1% solution of APTES in isopropanol (VM652, HD MicroSystems) before being spin-dried. The wafer is heated on a hotplate once more (135°, 3min) before being coated with the first layer of PI (1µm PI2611, HD MicroSystems). The curing of the PI is performed in 3 stages: (1) soft bake at 70°C for 3min, (2) soft bake at 110°C for 3min and (3) a hard bake at 200°C under nitrogen atmosphere in a convection oven (Heraeus T6060). Next, the wafer surface is dehydrated (150°C, 15min) and plasma activated (200W, 0.5mbar, 200sccm O<sub>2</sub>, 30s) after which the Ti/Pt/Ti layers (25/100/25nm) are deposited via sputtering. The patterning of the metal films can then begin with the spin-coating of a 0.7-micron layer of PR (AZ 10XT-07, MicroChemicals). The resist is baked at 110°C for 90s before being exposed using a mask aligner (MA6gen3, Süss). The illumination dose is set to 170mJ/cm<sup>2</sup> and the Cr mask, previously patterned via direct-write lithography, is placed in hard contact with the wafer. The wafer is then processed in a modular cluster tool (ACS 200, Süss) where the PR is hard baked (110°C, 90s) and developed for 87s using a KOH-based solution (AZ 400K, MicroChemicals). Next, a reflow of the PR is performed by placing the wafer on hotplate at 120°C for 2min. This treatment is intended to round off the patterns profile in order to mitigate the redeposition of material on the PR sidewalls during the subsequent removal of the Ti/Pt/Ti films via IBE (Nexus IBE350, Veeco). During the etching procedure, the wafer is tilted by a -10° so as to further reduce the buildup of metallic fences. The remaining PR is stripped using a combination of O<sub>2</sub> plasma (200W, 0.5mbar, 200sccm O<sub>2</sub>, 30s) and solvent baths (Microposit Remover 1165, Dow Chemicals) at 70°C.

**Shell layers patterning - Figure 2.18** Following the complete removal of the PR, the wafer surface is dehydrated (150°C, 15min) and plasma activated (200W, 0.5mbar, 200sccm O<sub>2</sub>, 30s) before going through another round of silanization (VM652, HD MicroSystems). Next, the wafer is placed on a hotplate for 3min at 135°C before being coated with the second layer of PI (1µm PI2611, HD MicroSystems). The curing of the PI is performed as



### 2.3 Core-shell Micropatterns for Improved Stretchable Interconnects

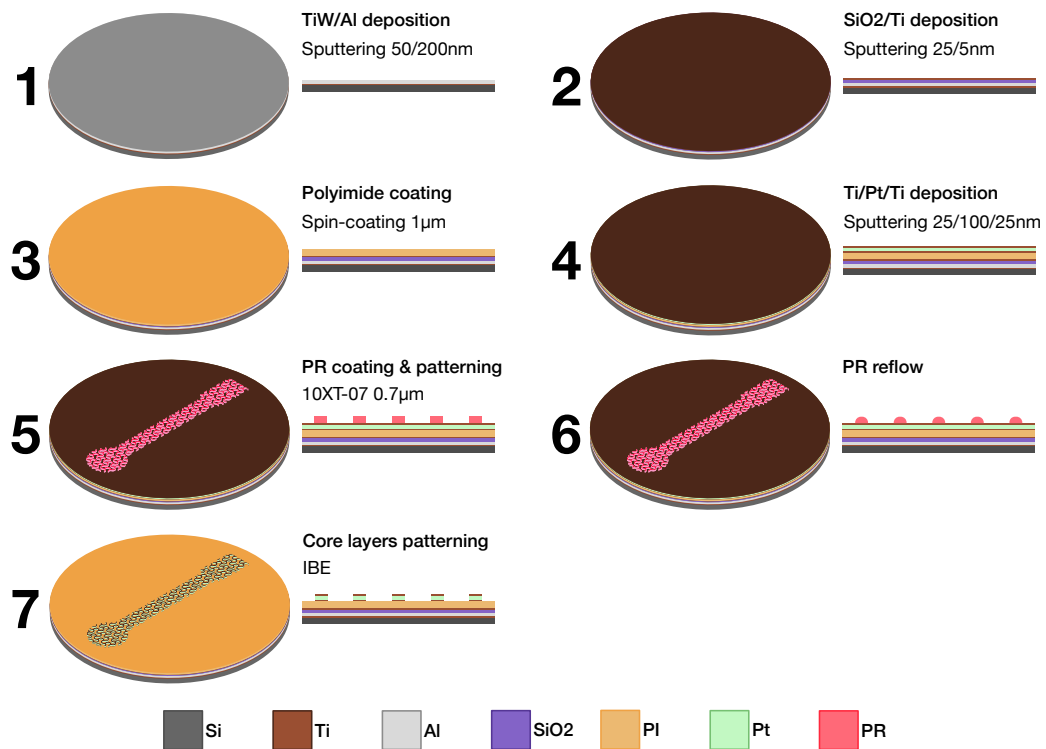


Figure 2.17: Phase 2 of the process flow - core layers patterning.

described above for the first layer. Following another dehydration step (150°C, 15min) and oxygen plasma (200W, 0.5mbar, 200sccm O<sub>2</sub>, 30s), the Ti/SiO<sub>2</sub> films (5/25nm) are deposited via sputtering (SPIDER600, Pfeiffer). The patterning of the shell layers begins with the coating of a 4-micron-thick layer of PR (AZ ECI3027, MicroChemicals). Proper adhesion between the SiO<sub>2</sub> and the resist is ensured with an HMDS treatment prior to spin-coating. The PR is exposed using a mask aligner (MA6gen3, Süss, 560mJ/cm<sup>2</sup>, hard contact). This alignment procedure is critical to the success of the process: a misalignment of less than 1μm is required to ensure the proper encapsulation of the core layers. The exposed PR layer is developed in an automatic cluster tool (MF CD 26, Shipley Microposit, 137s). Next, the SiO<sub>2</sub>/Ti/PI/Ti/SiO<sub>2</sub> layers are dry etched using a sequence of CHF<sub>3</sub>/He, O<sub>2</sub>, CHF<sub>3</sub>/He chemistries (Advanced Plasma System, SPTS). Upon completion of the etching procedure, the remaining PR is stripped using a combination of O<sub>2</sub> plasma (200W, 0.5mbar, 200sccm O<sub>2</sub>, 30s) and sonication in a solvent bath (Microposit Remover 1165, Dow Chemicals) at 70°C. The opening of the electrodes and contacts pads is then performed in a third lithographic step. First, the wafer is dehydrated (125°C, 3min) and coated with a 4-micron-thick layer of PR (AZ ECI3027, MicroChemicals). Next, the PR is exposed and developed using the same procedure as before, albeit with a slightly higher exposure dose (600mJ/cm<sup>2</sup>). Once the electrodes and contacts are exposed, the top SiO<sub>2</sub>/Ti and PI layers can be etched using the same chemistries as before. In order to prevent surface oxydation of the exposed core layers,

the top Ti of the Ti/Pt/Ti stack is also removed at this stage via IBE ( $-10^\circ$  tilt). Finally, the PR mask is stripped following the sequence of O<sub>2</sub> plasma (200W, 0.5mbar, 200sccm O<sub>2</sub>, 30s) and solvent baths (Microposit Remover 1165, Dow Chemicals) at 70°C.

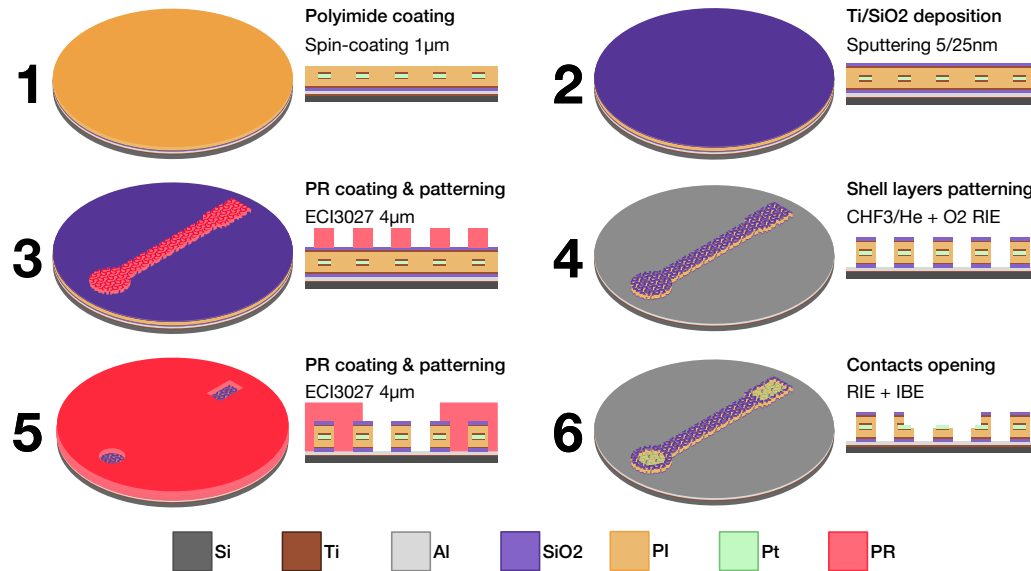


Figure 2.18: Phase 3 of the process flow - shell layers patterning.

**Top and bottom silicone encapsulations** The top and bottom silicone encapsulations are fabricated with the same method presented in section 2.2.2.1 and illustrated in figures 2.7 and 2.8. Briefly, a PET/PDMS/PET stack (23/75/23μm) is prepared and patterned with the openings for the electrodes and contacts via femto-laser machining. The stack is laminated on an acrylic carrier coated with PDMS and, following the removal of the top PET film, plasma bonded onto the interconnects wafer. Next, the resulting PET/PDMS/PI/Pt/PI stack is laser-cut into multiple parts and released from the Si carrier wafer via anodic dissolution of the sacrificial Al layer. In the meantime, a new wafer is coated with a layer of PSS and 75μm of PDMS. The curing of the PDMS layer is interrupted as soon as the gel point is reached (approximately 20min at 75°C). From there, each piece of the PET/PDMS/PI/Pt/PI stack is plasma activated and carefully laid down on the still-uncured PDMS surface. There, the capillary forces will pull the pieces into the fresh layer of silicone, ensuring proper bonding of the two halves. Finally, the curing of the PDMS is completed by placing the wafer back in an oven at 75°C.

**Electrodes coating and connector assembly - Figure 2.19** The coating procedure begins with the preparation of the Pt-PDMS composite, which is done following the same method presented in section 2.2.2.1. Next, the surface of the wafer is activated via oxygen plasma. Immediately after, the Pt-PDMS composite is screen-printed over both the electrode and contact sites using the top PET film as a shadow mask. Following the

## 2.3 Core-shell Micropatterns for Improved Stretchable Interconnects

removal of the PET, the connector, in the form of a flexible PCB, is placed on top of the contact using a custom pick-and-place platform. The FFC is custom designed in Autodesk Eagle and manufactured by a third-party. Finer details of the design, which exceed standard manufacturing capabilities, are realized afterwards via femto-laser machining. Following proper placement, the connector is secured using RTV silicone (RTV 734, Dow Corning). The whole assembly is left to rest overnight at room temperature before the final curing step in convection oven (55°C, 3h). The outline of the individual devices is then defined by laser-cutting through both the top and bottom silicone encapsulation. The resulting structures are released from the carrier wafer by dissolving the sacrificial PSS layer in a bath of deionized water.

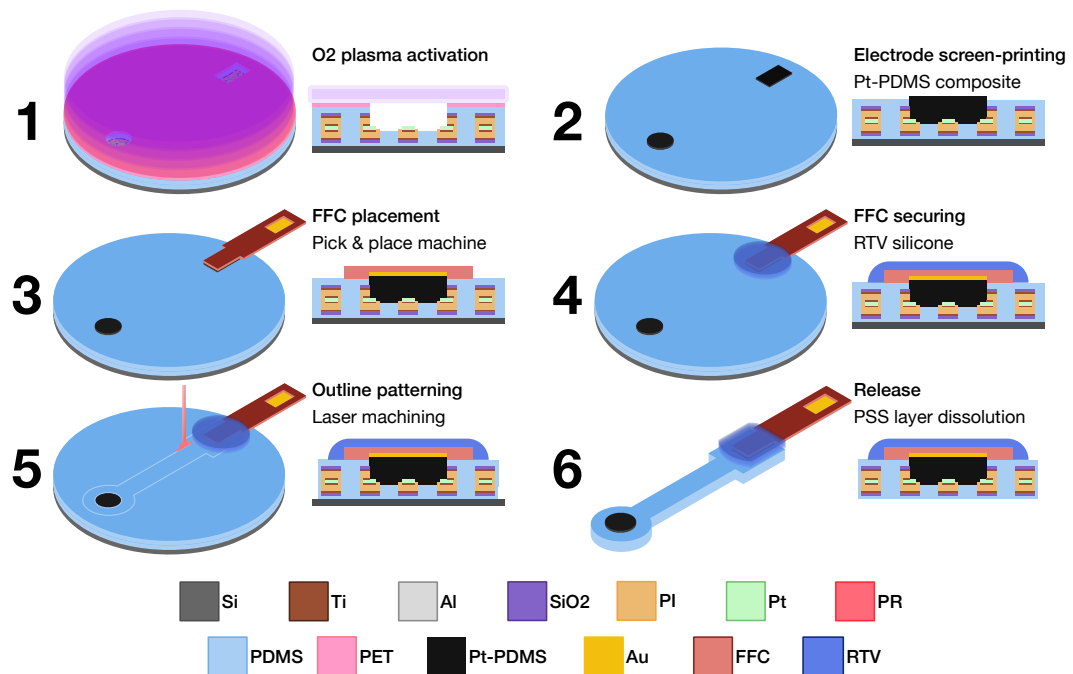


Figure 2.19: Phase 5 of the process flow - electrodes coating and connector assembly.

### 2.3.2.2 Electromechanical characterization

**Impedance spectroscopy** See methods in section 2.2.2.2.

**Chronopotentiometry** See methods in section 2.2.2.2.

### 2.3.3 Results

#### 2.3.3.1 Microfabrication

Figure 2.20 shows the proper transfer of the Y-shaped motifs to both the core and shell layers. The patterns are found to be within  $\pm 150\text{nm}$  of the target dimensions, a 65% improvement compared to first generation of devices. Detailed view of the encapsulated section of the track (Fig. 2.20B,C) reveals that the top SiO<sub>2</sub> is slightly narrower than the PI. This difference originates from the lateral shrinkage of the PR mask during the oxygen etching step. Consequently, a portion of the top SiO<sub>2</sub> is exposed during the second CHF<sub>3</sub>/He etch, leading to its removal as observed in figure 2.20C.

Imaging of the exposed electrode sites (Fig. 2.20D) demonstrates that the alignment of the core and shell layers was successful, resulting in the complete encapsulation of the metal films. Close-up view of the uncovered metal (Fig. 2.20E) reveals the presence of a very thin wall of polyimide along the periphery of the pattern. While the precise mechanism for this "skin" to survive the O<sub>2</sub> etching has yet to be understood, the fact that is also present along the periphery of the encapsulated section of the interconnects (Fig. 2.20F-G) would suggest a chemical modification of the PI surface by the CHF<sub>3</sub>/He gases used during the removal of the bottom SiO<sub>2</sub> layers. Interestingly enough, this skin does survive the anodic dissolution release process and eventually ends up falling over to the side during the bottom bonding procedure (Fig. 2.21B-C).

EDX analysis of the contact opening reveals the absence of Al at this location (Fig. 2.20G). Similarly to the first generation of devices, the exposed portion of the Al layer are etched during the removal of the top Ti layer from the electrode and contact sites (Fig. 2.18 step 6). While the release of the devices is still possible, the IBE process does lead to the formation of fences which stay trapped inside the silicone encapsulation.

#### 2.3.3.2 Neural interfaces gen 2

Using the process flow described in section 2.3.2.1, a large assortment of neural interfaces were developed and tested including ECoGs, ABI and spinal cord implants. These devices were deployed across a variety of animal models (mouse, rat, NHP), demonstrating the adaptability and scaling potential of the technology. This section will focus on two of them, the mouse ABI and the NHP ABI, presented here as a mean of comparison with the first generation of devices.

**Mouse ABI** The second generation of mouse ABIs were devised as an investigative tool of the mouse auditory pathway in chronic settings. Compared to the first iteration, the implants feature an additional channel for a total of 3 electrodes (diameter 150 $\mu\text{m}$ ). In terms of connector, this particular design maintained the use of a surface mounted

### 2.3 Core-shell Micropatterns for Improved Stretchable Interconnects

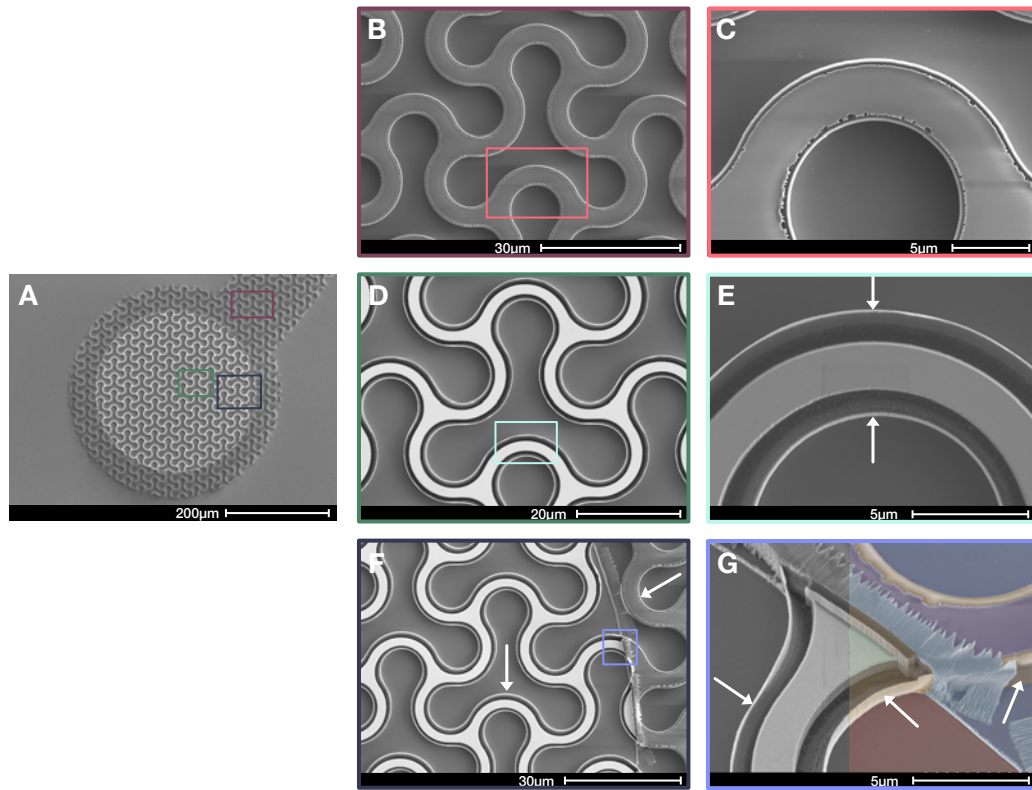


Figure 2.20: Microfabrication results following the completion of phase 3. **A** SEM image of a 300-micron-wide electrode patterned using the core-shell strategy. **B** SEM image of a fully encapsulated portion of the interconnects. **C** Detailed view of the shell layer show a slight recess of the top SiO<sub>2</sub> layer with regard to the PI. **D** SEM image of an exposed section of the interconnects, demonstrating the precise alignment between the core and shell layers. **E** Close-up view of an the core layer. The arrows point at the free-standing PI wall left along the periphery of the pattern after the opening of the contacts. **F** SEM image of the transition area between the encapsulated and exposed portion of the interconnect. The PI skin, indicated by the arrows, is visible along the side of the entire area. **G** Tilted view (30°) of the transition border offering a clear view of the free-standing PI skin (arrows). The right side of the image has been colorized to show SiO<sub>2</sub> in purple, PI in orange, Pt in green, Si in red and Al in blue.

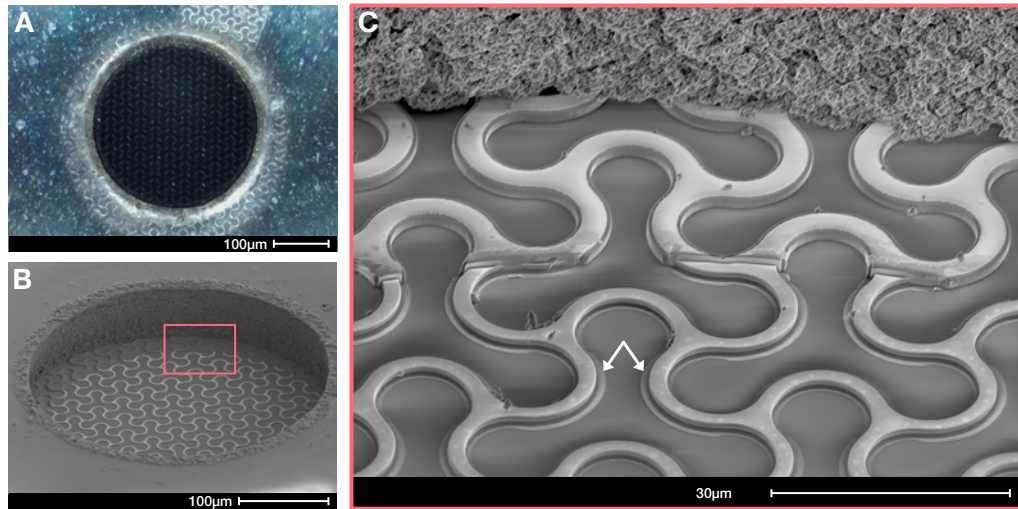


Figure 2.21: Microfabrication results following the completion of phase 5. **A** Microscope picture of an electrode after the bonding of the bottom silicone encapsulation. The conductive core layer is visible through the opening in the top PET/PDMS stack. **B** SEM image (tilt 30°) of an electrode opening following the removal of the top PET film. **C** Detailed view of the transition area reveals how the patterned interconnects are "floating" at the surface of the bottom PDMS. The PI skin, indicated by the arrows, has fallen over to the side during the bottom bonding procedure.

pin header albeit one with a smaller footprint in order to facilitate their fixation on the animal's head. The overall design is significantly denser due to both the increased track width (+80µm) and the reduced inter-track pitch (-260µm). The EIS data shows that the maximum phase value ( $-10.13^\circ \pm 6.7^\circ$ ) is reached at 100kHz, corresponding to an average impedance of  $8.8 \pm 2.9 \text{ k}\Omega$ .

**NHP ABI** The second generation of NHP ABIs were aimed at restoring auditory percepts via brainstem stimulation in chronic settings. The main benefit of this updated design come from the new connector scheme. Thanks to the direct integration of the FFC on the implant, the thickness of the implant at the level of contact pads is significantly reduced, from 5mm to 1mm. Furthermore, the custom nature of the FFC brings two improvements: (1) a 14-milimeter reduction of the cable width and (2) a reduction of the contact pitch, from 0.5mm to 0.35mm, which translates into a narrower contact fan-out. All these changes contribute to significantly improve the handling of the implant which is less prone to wobbling or to flipping over (see chapter 4). In terms of impedance, the EIS spectrum shows that the maximum phase ( $-4.25^\circ \pm 0.5^\circ$ ) is reached at 1kHz, corresponding to an average impedance of  $20.6 \pm 3.43 \text{ k}\Omega$ . These values fall in line with the magnitude of the VTs, for which the access voltages are found to be  $-1.96 \pm 0.35 \text{ V}$  and  $1.28 \pm 0.39 \text{ V}$  for the negative and positive pulse respectively.

### 2.3 Core-shell Micropatterns for Improved Stretchable Interconnects

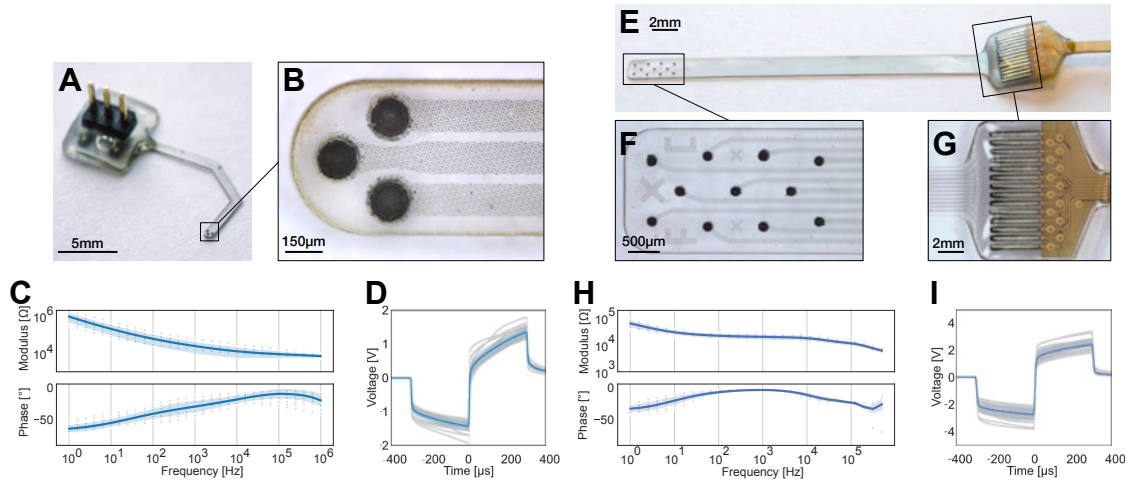


Figure 2.22: Second generation of soft neural interfaces. **A** Picture of a 3-channel mouse ABI connected to a surface mounted pin header. **B** Micrograph of the three electrodes coated with the soft Pt-PDMS composite. **C** Impedance modulus (top) and phase (bottom) typical of the mouse ABI electrodes ( $n=8$  devices, 3 electrodes each). The shaded area corresponds to the standard deviation. **D** Voltage transients of the mouse ABI upon biphasic current stimulation in PBS at  $100\mu\text{A}$  ( $n=8$  devices, 3 electrodes each). The shaded area corresponds to the standard deviation. **E** Picture of a 11-channel primate ABI connected to a custom-designed flexible flat cable. **F** Micrograph of the electrode grid. **G** Microscope picture of the transition area between the stretchable interconnects and the flexible flat cable used to interface with the device. **H** Impedance modulus (top) and phase (bottom) typical of the primate ABI electrodes ( $n=3$  devices, 11 electrodes each). The shaded area corresponds to the standard deviation. **I** Voltage transients of the primate ABI upon biphasic current stimulation in PBS at  $100\mu\text{A}$  ( $n=3$  devices, 11 electrodes). The shaded area corresponds to the standard deviation.



### 2.3.4 Summary and Discussion

**Summary** In this section, an updated method for the manufacturing of micropatterns-based neural interfaces was introduced. The second generation of devices relies on a new core-shell strategy in which the conductive layers (Ti/Pt/Ti) are completely enclosed inside the dielectric sheath (PI). To achieve this effect, the core is patterned with a scaled up version of the shell motif, which allows the two layers to perfectly interlock. The resulting interconnects are integrated between two silicone membrane and the electrodes sites are coated with Pt-PDMS composite. The implant can be interfaced with using a custom-designed flexible flat cable (FFC). The main changes to the manufacturing process are summarized below:

- The mask fabrication process is optimized to significantly reduce the time required to convert the design file prior to exposure, from 3 hours to 30min.
- The patterning of the conductive and dielectric layers is performed in two separate steps, allowing for the realization of a fully encapsulated interconnect.
- The photoresist used for the metal patterning step is changed from ECI 3007 to AZ 10XT-07 which allows for a post-development profile reflow and thus a reduction of the fencing effect.
- The design of the base motif is offset in order to compensate for the cumulated losses in critical dimensions caused by lithography and etching procedures.
- The contact pads are now coated with the same Pt-PDMS composite as the electrodes, avoiding the potential issues of early silver corrosion noticed in the first generation of devices.
- The use of bulky surface mounted connector is abandoned in favor of a custom-designed FFC, integrated directly on the device.

The resulting interconnects were successfully integrated in implantable devices targeted at both neural stimulation (ABI, spinal cord implant) and recording (ECoG). Attesting of the scalability of the kirigami process, these devices feature anywhere from 6 to 32 electrodes, across a scale range from 44 mm<sup>2</sup> to 170 mm<sup>2</sup>.

**Core-shell patterning** Beyond the technical difficulty of aligning core-shell layers with an accuracy lower than a micron, the main fabrication challenge of the core-shell process resides in the proper transfer of the Y-shaped motif via photolithography. The initial attempt relied on the same family of photoresist to pattern both the core and shell layers: the ECI3000 series. Unfortunately, the sharp profile of this resist caused significant sidewall redeposition during metal etching, leading to the fencing effect typical of IBE



### 2.3 Core-shell Micropatterns for Improved Stretchable Interconnects

(Fig. 2.23A-B). The concerns with the resulting interconnects were two-fold: (1) the fence could potentially change the electro-mechanical behavior of the sample at the macroscopic level and (2) parts of the fence could break during PR stripping and redeposit on the wafer surface, potentially shorting the tracks (Fig. 2.23C).

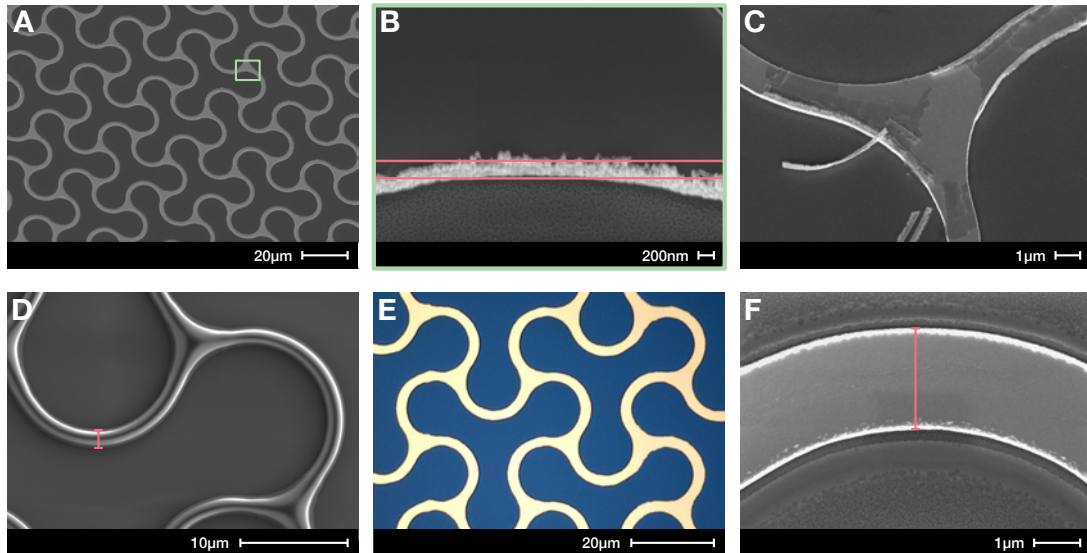


Figure 2.23: Optimization of metal layer micropatterning. **A** Tilted view ( $30^\circ$ ) of a Ti/P-t/Ti patterned using ECI3007. **B** Close-up reveals the presence of a large fence along the periphery of the patterns. The distance between the two red lines is 650nm. **C** SEM imaging performed half-way through the PR stripping process illustrates the significant risk of shorts caused by the redepositing on the wafer surface. **D** Initial attempt to use the AZ-10XT succeeded in creating a slanted PR profile but the resulting patterns were significantly below the target dimensions (marker =  $1.41\mu\text{m}$  instead of  $2.1\mu\text{m}$ ). **E** Attempts to offset the losses by varying the mask exposure dose resulted in significant reduction in pattern uniformity. **F** The final solution consists of introducing an offset in the Y-shaped motif at the level of the design itself. The optimization of the offset value results in a pattern with the correct dimensions (marker =  $2.103\mu\text{m}$ ).

One solution to mitigate the fencing effect consists in smoothing out the profile of the photoresist with a post-development reflow. Doing so required to transition to a new photoresist, the AZ 10XT-07. The challenge lies in the fact that this resist does not allow for an accurate transfer of critical dimensions from the mask to the wafer, as illustrated in figure 2.23D. Losses in accuracy can be compensated to varying degrees across the different stages of the patterning process:

1. Etching of the metal layer. Here, the losses originate mainly from the tilt of the wafer during the IBE process which results in a lateral attack of the areas covered by the photoresist. Unfortunately, the orientation of the substrate cannot be changed since it helps mitigating the fencing effect.

2. Exposure and development of the AZ 10XT-07. The potential gains are very limited here, as this family of photoresist is not very sensitive to changes in exposure dose.
3. Wet etching of the mask chromium layer. Since this operation is performed in a fully automated tool, there is no opportunity to intervene at this level.
4. Exposure and development of the mask PR layer. Changes at this stage have the greatest potential in terms of offsetting the transfer losses. Since the development step is performed in the same automated machine as the wet etching of the chromium layer, the only remaining option here is to optimize the exposure of the mask.

The first attempt of correcting the transfer losses relied on lowering the dose used in the direct write lithography of the mask's photoresist layer. A 8% decrease resulted in a final motif within 200 of the target dimension. However, this change also induced a significant reduction in pattern uniformity, with a noticeable variation in the width of meanders (Fig. 2.23E). The final solution consists in introducing an offset in the Y-shaped motif at the level of the design itself. The offset value was chosen in order to compensate not only for the losses linked to the lithographic process but also for those linked to the etching of the film. This optimization procedure was repeated for both the core and shell layers, resulting in a pattern that is within  $\pm 150\text{nm}$  of the target dimensions, depending on the location on the wafer (Fig. 2.23F). The remaining variations originate from the small non-uniformities which take place in the mask fabrication procedure: instabilities in the light source, imprecisions in the shutter/guiding system, small changes in developer and etchant contact times. These parameters will gradually become the limiting factor as a lithography process approaches its resolution limits (here  $1\mu\text{m}$ ). This is especially true of an academic cleanroom where the variety of users processes prevents extreme optimization, thus placing an upper limit on the achievable accuracy. These results showcase clearly the technological challenge at the core of the kirigami approach: delivering an accurate and uniform transfer of microscale motifs over large surface areas.

**Encapsulation** The main motivation for the development of the core-shell process was the need to completely enclose the metals layers inside the polyimide, thus preventing a direct ions pathway through the silicone. As shown in figure 2.3.3.1, the revised approach was successful in encapsulating the platinum core completely. In that regard, one of the benefit of the core-shell process is that the material stack could be potentially modified to incorporate one or more highly hermetic layers. One promising candidate is silicon carbide (SiC), due to its exceptional moisture barrier properties and its ability to bind with polyimide via the creation of strong carbide bonds. This latter point will become increasingly important: as the encapsulation technology improves, failure will

### 2.3 Core-shell Micropatterns for Improved Stretchable Interconnects

become more likely to take place at the interfaces between its constitutive layers.

Going back to the current material stack, close inspection of a completed device reveals the absence of silicone between the meanders of the micropatterns. As shown in Figure 2.24, the PDMS does not appear to fill these spaces.

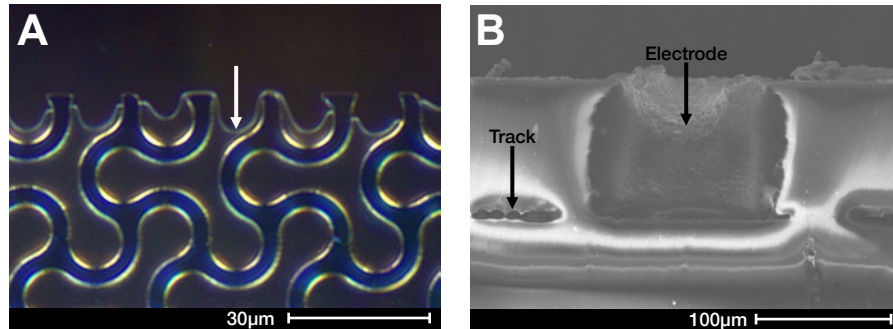


Figure 2.24: Limitations of the silicone encapsulation strategy. **A** Micrograph reveals the presence of empty spaces between the meanders of the encapsulated tracks. Arrow points at the border of the air gap. **B** SEM imaging of a device transection confirms that the PDMS membranes do not bond through the micropatterned tracks.

The presence of voids inside the encapsulation has shown to be a significant factor in the onset of the failure cascade [29, 88]. Indeed, as water molecules diffuse through the silicone, they will eventually reach these empty spaces and condensate. The potential consequences are three-fold:

1. As the volume of condensed water increases over time, pressure will build up at the interface between the top and bottom silicone membranes, eventually culminating in the delamination of the two layers.
2. Driven by osmosis, the diffusion of ions through the PDMS will accelerate, triggering the early onset of the corrosion cascade once the species reach the metal layers.
3. The presence of water under its liquid form will enable additional chemical reaction, such as the hydrolysis of  $\text{SiO}_2$ . From there, delamination can happen either because of the destruction of the passivation layer itself or because of the build-up of reaction byproducts.

A potential solution to achieve truly complete encapsulation consists in fabricating the interconnects "upside-down" such that the contact and electrode openings are facing down, against the carrier wafer. In this configuration, the top silicone encapsulation can be spin-coated directly on top of the tracks, ensuring the PDMS fills the gaps between the

meanders (Fig. 2.25B). The key steps of the upside-down process are illustrated in figure 2.25A. In order to validate the feasibility of the approach, a prototype was fabricated. The slanted opening of the bottom  $\text{SiO}_2/\text{PI}$  and subsequent patterning of the core/shell layers were successful, resulting in bottom-facing contacts (Fig. 2.25C). Following the spin-coating of a 75-micron-thick layer of PDMS, the structure was released via anodic dissolution of the Al layer. Unfortunately, the procedure was unsuccessful as a thin layer remained attached across the entire bottom surface of the stack (Fig. 2.25D). EDX analysis did not allow to determine the nature of the skin and consequently the reason for the failure has yet to be fully understood. In conclusion, while the upside-down process does appear to be a promising option to achieve full encapsulation, it will require further technological developments.

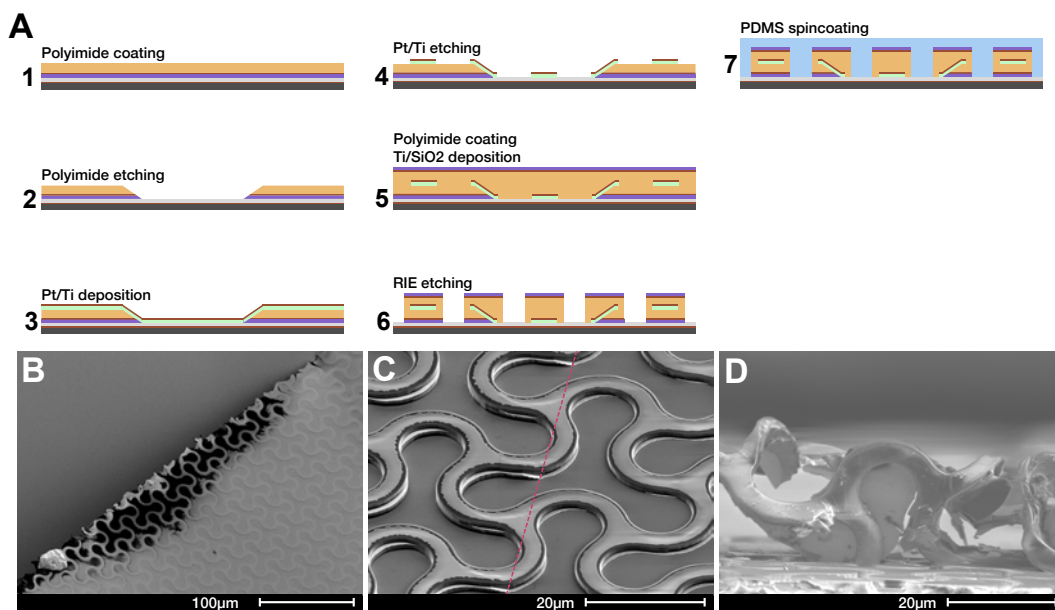


Figure 2.25: Proposed solution for a gap-less silicone encapsulation. **A** Summary of the proposed "upside-down" process. The creation of bottom-facing contacts allows the spin-coating of the first PDMS layer directly on top of the interconnects. **B** The spin-coating of fresh PDMS on top of the micropatterns does succeed in filling the gaps between the meanders. **C** SEM image of wafer processed using the upside-down approach. Although the core and shell layers are misaligned, the metal film can clearly be seen transition from the middle of the stack to the bottom at the level of the contact opening (dashed lines). **D** While the stack failed to release properly, the quality of the silicone overmolding can still be appreciated in the SEM picture of a torn interconnect.

**Connection scheme** The connection scheme has been a long standing, and often under-appreciated, challenge in the field of microfabricated neural interfaces [47]. The revised manufacturing process introduces a new interface paradigm in the form of a flexible flat cable (FFC) integrated directly on the implant. This connector, dubbed internally Flex-

### 2.3 Core-shell Micropatterns for Improved Stretchable Interconnects

---

Comb, consists of a custom-designed flexible printed circuit board (fPCB) with a series of "free-standing", gold-plated pads on one end (Fig. 2.26B). During assembly, each of these so-called fingers is aligned on top of the corresponding contact pad on the implant and the whole connector is lowered at once. Since the openings in the silicone are filled with Pt-PDMS composite, they form a sort of conductive well in which the individual finger will plunge upon placement of the FlexComb. This effectively establishes an electrical path between the fPCB and the stretchable interconnects which can now be interfaced with. Compared to the previous connector technology, this new approach has numerous benefits:

- The overall foot print of the FlexComb connector is significantly smaller than its off-the-shelf counterparts. Since the fPCB itself measures only 130 $\mu$ m, the thickness at the transition area is defined by the height of the silicone sealant added on top of the fingers. This results in a low profile connection (<1mm) with the dexterity of the assembly operator being the ultimate limiting factor. In terms of width, the FlexComb enables a reduction of the contact pitch, from 0.5mm to 0.35mm, which translates directly into a narrower contact fan-out. This gain is only limited by the capabilities of the third-party manufacturer and could potentially be further improved in the future.
- The custom nature of the FlexComb means that its design can be easily adapted to fit a wide array of devices and animal models. Depending on the application requirements, the same technology can be used to transition from a soft implant to an Omnetics connector, a ZIF connector or even cables (Fig. 2.26A). Furthermore, the FlexComb can be modified to help secure the device in-vivo by adding anchoring points in the form of reinforced rings along its sides (Fig. 2.26C).
- Since the FlexComb does not contain any bulky components, the conformability of the implant at the level of the contact pads is improved. This is important because during implantation the whole implant is placed subdurally, including the connector. The absence of rigid parts in the FlexComb means that it is less likely to create a local depression of the brain.

With that in mind, the use of the FlexComb in its current form should be limited to academic research settings. Indeed, while mainstream board manufacturers provide a low cost, fast turnover option to manufacture fPCBs, the technology is not built to survive exposure in wet ionic environments. Not only are the traces made of copper, a metal prone to fast corrosion, but the dielectrics sheets isolating them are bonded together using simple adhesive films. This type of assembly is unlikely to survive the 30 years period required in clinical settings. A potential solution to these concerns could consist in using high performance dielectric, such as liquid crystal polymers (LCP), combined with gold traces, a technology readily in use by the RF-PCB industry.

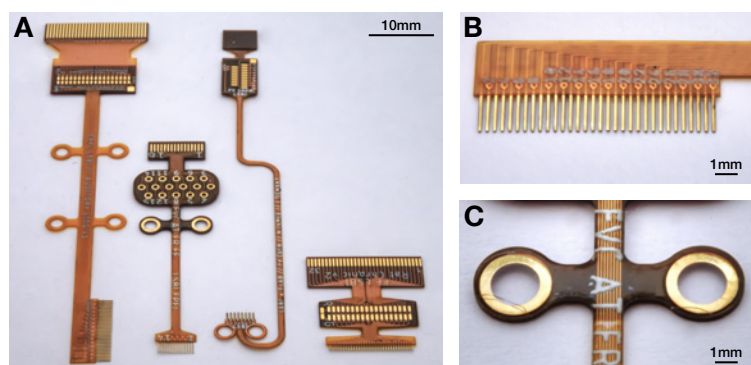


Figure 2.26: FlexComb connector. **A** Picture of various FlexComb connectors, demonstrating the versatility of the approach: the design can be adapted to best fit each application and to transition to any number of standard connectors such as Omnetics, ZIF or even wires. **B** Close-up view of the FlexComb fingers which form the transition interface from the soft electrode paddle to the flexible PCB. **C** Close-up view of an anchoring structure designed to help secure the implant following implantation.

**Outlook** In this section, the new and improved core-shell micropatterns have been shown to produce interconnects with superior electro-mechanical performances, leading to more robust neural interfaces. Nevertheless, a number of technological limitations remain to be addressed in future versions of the process:

- The fabrication of the silicone encapsulation needs to be modified in order prevent the creation of voids between the top and bottom PDMS membranes. While a proof of concept for a potential solution was introduced in the form of the "upside-down process", the electro-mechanical effects of a complete interlocking of the micropatterned tracks inside the silicone still needs to be characterized.
- The conductivity of the micropatterned interconnects has to be increased before this technology can be used in conjunction with fully implantable pulse generators. The main challenge lies in the limited voltage compliance (10 or 15V) characteristic of this class of devices. With the current impedance values and considering a device scaled up to human size, current stimulation would likely require a voltage close to the maximum allowable, without even accounting for the build up of fibrotic encapsulation over time. The potential solutions to this problem are limited. One option would be to use thicker metallization, but this approach is likely going to adversely affect the mechanical performances of the device. An other option would be to change the Y-shaped pattern in favor of a motif optimized for conductivity rather than local strain. Again, the trade-off here would lead to an increase in mechanical fatigue over time, potentially affecting the robustness of the device. A last option would be to engineer a dedicated IPG with a battery providing a higher voltage. Such endeavor would however likely prove prohibitively expensive and

technically challenging, as most IC components are not rated past 15V.

- The lithography process should be further optimized in order to ensure greater pattern uniformity across large area. This issue is particularly relevant when considering scaling up the technology to human-sized devices which will likely require the transition to larger substrates in order to be financially viable (e.g. 6 or even 8-inch Si wafer).
- In order to enable high spatial resolution neural recordings, the maximum number of electrodes, currently at 32, should be increased. High channel count neural interfaces could be implemented in one of two ways. The first option consists of fabricating a device with multiple levels of metalization, each enclosed inside its own polyimide shell. From a technical perspective, the implementation of this strategy is relatively straightforward, requiring "only" a very high degree of accuracy in the alignment of the different layers.

The second option relies on the transition to narrower interconnects ( $<50\mu\text{m}$ ) in order to wire a greater number of channels within the same horizontal plane. The issue is that, with the current implementation, the tracks cannot be made arbitrarily small since they need to fit at least one repetition of the pattern (width  $>52\mu\text{m}$ ). The solution would consist of scaling down the Y-shaped motif with respect to the track width. By patterning proportionally smaller cuts into the stack, the stretchable interconnects can maintain the same level of mechanical redundancy within a narrower profile. Concretely, creating smaller patterns requires the transition to smaller wavelengths than the ones used in standard lithography systems (436-365nm). The recent acquisition of a deep ultraviolet (DUV) stepper at the Center of Micro- and Nano- Technology makes this option a reality, with the potential to reach resolution down to 180nm. Compared to the multilayer approach however, the transition to DUV lithography has the disadvantage of being significantly more complex, especially with regard to patterning polymeric layer at such low resolution.

- The connection scheme needs to be replaced in favor of a solution more suitable for long-term implantation and for high channel count devices. In that regard, liquid crystal polymers constitute a promising alternative to the standard flexible PCBs introduced in the section [89]. Overall, the transition from stiff to soft materials and from the micro- to the macro-scale remains one of the major challenge to tackle in the field of soft neural interfaces.
- Looking at long-term implantation ( $>6$  months), the shell layer will require to be re-engineered using new materials in order to improved the hermeticity of the interconnects. A key candidate is silicon carbide which not only exhibits strong adhesion with polyimide [90] but can also be bonded to PDMS following oxygen plasma activation of its surface. The transition to a fully inorganic encapsulation strategy should also be explored, although there has been evidence that polymeric layers

provide an important stress buffer between stiff metallic tracks and stretchable elastomeric substrates [91].

All in all, while the revised core-shell process still fails to fully address the requirements for a chronically implantable, conformable neural interface established in section 2.1, it does enable new design and engineering strategies to address these limitations in the future.

## 2.4 Comparative electromechanical study

This section presents a thorough electromechanical comparison between stretchable interconnects fabricated with the original Y-shaped micropattern technology and the core-shell process. For the sake of simplicity, these two categories of devices will now be referred to as gen.1 and gen.2 respectively.

### 2.4.1 Sheet resistance

The equivalent sheet resistance of the patterned tracks was determined computationally through COMSOL FEA software. In particular, the effect of the two micro-pattern dimensions on sheet resistance was investigated. To that end, a 2D model of a portion of platinum track, with an out-of-plane thickness of 150nm, was constructed. The geometry is representative of a track with a width of 181.9 $\mu\text{m}$  and length of 934.7 $\mu\text{m}$ . This corresponds to an array of 8  $\times$  40 Y-shapes. In order to study the effect of patterning on sheet resistance, the simulation was computed for 3 geometries: gen.1 micropatterns, gen.2 micropatterns and a plain track. For gen.1, the Y-shaped motif corresponds to the standard geometric parameters discussed in section 2.2, i.e.  $L=26\mu\text{m}$ ,  $a=16\mu\text{m}$  and  $r=5.5\mu\text{m}$ . As discussed in section 2.3.1, gen.2 devices employ a scaled up version of the motif to form the core conductive layer, which corresponds to  $L=26\mu\text{m}$ ,  $a=17\mu\text{m}$  and  $r=6.5\mu\text{m}$ .

To extract the resistance of the 3 types of tracks an extremity was set as ground and a current density of 1J/m<sup>2</sup> was applied to the opposite extremity. The computation was conducted with a stationary study and a physics-controlled mesh. The resulting sheet resistances were obtained by computing the maximum surface voltage and applying Ohm's law. The sheet resistances were consequently obtained by multiplying the resistances by the width-to-length ratio of the track portion. In addition, the relative sheet resistances were calculated by dividing the sheet resistance of the patterned track by that of a plain track.

The results are summarized in table 2.1. From there, it can be understood that the transition from gen.1 to gen.2 was done at the cost of a 2-times increase in sheet resistance.



This is consistent with the change in the geometrical parameters which effectively reduce the width of the Y-shape segment by a factor of 0.51.

Technology	Sheet resistance [ $\Omega/\text{sq.}$ ]	Relative sheet resistance $R_i/R_{\text{Pt}}$
Plain Pt	0.749	1
gen.1	7.207	9.621
gen.2	13.84	18.483

Table 2.1: Simulated sheet resistance values for gen.1 and gen.2 interconnects compared to a plain Pt track of equivalent dimensions.

### 2.4.2 Electromechanical characterization

**Test sample** In order to improve comparability and to simplify manufacturing, a single design was used for all electromechanical testing. It consists of a dog-bone structure containing 16 parallel tracks, separated by a pitch of 1mm. The interconnects are 50mm in length with varying width: 104 $\mu\text{m}$ , 260 $\mu\text{m}$  and 520 $\mu\text{m}$  corresponding to a minimum repetition of 2, 5 and 10 Y-shaped patterns respectively. The different interconnect widths are distributed sequentially across the sample in order to prevent a bias in the results based on their physical location in the dog-bone structure. The interconnects can be interfaced with using a pair of custom-made flexible flat cables (FFCs) located on each end. A screen-printed layer of Pt-PDMS composite ensures the electrical connection between the FFC and the track contact underneath. In order to easily mount the samples on the different tools, each end of the samples is bonded to a laser-cut plexiglas support using RTV silicone. The plexiglas piece, which overlap with the samples over a length of 10mm, features two holes through which the samples can be bolted. Once the devices are fully assembled, a 40-millimeter-long portion of the track remains unclamped and ready for stretching.

**Hysteresis** In order to investigate the different deformation regimes taking place under tensile load, the samples undergo a series of strain cycles of gradually increasing magnitude. This measurement allows to capture the changes in the hysteresis of the interconnects which can subsequently be used to pinpoint the onset of plastic deformation in the materials.

The samples are elongated using a tensile tester (MTS Criterion 42) equipped with a 10N load cell. The electrical resistance of the interconnects is measured during stretching via a voltage divider ( $R_{\text{div}}=6.8\text{k}\Omega$ ) connected to a 16-bit Arduino microcontroller. A 16-channels multiplexer allows to quickly cycle through all tracks on a sample, resulting in an acquisition frequency of 50Hz. For each strain value, the sample is stretched and released at a speed of 0.1mm/s.

Figure 2.27 summarizes the results for gen.1 interconnects. The onset of plastic deformation appears very clearly in figure 2.27B: the 11% strain loop generates a jump in resistance due to the inelastic deformations which start to occur in the tracks. Beyond 11% elongation, the interconnects enter the plastic regime during each successive strain loop which results in a gradual increase in the relative resistance  $R/R_0$ . The fact that the damage is indeed unrecoverable is demonstrated by the fact that the loading curve of each loop  $n$  follows the unloading of the previous one  $n-1$ .

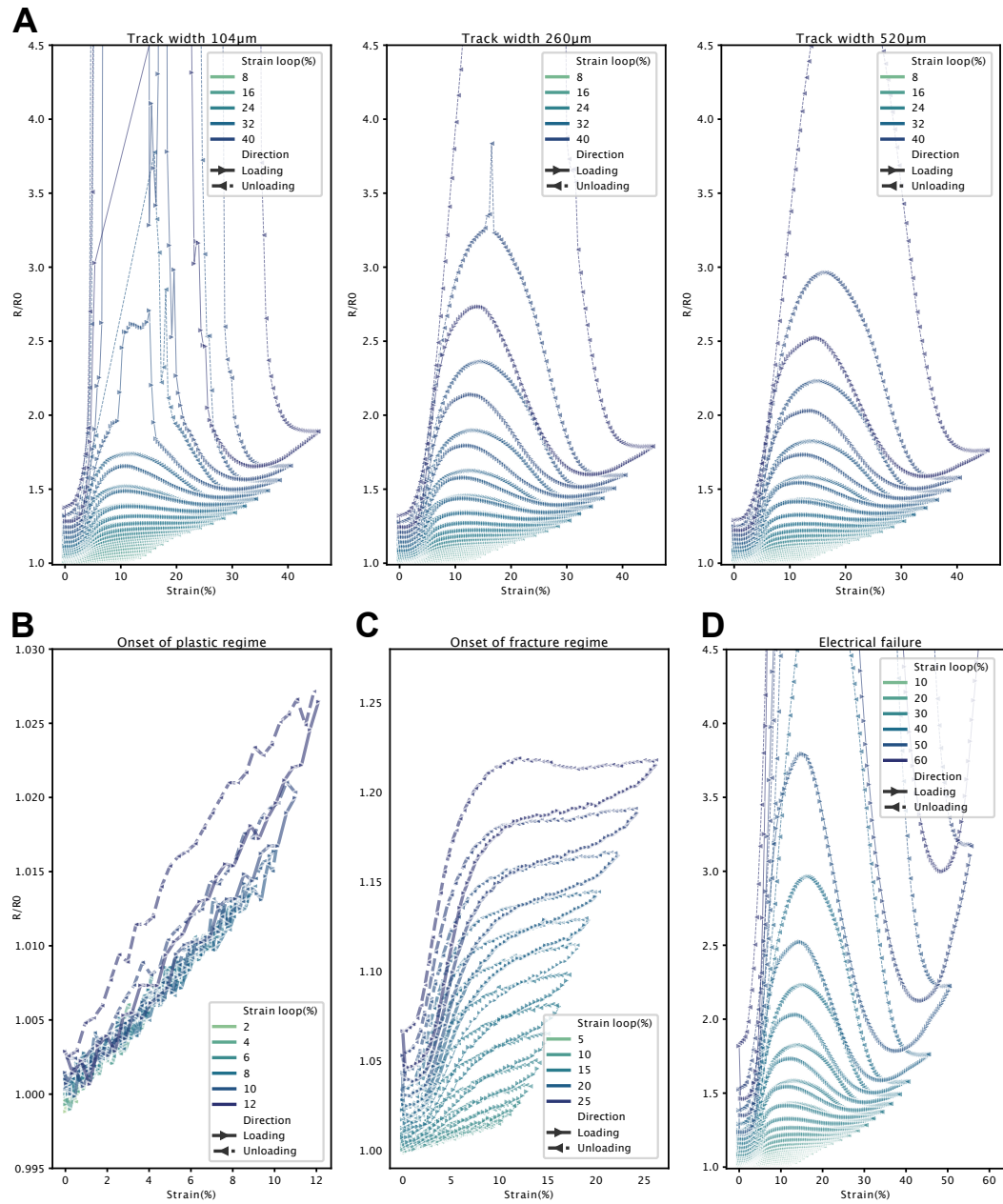


Figure 2.27: Averaged hysteresis of gen.1 interconnects.  $n=4$  for all conditions. **A** Global hysteresis behavior for track of varying width. **B** The onset of the plastic regime can be observed from the permanent increase in  $R/R_0$  values. **C** The onset of the fracture regime is indicated by the sudden increase in relative resistance during the unloading sequence at strain greater than 26%. **D** Total electrical failure indicated by open circuit  $R/R_0$ . Track width is 520  $\mu\text{m}$  in **B,C,D**

A new behavior begins to appear at strain beyond 26%: during the unloading sequence, the relative resistance increases again, exceeding even the values reached at peak strain

during the loop (figure 2.27C). The phenomenon is surprising because  $R/R_0$  is expected to remain stable as the strain decreases. Looking at the hysteresis at 27% strain, it can be seen that the loading curve follows closely the unloading of the 26% loop. This behavior indicates that the effects which led to the rise in relative resistance during unloading are plastic in nature. Furthermore, an even greater jump in  $R/R_0$  takes place when unloading the 24% strain. Despite this sudden surge, the relative track resistance eventually goes back to a normal value, albeit slightly higher than before. All subsequent strain cycles exhibit the same behavior, with the  $R/R_0$  peak in the unloading phase becoming larger and larger.

We hypothesize that the relative resistance peaks observed during the unloading sequence are caused by the sudden formation of cracks in the Y-shape segments. Beyond a strain value of 25%, the structures are believed to be too plastically deformed to return to their original resting state. As a result, they cannot follow the relaxing of the encapsulation materials. This creates a buildup of local stress which eventually initiates fractures in many of the Y-shape ligaments, leading to the observed increase in  $R/R_0$ . As the unloading sequence continues, the two ends of the torn segments are eventually squished together, which reestablishes almost full electrical contact. This would explain why the relative resistance goes back to normal when the applied strain is close to 0. When the next strain cycle begins, the two ends of the cracked segments start to separate again, which give rise to a rapid increase in relative resistance instead of the elastic regime observed in previous strain cycles. Verifying our hypothesis is unfortunately very challenging as it requires the ability to image with high resolution (e.g. SEM) the interconnects under strain through the top PDMS encapsulation. Additionally, the view should be tilted with respect to the sample in order to be able to appreciate the out-of-plane deflections. Such a system is currently not available internally but we would suggest instead to inspect a sample under SEM after stretching in order to investigate the presence of cracks. Doing so would require to remove the top silicone membrane without damaging the tracks which could be done via oxygen etching.

At strains between 40 and 60% (depending on the track width), complete failure of the tracks begins to take place (figure 2.27D). Fractures propagation reaches a critical point, resulting in the complete rupture of the electric path. At this point, the acquisition system indicates an open circuit value. Electrical failure was observed during both the loading or unloading sequence, depending on the type of device and track width.

Going back to our comparison, the trends for the gen.2 interconnects are overall similar to gen.1 (fig. 2.28A). The onset strain for the different deformation regime are however different. The elastic regime spans between 0 and 15% strain, while the plastic regime ends around 36% deformation (fig. 2.28B). The fracture onset regime described above takes place at strains beyond 36% (fig. 2.28C). Because gen.2 interconnects stay in the elastic regime for longer (+5% strain), the increase in  $R/R_0$  at equivalent strain is lower compared to the gen.1. We therefore expect gen.2 to exhibit less mechanical fatigue

## 2.4 Comparative electromechanical study

during cyclic stretching.

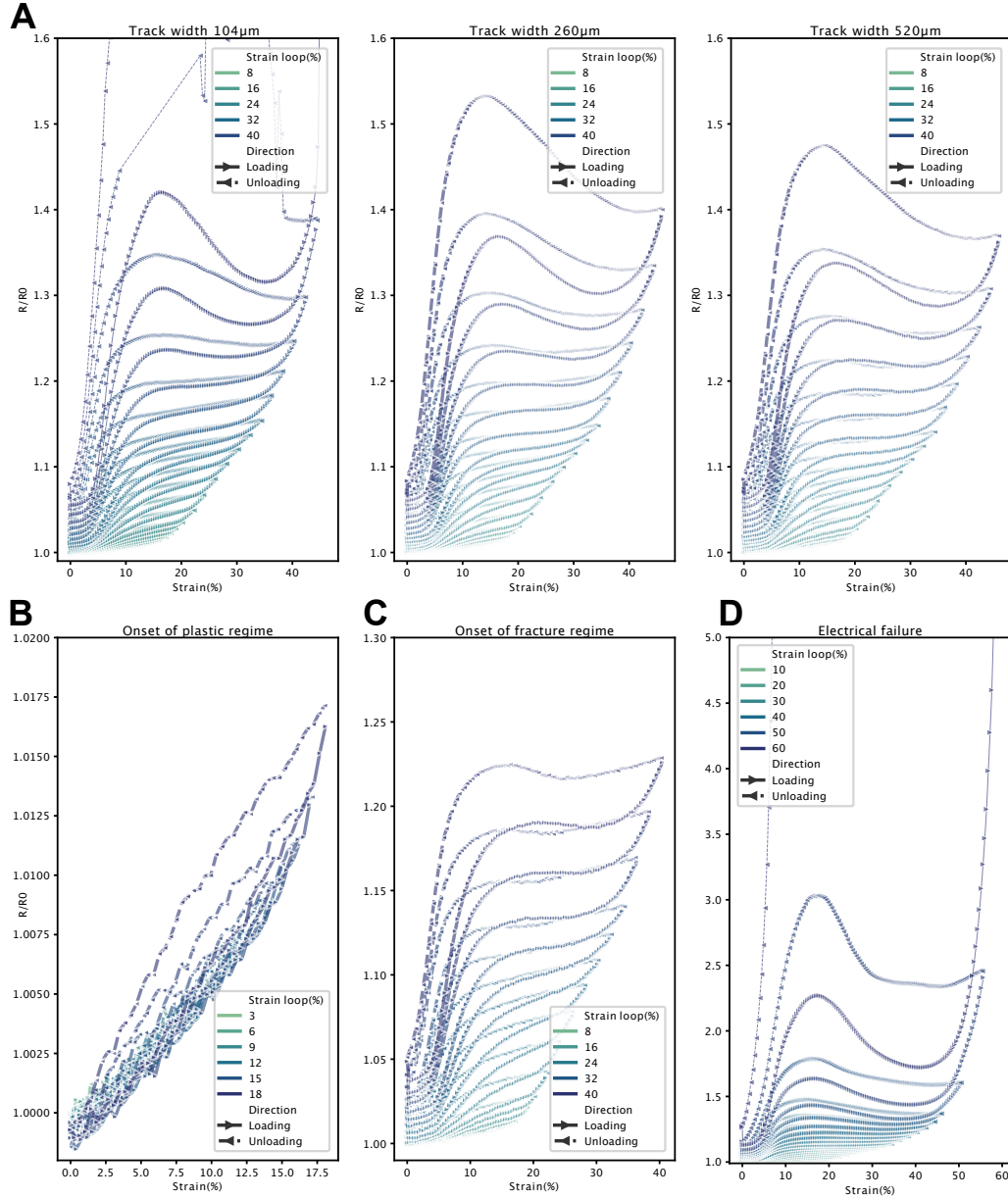


Figure 2.28: Averaged hysteresis of gen.2 interconnects.  $n=4$  for all conditions. **A** Global hysteresis behavior for track of varying width. **B** The onset of the plastic regime can be observed from the permanent increase in  $R/R_0$  values beyond 15% strain. **C** The onset of the fracture regime is indicated by the sudden increase in relative resistance during the unloading sequence at strain greater than 36%. **D** Total electrical failure indicated by open circuit  $R/R_0$ . Track width is 520μm in **B,C,D**

**Cyclic stretching** In order to evaluate the long-term mechanical robustness of the micropatterned interconnects, samples identical to the ones described above are mounted on a custom-made cyclic stretcher and elongated repeatedly by 9% at a rate of 1 cycle per second (1Hz). The initial strain target was 10%, chosen to match the identified elastic regime, but the limitations of the instrumentation made it impossible to accurately set the desired strain. The effective applied strain was therefore retro-computed from the position of the motor over time, as reported by the system. Similarly to the tensile test, the electrical resistance is measured using a voltage divider ( $R_{div}=6.8k\Omega$ ) connected to a 16-bit Arduino microcontroller. The cyclic stretcher and Arduino are controlled and synchronized together with a LabView interface.

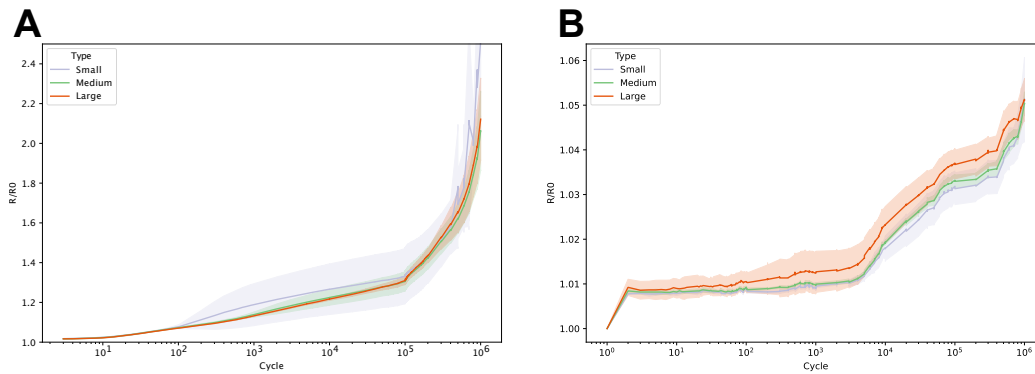


Figure 2.29: Cyclic stretching at 9% elongation up to 1 million cycles for **A** gen.1 devices and **B** gen.2 devices interconnects.  $n=4$  for all conditions.

The differences in performances between gen.1 and gen.2 over 1 million cycles are significant (figure 2.29). While the gen.1 interconnects exhibit an relative resistance increase of over 200%, gen.2 remains extremely stable with only a 5% increase. This massive gain in performance can be explain by the fact that the gen.2 tracks remain well within their elastic regime (1-15%) while stretching which translates into less mechanical fatigue. The rate of increase for  $R/R_0$  exhibit clear transition points, albeit after a different number of cycles for gen.1 and gen.2. Future work should focus on identifying the new mechanisms taking places each time the slope changes.

## 2.4 Comparative electromechanical study

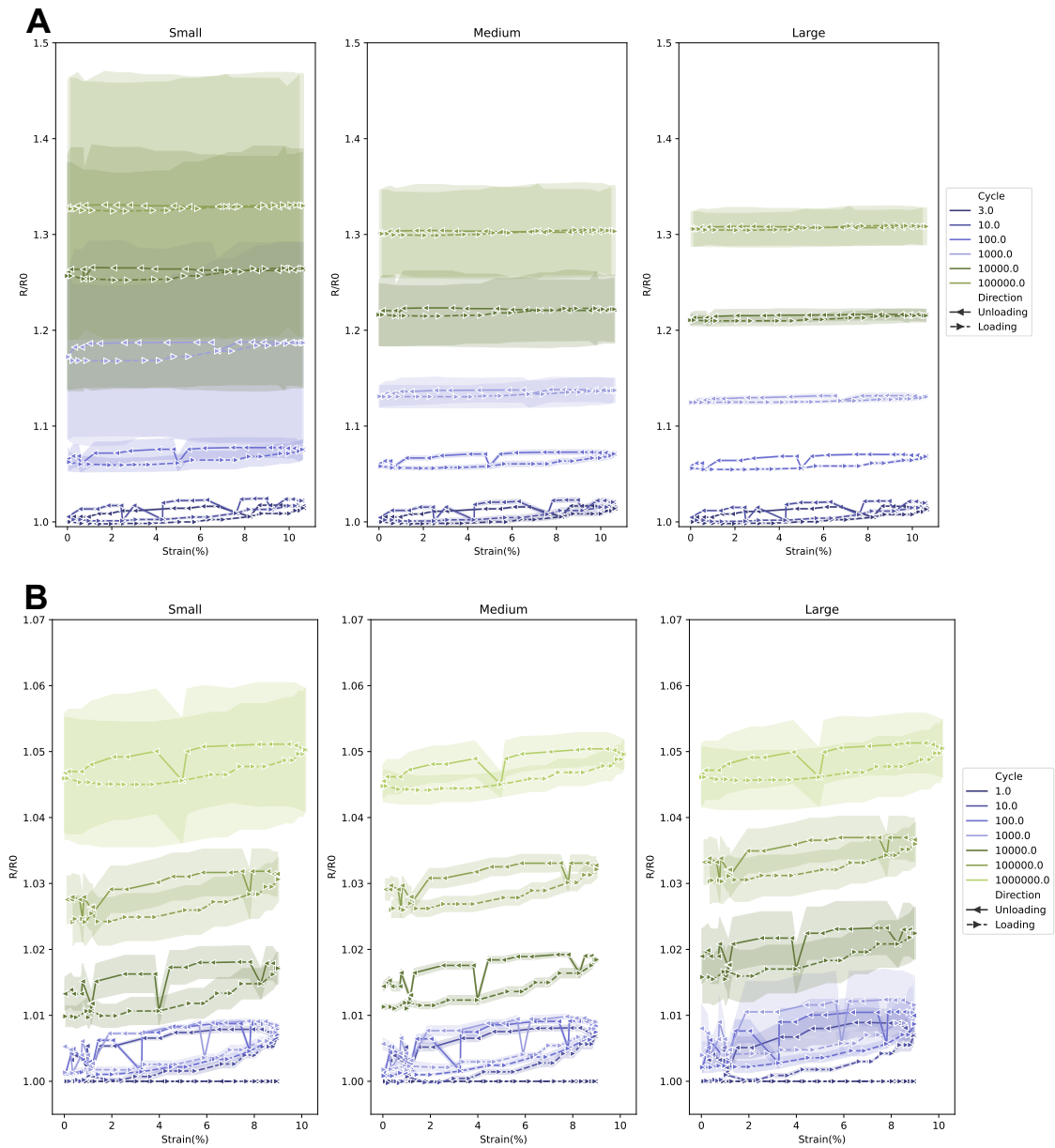


Figure 2.30: Hysteresis upon cyclic stretching for of **A** gen.1 and **B** gen.2 interconnects for the small, medium and large track width, from left to right respectively.  $n=4$  for all conditions.

Figure 2.30 present the same data but in a different format. The relative resistance over a complete cycle, i.e. the hysteresis, is plotted at key time-points. Unfortunately the acquisition frequency of the system combined with the cyclic speed do not allow to capture de finer details of the hysteresis behavior discussed above. Looking at the gen.1 curve (figure 2.30A), the benefit of electrical redundancy is noticeable through the differ-

ences in standard deviation across track width. Indeed, given an equal rate of failure of the Y-shapes segments (i.e. complete fracture), the increase in  $R/R_0$  is expected to be proportionally larger for narrower track, leading to a great spread in relative resistivity over time. Surprisingly, this behavior is not verified for gen.2 interconnects which exhibit comparable standard deviation across track width. This could indicate that the rate of complete fracture of the Y-shape segments is significantly lower for gen.2, thanks to its lower maximum local strain value. This would also explain by which mechanism gen.2 manages to maintain such a low  $R/R_0$  over 1 million cycles: the segments of the Y-shape are not being sectioned.

Another interesting trend in gen.2 is the fact that the change in  $R/R_0$  appears to be greater for larger tracks. This rather counter-intuitive observation could be explained by the influence of the tracks edges. Indeed, it is hypothesized that the Y-shape segments located at the edge of an interconnect (edge segments) behave slightly differently from those located in the middle as they have no neighbor on one side. In particular, we believe that the edge segments undergo less mechanical fatigue. Since in narrower tracks the number of edge segments is proportionally larger, it means they have a stronger influence on the overall electromechanical performance. Assuming the edge segments fatigue less, this would thus explain why the change in relative resistance  $R/R_0$  is less pronounced in narrow track. The fact that gen.1 do not exhibit this behavior is explain by the fact that for these tracks, the edge effect is very weak (1% change in  $R/R_0$ ) compared to the other sources of mechanical fatigue.

### 2.4.3 Hermeticity characterization

**Leakage current measurements** In order to assess the hermeticity of the micropatterned interconnects, samples with two interdigitated tracks are fabricated using the microfabrication process presented in section 2.2.2.1. The 520-micrometer-wide tracks are separated by a gap of 100 $\mu$ m and run side by side over a distance of 205mm. To ensure the validity of the measurement, each track forms a loop such that its impedance can be measured independently. Once again, a FFC allows to interface with the device. Each device is inserted in a sealed glass jar containing phosphate buffered saline (PBS 1x), together with a stainless steel needle which will be used as a counter electrode.

In this experiment, a 5V potential is applied between the interdigitated tracks and the resulting leakage current is measured with a potentiostat (PGSTAT128N, Metrohm). The current values are recorded over a period of 5s at a sampling rate of 10MHz, before being averaged. This allows to compensate the instabilities caused by the ions accumulating at the interface due to the applied bias voltage. Using the same parameters, the leakage current between each track and the external counter (stainless steel needle) is measured as well. At day 0, the samples are inserted in PBS and a first measurement is taken. The devices are then left at room temperature for 24h. At day 1, the samples



## 2.4 Comparative electromechanical study

measured again before being placed in an oven at 67°C in order to perform accelerated ageing. Based on Arrhenius law, this temperature corresponds to an acceleration factor of 8. From there, the leakage currents are measured at regular intervals. The results are shown in figure 2.31.

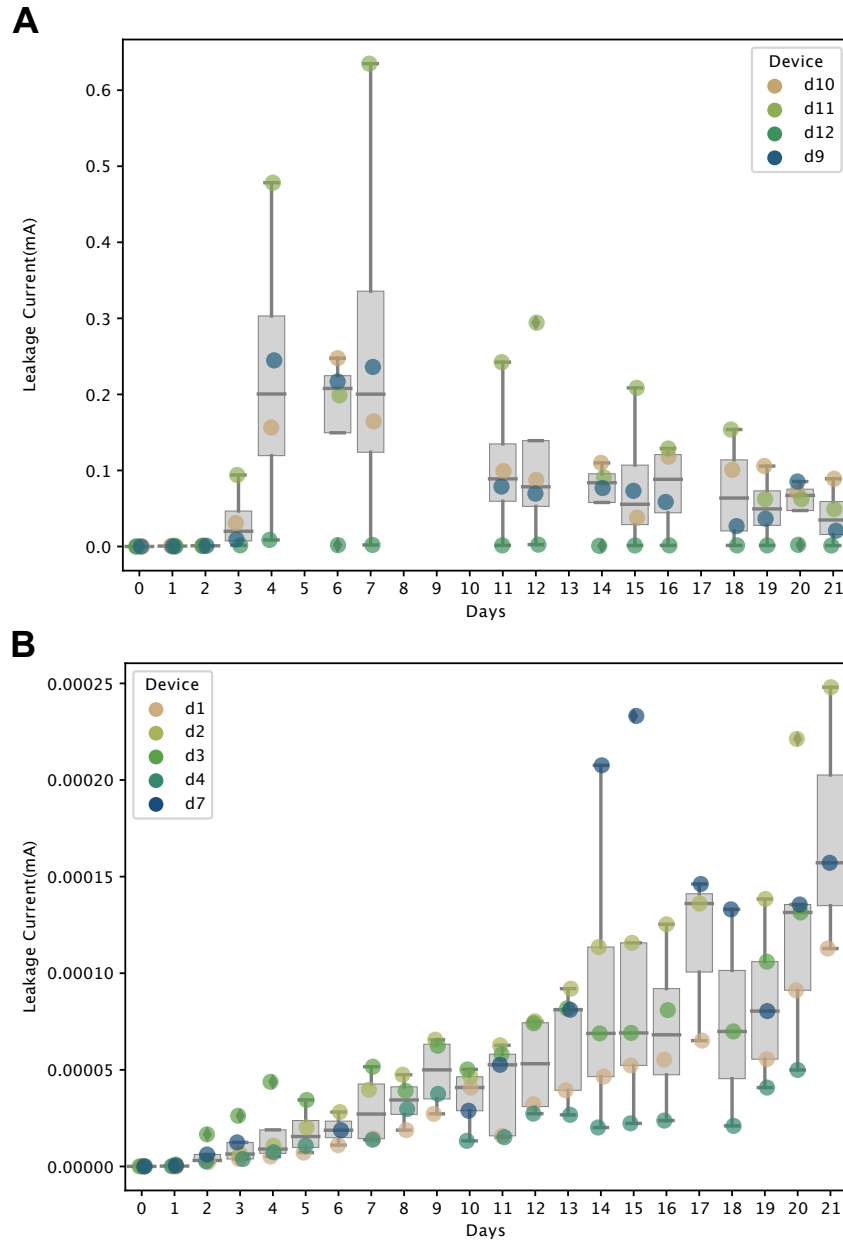


Figure 2.31: Leakage current measurement upon the application of a 5V bias. **A** Performances of gen.1 (note the scale). **B** Performances of gen.2.

The differences in performances between gen.1 and gen.2 are extremely significant. Af-

ter only four days at 67°C, the gen.1 devices already exhibit a leakage current of 0.2mA, 10'000 times more than gen.2 at the same time-point. The level of leakage current exhibited by the gen.1 interconnects confirms that the contribution of the exposed Pt sidewall (see section 2.3.4) is far from negligible.

The results shown in figure 2.31 make it clear that the benefits of the core-shell process in terms of hermeticity are massive. The absolute values in current should however be considered with care. Indeed, due to the nature of the measurement, the resistance of the track itself will influence the magnitude of the potential applied across the interface. This can be understood using a very basic electrical model for the interface composed of 3 resistance in series. Assuming the two interdigitated track are represented by resistance  $R_t$  and the encapsulation by the resistance  $R_e$ , the voltage drop  $V_e$  applied across the encapsulation during the leakage current measurement is given by:

$$V_e = \frac{V R_e}{R_e + 2R_t}$$

From the equation above, it is clear that samples are assessed under different conditions depending on the value of  $R_t$ . The influence of the track resistance can however be mitigated by the encapsulation resistance: for a sufficiently large  $R_e$ , changes in  $R_t$  are negligible. Based on the simulated sheet resistance (section 2.4.1), the theoretical track resistance for the device is found to be 700Ω for gen.1 and 1300 Ω for gen.2. Considering we are measuring  $R_e$  in the order of 500kΩ for gen.1 and 50MΩ for gen.2, this means that the track only account for somewhere between 0.1% and 0.001% of the total interface resistance which is, in effect, negligible. These considerations effectively validate the fact that the results shown in figure 2.31 are an accurate representation of the hermeticity of the sample under a bias of 5V.

## 2.5 Variation on a Theme: Fabricating a Soft and Optically Transparent Neural Interface

### 2.5.1 Introduction

A key advantage of engineered stretchability resides in its broad applicability since the strain-relief mechanisms are independent of the materials themselves. While this is was technically true for the first generation of Y-shaped kirigami, the specificity of the manufacturing made it difficult to translate the approach to new materials: the delicate balance between film thicknesses, pattern dimensions and etching time made it a not trivial endeavor. These limitations were lifted with the implementation of the new, core-shell strategy which alleviated much of the interdependency between the subsequent etching steps. In order to showcase the adaptability of this new process, the manufac-

## 2.5 Variation on a Theme: Fabricating a Soft and Optically Transparent Neural Interface

---

turing of transparent, stretchable interconnects is demonstrated in this section.

Transparent implants have long been an area of interest in neuroscience for their ability to combine electrical recording and stimulation with light-based interaction methods. These devices integrate high transmittance materials under the form of transparent interconnects, substrates and electrode coatings. Here, we propose a soft, transparent  $\mu$ ECOG based on the core-shell micropattern technology. Since this application is first and foremost a technological showcase, we focused our efforts on the interconnects, relying on the pre-established technology for the electrode coating (Pt-PDMS composite). The technological development was framed around the requirements of two of the most popular techniques: two-photon calcium imaging and optical stimulation of neurons expressing channelrhodopsin 2 (ChR2).

**Two-photon calcium imaging** Two-photon calcium imaging is a microscopy technique which relies on fluorescent emissions in order to observe neuronal activity. To generate this signal, the neuronal population of interest is first loaded with a calcium-sensitive dye or, more commonly, genetically engineered to express a calcium indicator. As a result, the fluorescence level of these neurons will be in direct correlation with their spiking activity. The recording per se is carried out by scanning an infrared laser beam across the brain surface, which excites the calcium tag, leading to the desired fluorescent emission. In two-photon microscopy, the energy of two long wavelength photons is used to achieve excitation instead of a single one. This allows to improve both the sharpness of the image and the penetration depth of the light. While two-photon imaging has been extremely successful at providing researchers with granular understanding of the spatial organization of neuronal circuits, this technique is characterized by a low temporal resolution inherent to the mechanism behind the signal - fluorescence [92]. Transparent neural interfaces have the potential to bridge this gap by coupling high temporal resolution electrical recordings with the circuit-level patterns revealed by light-based methodologies.

**Optical stimulation** Introduced in a series of breakthrough publications in the early 2000s [93, 94, 95, 96], optogenetics promised to solve the issue of targeted neural stimulation by offering cell-type and function-dependent selectivity. Optogenetics is a technology based on the genetic targeting and modifications of specific neuronal type with a light-sensitive ion channel. The activation or inhibition of the selected neuronal population is then made possible via illumination. From a device perspective, the need for a transparency arises when target of the optical stimulation is located in close proximity or directly on top of the recording sites of interest. In the case of optically opaque materials, the interconnects and electrodes will absorb the incoming light, preventing the proper activation of the neurons in the region and generating photo-electric artifacts. The ability to stimulate and record in a synchronous and colocalized fashion therefore

requires the development of a transparent implant.

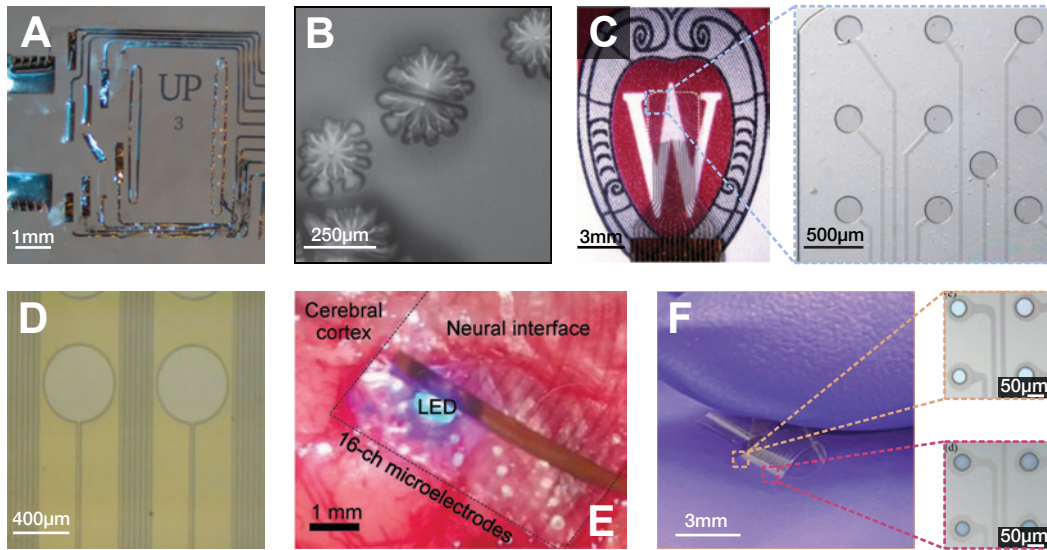


Figure 2.32: Examples of transparent substrates, conductors and coatings. **A** Picture of a device exhibiting severe delamination of the tracks and electrodes due to poor metal-parylene adhesion [97]. **B** Due to the limited thermal budget of parylene, processes requiring elevated temperatures can cause the film to burn, crack or bubble, as shown here. Adapted from [97]. **C** Transparent ECoG fabricated via the transfer of graphene monolayers onto a parylene substrate [98]. **D** Close-up view of an ITO electrode array patterned on parylene [99]. **E** Picture of a 16-channel ECoG fabricated using Ag/Au core-shell nanowires on a parylene substrate [100]. Optical stimulation is performed through the array using a  $\mu$ LED mounted on a FFC. **F** The electro-chemical performances of ITO electrodes can be improved using transparent coatings such as PEDOT:PSS. The uncoated and coated electrode sites are shown in the top and bottom inset respectively. Adapted from [101].

**Transparent neural interfaces** Numerous approaches to transparent electrode arrays have been proposed to this day, consisting in various combinations of transparent substrates, interconnects and coatings. Among the substrates, parylene constitutes certainly the most widely used material [102, 103, 104] due to its high transmittance properties, mechanical flexibility and biocompatibility [105]. Its limited thermal budget and chemical inertness can however make its processing challenging, in particular in terms of adhesion with metallic layers and itself [97]. Alternative substrate materials include other plastics, such as PET [106, 107], as well as elastomer, such as PDMS [108]. With regard to interconnects and electrode sites, transparency can be engineered in two ways: (1) using intrinsically transparent materials or (2) using structures smaller than the critical wavelength such that they do not interact with the incoming light. The former approach encompasses mainly Indium Tin Oxide (ITO), a brittle but highly transparent alloy

## 2.5 Variation on a Theme: Fabricating a Soft and Optically Transparent Neural Interface

(>80% transmittance in the visible spectrum). In that regard, a significant challenges resides in obtaining ITO films with a low sheet resistance, which requires careful tuning of the deposition parameters. In the same category, PEDOT:PSS, a conductive polymer, has been the subject of an increased focus in the fields of neuro-engineering both as standalone conductor [109], an additive [110] and an electrode coating [101]. With regard to conductors based on nano-scale structures, approaches using graphene [98], carbon nanotubes [111] and nanowires [100] have all been demonstrated promising results in terms of electrical, optical and mechanical properties. Their patterning however, which rely on transfer printing or screen printing, often proves challenging.

**Requirements and device concept** The implementation of a strategy for multimodal recording and stimulation necessitates the development of a transparent, conformable neural interface. The requirements for such a device are summarized below:

- The interconnects should be able to deform elastically within a range of elongation comprised between 1 and 5%.
- The device should be able to sustain a larger, one-time mechanical deformation (20-40%) which is likely to take place during implantation.
- The electrodes impedances should be low enough to allow stimulation using research-grade current pulse generators whose voltage compliances typically range from 40 to 100V. This places requirements on both the conductivity of the interconnects and the coating of the electrodes.
- The manufacturing process should allow to pattern narrow tracks (<100 $\mu$ m) in order to produce devices suitable for small animal models (mouse, rat) which are typically used in optogenetics.
- The interconnects should exhibit a high transmittance index (>80%) across a wide band of wavelengths (400-1000nm) such that: (1) incoming light does not generate photo-artifacts and (2) exiting light is not absorbed or diffracted (e.g. fluorescence signal).
- The materials should not exhibit auto-fluorescent behavior which could interfere with imaging techniques.

In order to fulfill those requirement, the kirigami process had to be transferred to a new materials stack. Since polyimide exhibits both a significant absorbance below 500nm and a strong auto-fluorescent behavior, the shell layer is replaced with parylene-C, which closely matches its mechanical properties. The platinum core is discarded in favor of ITO which has the advantage of being patternable using the same IBE process as its metal counterpart. Furthermore, it is hypothesized that the strain relief mechanism of

the Y-shaped motif will help address the issues related to the brittleness of this material. The soft encapsulation is left unchanged, constituting of two PDMS membranes plasma-bonded on each side of the interconnects. Similarly, the electrodes are coated with a Pt-PDMS composite which, while being opaque, provides a quick and easy way to validate the approach on a device level.

The manufacturing process for transparent, stretchable interconnects is described in section 2.5.2.1 and the results in section 2.5.3.4. The benefit of the kirigami approach are studied in section 2.5.3.3, in which the electro-mechanical performances of the interconnects are characterized. Finally, the process limitations are discussed in section 2.5.4 alongside suggestions of future improvements.

### 2.5.2 Methods

#### 2.5.2.1 Process flow

**Design** The design strategy used for the fabrication of transparent micropatterned interconnects is identical to the one presented in section 2.3.2.1 for the core-shell process.

**Core layers patterning- Figure 2.33** The fabrication process begins with the sputtering (SPIDER600, Pfeiffer) of a tungsten-titanium alloy film (TiW, 50nm) followed by aluminium (Al, 100nm) on a 4-inch silicon wafer. Next, the wafer surface is dehydrated at 150°C for 15min (UM100, Memmert) and cleaned from organic contaminants with an oxygen plasma treatment (GiGAbatch, Tepla at 600W, 0.8mbar, 400sccm, 2min). Soon after, a 25nm layer of SiO<sub>2</sub> is deposited via RF magnetron sputtering (SPIDER600). Following another dehydration step in a convection oven and O<sub>2</sub> plasma activation (600W, 0.8mbar, 400sccm, 1min), the wafer surface is treated with 3-methacryloxypropyl trimethoxysilane (A174, Merck Milipore) in order to improve the adhesion between the SiO<sub>2</sub> and parylene layer. The process is performed via full immersion in a solution of IPA, DI water and A174 (ratio 150:10:1) for 5min. The wafer is then rinsed with IPA before being dried in an oven at 100°C for 10min. Next, a 1-micron-thick layer of parylene is deposited via CVD (C-30-S, Comelec), followed by the sputtering of ITO at room temperature (SPIDER600, 500W, Ar 15sccm, 2.93nm/s). The deposition time was varied depending on the sample to reach thickness of 100, 150 or 200 nanometers. The patterning of the ITO film is achieved using a 1-micron layer of PR (AZ 10XT-07, MicroChemicals) which is spin-coated following a 20-minute dehydration step at 125°C. The resist is baked at 110°C for 90s before being exposed using a mask aligner (MA6gen3, Süss). The illumination dose is set to 160mJ/cm<sup>2</sup> and the Cr mask, previously patterned via direct-write lithography, is placed in hard contact with the wafer. The wafer is then processed in a modular cluster tool (ACS 200, Süss) where the PR is hard baked (110°C, 90s) and developed for 93s using a KOH-based solution (AZ 400K, MicroChemicals). Next, a reflow of the

## 2.5 Variation on a Theme: Fabricating a Soft and Optically Transparent Neural Interface

PR is performed by placing the wafer on hotplate at 125°C for 2min. This treatment is intended to round off the patterns profile in order to mitigate the redeposition of material on the PR sidewalls during the subsequent removal of the ITO films via IBE (Nexus IBE350, Veeco). During the etching procedure, the wafer is tilted by a -10° so as to further reduce the buildup of fences. The remaining PR is stripped using a combination of O<sub>2</sub> plasma (200W, 0.5mbar, 200sccm O<sub>2</sub>, 60s) and solvent baths (Microposit Remover 1165, Dow Chemicals) at 70°C.

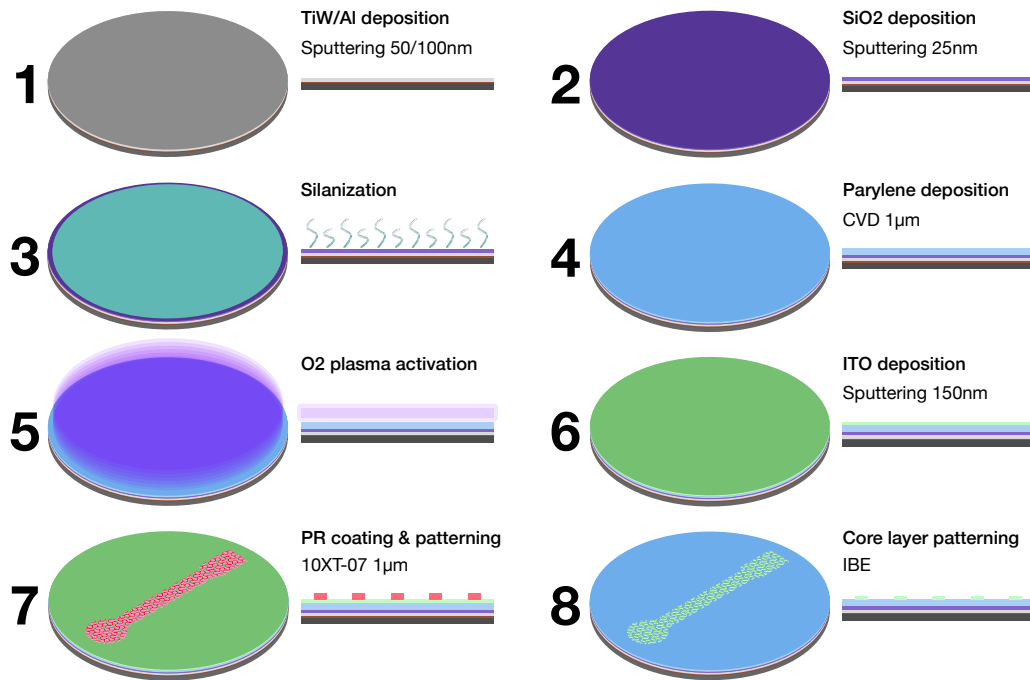


Figure 2.33: Phase 2 of the process flow - core layer patterning.

**Shell layers patterning - Figure 2.34** Following an O<sub>2</sub> plasma treatment (200W, 0.5mbar, 200sccm O<sub>2</sub>, 60s), 1-micron-thick layer of parylene is deposited via CVD. The wafer surface is then treated once more with silane (A174), using the same immersion technique as before. Next, a 25nm layer of SiO<sub>2</sub> is deposited by PECVD at 200°C (Plas-malab System 100, Oxford Instruments), concluding the material stack buildup. The patterning of the shell layers begins with the coating of a 4-micron-thick layer of PR (AZ ECI3027, MicroChemicals). Proper adhesion between the SiO<sub>2</sub> and the resist is ensured with an HMDS treatment prior to spin-coating. The PR is exposed using a mask aligner (MA6gen3, Süß, 600mJ/cm<sup>2</sup>, hard contact) and developed in an automatic cluster tool (MF CD 26, Shipley Microposit, 137s). Next, the SiO<sub>2</sub>/parylene/SiO<sub>2</sub> layers are dry etched using a sequence of CHF<sub>3</sub>/He, O<sub>2</sub>, CHF<sub>3</sub>/He chemistries (Advanced Plasma System, SPTS). Upon completion of the etching procedure, the remaining PR is stripped using a combination of O<sub>2</sub> plasma (600W, 0.8mbar, 400sccm, 30s) and a solvent bath (Microposit Remover 1165, Dow Chemicals) at 70°C. The opening of the electrodes and

contacts pads is then performed in a third lithographic step. First, the wafer is dehydrated (125°C, 3min) and coated with a 4-micron-thick layer of PR (AZ ECI3027, MicroChemicals). Next, the resist is exposed and developed using the identical parameters as before. The top SiO<sub>2</sub>/Ti and parylene layers are then etched using the same CHF<sub>3</sub>/He and O<sub>2</sub> chemistries. Finally, the PR mask is stripped following a sequence of O<sub>2</sub> plasma (600W, 0.8mbar, 400sccm, 30s) and solvent baths (Microposit Remover 1165, Dow Chemicals) at 70°C.

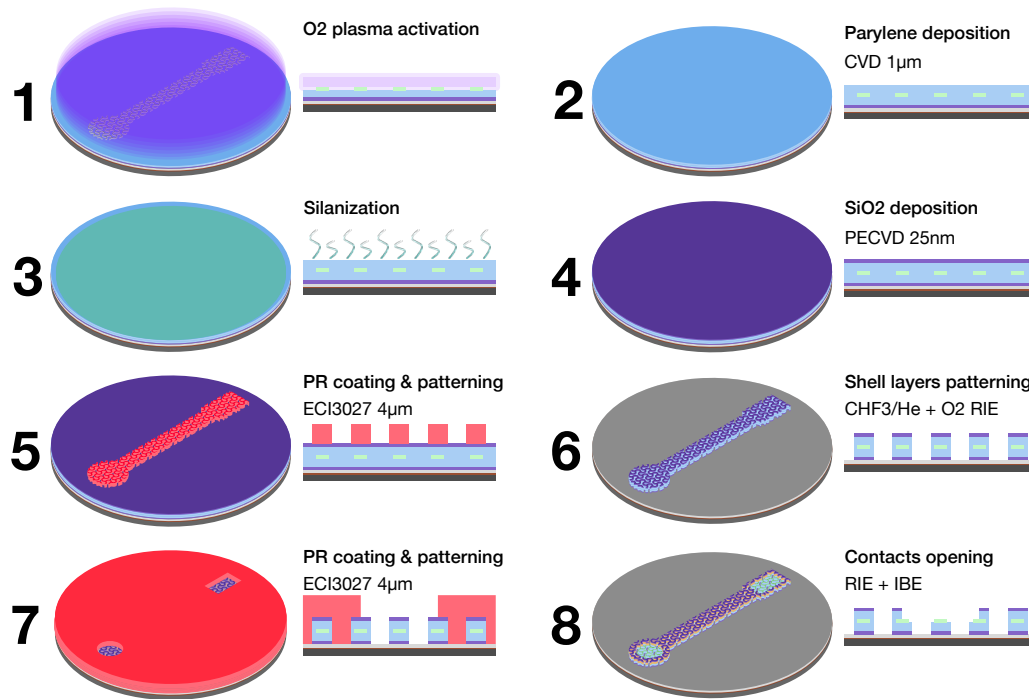


Figure 2.34: Phase 3 of the process flow - shell layer patterning.

**Silicone encapsulation, electrodes coating and connector assembly** The methods used to fabricate the top and bottom silicone encapsulation as well as to coat the electrodes and assemble the connector are identical to the ones presented in section 2.3.2.1 for the core-shell process.

### 2.5.2.2 Electromechanical characterization

**Sheet resistance measurements** In order to determine the optimal thickness for the core layer of the micropatterns, the resistivity of different ITO thin films is assessed. The test samples consist of 3 float glass wafers coated with parylene (1µm) on top of which a layer of ITO is sputtered, varying the deposition time in order to reach thicknesses of 100, 150 and 200nm respectively. Each wafer is then taped on top of a paper grid which delimits sectors of 1cm by 2cm. The ITO and parylene layers are subsequently divided



## 2.5 Variation on a Theme: Fabricating a Soft and Optically Transparent Neural Interface

with a razor blade into 18 zones which follow the lines drawn on the paper. Next, a 4-point probe resistance measurement is taken at the center of each of the zone using a source meter (Keithley). The probe itself is made of 4 spring-loaded pins mounted on a micro-manipulator. The sheet resistance can then be extracted from the Van Der Pauw formula for 4-point measurements:

$$R_s = \frac{\pi}{\ln(2)} * \frac{V}{i} [\Omega/sq.]$$

where  $R_s$  is the sheet resistance,  $i$  the applied current and  $V$  the measured voltage. The resistivity of the three samples is calculated by multiplying the measured sheet resistance with the film thickness.

**Transmittance measurements** The transparency of the different layers was assessed by measuring the percentage of transmitted light over a wavelength spectrum comprised between 300 and 1000nm. The test samples consist of 3 float glass wafers coated with parylene (1 $\mu$ m) and coated with an ITO film of varying thickness (100, 150 and 200nm). A fourth parylene-coated wafer is also prepared, as a mean of comparison. The transmittance of all four samples is then measured over the selected wavelength spectrum using a transmittometer (F20-UV, FilmMetrics) in air.

**Adhesion test** In order to assess the effect of the SiO<sub>2</sub> depositions methods and various surface treatments on the strength of the PDMS-SiO<sub>2</sub>-parylene adhesion, a series of T-peel tests were performed.

To prepare the test samples, six 4-inch Si wafers are treated with HMDS and coated with 10 $\mu$ m of parylene (C-30-S, Comelec). Three conditions are investigated, each applied to two wafers: (1) MPS silanisation via immersion in solution (IPA:DI:A174 ratio 150:10:1), (2) oxygen plasma activation (200W, 0.5mbar, 200sccm O<sub>2</sub>, 60s) and (3) no surface treatment. 25nm of SiO<sub>2</sub> are then sputtered on half of the wafers (one for each surface condition). The deposition is performed with a RF source bias at 1000W, 98sccm Ar, 13sccm O<sub>2</sub> which corresponds to a rate of 0.2nm/s. On the other three wafers, the 25nm of SiO<sub>2</sub> are formed by PECVD (Plasmalab System 100, Oxford Instruments) at 200°C. To create pull tabs, a sacrificial layer of PSS is spincoated at 3200rpm and baked for 3min at 135°C. The wafers are then partially immersed in DI water for about 1h in a vertical wafer holder, such that a 3-centimeter-wide strip of PSS is left. Next, the silicone side of a PET/PDMS stack (23/50 $\mu$ m) is plasma activated and bonded on each of the wafer. The samples are then put under a weight and placed in an oven at 75°C. The next day, the top PET film is peeled off and a series of rectangle (8.3cm by 7cm) are cut through the whole stack via femto-laser machining. The strips are peeled off the wafer and the pull tabs are separated by soaking them briefly in DI water to dissolve the PSS. The samples

are mounted on a tensile tester (MTS Criterion 42), configured with a load cell of 10N. The peeling rate is set to 0.5 mm/s and the force/displacement is recorded using the instrument's software.

**Impedance spectroscopy** See methods in section 2.2.2.2.

**Chronopotentiometry** See methods in section 2.2.2.2.

### 2.5.3 Results

#### 2.5.3.1 Materials characterization

**Sheet resistance** The material selection process begins with the evaluation of the transparency/conductivity trade-off for various thicknesses of ITO. Figure 2.35 depicts the spacial distribution of the sheet resistance across parylene coated wafers for 100, 150 and 200nm of ITO. All samples were sputtered at room temperature under same conditions (500W RF bias, 15sccm Ar flow, 5 $\mu$ bar chamber pressure), varying only the deposition time. The three film thicknesses exhibit higher sheet resistance at the center of the wafer. The nature of the measurement is such that for a fixed injected current, the voltage drop will be lower where the film is thicker and vice versa. Thus, what appears as a decrease in sheet resistance is caused by variation in the films thicknesses. This is surprising because non-uniformities in the sputtering process are typically expected to lead to thicker film in the center whereas here, it is the opposite. This phenomenon points toward a growth mechanism specific to ITO film and will be further studied through elispometry.

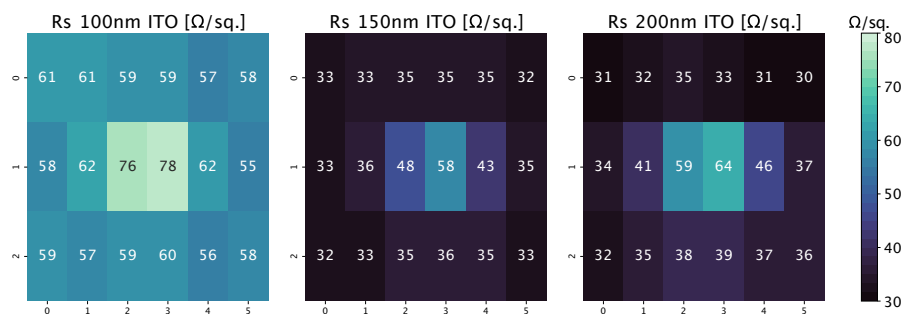


Figure 2.35: Sheet resistance measurements of sputtered ITO for various film thicknesses. The average sheet resistance for 100nm ITO appears notably higher at  $60.82 \pm 6.17 \Omega/\text{sq.}$  with the 150nm and 200nm films sitting within the margin of error of each other ( $36.61 \pm 6.53 \Omega/\text{sq.}$  and  $38.3 \pm 9.38 \Omega/\text{sq.}$  respectively)

## 2.5 Variation on a Theme: Fabricating a Soft and Optically Transparent Neural Interface

Looking at variation across the three samples, the sheet resistance trend is consistent with results from the literature [112]. For all deposition thicknesses, the sheet resistance of ITO is found to be significantly higher than the one of platinum (0.5-1  $\Omega/\text{sq}$ ). In order to improve the conductivity of ITO, the deposition can be performed at higher temperature which effectively increases the crystallinity of the film [101]. The strategy can however has its limitation, as the temperature should not exceed the thermal budget of the parylene substrate (glass transition temperature  $\sim 90^\circ\text{C}$  [97]).

**Transmittance** The transmittance measurements for all three different thickness of ITO are shown in figure 2.36, alongside the measurement for bare parylene. In order to offset the losses caused by the carrier, the transmittance values of the different samples were divided by the transmittance of a float glass wafer, which was found to be around 90% in the spectrum of interest (400-1000nm). Varying the ITO thickness results in only modest changes in transparency, with the 100-nanometer-thick layer displaying the best performances below 650nm and the 150nm sample surpassing it beyond that point. Given the results, the variations in transmittance can likely be attributed to the interlayer interferences, which become constructive or destructive depending the length of the optical pathway, rather than the losses in the bulk material.

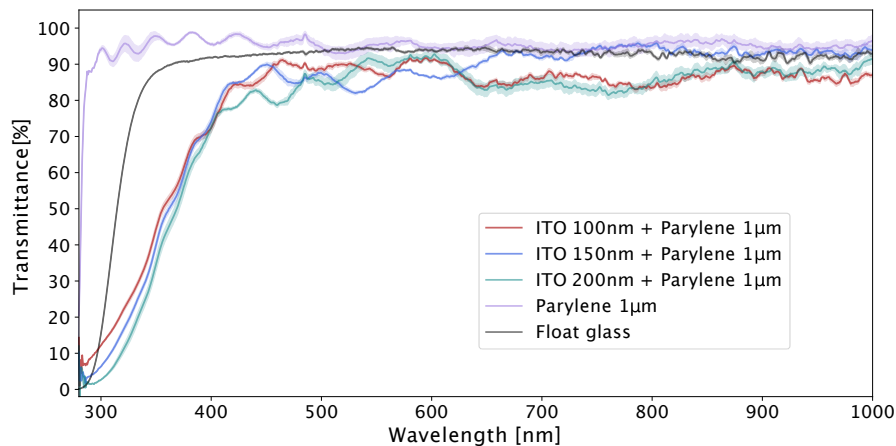


Figure 2.36: Mean direct transmittance of various ITO film thicknesses on  $1\mu\text{m}$  Parylene. The data was adjusted to account for the float glass substrate. Shaded areas correspond to the minimum and maximum values boundaries.

**Adhesion** Inter-layer adhesion represents a key challenge in the development of parylene-based devices. Due to the transparency requirements, common adhesion layers such as chromium and titanium cannot be used to form strong bonds between organic and inorganic materials. In the core-shell process, the most critical interface is located between the top  $\text{SiO}_2$  layer and the parylene, as its strength governs the outcome of the bonding of the top PDMS membrane. Indeed, the lack of adhesion between these two

layers can cause the top PDMS encapsulation to delaminate from the wafer, tearing away the top SiO<sub>2</sub> with it. In order to assess the best strategy, a series of T-peel tests are conducted, comparing three surface treatments (O<sub>2</sub> plasma, silanization, no activation) and two deposition methods (sputtering, PECVD). Unfortunately, only the samples fabricated using a combination of silanization and PECVD displayed measurable adhesion (Fig. 2.37). In this configuration, the measured average adhesion strength (37.9 N/m) is comparable with that of a Parylene-Parylene interface (38 N/m), as reported by Origoza-Diaz et al [97]. Interestingly, the effectiveness of the silanization treatment does depend on the deposition process, as sputtered SiO<sub>2</sub> samples failed to provide good adhesion between the PDMS and the parylene. This difference can be attributed to the high kinetic energy of the sputtered species which can destroy the silane bonds presents at the surface of the wafer.

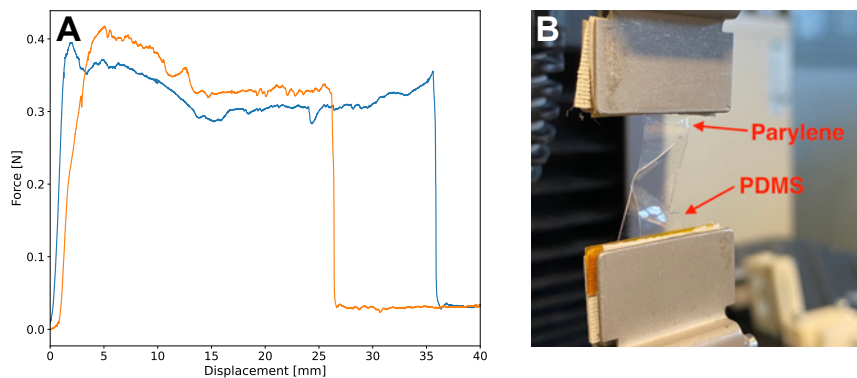


Figure 2.37: Characterization of the PDMS-Parylene adhesion strength. **A** T-peel test results for samples combining surface silanization and PECVD of SiO<sub>2</sub>. **B** Picture of a delaminated sample.

### 2.5.3.2 Microfabrication

Based on the measurements of transmittance and sheet resistance, a thickness of 150nm is selected for the ITO layer as the best trade-off between transparency and conductivity. Using this parameter, the core-shell process presented in section 2.5.2.1 is used to manufacture a series of fully transparent devices. Figure 2.38A shows the proper transfer of the Y-shaped motifs to both the ITO core layer and the parylene shell. The patterning was optimized using the same strategy discussed in 2.3.4, which consists of introducing an offset in the the Cr mask motifs.

Imaging of the exposed electrode sites (Fig. 2.38B) reveals a slight misalignment between core and shell layers, resulting in parts of the ITO being exposed in the encapsulated portion of the interconnect. Nevertheless, the contact opening is closer to the desired result than the polyimide process (Fig. 2.20), with the bottom parylene layer still intact (Fig. 2.38C-D). Since in both cases the etching time is determined by monitor-

## 2.5 Variation on a Theme: Fabricating a Soft and Optically Transparent Neural Interface

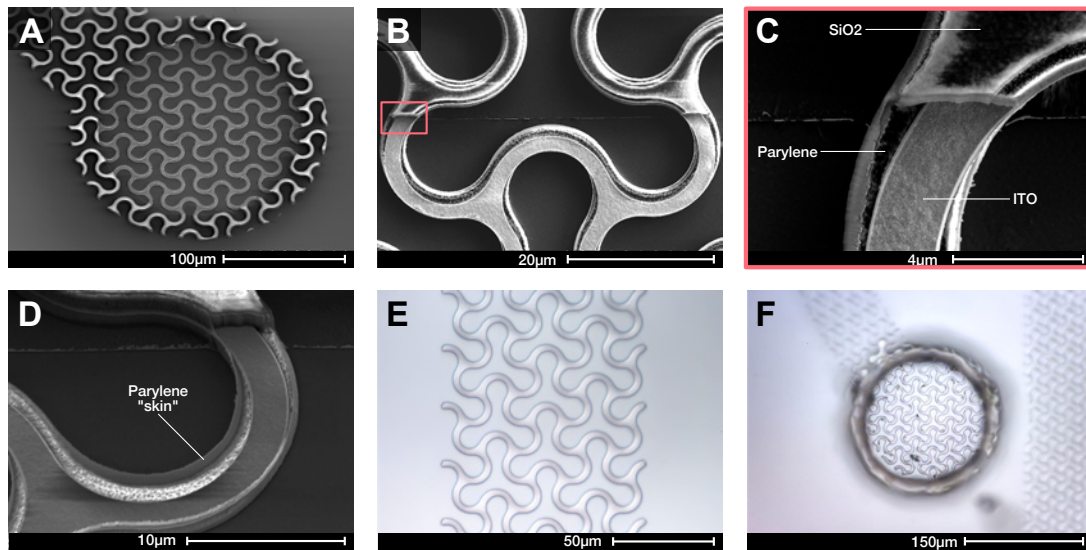


Figure 2.38: Imaging of the micropatterned parylene/ITO/parylene stack. **A** SEM picture of an electrode site following the completion of phase 3 (shell layers patterning). **B** SEM picture of the transition between covered and exposed ITO. The image reveals a slight misalignment between the core and shell layers. **C-D** Close-up views of the patterned stack show a slight recess of the top SiO<sub>2</sub> layer as well as a vertical "skin" along the periphery of the meanders. **E-F** Micrographs of a transparent interconnect (**E**) and electrode site (**F**) after PDMS encapsulation. Debris resulting from the laser machining of the top membrane can be seen at the bottom of the opening.

ing the etching by-products in the chamber, it appears that end-point detection curve is slightly better tuned for the parylene process.

Interestingly, the patterned stack does exhibit the "skin" observed in the polyimide process along the sides of the meanders (see Fig. 2.20), which would indicate that the CHF<sub>3</sub>/He gas mixture does affect parylene in the same way. Similarly, the top SiO<sub>2</sub> presents an identical profile in both processes, with slight narrowing compared to the polymer. This is to be expected since the recess is a product of the lateral shrinkage of the PR which occur in both cases (see section 2.3.3).

### 2.5.3.3 Electromechanical characterization of transparent, stretchable interconnects

The characterization of the ITO-based interconnects was performed using identical methods and samples to those described in section 2.4.

**Hysteresis** Figure 2.39 presents the change in relative resistance upon the application of strain cycles of gradually increasing magnitude. While the electromechanical behavior of the transparent interconnects follows the trends identified in 2.4, the onset strain for the different deformation regime is significantly lower. The effect of the plastic deformation appears clearly in figure 2.39 for strain values above 4%. Similarly, the onset of the fracture regime and subsequent electrical failure are observed at 8 and 10% respectively. The differences with the Pt-based interconnects can be attributed to two factors: the brittleness of the ITO layer which, unlike Pt, has a fracture limit lower than 1% strain and the poor adhesion of the parylene layers unlike the polyimide in the Pt-based interconnects.

### 2.5.3.4 Transparent neural interfaces

In order to evaluate the performances of the transparent, stretchable interconnects at the device level, a soft  $\mu$ ECOG is fabricated using the process flow described in section 2.5.2. The implant, shown schematically in figure 2.40, is designed to map the auditory cortex of a rat animal model. It consists of an array of 24 circular electrodes as well as set of test structures designed to verify the integrity of the device.

**In-vitro characterization** The EIS data show that the maximum phase (closest to 0°) is reached at 40Hz, corresponding to an average impedance of  $221 \pm 98$  k $\Omega$  (Fig. 2.41A). The brittle nature of the material makes the implant prone to mechanical damage during handling, which might explain the large standard deviation. The voltage transients, shown in figure 2.41B, reveal that the voltage drop at the interface reaches values up to 30V for some channels, a 10 times increase compared to platinum-based devices of

## 2.5 Variation on a Theme: Fabricating a Soft and Optically Transparent Neural Interface

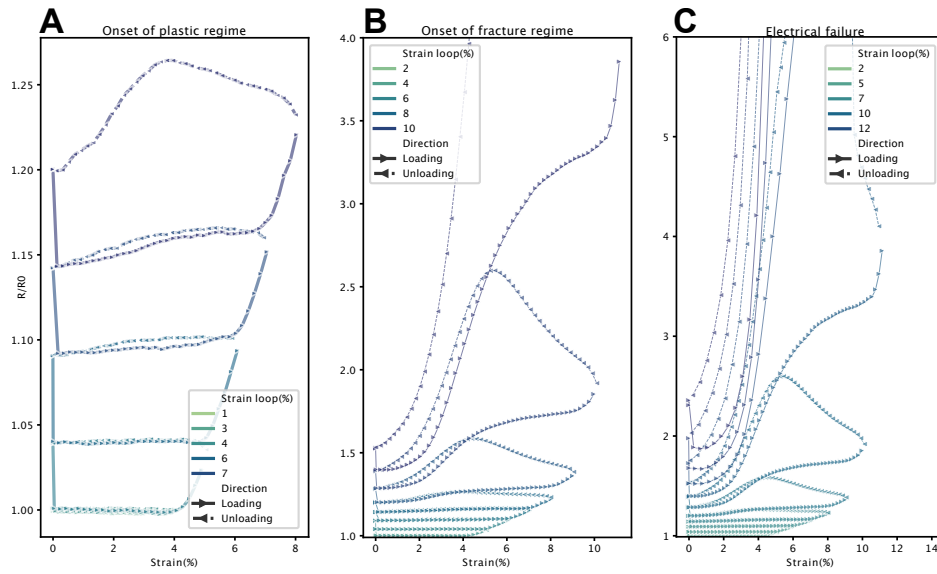


Figure 2.39: Average hysteresis of transparent stretchable interconnects.  $n=4$  for all conditions. Track width is  $520\mu\text{m}$ . **A** The onset of the plastic regime can be observed for strains beyond 4%. **B** The structures enter the fracture regime past 8% strain. **C** Electrical failure begins to take place at strain beyond 11%.

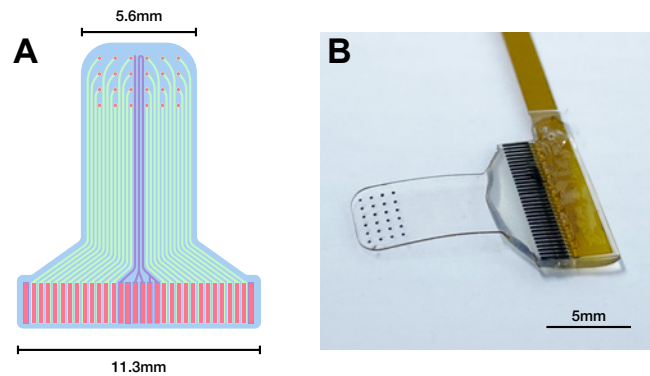


Figure 2.40: Transparent, soft  $\mu\text{ECoG}$ . **A** Schematic of the device. The 24 channels are colored in green, the electrodes and contact pads in red and the test structures in purple. **B** Picture of fully assembled  $\mu\text{ECoG}$ .

similar dimensions. In order to extract the intrinsic resistance of the ITO interconnect, one can look at the impedance spectrum at high frequency. In this state, the double layer capacitance is effectively shorted, cancelling the contribution of the electrode interface. In the case of the transparent  $\mu$ ECoG, the mean impedance at 500kHz reaches  $26 \pm 5$  k $\Omega$ . In comparison, the resistance for an equivalent track in plain ITO is estimated at 10k $\Omega$  using a sheet resistance of 50 $\Omega$ /sq.

The direct transmittance spectrum of the device, assessed using the same setup as the bare ITO films (F20-UV transmittometer, FilMetrics), is shown in figure 2.41C. The measured values fall slightly short of the 85% target defined in the requirements. Considering the results observed on non-patterned stack of materials, these measurements should be attributed to a combination of (1) losses in the bulk material, (2) the internal reflections occurring at the interface between each material and (3) diffuse reflections caused by the Y-shaped pattern itself.

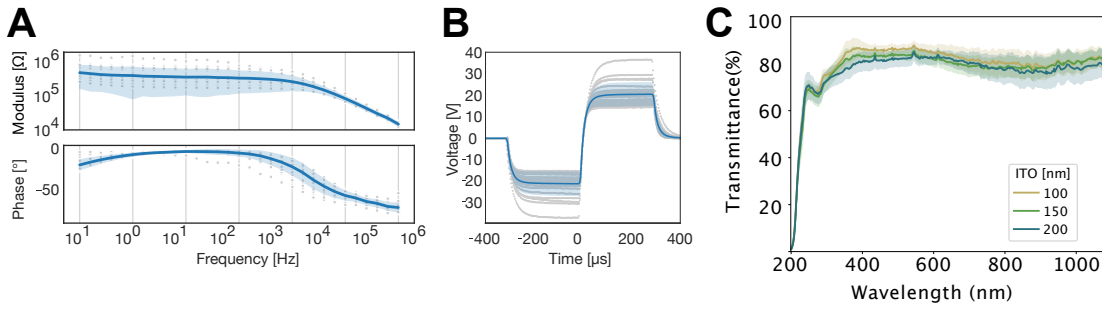


Figure 2.41: Characterization of the  $\mu$ ECoG in-vitro. **A** Impedance spectrum measured in a 3-electrode configuration. **B** Average voltage transients following the injection of a 100 $\mu$ A biphasic current pulse. **C** Mean direct transmittance through the interconnect area of transparent  $\mu$ ECoG with various ITO film thicknesses. The data was adjusted to account for the float glass substrate. Shaded areas correspond to the minimum and maximum values boundaries.

**In-vivo experimentation** In order to validate the capabilities of the transparent ECoG in-vivo, the device is used to record evoked potentials in a rat auditory cortex. This particular target was chosen for its familiarity to the experimenters (see chapter 3), rather than its relevance to the application at hands.

Briefly, a wild type rat is put to anesthetized using an injection of ketamine. Following a craniotomy above the auditory cortex, the dura is open and the ECoG is put in position on top of the auditory cortex. Next, the ECoG is connected to a wireless recording system (W2100-HS32, Multichannel Systems) which amplifies and digitizes the signal before sending the data to the acquisition computer. The animal is fitted with a pair of earbuds and presented with a series of acoustic stimuli. The sounds used to generate frequency specific AEPs consist of a 500ms tone-burst followed by 500ms of silence, presented



## 2.5 Variation on a Theme: Fabricating a Soft and Optically Transparent Neural Interface

in a continuous fashion for a duration of 3 minutes.

Figure 2.42A presents the recorded response to a 5kHz tone burst. Here, the raw signal was filtered between 1 and 1kHz and averaged over the period of the acoustic stimuli (1s). A clear ON and OFF response matching the frequency of the auditory stimulus can be seen on the single channel trace (figure 2.42B).

In order to validate the ability of the ECoG to discriminate cortical signals, the frequency of the tones is varied between 5 and 10kHz. An activation heatmap is built by extracting the peak amplitude from the average response over the period of the acoustic stimuli (figure 2.42C). The computed map exhibit a clear shift in response across the two frequencies, with the maximum amplitude being spatially different for each sound stimulus.

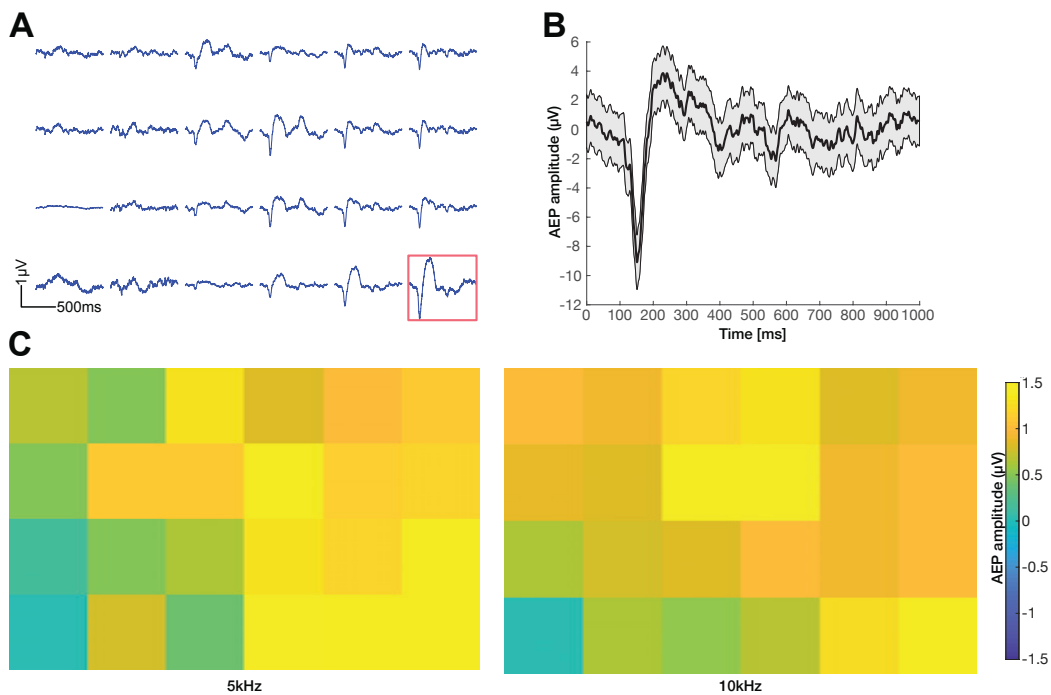


Figure 2.42: Auditory cortex recordings in rat. **A** Averaged response to a 5kHz tone burst stimulus. **B** The single channel trace (channel 6, red box) demonstrate a clear ON (green arrow) and OFF (red arrow) response matching the frequency of the auditory stimulus. The shaded area indicates standard deviation. **C** Color map of the auditory cortex response to 5kHz and 10kHz tone burst stimulus.

The experiment is concluded with the recording of the in-vivo impedance spectrum and voltage transients. The mean impedance at 40Hz climbs to a value of 379 kΩ with the voltage drop showing a similar increase (Fig. 2.43). With the change of medium, from PBS to neural tissue, an increase in impedance is expected although in this case damaged tracks caused by device manipulation are most likely to be the major contributing factor.

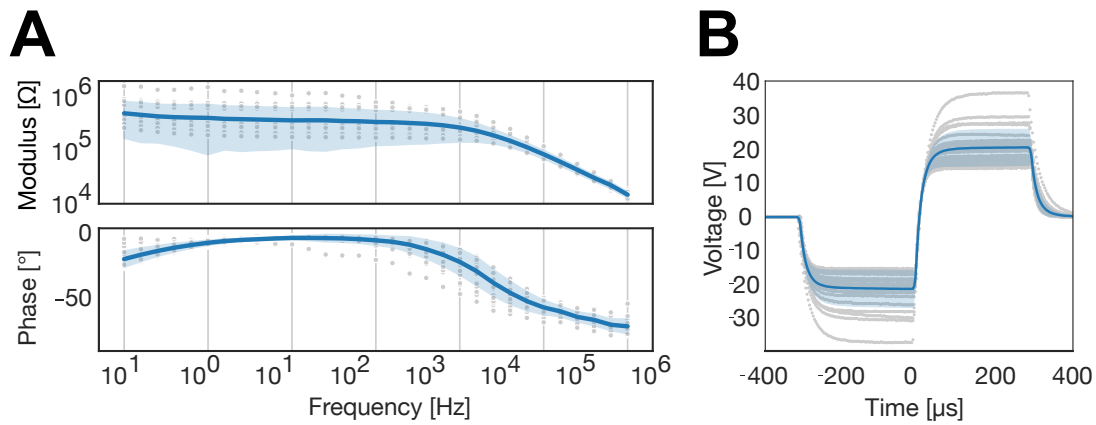


Figure 2.43: Characterization of the  $\mu$ ECoG in-vivo. **A** Impedance spectrum measured in a 2-electrode configuration. **B** Average voltage transients following the injection of a  $100\mu\text{A}$  biphasic current pulse.

This succinct experiment allowed us to validate the in-vivo functionality of a device built with transparent, stretchable interconnects. Future work should focus on demonstrating the use of combined recording modalities, such as 2-photon imaging and optical stimulation.

### 2.5.4 Summary and Discussion

**Summary** In the section, the core-shell strategy is applied to a new multilayer stack of materials in order to produce transparent and stretchable interconnects. To do so, the polyimide shell and platinum core are replaced with parylene and ITO as the dielectric and conductive layer respectively. The silicone encapsulation as well as the electrodes coating are left unchanged from the original process. The main development steps are summarized below:

- The transmittance/conductivity trade-off of sputtered ITO is characterized and the optimal film thickness (150nm) is selected for the fabrication of functional devices.
- The adhesion strength between the top  $\text{SiO}_2$  and the parylene shell is analyzed and the best performing strategy, obtained by combining a silane surface treatment with PECVD of the silicon dioxide layer, is selected for device manufacturing.
- The offset of the Y-shaped motif is updated in order to compensate for the transfer losses occurring during the photolithographic patterning and etching of the new parylene/ITO/parylene stack.

## 2.5 Variation on a Theme: Fabricating a Soft and Optically Transparent Neural Interface

These modifications enable the reliable manufacturing of transparent, stretching interconnects. Under uniaxial tensile load, the micropatterned tracks were able to sustain an 10% elongation before electrical failure.

In order to assess the performances of the transparent interconnects at the device level, a soft ECoG array is fabricated and characterized in-vitro and in-vivo. The implant, designed for recording of the rat auditory cortex, features 24 circular electrodes with a diameter of 160  $\mu\text{m}$ . The maximum phase impedance in-vitro is reached at 40Hz, corresponding to an average value of 221k $\Omega$ . This value increases to 379 k $\Omega$  when measured in-vivo, a different consistent with the change in medium. The VTs curves, collected both in PBS and in the animal, reveals a significant resistive drop caused by the low conductivity of the micropatterned ITO layer. In terms of neuro-physiological recordings, the device was able to record evoked LFPs from the auditory cortex of a rat, demonstrating its functionality.

**Outlook** The development work presented in this section lays for the foundations for the creation of a fully transparent, soft neural interface. While the fabricated ECoG was successfully used to record LFPs induced by acoustic stimulation, many of the combined recording and stimulation modalities have yet to be tested. In particular, the effect of the transparent micropatterned stack on the resolving power of 2-photon microscopy should be investigated. Similarly, much remains in the way of mechanical characterization, with the adhesion between ITO and parylene being unaddressed so far. It is critical for the micropatterned stack to behave cohesively from a mechanical stand-point, which necessitates strong bonds between each of the constitutive layer.

Looking at the performances of the the device, the achieved level of transparency allows to perform optical stimulation through the interconnects without generating a noticeable artifact. From an electrical stand-point, while the increased tracks resistance compared to the standard PI/Pt process does not affect the recording capabilities of the fabricated device, the matter is very different for electrical stimulation. With the current level of performances, research-grade pulse generators are just capable of supplying the voltage required to drive microampere-level current through the micropatterned ITO, with their medically approved counterparts being completely out of the question.

A potential solution to the conductivity and adhesion concerns raised so far consists of including an annealing step prior to the bonding of the top PDMS membrane. Annealing of parylene should, according to the literature [113], enhance the parylene-parylene adhesion, thereby improving the mechanical robustness and hermeticity of the devices. Additionally, thermal treatment of sputtered ITO has been shown to decrease the sheet resistance and opacity of the films [114]. The implementation of such process is not straightforward however, due to the large difference in the thermal expansion coefficient between the two materials on one hand, and on the other, to the level of atmospheric

control required in the furnace. Indeed, in order to avoid oxidation of the parylene film, the process needs to be performed under vacuum or nitrogen atmosphere.

From the perspective of the core-shell process, this endeavor proves that the new patterning strategy can be applied to a different material stack with only minor changes in the process. While the creation of a transparent neural interface is interesting in its own right, the real appeal resides in the integration of high performance hermetic materials as part of the shell. Such innovation could prolong greatly the lifespan of the array by slowing the diffusion of ionic species over time.

## 2.6 Conclusion

This chapter described the microfabrication processes and process improvements for the fabrication of soft and conformable implants targeted at the stimulation or recording of neural tissue. The mechanical compliance of the devices is enabled by the use of a thin elastomeric membrane as the substrate, Pt-PDMS composite as the electrode coating, as well as the integration of stretchable interconnects. The manufacturing of a reversibly elastic conductive layer is achieved via the periodic patterning of a Y-shaped motif through a multilayer stack of PI/Pt/PI. The newly developed core-shell process allows the fabrication of devices with improved electro-mechanical properties. The interconnects engineered using this method are able to elongate up to 15% before deforming plastically and can sustain repeated uniaxial deformation without significant mechanical fatigue (+6% increase over 1mio cycles). Furthermore, the leakage current measured in accelerated ageing conditions was reduced by a factor of 1000 in comparison with the previous generation of implants. On a device level, the integration of a new connector allowed to reduce the device footprint (from 5mm to 1mm in thickness) and to increase the reliability of the connection scheme. In addition to these improvements, the core-shell strategy retained all of the advantages of the original process, including the ability to fabricate small to large scale implants with customized shapes, electrical layouts and electrodes grid geometries. Overall, while the revised core-shell process fails to fully address the requirements that were described in the introduction of this thesis, it does enable new design and engineering possibilities to address these limitations and to potentially push the technology beyond neural interfaces.

In that regard, the most interesting aspect of the kirigami approach resides in the fact that it can be applied indiscriminately of the nature of materials stack. Indeed, this strategy could be potentially used to engineer stretchability not only in passive components like interconnects, but also in active ones such as LEDs or transistors. As demonstrated in this chapter, these devices could be composed of any combination of organic and inorganic materials without compromising the fundamental working principle behind the stretchability of the whole structure. For instance, one could form a basic, stretchable light emitting device by integrating an electroluminescent polymer such as Alq3

(8-hydroxyquinoline aluminum) as the core layer. This polymer has been demonstrated to emit green light when sandwiched between an ITO cathode, a Mg:Ag anode and a hole transporting layer of aromatic diamine [115]. This material stack could be easily deposited via the same techniques (sputtering, organic molecular beam deposition) before being micropatterned through a combination of oxygen and ion-beam etching. With regard to the shell layer, Parylene would consist of a suitable candidate thanks to its natural transparency. The development process required to implement these new materials would be very similar to the one demonstrated in section 2.5 of this thesis, with the critical points being the interlayer adhesion and the accurate transfer of the Y-shaped pattern.

An aspect which remained unexplored in this thesis, is the ability to vary the Y-shape pattern across the same device. Indeed, by tuning the geometrical parameters  $L$ ,  $a$  and  $r$  (see fig 2.3), the electromechanical properties of the interconnect can be tuned at will. In particular, local variations of the pattern could be implemented over distances of a few hundreds of microns to engineer smooth gradual change in the elastic characteristic of a device. This principle can be leveraged to form so-called strain gradient around rigid components (e.g.  $\mu$ LED, bare dies) in order to prevent the concentration of stress at the interface between the stiff and soft part of the system. In the context of the devices presented here, strain gradients could be used to minimize stress at the level of the transition with the connector or to build hybrid systems featuring rigid elements such as LEDs or integrated circuits (e.g. multiplexer). Alternatively, variations in the Y-shape geometrical parameters could be used to tune the local resistivity of the patterned interconnects. By carefully optimizing the local elasticity vs resistivity trade-off based on the expected strain in different part of the device, the overall resistance of the interconnects could be minimized. This level of optimization could prove critical to the development of an implant compatible with clinical IPG (compliance voltage 10-15V).

With regard to the potential manufacturing of higher density electrode array (>32 channels), the minimum track width constitutes the main limiting factor. Indeed, in the current implementation of process, the minimum track width is  $21\mu\text{m}$ , a limit fixed by the geometrical parameters of the Y-shape pattern (figure 2.3). In effect however, integrating such structure is impractical as it effectively consists of a serpentine interconnect which does not provide any mechanical redundancy. Interestingly, while the geometrical parameters do define the minimum track width, they are, in effect, unitless. As such they can be arbitrarily scaled with respect to the structure being patterned. This approach could be potentially used to either (1) maintain the current track width but increase the mechanical redundancy in an equally wide track or, more interestingly, (2) maintain the same level of redundancy in a significantly narrower track. For example, scaling down the Y-shaped pattern by a factor of 10 would enable 3 level of redundancy within a 10-micron-wide track. However, the critical dimension would also be reduced by an identical factor, from  $5\mu\text{m}$  down to  $500\text{nm}$ , far beyond the capabilities of UV lithography (i-line resolution  $\sim 1\mu\text{m}$ ). This technical challenge could be addressed by the transition

to more advanced lithography systems such as DUV stepper or e-beam lithography. This techniques will technically allow to pattern the same motif at increasingly smaller scale, thereby making it possible to fabricate increasingly smaller stretchable interconnects while maintaining equivalent mechanical robustness.

Both the original and core-shell microfabrication processes were used to manufacture a large array of neural interfaces, some of which were readily introduced in the results sections above. In the next chapters, these devices will be described in details alongside the applications for which they were developed and the experimental conditions in which they were implanted. Although the fabrication process and in-vivo experiments are presented in separate chapters of this thesis, their development and execution was carried out simultaneously, with many of the technological innovations stemming directly from the requirements of the applications themselves.

## 3 Application: ECoG

**Outline** This chapter describes the development of a soft  $\mu$ ECoG for the recording of the auditory cortex. The device is first validated acutely in rats before being translated to non-human primates where it is deployed chronically. The chapter is organized in 3 sections:

1. **Introduction** on electrocorticography in the clinic, its limitation and overview of the potential benefits of soft, microfabricated ECoGs.
2. **Acute study in rodents** demonstrates the use of the Y-shaped micropattern technology for the recording of auditory evoked potentials in rats, establishing the potential of the  $\mu$ ECoG as a tool for fundamental neuroscientific research on the auditory system.
3. **Chronic study in non-human primate** presents the development of a soft  $\mu$ ECoG for the long-term recording of auditory evoked potentials in a rhesus macaque. This section discusses the implant design, the results and the potential limitations after 4 months of implantation.

**Acknowledgments** The results presented in this chapter were made possible thanks to the work of Alix Trouillet, Emilie Revol, Florian Fallegger, Laurine Kolly, Jocelyne Bloch and the staff of the platform of translational neurosciences at the university of Fribourg. *Acute rodents experiments* ATR and ERE performed the experiments and analyzed the recordings. *Chronic non-human primate experiments* ATR, ERE and FFA helped plan and perform the experiments. JBL performed the  $\mu$ ECoG implantation surgery. FFA co-developed the interface system (FlexComb, pedestal) and helped with the assembly of the device. LKO helped with the characterization of the  $\mu$ ECoG. ATR and ERE trained the primate, performed the auditory stimulation experiments and analyzed the recordings.

**Scientific contributions** The content of this chapter is being integrated into a scientific article:

- Alix Trouillet, **Florent-Valéry Coen**, Emilie Revol, Florian Fallegger, Laurine Kolly, Divya Chari, Alejandro Garcia, Christian M. Brown, Jocelyne Bloch, Daniel J. Lee, Stéphanie P. Lacour. "Soft auditory brainstem implant restores tonotopy with high auditory acuity", *in preparation*.
- Alix Trouillet, Emilie Revol\*, **Florent-Valéry Coen\***, Florian Fallegger, Stéphanie P. Lacour. "Soft  $\mu$ ECoG as an auditory cortical implant to restore hearing", *in preparation*.

### 3.1 Introduction

Electrocorticography is a neurodiagnosis technique which consists of placing an electrode array on the surface of the brain in order to record the neural activity of the underlying tissue. Clinical ECoG grids are currently used mainly for functional brain mapping in drug-resistant epileptic patient [116]. The approach consists of recording brain activity over a period of a few weeks in order to localize the foci of epileptic activity [117]. The collected data then allow to guide the surgical approach during which the affected tissue is resected. ECoGs are also used intra-operatively during the brain resection procedure itself, in order to avoid cutting critical areas of the cortex, such as the ones responsible for speech and motor functions. This neuronavigation technique is also applied during other delicate surgical approaches, such as tumor resection [118].

In recent years, clinicians and researchers have attempted to use ECoGs in order to decode speech and motor intents from the brain activity of paralyzed patient. The captured data is then used to control a computer or a robotic assistive devices, forming a so-called brain-machine interface (BMI) [119]. Current efforts are however limited by the low spatial resolution of the available hardware. Indeed, contemporary ECoG grids are composed of a grid of stiff PtIr disks, whose size ( $>1\text{mm}$ ) and pitch (10mm) greatly limit the achievable resolution with which brain activity can be mapped. Furthermore, due to the mechanical properties and thickness of their constitutive elements, these devices exhibit a high bending stiffness and as such do not conform optimally to the complex topology of the brain surface (fig. 3.1A).

Soft bioelectronics interfaces constitute a compelling alternative to the stiff, macroscale implants used in the clinic. By combining standard microfabrication techniques with polymeric materials, researchers have developed flexible microelectrocorticography grids ( $\mu$ ECoGs) capable of conforming closely to the morphology of the brain [120]. The transition from hand manufacturing to cleanroom tools and technologies also enables a significant increase in electrode density, allowing to record brain activity with a much



higher spatial resolution than before [121]. This aspect is particularly relevant for BMI where a finer mapping of neural signal will lead to a better understanding of the patient's intent.

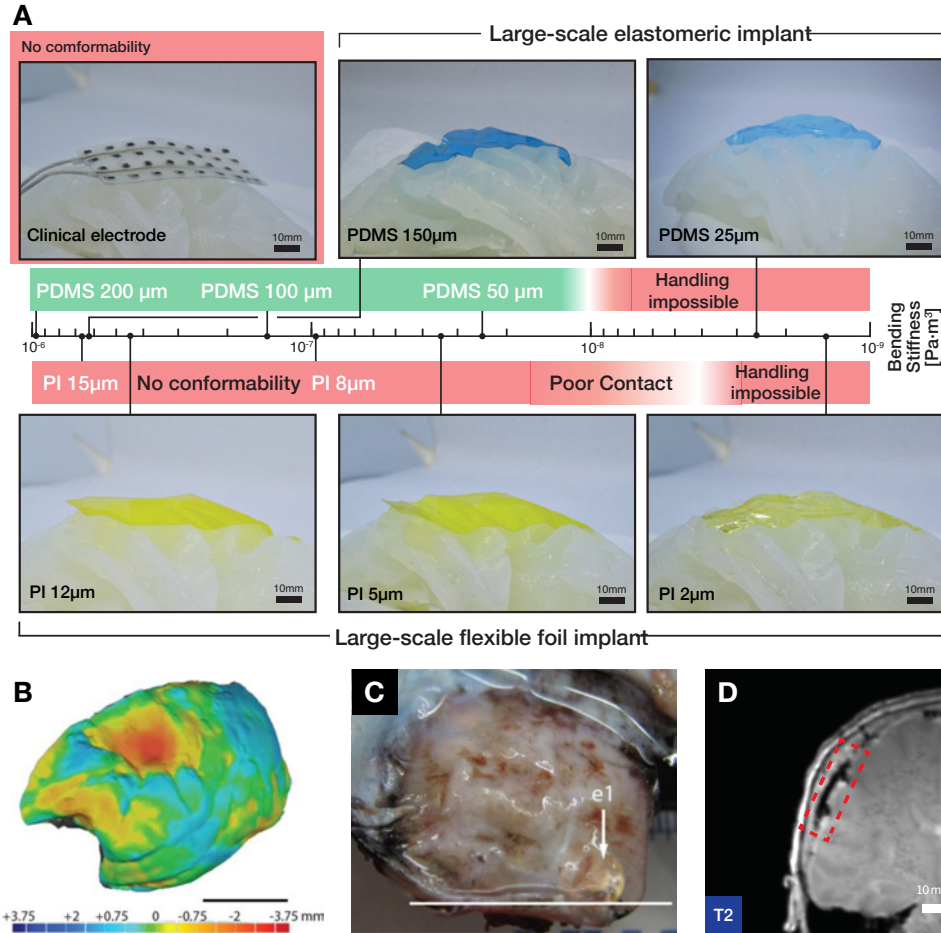


Figure 3.1: Limitations of the current clinical ECoG technology. **A** Study of the conformability of various mock-up ( $4 \times 10 \text{ cm}^2$ ) on an agarose brain model. The corresponding bending stiffness is reported on the scalebar together with a qualitative assessment of the conformability and handleability. Adapted from [122]. **B, C** Surface topography and picture of a severe depression in the cortex resulting from the implantation of a clinical ECoG grid. **D** MRI of a clinical ECoG exhibit a clear shadowing effect around the location of the device (indicated by the red box) [122].

Microfabricated ECoGs also present the advantage of being highly customizable: the device geometry can be adapted to a wide range of animal models, from mouse to non-human primates. The ability to seamlessly scale a technology across species is especially compelling from a translational perspective, because it allows to establish a technological bridge between fundamental, neuroscientific research and the clinic. Decreasing the device footprint relative to the animal size also promises to improve

bio-integration, especially when this strategy is combined with the integration of soft materials such as silicones or hydrogels. In comparison, stiff clinical implants have been shown to trigger severe fibrotic encapsulation over time and to even cause depression of the brain [123]. This type of potential damages is especially concerning when considering these devices are mainly used on readily unstable brains and could thus potentially worsen the patient's condition (e.g. in the case of epilepsy).

MRI safety and compatibility is another major limitation of current clinical arrays [124]. Due to the important quantity of metal constituting the electrode, clinical implants create large artefacts when imaged in an MRI scanner. The shadow of the implant will hide the details of the surrounding tissue, which prevents the precise localization of the device. This issue is particularly relevant in the context of epilepsy monitoring because the artifacts prevent the correlation between electrocorticography and imaging data. Another point of concern relates to heat generation. Changing magnetic fields, such as the one used in an MRI scanner, will cause Eddy currents to circulate in bulk metal pieces, whose temperature will then rise due to Joule heating. The PtIr disks in clinical arrays are large enough to exhibit this effect and the generated heat would have to be dissipated in the surrounding tissue. Even modest increase in temperature have been shown to cause significant brain damage, a concerning proposition when considering the application at hand [125]. While the notion of MRI compatibility and safety has only just begun to enter the conversation on soft neural interfaces, early studies on this new kind of devices have shown promising results [122, 126].

### 3.2 Acute Study in Rodents

This section introduces a  $\mu$ ECoG for the recording and stimulation of the rat auditory cortex in acute settings. The implant was developed as a precursor to the  $\mu$ ECoG for non-human primates which will be presented in the next section. With this device, the objectives were three-fold:

1. Validate the recording capability of the Y-shaped micropattern technology.
2. Develop a tool for fundamental neuroscientific research on the auditory system.
3. Establish a technological framework for auditory research before transitioning to large animal model (non-human primates). This aim includes the acquisition of supporting systems and instrumentations, the development of robust recording and stimulation protocols as well as the formulation of a data analysis pipeline.

### 3.2.1 Methods

**Device fabrication** The rat  $\mu$ ECoG was manufactured using the process presented in section 2.2. It features a grid of 25 electrodes (diameter  $160\mu\text{m}$ , pitch  $400\mu\text{m}$ ) covering an area of  $1.6$  by  $1.6\text{ mm}^2$ , which corresponds to the estimated dimensions of the rat auditory cortex. The connecting scheme is composed of a custom-design flexible flat cable (FlexComb connector) shaped into a strain-relief serpentine. The design also features several anchoring point intended to stabilize the device in place following implantation. Each electrode can be addressed individually via an Omnetics connector, soldered at the end of the FlexComb connector. The ground and reference channels are shorted together and routed through an external aluminum wire.

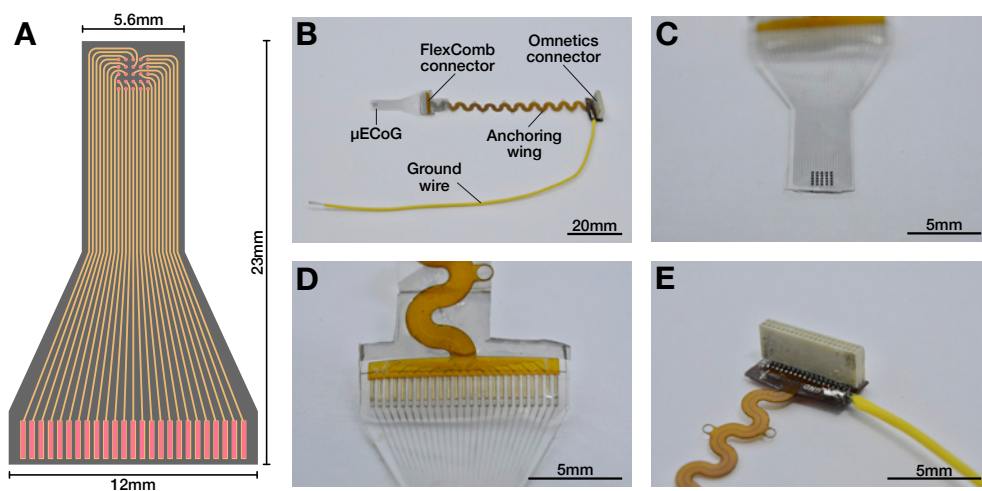


Figure 3.2: Design features of the soft rat  $\mu$ ECoG. **A** Schematic of the device. **B** Picture of the whole device. **C** Detailed view of the soft electrode paddle. **D** Close-up picture of the FlexComb connector. Since the  $\mu$ ECoG was fabricated during a transition period in the process, the FlexComb is still connected using conductive silver paste. **E** Detailed view of the Omnetics connector interface, ground wire and anchoring wings.

**Auditory stimulation experiments** A wild type rat is put to anesthetized using an injection of ketamine. The skin is cut and a craniotomy is performed in order to expose the surface of the brain between coordinates  $x$  and  $y$ . Following dural resection, the  $\mu$ ECoG is slid under the dura and pushed on top of the auditory cortex using anatomical landmarks to guide the insertion. Next, the  $\mu$ ECoG is connected to a wireless recording system (W2100-HS32, Multichannel Systems). The device, based on the low-power RHA2132 chip (Intan Technologies), amplifies and digitizes the signal before sending the data wirelessly to the acquisition computer. The sampling rate is software defined at a value of  $2\text{kHz}$ . The animal is fitted with a pair of earbuds and presented with a series of acoustic stimuli. The sounds used to generate frequency specific AEPs consist of a  $500\text{ms}$  tone-burst followed by  $500\text{ms}$  of silence, presented in a continuous fashion for a dura-

tion of 3 minutes. In order to map the tonotopy of the rat auditory cortex, the frequency of the tones is varied across trials, ranging from 100Hz to 20kHz. The collected data are analyzed using a custom MatLab (MathWorks) script. For each frequency, the recorded raw signal is filtered between 1 and 1kHz and averaged over the period of the acoustic stimuli (1s).

**Cortical stimulation experiments** In order to investigate the potential to evoke auditory percept through stimulation of the auditory cortex, a wild type rat is fitted with a  $\mu$ ECoG on each hemisphere (figure 3.5A). The surgical procedure begins with the anesthesia, performed via a ketamine injection. Next, a double craniotomy is performed, exposing the parietal bone on each side of the brain. Following durectomy, the  $\mu$ ECoG are placed on top of the auditory cortex using the insertion method described above (figure 3.5B-C). The proper placement of the two devices is verified by recording AEPs through each one of them. To do so, the  $\mu$ ECoG is connected to a wireless recording system (W2100-HS32, Multichannel Systems) and the animal is presented with a series of tone-burst acoustic stimuli. One of the  $\mu$ ECoG (device A) remains attached to the wireless recording system while the other (device B) is connected to a current pulse generator (PG2100A, AM System). A series of electrical stimuli are then sent through the device B while the contralateral response is being recorded using device A. The stimulation pattern consist of a train of symmetric, biphasic current pulses, with each phase lasting 300 $\mu$ s. In order to assess the impact of the stimulation, the amplitude of the current pulse is varied from 100 to 600 $\mu$ A across trials. The collected data are analyzed using a custom MatLab (MathWorks) script. For each current amplitude, the recorded raw signal is filtered between 1 and 1kHz and averaged over the period of the acoustic stimuli (1s).

**Impedance spectroscopy** In-vitro EIS is performed using a potentiostat (Reference 600, Gamry Instruments) in a 3-electrode configuration. The Ag/AgCl reference electrode, platinum counter electrode and implant under test (working electrode) are immersed in PBS (1x) and the impedance spectrum is measured between 0.1Hz and 1MHz using an input signal amplitude of 100mV (root-mean-square).

**Chronopotentiometry** In-vitro voltage transients (VTs) are measured in PBS (1x) upon the application of symmetric, biphasic, cathodic-first, current pulses between the electrode under test and a platinum counter electrode. The pulses amplitude is set to 100 $\mu$ A and their duration to 600 $\mu$ s (300 $\mu$ s/phase), with an inter-pulse period of 10ms. The resulting VTs are collected via an oscilloscope (MDO3014, Tektronix) connected across the two poles of the current pulse generator (ISP2100, A-M Systems). For each device, the access voltage, i.e. the purely resistive drop occurring at the onset of a current pulse, is estimated by averaging the voltage values over the first  $\mu$ s of each phase.

### 3.2.2 Results & Discussion

**Device characterization** Electroimpedance spectroscopy (EIS) and chronopotentiometry were performed on four  $\mu$ ECoGs, following the completion of the manufacturing process. The EIS data shows that the maximum phase is reached at 80kHz, corresponding to an average impedance of  $12.8 \pm 3.2$  k $\Omega$ . At this frequency, the electrode behaves almost like a purely resistive circuit (phase close to  $0^\circ$ ), a state that is similar to the one being "felt" by the generator when injecting current pulses. Indeed, imposing a sudden change in current (e.g. by injecting a square pulse) through a electrode corresponds to the application of a very high frequency voltage, a situation in which the double layer capacitance at the interface is effectively short-circuited (phase close to  $0^\circ$ ). As a result, the mean impedance at maximum phase provides the best assessment of the stimulation capabilities of the implant. This is confirmed by the plots presented in figure 3.3B, which show a resistive drop (access voltage) around 1.1V upon the injection of a biphasic current pulse of 100 $\mu$ A (predicted value =  $12\text{k}\Omega \times 100\mu\text{A} = 1.2\text{V}$ ). The average drop was computed by considering the first 5 $\mu$ s of each phase.

Looking the phase angle, it can be seen that the average cutoff frequency is located at  $f_{\text{cutoff}} = 40\text{Hz}$ . Above this frequency, the electrodes behavior is predominantly resistive (phase  $> -45^\circ$ ) which means the incoming signals are represented authentically. Below  $f_{\text{cutoff}}$  however, signals are transmitted predominantly through the capacitive part of the interface, which means they do experience some level of non-linear distortions (i.e. filtering, phase shifting) [127]. Since the phase value remains relatively close to the limit (average minimum phase =  $-60^\circ$ ), it is expected that the  $\mu$ ECoG will not exhibit significant signal distortion. Nevertheless, any conclusion based on the low frequency components of the recorded signal should be considered with skepticism.

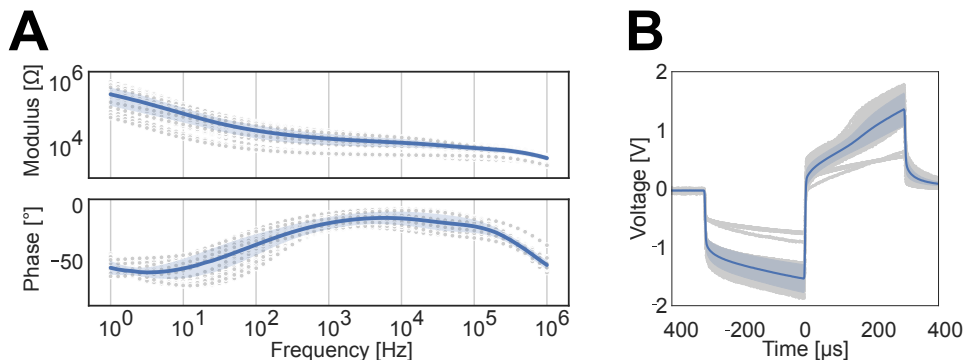


Figure 3.3: In-vitro characterization of the rat  $\mu$ ECoG. **A** Average impedance spectrum as measured in-vitro ( $n = 100$  electrodes over 4 devices). The shaded area represents the standard deviation. **B** Average voltage transient upon the injection of 100 $\mu$ A biphasic current pulse ( $n = 100$  electrodes over 4 devices). The shaded area represents the standard deviation.

**Auditory stimulation experiments** In order to evaluate the recording capabilities of the Y-shaped micropattern technology, auditory evoked potentials (AEPs) are captured in wild type rat using a 25-channel  $\mu$ ECoG (fig. 3.4A). The device is inserted through a slit-like opening in the skull and slid on top of the auditory cortex (fig. 3.4B). Once averaged over the stimulation frequency, the recorded signals exhibit a clear ON and OFF peak which confirms both the recording capabilities of the ECoG and the placement of the device (fig. 3.4C).

Next, the animal is presented with tone-bursts of frequencies ranging from 100Hz to 20kHz in order to establish the tonotopy of the rat auditory cortex. For each frequency, an activation heatmap is built by extracting the peak amplitude from the average response over the period of the acoustic stimuli. An example of an acoustic map recorded by the  $\mu$ ECoG is shown in figure 3.4D.

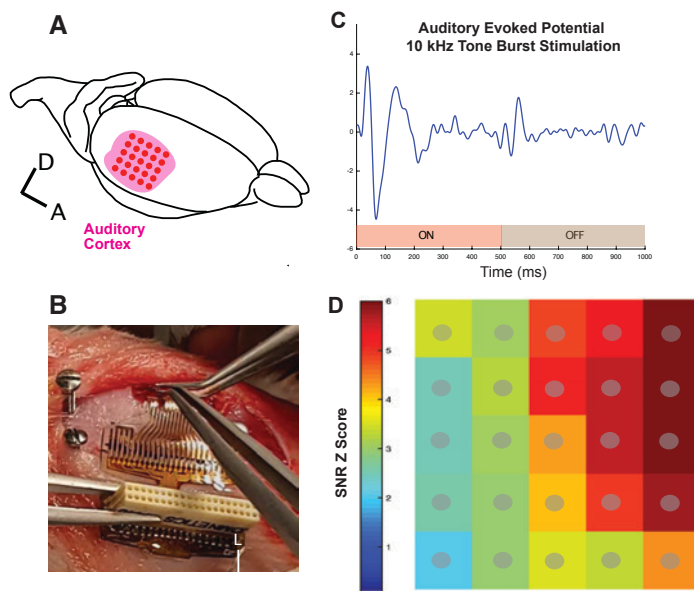


Figure 3.4: Auditory Evoked Potentials recording using soft  $\mu$ ECoG. **A** Location of the device on the auditory cortex. **B** Surgical procedure of  $\mu$ ECoG implantation. **C** Example of auditory evoked potential (AEP) of one channel. **D** Map of AEPs across the  $\mu$ ECoG grid.

**Cortical stimulation experiments** The cortical stimulation experiments were devised to investigate callosal projections and to assess whether neural activity could be elicited from one cortex to the other. To do so, two  $\mu$ ECoGs were implanted on the auditory cortices of a wild type rat. The first step consisted in finding the activation threshold. A train of current pulses (biphasic, cathodic first, 150 $\mu$ s, 1.1 or 2.2Hz) was injected between electrode x and y and its amplitude was slowly ramped up. The average traces, shown in figure 3.5D, exhibit a clear activation of the contralateral cortex beyond 200 $\mu$ A. Further-

more the response increase as the current amplitude ramps up, which demonstrates the ability to elicit and modulate a response from one cortex to another.

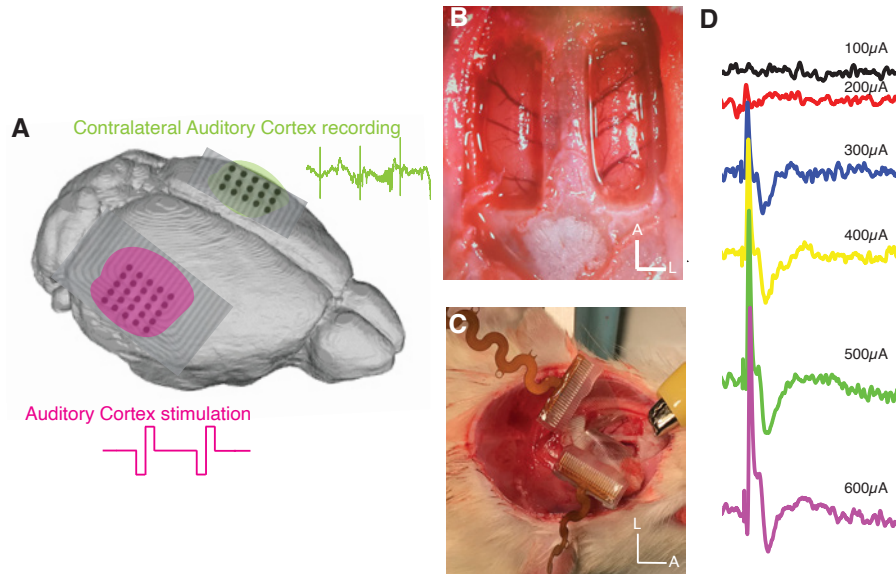


Figure 3.5: Cortical prosthesis experimental design and preclinical assessment in rats. **A** Schematic of experimental design to assess efficiency of cortical stimulation; one  $\mu$ ECoG is used to stimulate the ipsilateral AC, another  $\mu$ ECoG is placed contralaterally to assess electrically evoked responses. **B** Surgical approach with 2 slits where  $\mu$ ECoG are inserted and slid as seen in **C**. **D** Preliminary data from pilot study; monopolar cortical stimulation elicits a response in the contralateral auditory cortex which amplitude increases with stimulation power.

Next, the electrical stimuli are applied through varying electrode pairs. The computed response heat maps on the contralateral cortex are shown in figure 3.6. The peak activity shows a clear shift in location as a function of the electrode pair, which effectively demonstrates that the contralateral response can be tuned by spatial modulation of the stimulation. These results suggest that contralateral cortical stimulation could be used to elicit auditory percepts and potentially restore hearing. These findings will be the subject of further studies, including chronic experiments, behavioral tasks and histological analysis.

### 3.3 Chronic Study in Non-human Primate

This section introduces a  $\mu$ ECoG for the recording of the auditory cortex in non-human primates (NHPs). This device was developed in conjunction with an auditory brainstem implant (ABI) which will be presented in the next chapter of this thesis. The objectives were two-fold: firstly, to assess the recording capabilities of the Y-shaped micropattern technology in chronic settings and secondly, to provide a tool to evaluate the effective-



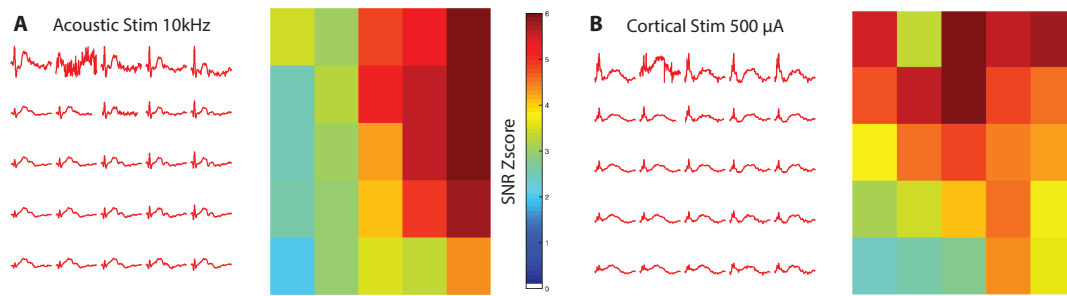


Figure 3.6: Comparison of Acoustic tonotopic map and Electric tonotopic map. **A** AEPs recorded across  $\mu$ ECoG array in response to 10kHz acoustic tone burst. The corresponding color map is shown on the side and represent the peak-to-peak amplitude of the responses. It gives a direct visualization of the zone highly sensitive to this band of frequency. **B** eAEPs recorded contralaterally in response to electrical stimulation of the auditory cortex at 500  $\mu$ A. The corresponding color map is shown on the side. The 2 maps are comparable showing the activation of the same zone of the cortex.

ness of the ABI stimulation. Current clinical methodology in that regard relies solely on patient's perception and auditory brainstem responses (ABRs). While a form of feedback can be gathered from behavioral experiment in NHPs, this approach does not provide a granular enough appreciation of the stimulation efficacy. Similarly, ABRs are only indicative of the activation of the auditory pathway and as such cannot be relied upon to assess or tune the stimulation. As a result, an investigative tool with a finer sensitivity needed to be developed.

### 3.3.1 Methods

**Device fabrication** The ECoG was manufactured using the microfabrication process presented in section 2.3. It features 28 electrodes of  $300\mu\text{m}$  in diameter covering an area of  $4 \times 10 \text{ mm}^2$ , which corresponds to the estimated dimensions of the auditory cortex in rhesus macaque. The four remaining channels are reserved for test structures implemented to validate the functionality of the device over time (fig 3.7A). Channel 1 and 31 stop at the level of the FlexComb connector and thus can be used to monitor potential encapsulation failures occurring at the transition between the soft electrode pads and the custom-made FFC. Channel 2 consists of a track buried inside the FFC which allows to verify the integrity of the flexible PCB itself. Channel 32 leads to an electrode placed out of the area of interest in order to record neural activity away from the auditory cortex. The ground and reference channel are shorted together and routed through a teflon-coated, platinum wire. The FlexComb connector features a pair of anchoring "wings" to secure the implant in place at the exit of the craniotomy (fig 3.7B).

The interface with the recording system consists of an Omnetics connector soldered



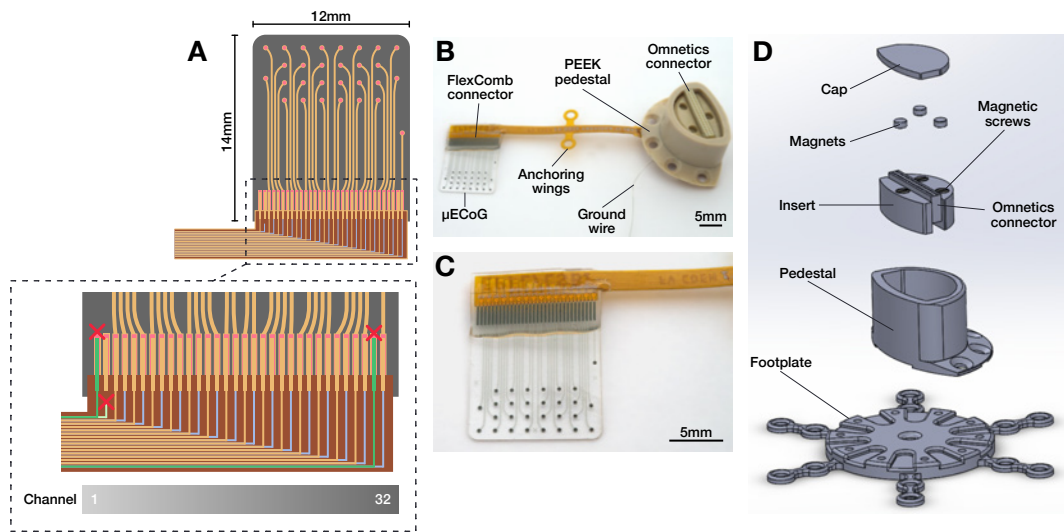


Figure 3.7: Design features of the soft NHP  $\mu$ ECoG. **A** Schematic of the device. The inset details the test structures implemented to monitor the functionality of the device over time. **B** Picture of the device, assembled inside the custom-designed PEEK pedestal. **C** Detailed view of the soft electrode paddle. **D** Exploded view of the pedestal assembly.

at the end of the FlexComb cable. The Omnetics connector is sealed inside a custom-designed PEEK (Polyether ether ketone) pedestal which provides an access port to the implant (fig 3.7D). The pedestal is engineered to be anchored on the skull using a footplate with bendable feet through which self-taping screws will be inserted. This approach has the advantage of not requiring a titanium mesh to be placed subcutaneously, a common anchoring strategy which often leads to infection. A magnetically attached cap prevents fluids and debris from entering when the recording system is not plugged in. The three magnetic screws inserted inside the pedestal can be removed during imaging to avoid generating artifacts. The ECoG pedestal is designed to be combined with a second one, containing the access port to an auditory brainstem implant (see Chapter 4). The implants were sterilized pre-operatively using a hydrogen peroxide plasma treatment ( $\text{H}_2\text{O}_2$ , 55°, 0.01mbar, 3x5min).

**Surgical procedure** ECoG placement was done under anesthesia. A craniotomy was performed on the temporal bone following coordinates of the Auditory Cortex (AP -8.55 - 17.10 ML 4 5; Macaque Brain Atlas) and superficial landmarks as well as MRI data of the animal. The soft ECoG was slid subdurally at the surface of the auditory cortex (fig. 3.8A) and secured at the edge of the craniotomy using a titanium bridge. After dura closure and bone flap replacement, the pedestal was screwed at the top of the skull (fig. 3.8B).

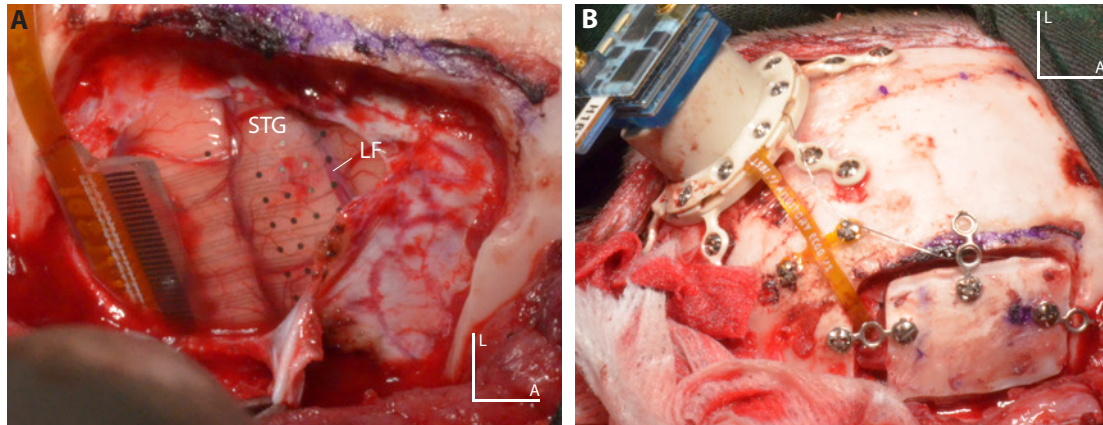


Figure 3.8: Soft ECoG implantation in Non-human primate. **A** The soft ECoG is slid subdurally at the surface of the superior temporal gyrus (STG) and the lateral fissure (LF) where the secondary and primary auditory cortex are. **B** View of the system after dura and bone flap closure. The ground is secured between the skull and the dura. The ECoG pedestal is screwed on top of the skull and the flex is secured using anchoring wings and self-drilling screws. L: Lateral A: Anterior

**Auditory evoked potentials recordings** The auditory evoked potentials (AEPs) are generated using a tone-burst train of varying frequencies (500Hz to 40kHz). At each frequency, the stimulus (500ms sound on, 500ms sound off) is presented continuously for 2 minutes. The sound queues are generated using a custom MatLab (MathWorks) script and delivered in a closed field configuration using a pair of magnetic speakers (MF-1, Tucker-Davis Technologies). The resulting AEPs are acquired by connecting the  $\mu$ ECoG to a wireless recording system (W2100-HS32, Multichannel Systems). The device, based on the low-power RHA2132 chip (Intan Technologies), amplifies and digitizes the signal before sending the data wirelessly to the acquisition computer. The sampling rate is software defined at a value of 2kHz. The resulting data are analyzed using a custom MatLab (MathWorks) script. For each frequency, the recorded raw signal is filtered (bandpass 1 to 100Hz, notch 50Hz) and averaged over the period of the acoustic stimuli (1s) (figure 3.9).

**Impedance spectroscopy** In-vitro EIS is performed using a potentiostat (Autolab PG-STAT128N, Metrohm) in a 3-electrode configuration. The Ag/AgCl reference electrode, platinum counter electrode and implant under test (working electrode) are immersed in PBS (1x) and the impedance spectrum is measured between 0.1Hz and 500kHz using an input signal amplitude of 100mV (root-mean-square).

In-vivo EIS data are collected using a portable potentiostat (Reference 600, Gamry Instruments) in a 2-electrode configuration with the reference and counter channels shorted

### 3.3 Chronic Study in Non-human Primate

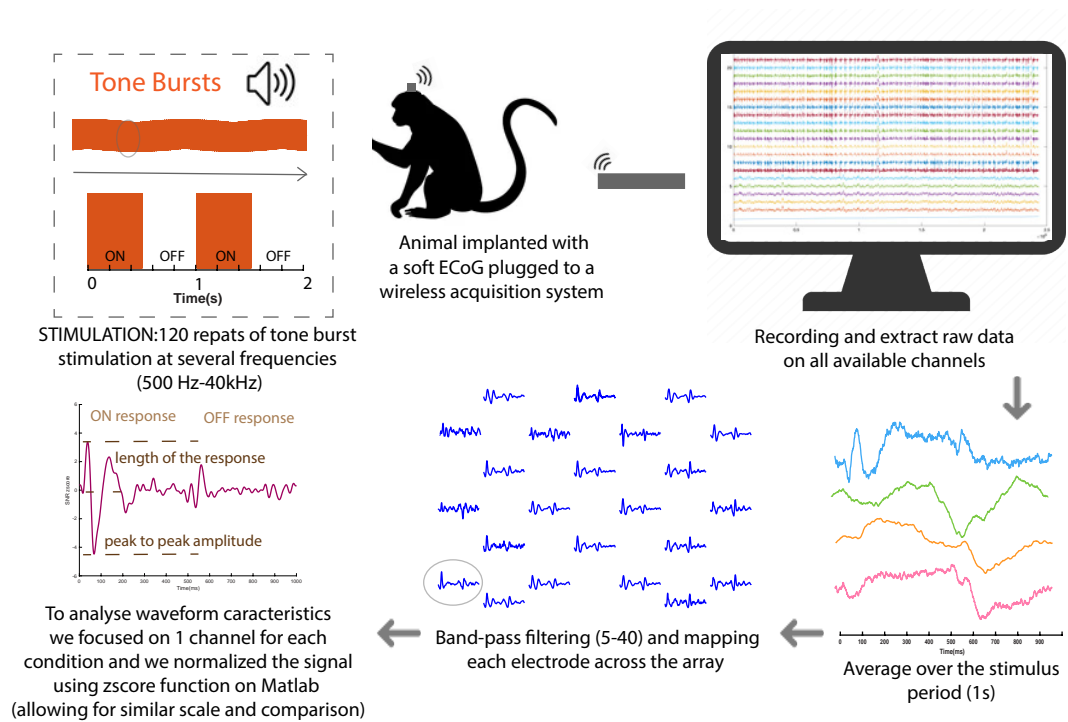


Figure 3.9: Experimental setup and analysis pipeline for the recording of Auditory Evoked Potentials (AEPs) using the implanted soft  $\mu$ ECoG

together and connected to the ground wire of the implant. The impedance spectrum is measured between 0.1Hz and 1MHz using an input signal amplitude of 100mV (root-mean-square). A breakout PCB connected inside the pedestal allows easy access to the individual channels.

**Chronopotentiometry** In-vitro voltage transients (VTs) are measured in PBS (1x) upon the application of symmetric, biphasic, cathodic-first, current pulses between the electrode under test and a platinum counter electrode. The pulses amplitude is set to 100 $\mu$ A and their duration to 600 $\mu$ s (300 $\mu$ s/phase), with an inter-pulse period of 10ms. The resulting VTs are collected via an oscilloscope (MDO3014, Tektronix) connected across the two poles of the current pulse generator (ISP2100, A-M Systems).

In-vivo VTs are collected using the same setup but this time with the counter electrode connected with the ground wire of the implant. A breakout PCB connected inside the pedestal allows easy access to the individual channels.

**Magnetic Resonance Imaging** MRI sequences were acquired on a Siemens Magnetom Prisma machine by first sedating the animal using ketamine. T1, T2 and turbo spin echo sequences were used to image the brain and implant with different contrasts, respectively. The acquired images were exported in the open DICOM format and visualized on an open-source DICOM viewer (Miele LXIV).

**Computed Tomography** A CT scan was acquired with slice thickness of 0.6mm by first sedating the animal using ketamine. A reconstruction for soft tissue was used to export the images in the open DICOM format and visualized on an open-source DICOM viewer (Miele LXIV).

### 3.3.2 Results

**Device characterization** Prior to implantation, the  $\mu$ ECoG was characterized via electroimpedance spectroscopy and chronopotentiometry. Looking at the EIS data in figure 3.10A, the impedance at maximum phase ( $-5.9^\circ$ ) is found at frequency of 1kHz, corresponding to a mean value of  $4 \pm 0.4$  k $\Omega$ . Once again this number can be matched with the resistive drop shown in figure 3.10B, as they effectively capture the impedance seen by the pulse generator when applying sudden change in current. The resistive drop (access voltage) averages to  $-0.35 \pm 0.17$  V and  $0.48 \pm 0.13$  V over all channels for the a biphasic current pulse of 100 $\mu$ A (average computed over the first 5 $\mu$ s of each phase). The impedance computed from these values is equal to  $0.35 \times 100\mu\text{A} = 3.5$  k $\Omega$  and  $0.48 \times 100\mu\text{A} = 4.8$  k $\Omega$ , which falls in line with the EIS data.

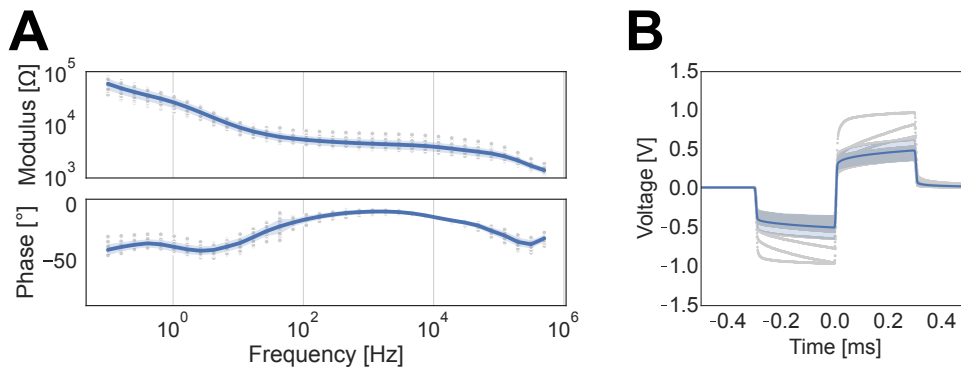


Figure 3.10: In-vitro characterization of the NHP  $\mu$ ECoG. **A** Average impedance spectrum as measured in-vitro ( $n = 28$  electrodes). The shaded area represents the standard deviation. **B** Average voltage transient upon the injection of  $100\mu\text{A}$  biphasic current pulse ( $n = 28$  electrodes). The shaded area represents the standard deviation.

Looking once again at figure 3.10A, it can be seen that the electrodes behavior is predominantly resistive with the phase angle remaining above  $-45^\circ$  across the whole frequency range. This type of curve indicates that the cutoff frequency is located at the tail end of the spectrum, below 1Hz. Because signals above the cutoff frequency are transmitted predominantly through the resistive part of the interface, they do not experience the non-linear distortions induced by its capacitive component (i.e. filtering, phase shifting) [127]. As a result, the EIS data effectively demonstrates that the  $\mu$ ECoG is able to authentically represent signals across the whole frequency range shown in figure 3.10A (1Hz-500kHz).

**ECoG recordings** Following the surgical procedure detailed previously (fig 3.8), a Rhesus macaque is implanted with a 28-channel, soft  $\mu$ ECoG. The placement of the device is confirmed intra-operatively using both anatomical landmarks and AEPs recordings at a few key frequencies. After a recovery period of ten days, the responses to acoustic tone-burst stimulation are recorded on a weekly basis in awake settings. An example of a typical recording is shown in figure 3.11. While the signal over a single trial does allow to discern evoked activity, averaging the data over the stimulus period immediately brings out a clear ON and OFF peak (figure 3.11A).

In order to build a tonotopic map of the auditory cortex, the frequency of the tone burst is varied from 500Hz to 40kHz. For each frequency, the signal is averaged over the stimulus period (500ms ON + 500ms OFF) and the AEP amplitude on each channel is extracted. The collected data (figure 3.11B) exhibit a clear shift in activity as a function of stimulation frequency, demonstrating the ability of the  $\mu$ ECoG to effectively map AEPs. Figure 3.11C presents a complete activation map for a stimulus frequency of 8kHz. The peak-to-peak amplitude (zscored) can be extracted in order to create a color map which

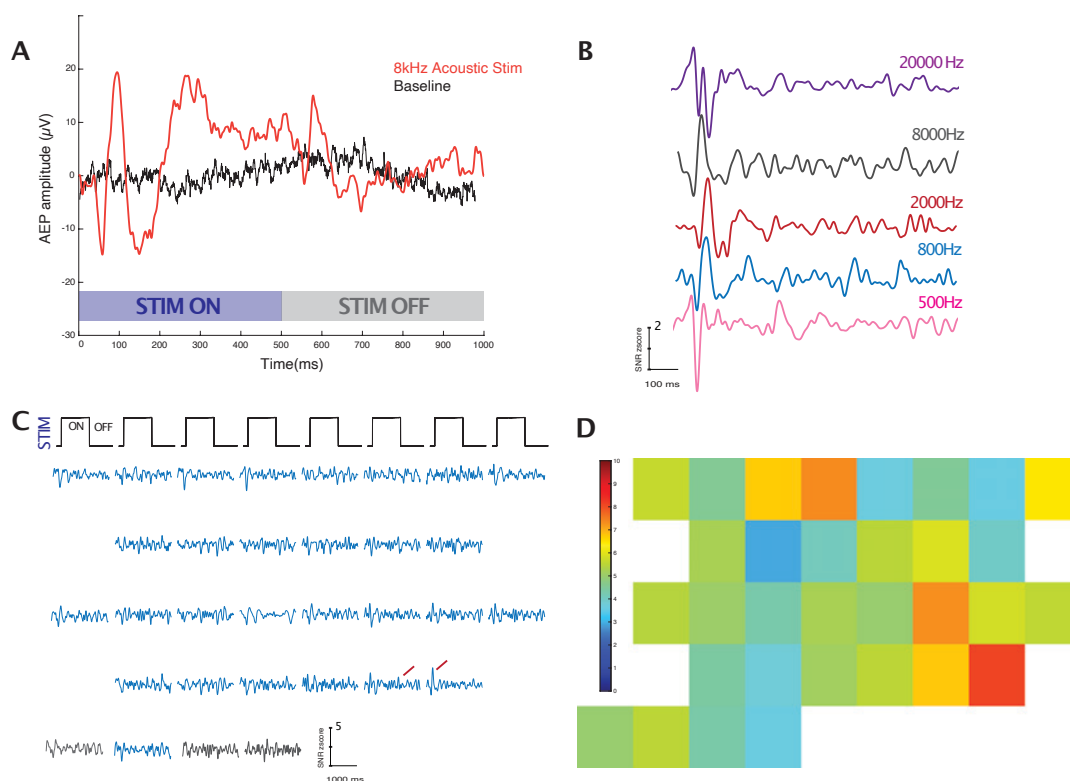


Figure 3.11: Soft ECoG recordings in NHP allow for tonotopic mapping. **A** Averaging of the filtered ECoG data of a single channel. The orange trace represents the response to an acoustic tone burst at 8kHz (500 ms ON 500 ms OFF). In comparison to the baseline (no stimulation, black trace), peaks of depolarization are visible at both the onset and the offset of the stimulus. **B** Responses of a single channel (example of channel 7 here) in response to different frequencies of stimulation. The signal is specific to each acoustic frequency and varies in amplitude and shape allowing for tonotopic mapping of the auditory cortex. **C** Responses of all channels at 8kHz and mapped across the entire ECoG array (black traces represent test channels). This map reveals the specificity of each response. Even neighboring channels show differences as highlighted in red; one channel shows a big OFF response while the one next to it does not but instead shows a massive ON response. **D** Colormap representing the peak-to-peak amplitude (zscored) of each channel across the ECoG array. Each square represents 1 electrode.

resumes the level of activity across the electrode grid (figure 3.11D).

Figure 3.12 presents the evolution of the AEPs map at 8kHz over over the course of four months. The activation profile remains robust overtime, the signal to noise ratio allow to reveal strong AEP till week 16. While the specificity of each channels stays strong for the first 2 months, it seems to decrease afterwards. The activation profile seems to become more homogenous accross the array demonstrating a loss of independance between the channels. While a consistent center of activation is noticeable towards the lower right side of the grid, the overall activation profile appears to fluctuate. The recording set at week 8 stands out in particular where the activation seems homogeneous over the whole electrode array.

Overall, the ability to record evoked potentials remains constant over time, with the response being concentrated toward the right side of the array. Combined with the other methods used to characterize the implant over the same period of time, this effectively demonstrates the ability to record AEPs using the soft  $\mu$ ECoG for a period of over 3 months.

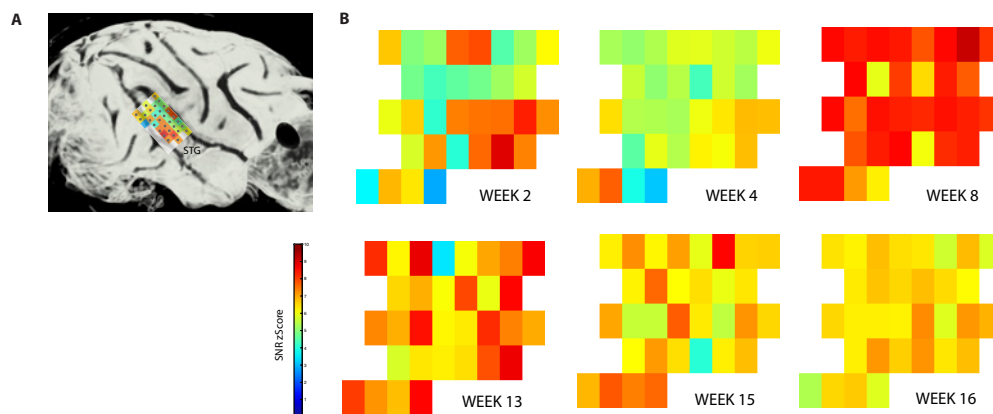


Figure 3.12: Evolution of the peak-to-peak amplitude of the ON response at 8000 Hz over time. **A** MRI reconstruction of the NHP brain implanted with the soft ECoG. The electrode grid is represented in place (at the surface of the STG) as a tonotopic map. **B** The analysis of the tonotopic maps shows a good signal to noise ratio of the AEPs using the soft ECoG. The response is strong (in average more than twice above the noise level (Zscore 2)). The bigger responses at 8000Hz are localized in the right quadrant of the array. The analysis over time shows that the response can be detected over the 4 months implantation. However, at week 16, the specificity of each channels seems to decrease, showing more homogenous amplitude profile.

**Functionality over time** The functionality of the  $\mu$ ECoG over time is assessed using voltage transients (VTs) - the measurement consists of recording the voltage required to



push a 100 $\mu$ A biphasic current pulse through each electrode. The collected data allows to assess the status of the implant from a purely electrochemical perspective.

Figure 3.13 shows the recorded VTs for all electrodes across a period of 3 months. The data reveals that the implant was unaffected by the sterilization procedure but that it suffered a slight degradation in performances directly following implantation. This decrease likely originates from small mechanical deformation to the interconnects caused by hand manipulation during surgical placement. From there, the voltage increases slowly over time most likely due to a combination of scar tissue formation and degradation of device. After one month, the standard deviation increases significantly, with some channels exhibiting a large change in their capacitive behavior.

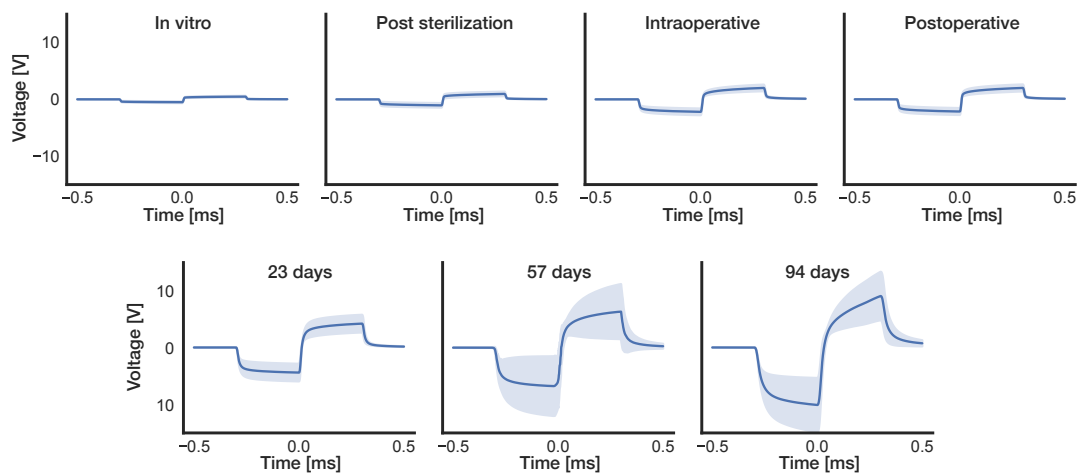


Figure 3.13: Evolution of the voltage transients of the soft  $\mu$ ECoG. Shaded area indicates standard deviation. Current pulse amplitude was 100 $\mu$ A.

**Imaging of the implant *in vivo*** The animal implanted with the soft  $\mu$ ECoG was imaged under CT and MRI scan at the 3 months timepoint as shown in Figure 3.14. The position of the electrode array including the electrode contacts are visible under the CT-scan Figure 3.14A,B. This validates the placement and securing of the implant over the span of 3 months implantation. The electrode array is placed flat over the cortex and the boneflap is in place, held by the titanium bridges anchored into the bone (visible as well). Additionally, with the soft tissue contrast available in the MRI sequence in Figure 3.14D-F, a small pocket of tissue with different contrast is visible as well as the silicone outline of the implant. From the white contrast, it can be deduced that it is a small layer of encapsulation around the implant, measuring around 2.5mm in total thickness with the implant in the middle of the section.



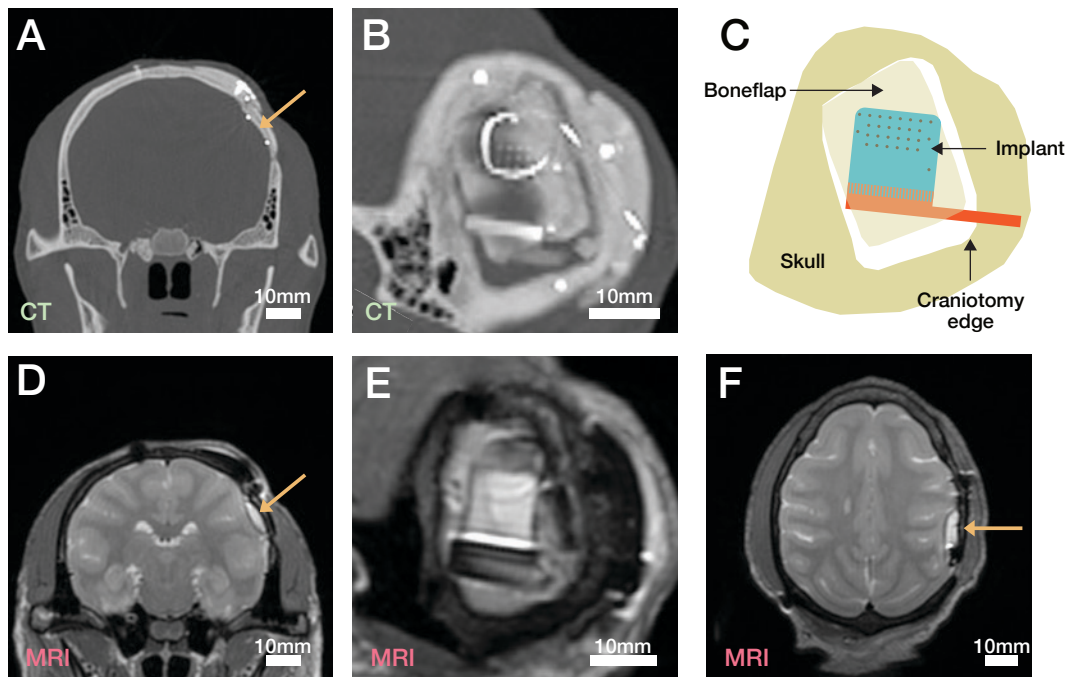


Figure 3.14: Imaging of the implanted  $\mu$ ECoG after 3 months of implantation under CT and MRI scan. **A** Coronal section of the CT-scan at the location of the implant. **B** Parallel view of the implant (located in A by an orange arrow) in CT-scan. The loop visible over the implant is the ground wire. **C** Schematic view of B and E noting the different components visible on the images. **D** Coronal section of the T2-weighted MRI sequence at the location of the implant. **E** Parallel view of the implant (located in D by an orange arrow) in the T2-weighted MRI sequence. **F** Axial section of the T2-weighted MRI sequence at the location of the implant. Note the presence of a small amount of tissue with higher contrast at the location of the implant.

### 3.3.3 Conclusion

#### Summary & discussion

The developed micropatterned core-shell interconnects presented in Chapter 2 were used to fabricate small to large electrode arrays for rats and non-human primates. The reliability and design freedom enabled by the optimized microfabrication process permitted the use of these soft  $\mu$ ECoG in new experiment paradigm both in recording and stimulation. In each case, the system (array dimensions, electrode layout, FlexComb geometry and connector) was engineered to bring the best usability to the in vivo experimenter.

In rats, the 25-channel soft  $\mu$ ECoG with an electrode coverage of  $1.6 \times 1.6 \text{ mm}^2$  was inserted through a small slit in the skull over the auditory cortex. The optimal thickness

of the silicone encapsulation permitted the sliding of the array over the brain without affecting the activity. The so-positioned devices could precisely record high SNR auditory evoked potentials when stimulating the animal with sound cues. By presenting acoustic bursts frequencies different patterns of activity could be recorded and mapped spatially over the array. This permitted to build a tonotopic map of the auditory cortex that was visible across multiple animals on both hemispheres (not shown here). This shows both the reliability of the experimental setup as well as the technology as the devices were reused over multiple surgical instances. For chronic experiments in the rat, re-design of the FlexComb connector needs to be undertaken. Indeed, the size of the presented connection scheme here does not allow for the implantation of the device over the animal's head over longer periods of time. The connector would need to be embedded on top of the skull using dental cement. Additionally, the animals would need to be habituated to plug the wireless headstage in and out. For investigation of the cortical response to sound cues over time, tonotopic map would need to be constructed for each measurement point and compared. Changes could then be attributed to cortical reorganization with ageing, deterioration of the neural interface (such as increase in electrode impedance or diffusion of ionic species inside the encapsulation and connector) but also tissue responses due to the presence of the implant. Indeed, the tissue response to subdural implantation with this surgical approach has not been tested before and would call for histological analysis of the cellular response.

In the rat, by stimulating one hemisphere with a  $\mu$ ECoG and recording the evoked potentials on the contralateral side with a second  $\mu$ ECoG, interhemispheric connection of auditory cortices was shown. This implies that cortical stimulation with a "simple" surface electrode array could elicit sound percepts without targeting lower auditory structures such as the auditory brainstem necessitating more invasive and complicated surgical approaches. These preliminary experiments show the great potential of using surface arrays on the cortex to restore deafness. Furthermore, control experiments (not presented here) can outrule non-specific activation of the auditory cortex by stimulating or recording outside of auditory cortices. . Adjustments to the stimulation protocol such as pulse width combined with pulse trains inspired by similar cortical interfaces (e.g. visual cortex) could restore percepts closer to natural ones. Finally by employing artefact cancellation methods on the stimulation hardware or in the data analysis methods would permit to recover more signal generated from the evoked potential.

In non-human primates, a  $\mu$ ECoG with a larger footprint ( $4 \times 10 \text{ mm}^2$ ) was designed to target the primary auditory cortex. The device was integrated into a transdermal port affixed to the head of the animal for chronic implantation. The device can be used in awake recording sessions by plugging a wireless headstage into the headplug. Auditory tone bursts at different frequencies presented to the animal elicited evoked potentials captured by the implanted microelectrode array over a period of 3 months. From these recordings, tonotopic maps can be constructed and permit the granular analysis of the

hearing response of the animal unlike auditory brainstem responses. Over time, the specificity of each individual electrode seemed to decrease, which could be related to the intrusion of ionic species and water into the implants. In previous technology iterations, unencapsulated interconnects would be the primary source of ion and water ingress into the electrical system of the implant. With the newly developed core-shell technology and from the leakage measurements performed in ageing experiments in saline solution (presented in Chapter 2) this can be ruled out in the present case. The connector on the other hand is only encapsulated with a silicone sealant and presents very small inter-pad distances. From the electrical measurements of the control structures present on the implant, a decrease in insulation can be measured indicating such as trend. This is a component to be optimized in further iterations of the soft implant technology. Another source for the increased correlation between the electrodes over time is the appearance of a small fibrotic encapsulation around the implant visible on the MRI. This separates physically the electrode contact from the surface of the cortex leading to a more generalized response over all electrodes. This fibrotic encapsulation could be appearing for multiple reasons. First, during the implantation procedure the dura mater was cauterized extensively to avoid bleeding during durotomy. This procedure could however lead to necrosis of the tissue and thus inflammatory response. Next, as the dura mater retracted during the  $\mu$ ECoG placement, a piece of muscle was used to bridge between both dura mater edges to avoid a cerebrospinal fluid leak. This foreign body in the subcranial space could also lead to a macrophage response, generating a macroscopic capsule around the implantation site. Finally, the implant itself, even though composed of small silicone membranes could generate an inflammatory response. In the future, more care will be given to safekeep the dura mater to avoid this effect.

Nevertheless, this implanted device will be of tremendous use to fine-tune the stimulation thresholds and parameters in the ABI experiment as presented in the next chapter.

**Outlook** As shown in this chapter, the microfabrication enables the tailoring of the neural interface to a specific application. This would also be enabled when translating this technology to humans. In the case of a recording array for brain-machine interfaces for example, pre-operative MRI could be used to precisely design the implant to the specific brain anatomy of the patient and be perfectly suitable for that surgery. Additionally, by carefully engineering the connection scheme, precise positioning of the leads and possible IPG/recording electronics would be possible on the skull. The electrode arrays designed in this chapter were designed for maximum 32 channels as they were connected to amplifiers that could be plugged on the head of the animal. However this is only a limitation of this particular plug and play system. Higher number of channels can be achieved by integrating amplifier circuits with more channels closer to the implant, such as within the pedestal system in animal models or in implanted devices in humans. This would enable more to capture more information from the brain and increase the de-

coding power of the implant. The cortical stimulation is an interesting use-case of the soft microelectrode technology, as in humans, part of the auditory cortex is situated deep in the lateral sulcus. Only implants that can bend down and conform to this three dimensional anatomy would be able to safely be used in that situation. Restoration of auditory percepts as well as other applications such as treatment of severe tinnitus could then be envisioned.

## 4 Application: Auditory Brainstem Implant

**Outline** This chapter describes the development of a soft auditory brainstem implant, a device dedicated to the stimulation of the cochlear nucleus. The implant is developed in the context of a translational study which aims at restoring the natural hearing tonotopy and auditory acuity threshold in non-human primates. The chapter is organized in 3 sections:

1. **Introduction** on auditory brainstem implants in the clinic and overview of the current limitations.
2. **Methods** details the experimental plan of the study and the investigative tools developed to answer the research hypothesis.
3. **Results and discussion** presents the outcomes of both acute and chronic experiments on auditory brainstem stimulation in non-human primate.

**Acknowledgments** The results presented in this chapter were made possible thanks to the work of Alix Trouillet, Emilie Revol, Florian Fallegger, Laurine Kolly, Divya Chari, Alejandro Garcia, Christian M. Brown, Daniel J. Lee and the staff of the platforms of translational neurosciences in the university of Fribourg and the University of Washington (Seattle, USA). ATR, ERE, FFA, DCA, AGA, CBR and DLE helped plan and perform the experiments. FFA co-developed the interface system (FlexComb, pedestal) and helped with the assembly of the device. LKO helped with the characterization of the ABI. ATR and ERE trained the primate and ATR analyzed the neural recordings.

**Scientific contributions** The content of this chapter is being integrated into a scientific article:

- Alix Trouillet, **Florent-Valéry Coen**, Emilie Revol, Florian Fallegger, Laurine Kolly, Divya Chari, Alejandro Garcia, Christian M. Brown, Jocelyne Bloch, Daniel J. Lee,

Stéphanie P. Lacour. "Soft auditory brainstem implant restores hearing tonotopy with high auditory acuity. ", *in preparation*.

### 4.1 Introduction

**Neuroanatomy** In normal hearing humans, it is the cochlea which is responsible for converting incoming sound waves into electrical pulses that can be processed by the brain. At the center of this transcription mechanism is an array of sensory receptors called hair cells. Hair cells are mechanotransducers: under the action of an incoming pressure wave, they release neurotransmitters that, in turn, will trigger an action potential in the neighboring nerve fiber. One of the most interesting aspects of the cochlea is the fact that it is organized in a tonotopic fashion: high frequencies are transcribed by the hair cells located at the base of the spiral, while low frequencies are processed at the apex.

From the cochlea, action potentials travel along the auditory nerve (AN) to reach the cochlear nucleus (CN). From there, sound information is relayed and partially processed across three intermediary relays before finally reaching the auditory cortex (fig. 4.1). A particularity of the auditory pathway is that each nerve fiber will carry a specific frequency over the dynamic range, a fact which remains true from the cochlea all the way to the auditory cortex. As a result of this neuroanatomical characteristic, the tonotopic organization of the cochlea will be mirrored across all the relays of the auditory pathway.

**Auditory implants** Auditory implants provide meaningful sound perception to patients suffering from severe hearing loss who cannot benefit from non-invasive hearing aids. To do so, they leverage the tonotopic organization of the auditory pathway and encode sounds percepts by delivering spatially specific electrical stimuli. Among the treatments to address profound deafness and neuroprosthesis in general, cochlear implants (CIs) are widely considered a resounding success story with over 700'000 patients implanted world-wide according to the National Institute on Deafness and other Communication Disorders (NIDCD). These devices allow to restore hearing percepts in deaf or hard-of-hearing patients by electrically stimulating the spiral ganglion neurons (SGNs) located inside the cochlea. Unfortunately, there exists a subset of deaf patients who cannot benefit from CI due either to an absent/damaged cochlea or to an injured/atrophied auditory nerve.

Among those non-eligible for a CI implantation, the largest cohort is composed of patients suffering from Type II Neurofibromatosis (NF2). This rare genetic disease causes the growth of tumors around the VIII cranial nerve, referred to as benign vestibular schwannomas. While the presence of these tumors alone can damage the auditory nerve, the most common cause for deafness in NF2 patients is actually the surgical procedure re-

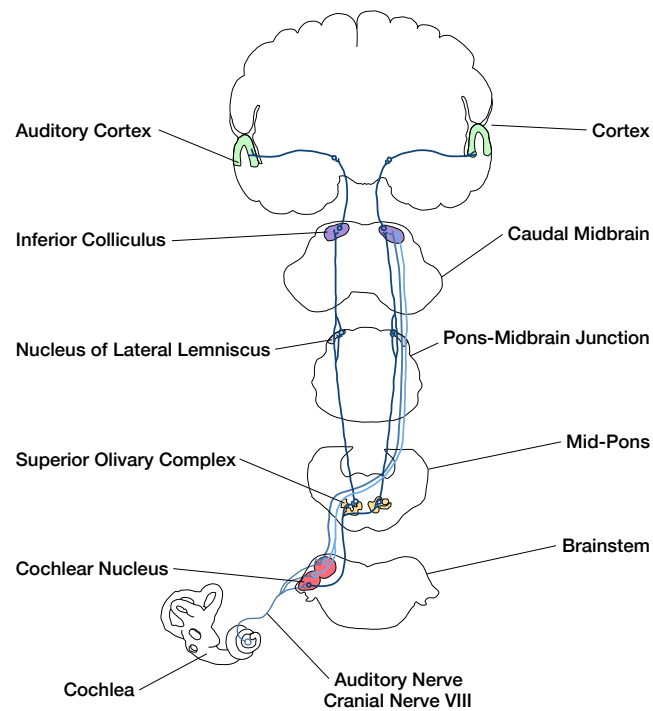


Figure 4.1: Simplified diagram of the auditory pathway illustrating the principal projections from the cochlea to the auditory cortex.

quired to remove them. Indeed, the efforts to resect the tumorous tissue often results in the destruction of the nearby auditory nerve, rendering the patient deaf.

The solution consists of intervening further up the auditory pathway, at the level of the brainstem. By delivering electrical stimuli directly to the cochlear nucleus, the inner ear and VIIIth cranial nerve are effectively bypassed, thus providing those affected with an alternative to cochlear stimulation. The electrical interfaces used to stimulate the cochlear nucleus are referred to as Auditory Brainstem Implant (ABI).

**ABIs in the clinic** Three companies currently offer clinically approved ABIs: Cochlear, MED-EL and Neurelec. All available designs are fairly simple, constituting of a 5mm-thick silicone paddle with 12 to 21 contacts depending on the model. The electrode grid is composed of platinum disks of 1 millimeters in diameter. All designs feature a mesh-like structure in order to anchor the device following its insertion. The rest of the device is directly inherited from cochlear implant, with the electrode paddle being connected to an implantable stimulator and receiver while the microphone and speech processor are placed externally, behind the hear of the subject.

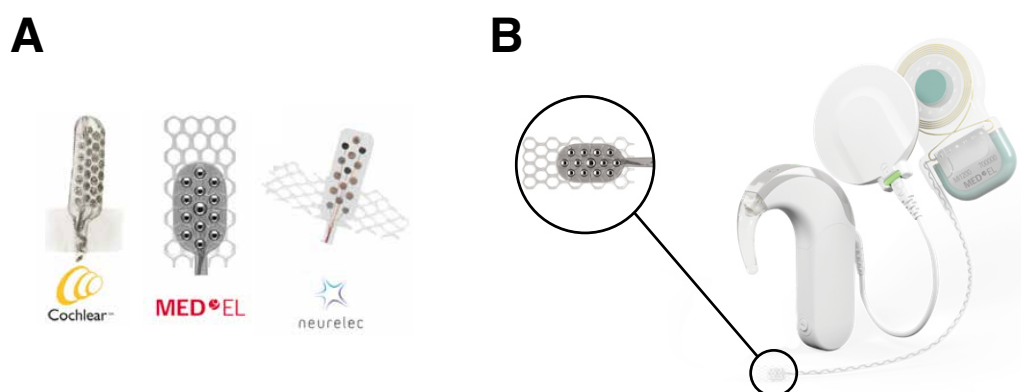


Figure 4.2: Clinical ABI designs. **A** Range of currently available ABI paddles. From left to right: Cochlear, MED-EL, Neurelec. **B** Picture of a complete ABI system from MED-EL including the implantable stimulator, wireless transceiver and speech processor.

**Clinical outcomes and issues** While most CI users show a high degree of open set speech recognition, this consistent level of performances has unfortunately yet to be matched by ABI beneficiaries. In fact, the majority of ABI users are only able to appreciate general environmental sounds and have thus to remain reliant on lip reading for speech perception [128]. Furthermore, the range of possible outcomes seems comparatively wider, with large differences in the quality of the auditory percepts across patients. Brain plasticity appears to play a critical role in that regard, with children under 2 years old being amongst the better performing ABI users. Nevertheless, most clinics report the performances of ABI users to significantly lag behind those of CIs, even within the restricted context of pediatric cases [129].

In addition to poorer hearing outcomes, ABI users also often report side-effects in the form of dizziness, tingling in the arms and legs, as well as facial twitching. These sensations are believed to originate from the spreading of current to nearby, non-auditory structures such as the VIIth cranial nerve which controls facial muscles. In order to prevent discomfort to the patients, audiologists will routinely deactivate the electrodes causing side-effects during the post-operative assessment phase.

Interestingly, a study from Barber et al. has shown that both speech perception and the number of deactivated electrodes are correlated with the orientation of the electrode paddle [130]. Furthermore, the ABI positioning itself has been found to differ significantly across patients, so much so that it is considered the main contributing factor in the variability of ABI implantation outcomes. Large differences in orientation can be explained by the complexity of the surgical procedure, which has to be performed without bone or surface landmarks [131], and by the high risks of device migration post implantation. Indeed, any amount of torque applied to the ABI cable following its placement can lead to a complete or partial dislocation of the device out of the lateral recess. In addition



to these considerations on paddle orientation, the study by Barber et al. also highlights inconsistencies across stimulation channels, with some electrodes having significantly lower activation threshold than their direct neighbors. The presence of these "sweet spots" is believed to be indicative of a poor conformability by the ABI, with only part of the paddle being in close contact with the CN. This lack of compliance with the anatomy could also explain why ABI orientation has such a strong influence on hearing outcome. Indeed, in the case of a stiff paddle, the positioning of the array with respect to the curved surface of the CN directly determines the distance between each electrode and the target tissue. Non-conforming electrodes naturally cause more current to leak outside the CN, resulting in a less purposeful stimulation and poorer hearing outcomes overall.

The issues discussed above highlight the limitations of the current clinical strategy for the stimulation of the auditory brainstem. In this thesis, it is proposed to address these challenges by fabricating a device capable of better conforming to the natural curvature of the CN. Doing so requires to transition away from the stiff clinical implants in favor of a soft microelectrode array. The hypothesis is that the soft ABI will provide a more purposeful stimulation of the CN by (1) lowering activation threshold and (2) reducing side effects and thus the number of deactivated electrodes. Furthermore, the improved conformability of the array is expected to decrease the variability in hearing outcomes by alleviating the influence of the paddle orientation on the contact surface between the electrode grid and the CN.

## 4.2 Methods

### 4.2.1 Experimental design

In order to determine whether a soft ABI can restore the tonotopy of natural hearing, such a device had to be fabricated, implanted and tested in-vivo. From a translation perspective, non-human primates (NHPs) constitute the most relevant animal model due to the close resemblance between the human anatomy and theirs. Since the auditory outcome cannot be assessed through direct feedback from the animal, the validation of the soft ABI is articulated around two complementary metrics:

- **Behavioral data** For the purpose of our experiment, the subjects are trained to perform a discrimination task based on the frequency of sound queues. The goal is to compare the performances of the animals when presented with an artificial sound produced through the ABI instead of an auditory stimulus.
- **Auditory cortex recordings** In addition to the soft ABI, the subjects are implanted with a soft  $\mu$ ECoG. The device, introduced in the previous chapter of this thesis, is used to record the activity of the auditory cortex. These measurements will allow to contrast and compare the tonotopy of natural and artificial hearing, providing a

granular appreciation of the ABI ability to recruit the auditory pathway.

We believe that the combination of the behavioral data and auditory cortex recordings will provide a robust quantification of the soft ABI efficacy. The complete experimental plan, summarized in figure 4.3, is divided in seven phases:

- **Phase 1** Two rhesus macaques (*macaca malutta*) are trained to perform the frequency discrimination task. In short, the animals are presented with sound queues and taught to activate a lever whenever the frequency of the sound increases (fig. 4.4). Their performance can be quantified by recording the position of the lever with respect to incoming sound frequency.
- **Phase 2** A first animal is implanted with a soft  $\mu$ ECoG. The device is used to map the natural tonotopy by recording the auditory cortex activity in response to sound bursts (single frequency auditory stimuli). Additionally, auditory cortex recordings are performed during the execution of the trained task. As it should be clear by now, the implementation and results of the second experimental phase were the subject of the third chapter of this thesis.
- **Phase 3** The same animal is implanted with a soft ABI. Using the output from the  $\mu$ ECoG, the stimulation paradigm is then optimized in order to restore as well as possible the natural tonotopic map established in phase 2.
- **Phase 4** The optimized stimulation paradigm established in phase 3 is used to evoke auditory percepts during the frequency discrimination task. Because the hearing capabilities of the subject are preserved following ABI implantation, a direct comparison between natural and artificial hearing performances will be possible.
- **Phase 5** The second subject is implanted with a soft  $\mu$ ECoG. The design of the array will be updated based on the outcomes of the first animal, potentially providing a more detailed map of the natural tonotopy of the auditory cortex.
- **Phase 6** The second subject is implanted with a soft ABI. The stimulation paradigm established in phase 3 is tested and potentially updated based on the auditory cortex recordings.
- **Phase 7** The natural and artificial hearing capabilities of the second animal are assessed within the framework of the frequency discrimination task.

The experimental framework described above will not only provide us with the tools to assess the efficacy of the soft ABI but also allow us to gain a better fundamental understanding of the primates auditory pathway. In order to ensure the success of this project, the chronic implementation was preceded by a series of two acute ABI/ $\mu$ ECoG

implantations in NHP. These terminal experiments allowed us to rehearse the surgical approach and refine the design of the ABI and brought the first proof of concept of soft ABI functionality in NHP (fig. 4.5). At the time of writing, we have reached phase 3 of the chronic experiment and are beginning to establish the optimal stimulation paradigm for the restoration of natural auditory percepts.

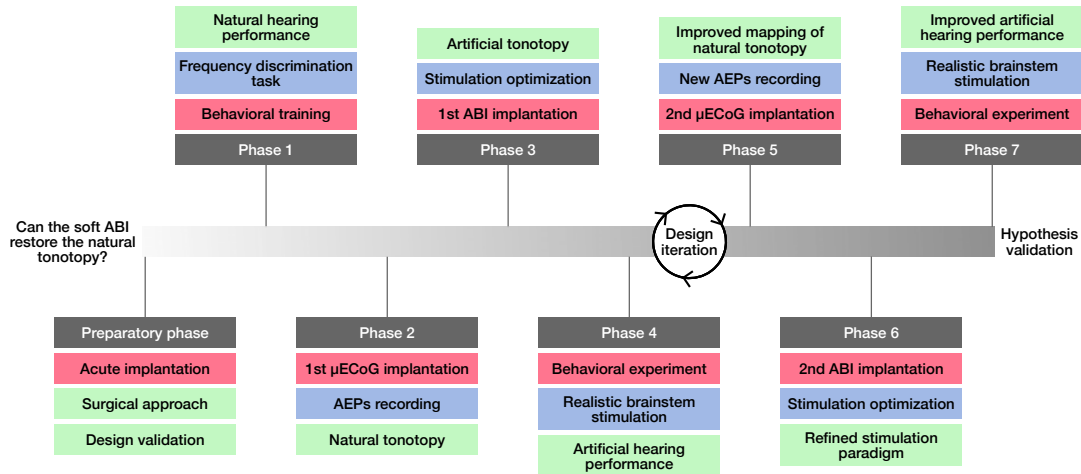


Figure 4.3: Experimental design for the validation of the soft ABI as tool to restore natural hearing. Milestones are indicated in red, tasks in blue and outcomes in green.

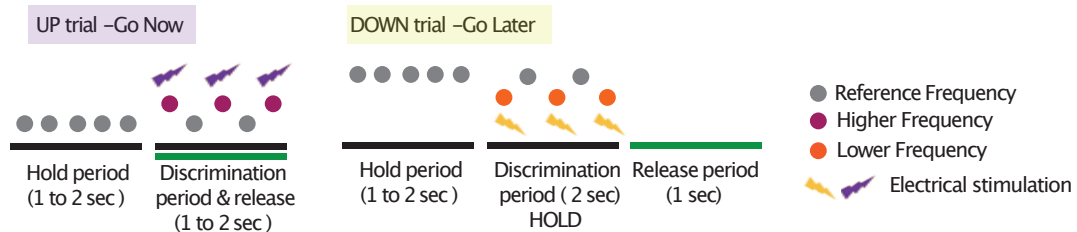
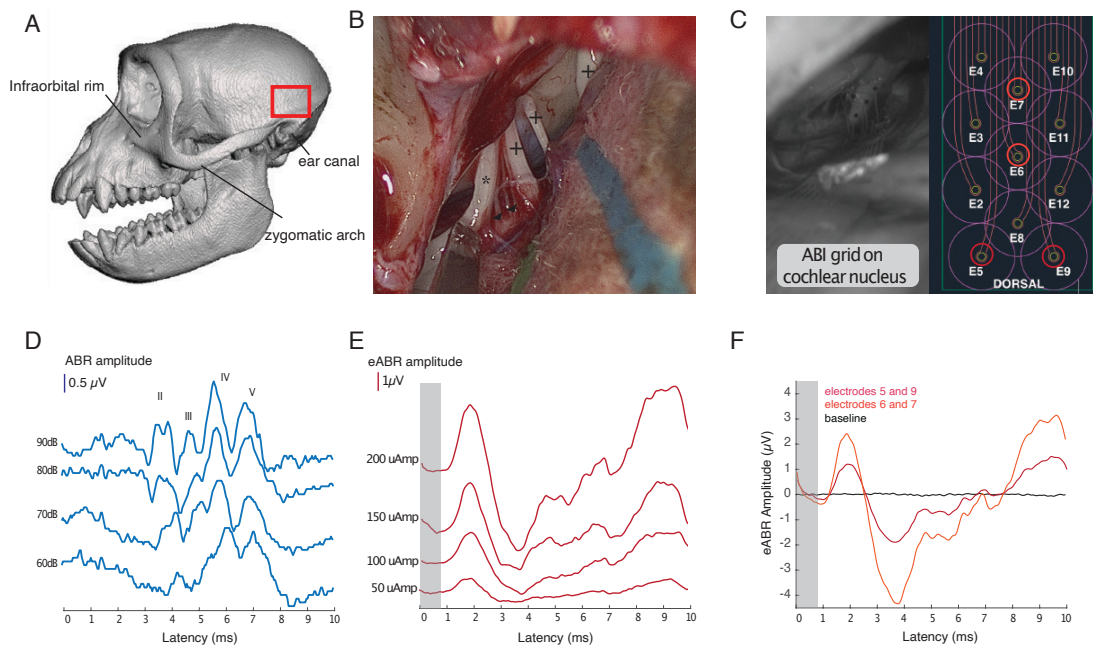


Figure 4.4: Frequency discrimination task design for non-human primates. The task is directional where the subject must define if the frequency that is played is of a higher (UP trial) or lower pitch (DOWN trial) compared to a frequency of reference. The task is then performed again using cortical stimulation.

#### 4.2.2 Surgical approach

**Clinical background** Surgically speaking, the placement of an ABI is a challenging endeavor because the cochlear nucleus (CN) cannot be directly accessed. Instead, the ABI has to be inserted blindly in the lateral recess of the fourth ventricle where it will tuck right against the CN (fig 4.6C). Two surgical approaches are currently used in the clinic: translabyrinthine and retrosigmoid (fig 4.6A-B). The techniques are inherited from the tumors resection operations which generally precede ABI implantation in NF2 patient.



**Figure 4.5: Soft ABI functionality and implantation feasibility: Proof of Concept** **A** Schematic representation of a macaque skull. Important landmarks are annotated. The red square represents craniotomy placement. **B** Endoscopic view of cranial nerves landmarks for the ABI insertion. **C** Pictures of a soft ABI at the entrance of the lateral recess of the 4th ventricle and schematic of the electrode grid with numbers of contact. **D** ABR traces recorded at several decibels showing the first 5 waves. Scale bar is 0.5  $\mu\text{V}$  **E** eABR traces recorded at several stimulation amplitude when stimulating ABI bipolarly between electrode 5 and 9. Scale bar is 1  $\mu\text{V}$  **F** eABR traces showing a comparison of amplitude in baseline, and when 2 different pairs of electrodes are stimulated at 150  $\mu\text{A}$ .

The translabyrinthine approach (TLA) consists of drilling an opening straight through the mastoid bone in order to access the inner ear. This approach provides the otologist with a familiar and direct view of the anatomy, without needing to retract the cerebellum which reduces trauma. Unfortunately, because the opening is performed through the mastoid, the cochlea and vestibular labyrinth are generally destroyed during the approach, rendering the patient deaf, without hope of residual hearing. In comparison, the retrosigmoid approach (RSA) allows to preserve the inner ear, offering to maintain a form of residual hearing following the surgery. The RSA, however, is technically more challenging and requires cerebellar retraction to access the auditory nerve.

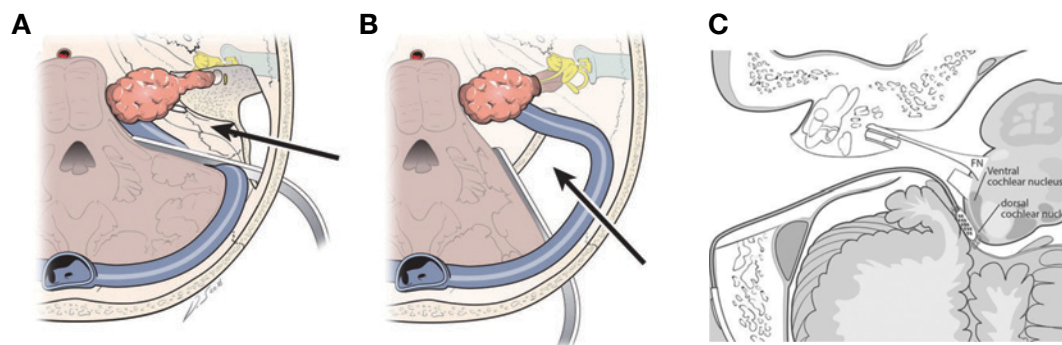


Figure 4.6: Possible surgical approaches for the resection of vestibular schwannomas and subsequent placement of the ABI. Adapted from [132]. **A** The translabyrinthine approach provides clear view of the tumors and auditory nerve without the need for cerebellar resection. **B** While the retrosigmoid approach requires severe cerebellar retraction to expose the auditory nerve, it keeps the vestibular labyrinth and cochlea intact. As a result, the subject is able to retain the hearing capabilities provided by the middle ear. Arrows in **A** and **B** indicate the direction of visual field. **C** Diagram of an ABI placed through a translabyrinthine approach. In the drawing, the auditory nerve has been entirely resected following the removal of the tumor.

**Non-human primate implantation** Since the natural hearing capabilities of the animal needed to be preserved, the soft ABI was placed using a retrosigmoid approach. The implantation procedure, shown in Figure 4.7, begins with the intravenous administration of propofol and fentanyl as anesthetics. Next, the animal is intubated and placed on the surgical table over a heating blanket, before being covered with sterile drapes. From this point on, heart rate, body temperature and blood oxygen pressure are monitored continuously. A skin incision is then performed behind the left ear. The underlying muscles are separated from the skull using a retractor, unveiling the temporal and mastoid bone underneath. A cranial window, measuring approximately 2 by 2 cm, is opened using a bone drill. Next, the dura mater is cut and flipped over, giving access to the cerebellum that is retracted to expose the cranial nerves. The ABI pedestal is then secured in place on top of the skull (Figure 4.7D) and the rest of the device is tunneled subdurally.

## Chapter 4. Application: Auditory Brainstem Implant

The electrode paddle is anchored at the entrance of the craniotomy using two screws inserted through dedicated structures of the FlexComb connector. Using an endoscope to guide the approach, the ABI is placed in the lateral recess of the fourth ventricle (Figure 4.7B). Since the positioning of the implant cannot be directly validated visually, its functionality is assessed by stimulating through a group of key electrodes and recording the resulting electrically evoked auditory brainstem responses. Once the placement of the implant has been confirmed, a muscle plug is tucked against it in order to stabilize it, followed by a layer and Tisseel (fibrin sealant) followed by DuraSil to close the dura mater (Figure 4.7C). The two ground wires is placed subcutaneously before suturing the muscles and the skin. Upon completion of the procedure, the natural and artificial hearing capabilities of the animal are verified through the recording of auditory evoked and electrically evoked brainstem responses.

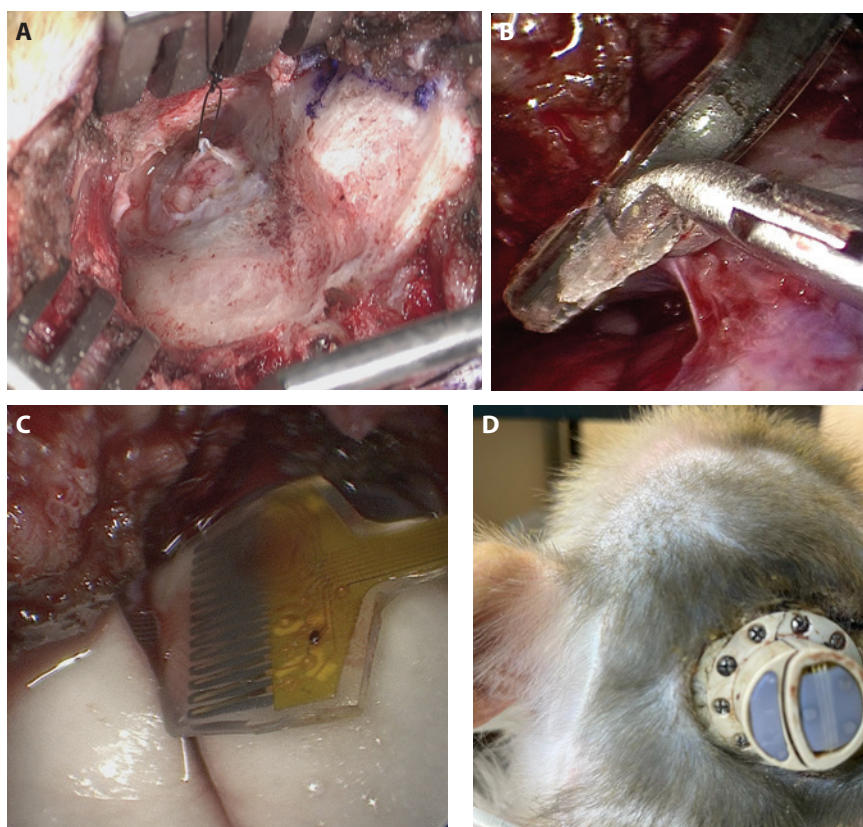


Figure 4.7: Chronic implantation of the Soft ABI. **A** Retrosigmoid approach. Craniotomy, dura opening and cerebellum exposure. **B** Placing Soft ABI in the lateral recess using insertion tool and ABI spine. **C** Securing the ABI below the flex comb using fibrine and artificial dura (white substance). **D** View of the whole system from the back of the head of the animal at the right side of the left ear after 2 weeks post-operatively.

**Neurophysiology** Auditory Brainstem Response (ABRs) are the most common technique used to assess a patient's hearing ability in the clinic. ABRs consist of far field measurements of the cumulated response of the auditory pathway to an external acoustic stimulus (usually in the form of a click). The signal is collected by placing one electrode on the vertex of the subject and another electrode next to the ear opposite of the one being presented with auditory queues. In normal hearing subject, an ABR trace presents five to seven peaks, depending on the quality of the recording (Fig. 4.8). In humans, the first two peaks, designated by roman number I and II, are generated from the distal and proximal part of the auditory nerve, respectively. Wave III is thought to arise mainly from the cochlear nucleus, while IV and V are considered to originate from the superior olivary complex and lateral lemniscus. When they can be observed, peaks VI and VII are associated with the activity of the inferior colliculus [133]. More so than the amplitude of the peaks, it is the timing between them that is of interest for audiologists, since the ABR wave latencies are very sensitive to changes in conduction velocity along the auditory pathway. As an audiometric test, the ABR is thus used for two major purposes: (1) to assess the ability of the auditory system to transmit information beyond the auditory nerve and (2) to estimate hearing threshold in the diagnosis of hearing impairment.

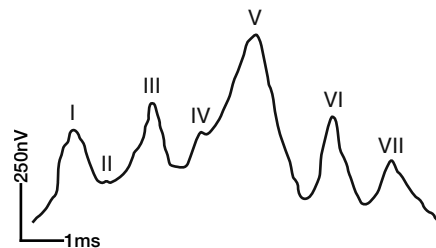


Figure 4.8: Example of a typical ABR trace in a healthy human [?].

### 4.2.3 ABI design & design validation

The particularity of the surgical approach meant that a significant engineering effort had to be made in order to design not only the soft ABI itself but also the supporting components around it. A picture of the complete system is shown in figure 4.9. It is composed of four parts:

1. The soft electrode paddle itself, featuring 11 individually addressable contacts.
2. A resorbable insertion guide to help place the array next to the CN.
3. An imaging marker to be able to locate the device via magnetic resonance imaging (MRI) and computed tomography (CT)
4. A custom-designed pedestal to be able to interface with the device transdermally once implanted.



## Chapter 4. Application: Auditory Brainstem Implant

This subsection will discuss in details the design challenges related to each of these elements as well the technological solutions developed to address them.

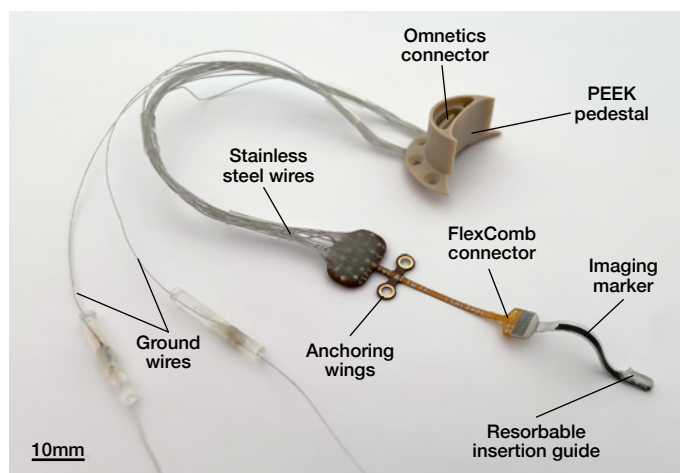


Figure 4.9: Picture of the soft ABI assembly.

**ABI design** The design process for the soft ABI began with a set of ex-vivo experiments in order to determine the optimal geometry for the device. For this purpose, simple, graduated strips of silicone were fabricated with various combinations of thicknesses, lengths and widths. Sham surgeries were performed on two rhesus macaque cadaver heads and the quality of fit of each design was assessed via endoscopic imaging. This data was supplemented with the surgeon's feedback regarding handleability and overall feel of the device. Based on this study, the optimal ABI dimensions were found to be 150 $\mu$ m in thickness and 2mm in width. The length of the array was initially set to 40mm, although it would later be decrease by 10mm to fit the anatomy of female subjects, which are much smaller.

A first iteration of the soft ABI was fabricated based the original micropatterned interconnects technology presented in section 2.2. The device, shown in figure 4.10A, was tested in-vivo during an acute experiment on a pigtail macaque. This first study allowed to validate the surgical approach, the placement of the device and the ability to evoke auditory responses. Critical feedback regarding the device handleability was also collected, in particular with respect to the connector and flexible flat cable. It was assessed that these components were adding an excessive amount of rigidity to distal end of the implant. Indeed, any amount of torque applied to the flexible flab cable would cause the electrodes paddle to pop out of the lateral recess, rendering the placement and anchoring excessively difficult.

A second iteration of the soft ABI was developed to address this issue (fig. 4.10B). It was built with the new and improved core-shell micropatterned interconnects and features



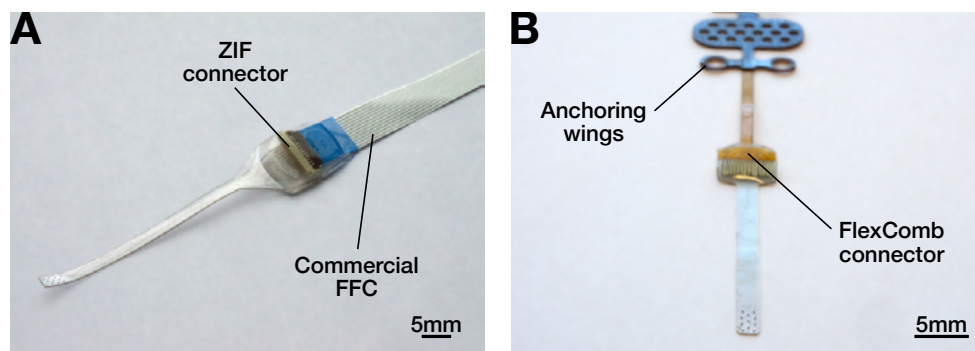


Figure 4.10: Design iterations for the soft ABI. **A** First iteration of the soft ABI based on the original micropatterns process. **B** Second iteration of the design, built using the new and improved core-shell micropatterns process.

a narrow FlexComb connector that significantly reduced the perceived stiffness of the array. Additionally, the FlexComb connector is used to transition to individual, teflon-coated, stainless steel wires. This configuration offers more versatility to the surgeon in terms of orienting the ABI relative to the pedestal (anchoring point). This new approach therefore allows to minimize the torque applied to the implant during surgery, effectively reducing the risk of the paddle accidentally popping out.

Besides the new connection scheme, the soft ABI features 11 electrodes of  $100\mu\text{m}$  in diameter, distributed over an area of  $2 \text{ by } 6 \text{ mm}^2$ . The 5 remaining channels are attributed to a set of test structures, implemented to monitor the functionality of the device over time (see figure 4.11). Channels 1 and 14 are terminated at the transition between the FlexComb connector and the soft electrode paddle. They allow to monitor the integrity of the RTV encapsulation on top of the connector. Channels 15 and 16 are terminated inside the flexible PCB, at different location in the design. Finally, channel 7 and 8 are connected to the same electrode. As such, they form an electrical bridge that can be use to measure the evolution of the contact resistance at the level of the FlexComb connector.

The main difference between the two generations of soft ABI are summarized in table 4.1. The in-vitro characteristics of these devices were previously shown in figure 2.11 and 2.22 respectively.

**Resorbable insertion guide** A major challenge related to ABI implantation is the handling of the implant during the surgical procedure. While surface electrode grid such as ECoG can be easily laid on top of the target tissue, the ABI needs to be placed in contact with a deep structure of the brain - the cochlear nucleus. Proper placement is achieved by pulling the paddle past the cerebellum and pushing it into the lateral recess of the fourth ventricle. This series of manipulations constitutes an issue for the soft ABI

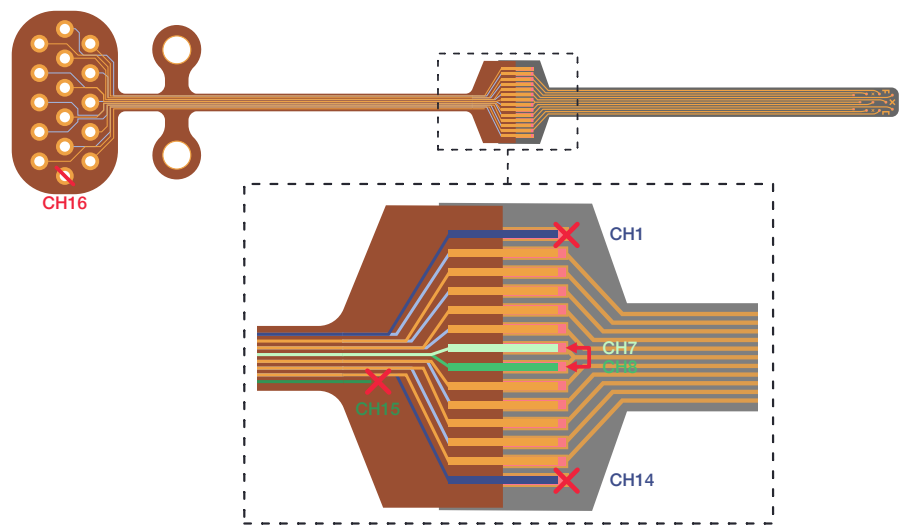


Figure 4.11: Schematic of the soft ABI. The inset details the test structure implemented to monitor the functionality of the implant over time.

Component	ABI gen 1	ABI gen 2
Interconnects	Original micropatterns	Core-shell micropatterns
Electrodes	11	11
Dimensions	40 x 2 x 0.15 mm	30 x 2 x 0.15 mm
Connector	ZIF + commercial FFC	FlexComb
Test structures	NO	YES (5)
Anchoring structures	NO	YES (2)

Table 4.1: Summary of the differences between the two generations of ABI.

because, unlike its clinical counterpart, it cannot be pushed or grasped firmly without risking damaging the device. In order to address this problem, the soft ABI is fitted with a temporary insertion guide. The structure consists of a hydrosoluble ridge affixed at the back of the electrode paddle. The guide is made of polyvinyl alcohol (PVA), a water soluble polymer commonly used in medical applications because of its biocompatibility and non-toxicity. With regard to the design and manufacturing of the hydrosoluble guide, the engineering challenges are two-fold: (1) producing a predetermined geometry with a sufficient resolution ( $<500\mu\text{m}$ ) and (2) tuning the dissolution rate in order for the ridge to last throughout the entire surgical procedure ( $>2\text{h}$  accounting for adjustments of the placement).

The solvability of PVA is mainly governed by two material characteristics: the degree of hydrolysis and the degree of polymerization. The degree of hydrolysis describes the ratio of hydroxyl to acetate groups in the material with less hydrolyzed blend corresponding to a larger amount of acetate groups. Since hydroxyl groups exhibit a high affinity for water, they induce strong inter and intramolecular hydrogen bonding, which, in turn, inhibit the solubility in water. On the contrary, residual acetate groups in partially hydrolyzed PVA are hydrophobic. As their number increases, steric hindrance increases as well, which inhibits the formation of hydrogen bonds between the molecular chain, resulting in a high solubility. To put it simply, the degree of hydrolysis is inversely proportional to the solubility of the PVA formulation. Similarly, a high degree of polymerization will translate into a lower solubility, as longer polymer chains exhibit stronger inter and intramolecular hydrogen bonding. With this in mind, a PVA blend with a high molecular weight (186k) and degree of hydrolysis (89%) was chosen for the manufacturing of the insertion guide (SKU 363103, Sigma Aldrich).

Early prototypes were fabricated via injection molding. To this end, a liquid solution was first prepared by dissolving PVA powder in deionized (DI) water at  $85^{\circ}\text{C}$ . The resulting blend was then injected into a silicone mold and placed in a  $55^{\circ}\text{C}$  oven in order for the water to evaporate. The PVA injection and drying steps were repeated two times before finally demolding the part. Finally, the resulting block of PVA (fig. 4.12A) was cut into smaller pieces with a razor blade. Unfortunately, the fabricated parts exhibited a significantly faster dissolution than anticipated (fig. 4.12C). This behavior was attributed, in large part, to the large amount of voids in the structures. Indeed, the presence of gaps would increase the effective surface area in contact with the surrounding liquid, leading to a faster dissolution. As for the voids themselves, they likely originate from micro-bubbles in the solution which have dilated during the drying step and subsequently failed to escape due to the high viscosity of the blend.

In order to reduce the dissolution rate of the structure, a new version of the insertion guide was produced via 3D printing (fig. 4.12D). In this new method, a PVA filament (AquaSolve PVA, Form Futura) is thermally extruded and shaped using a commercial 3D printer (i3 MK3S, Prusa Research). The printer parameters were set as follows: nozzle

## Chapter 4. Application: Auditory Brainstem Implant

size 0.4mm, bed temperature 65°, layer thickness 0.1mm, speed 45mm/s. The formulation of the PVA filament is unfortunately not disclosed by the manufacturer. While the quality of the printed parts is not optimal, in particular in terms of surface finish, the dissolution behavior is significantly improved. Indeed, thermally extruded PVA does not exhibit any voids, resulting in a much slower and steadier dissolution rate (fig. 4.12E). The challenge in 3D printing a part with fine details originates from the use of a pure PVA filament. Filaments with additives can significantly improve printability however their biocompatibility status is often unknown which makes them unsuitable for use in chronic experiment.

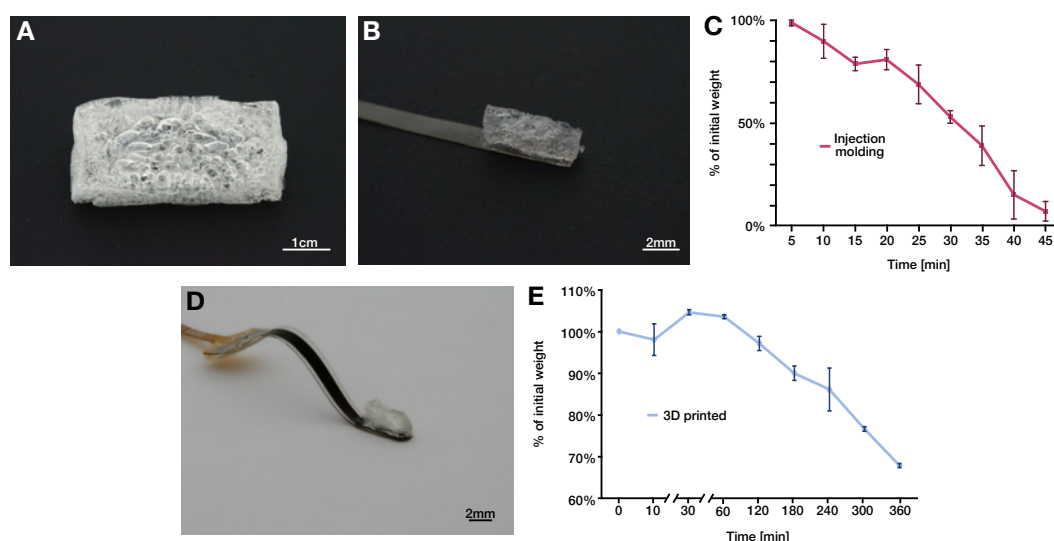


Figure 4.12: Fabrication of a temporary insertion guide. **A** Monolithic PVA block resulting from the injection molding and subsequent drying of a PVA/H<sub>2</sub>O solution. The structure presents a large amount of air bubbles, trapped inside during the drying process due to the high viscosity of the blend. **B** The first resorbable insertion guides were fabricated by slicing PVA block like the one shown in A. **C** Dissolution rate of a square test samples (20 x 20 x 2 mm) in PBS at 37°C. The structures fabricated via injection molding exhibited a faster than desired dissolution rate due in large part to the presence of numerous voids inside the bulk of the material. **D** The updated resorbable insertion guides were fabricated 3D printing using a PVA filament. **E** Dissolution rate of a square test samples (20 x 20 x 2 mm) in PBS at 37°C. The 3D printed exhibited significantly improved dissolution rate with regard to the targeted application (>2hours).

To assemble the 3D printed guide on the soft ABI, the surface of the implant is first activated using oxygen plasma (100W, 0.2mbar, 30s in a PCCE Nano, Diener). Next, a droplet of 20 wt% of PVA in DI water is spread on the back of the electrode array and the 3D printed part promptly placed on top. The assembly was left to dry at room temperature for 8 hours.

**Imaging marker** Imaging has become an increasingly important investigative tool in analyzing the outcomes of ABI implantation [130]. Similarly in the context of our project, the ability to link array localization with elicited activity would provide a powerful insight into the performances of soft ABI. Unfortunately given the dimensions of the NHP ABI, it was unlikely that the implant would appear either on MRI scans (slice thickness 0.6mm) or CT scans (slice thickness 0.62mm). A potential solution consists in implementing a marker at the back of the array using the Pt-PDMS composite. The rationale is that a large, conductive surface composed of a dense material would provide the necessary contrast to resolve the array position. The decision was therefore taken to pattern a simple strip at the back of the array, in order to maximize contrast with the surrounding tissue (fig. 4.13). The pattern was implemented via screen-printing of the Pt-PDMS composite through a PET shadow mask.



Figure 4.13: Picture of the imaging marker at the back of the electrode paddle.

**Pedestal** In the context of chronic in-vivo experiments, it is critical for the implanted device to feature a transdermal access port that is both mechanically robust and safe for the animal. In the soft ABI, the interface with the external stimulator consists of an Omnetics connector sealed inside a tailor-made pedestal. The custom parts were machined out of polyether ether ketone (PEEK) (fig. 4.14A), a high performance thermoplastic that is both biocompatible and extremely robust mechanically [134]. Furthermore, PEEK is radiolucent and non-conductive, making it X-rays transparent and MRI safe. The particularity of this design is that it can be seamlessly be assembled with the second pedestal enclosing the  $\mu$ ECoG connector (see fig. 4.14B-C and chapter 3). The ABI pedestal is anchored on the same footplate as the  $\mu$ ECoG, providing a seamless, monolithic interface which reduces trauma and the likelihood of infection compared to a dual pedestals approach. A magnetically attached cap prevents fluid from entering the access port when the device is not used.

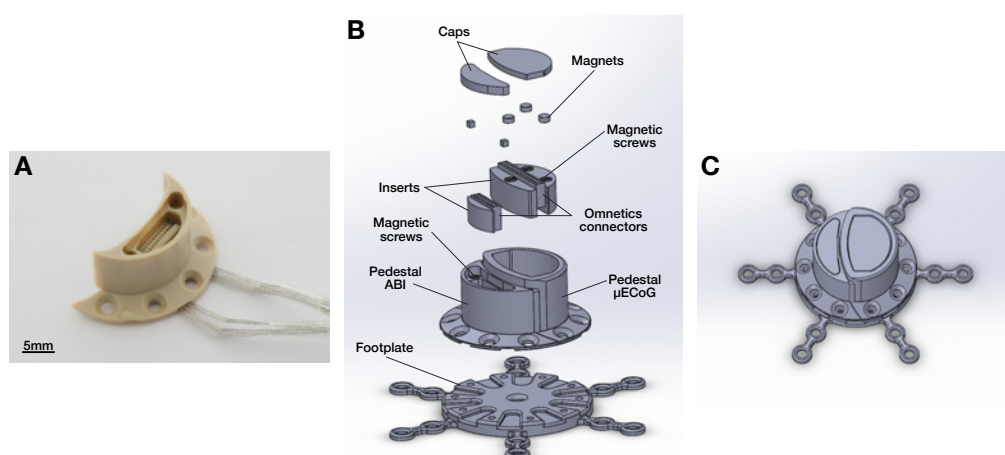


Figure 4.14: Double pedestals system allowing to seamlessly assemble the interface for the ABI and the  $\mu$ ECoG. **A** Picture of the ABI pedestal. **B-C** The two pedestals were designed to be assembled together, forming monolithic interface that minimize trauma and the risk of infections.

### 4.2.4 Stimulation & recording protocols

**Acoustic stimulation** In order to measure the natural hearing capabilities of the animal, two types of acoustic stimuli were presented to the animal: tone bursts and clicks. Both stimuli were delivered through earbuds placed in the ear of the animal (closed field configuration). The tone burst were generated through a custom MatLab script. They consist of a 500ms-long, single frequency sound followed by 500ms of silence, presented repeatedly for a duration of 3 minutes. In order to map the natural tonotopy of auditory cortex, the frequency of the tones is varied across trials, ranging from 100Hz to 20kHz. Clicks consist of a broad spectrum, short duration sounds (100 $\mu$ s) which are meant to recruit spiral ganglion neurons across the whole dynamic range. Here, they were generated using a specialized neurophysiology system (NIM-Eclipse, Medtronic). The clicks were presented at a frequency of 21Hz over 1024 repetitions for each recording, varying the sound intensity across trials.

**Electrical stimulation** Current pulses were delivered through the soft ABI using either a standalone pulse generator (IPG 2100A, AM Systems) or a comprehensive neurophysiological system (NIM-Eclipse, Medtronic). The current pulses were delivered in monopolar and bipolar configuration, with varying amplitude (0.05mA - 1mA) and frequency (21Hz). The pulse duration (300 $\mu$ s) was kept the same across trials.

**Auditory brainstem responses** The auditory brainstem responses (ABRs) are acquired using a dedicated neurophysiology system (NIM-Eclipse, Medtronic). A set of four needles are placed subcutaneously on the vertex, in the leg and behind each ear, allowing to assess hearing functionality on both side. The response are averaged automatically by the system based on the number stimulus repetitions defined at the start of each trials.

**Auditory cortex recordings** The auditory evoked potentials (AEPs) are acquired by connecting a soft  $\mu$ ECoG placed on the auditory cortex of the animal to a wireless recording system (W2100-HS32, Multichannel Systems). The device, based on the low-power RHA2132 chip (Intan Technologies), amplifies and digitizes the signal before sending the data wirelessly to the acquisition computer. The sampling rate is software defined at a value of 2kHz. The resulting data are analyzed using a custom MatLab (MathWorks) script. For each frequency, the recorded raw signal is filtered between 1 and 100Hz and averaged over the period of the acoustic stimuli (1s).

### 4.3 Results and Discussion

Following the acute experiments and the proof of concept presented in Fig 4.5 we have successfully implanted a soft ABI on one animal in a chronic context as presented in Figure 4.7. First, a retrosigmoid approach enabled to access the dura mater as shown in Figure 4.7A. By retracting the cerebellum, the soft ABI held by the temporary spine using alligator forceps as seen in Figure 4.7B and inserted in the lateral recess. The implant was secured in place using a piece of muscle inserted along the silicone paddle length and covering the area in fibrine glue. Finally the dura mater was closed using artificial dura visible in Fig 4.7C. The animal has been previously trained to perform the frequency discrimination task described above and has been successfully implanted with the soft ECoG array on its right auditory cortex (see results in Chapter 3). The pedestal system of the ABI presented in Figure 4.14 was fixed next to the first pedestal with success (see Fig 4.7D) and could be used to stimulate with the ABI while recording the ECoG. The animal recovered quickly with no sign of vestibular defect or cerebrospinal fluid leak.

Two weeks post ABI surgery, we have performed a series of recordings to assess the positioning and the functionality of the chronic soft ABI. ABRs were normal, displaying the typical waves and demonstrating that the surgery was performed without causing any lesion of the auditory system of the animal (data not shown). Moving on to electrical stimulation of the auditory pathway, we have successfully recorded eABRs stimulating several electrodes (in monopolar versus the ground) or pairs of electrodes (bipolar). eABRs were modulated in amplitude with the stimulation power and according to electrode placement on the ABI pad (data not shown). Additionally, muscles of the face innervated by the cranial nerves situated close to the cochlear nucleus were not recruited extensively following the ABI stimulation (data not shown here). We therefore

demonstrated that the ABI was in place at the surface of the cochlear nucleus and was functional 2 weeks post-surgery.

As the ultimate test, we were able to record electrically Evoked Auditory Potentials at the surface of the macaque auditory cortex shown in Figure 4.15. The response is similar in shape and amplitude to acoustic AEPs and is modulated with stimulation power. We pinpointed the stimulation threshold between 0.5 mA and 0.6 mA. The signal seemed to reach a saturation above 0.9 mA with no further change in evoked potential amplitude (Fig (Figure 4.15A)). We have also performed a control experiment using the ground to stimulate, which showed no response and proved our stimulation to be specific to the auditory pathway. In addition, we have revealed a specificity of the response depending on which electrode pairs were used to stimulate. Some electrode pairs were not able to trigger a response in the auditory cortex as visible in Figure 4.15B.

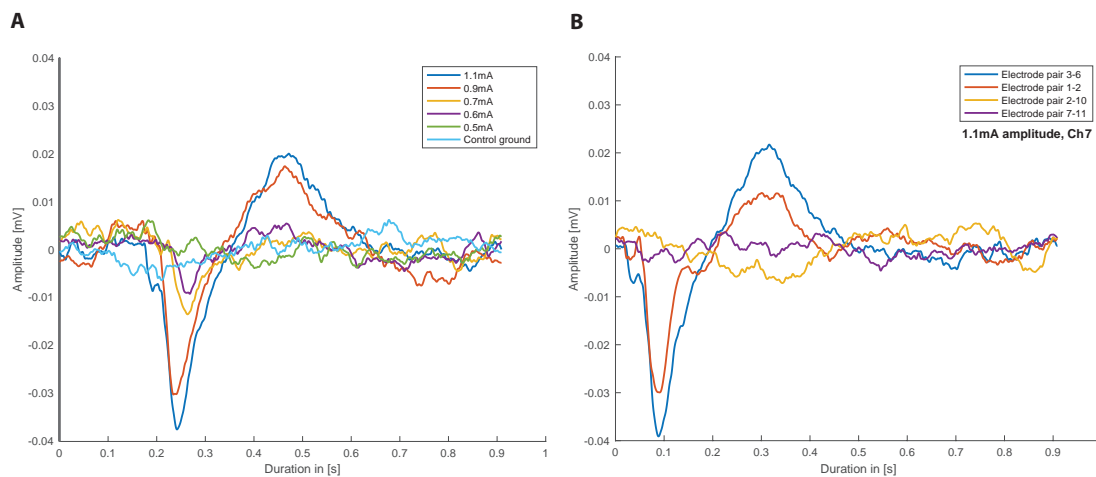


Figure 4.15: Soft ABI Evoked Auditory Potentials in a chronic model of NHP. **A** electrically Auditory Evoked Potentials measured with the ECoG array 2 weeks after ABI implantation. The amplitude of the response is modulated with the power of stimulation. This is the first demonstration of functionality of an ABI in a chronic model of NHP. This demonstrates that the securing procedure for the soft ABI was adequate as for 2 weeks post implantation. **B** eAEPs measured on channel 7 of the ECoG array when stimulating several electrode pairs at 1.1 mA. The responses are modulated in amplitude depending on where the stimulation occurs on the cochlear nucleus.

### 4.3.1 Conclusion

**Summary, Discussion and Outlook** These data are preliminary and several experiments will follow to validate the efficiency of the soft ABI at restoring hearing percepts up to high quality auditory function. Full electrical tonotopic maps will be established and compared to acoustic tonotopic maps both in sedated and awake experiments. This



will answer the specificity of the electrical stimulation of the Soft ABI and its ability to restore tonotopic hearing perception. These series of recording will be accompanied by several controls to ensure that the animal is actually feeling the ABI stimulation as an auditory cue: stimulation of electrode pairs with no evoked potentials on the cortex, activation threshold shift when stimulating in presence of a background noise, absence of responses when recording away from the auditory cortex, among others. The goal of these experiments will try to assess the auditory acuity that we are able to reach with the ABI. Finally, we will train the monkey to perform the task alternatively replacing the auditory cue with the electrical stimulation. This experiment will be the final proof that the soft ABI allows for high quality hearing percept. Additionally, imaging under CT and MRI will enable the precise localization of the implant and possibly relate it to known anatomy of the cochlear nucleus. The tracking of the implant position over time will be crucial to also control for the mechanical stability of the implant as well as observing the tissue reaction to the implantation over the brainstem.

While the fine neurophysiological assessment of the device capacity is just starting, we can already conclude that we successfully implemented a working device. This was allowed by careful engineering of the implantation tools and procedure, the connection scheme to the implant, the tunnelling of the cables under the skin and the sequential placement of the connector pedestal following the first ECoG surgery. With this we have developed the first chronic model of non-human primate to test the auditory brainstem implant. The several iterations of the soft ABI made possible its surgical handling as well as successful implantation at the surface of the cochlear nucleus. From the results already obtained, the system engineered to keep it in place in a rhesus macaque is successful.



## 5 Application: Spinal Cord Stimulation

**Outline** This chapter describes the development of a spinal cord implant for the restoration of upper-limb motor functions in rats. This device was developed as a supplement to the work on the auditory system presented previously. As such, it was conceived as a way to assess the performances of the core-shell micropattern technology in a mechanically challenging environment. The chapter is organized in 3 sections:

1. **Introduction** provides a brief overview of epidural electrical stimulation as a therapy and discusses the challenges associated with developing an implant for such purpose.
2. **Methods** details the investigative tools developed to perform this study including the soft spinal cord implant.
3. **Results and discussion** presents and discusses the neurophysiological and technological outcomes after 10 days of implantation.

**Acknowledgments** The results presented in this chapter were made possible thanks to the work of Maria Pasquini, Nicholas D. James, Inssia Dewany, Stefano Lai, and Jacopo Carpaneto. MPA, SLA, and JCA conceived the characteristics of the neurorobotic platform. MPA designed and developed the neurorobotic platform. NJA performed the spinal cord implantation. MPA, NDJ and IDE collected and analyzed all the neurophysiological data.

**Scientific contributions** The content of this chapter partially based on a scientific article:

- Maria Pasquini\*, Nicholas D. James\*, Inssia Dewany\*, Florent-Valéry Coen, Newton Cho, Stefano Lai, Selin Anil, Jacopo Carpaneto, Quentin Barraud, Stéphanie P.

Lacour, Silvestro Micera\* & Grégoire Courtine\* "Preclinical neurorobotic platform to develop therapies for upper-limb movement recovery", *Science Robotics* 6.53 (2022).

### 5.1 Introduction

Epidural electrical stimulation (EES) has been extensively used in the clinic to relieve the symptoms of patients suffering from neuropathic chronic pain [48, 135]. The approach consists of chronically implanting an electrode paddle at the surface of the spinal cord in order to stimulate electrically the underlying nervous tissue. Through targeted stimulation, the pain signals can be decreased or even completely blocked, providing relief to the patient. In recent years, it has been proposed to adopt a similar strategy in order to restore locomotion following spinal cord injury (SCI). The fundamental idea is to stimulate the dorsal roots of the spinal cord, which are the points of origin for the different nerves that control the muscles required for locomotion. Since the dorsal roots leave the spinal cord at the level of each vertebrae, they can be stimulated individually in order to specifically activate certain muscles. This strategy has been successfully implemented in rodents as well as larger animal models in order to restore movements in paralyzed limb following partial or complete spinal cord transection [136, 137]. Furthermore, the combination of intense physiological rehabilitation with EES has been shown to reactivate or even reestablish part of the spinal neural circuitry, enabling the subject to move without the assistance of the stimulation. More sophisticated approaches were also engineered by combining cortical recordings with EES in order to establish a closed-loop stimulation system. In that study, movement intents were successfully decoded from the motor cortex and used to trigger specific stimulation patterns to the dorsal roots.

While EES as a therapy to restore locomotion has shown promising results in research settings, its translation to the clinic is heavily limited by the designs of the commercially available spinal cord implants. Current electrode paddles have been engineered for pain management applications and as such, provide poor coverage of the dorsal roots: they are too narrow to reach both sides of the spinal cord and too short to cover all the necessary vertebrae. More importantly, commercial electrode arrays are extremely stiff which means they put a significant amount of mechanical constraints on the spine. Their stiffness also makes them unsuitable for implantation in highly mobile parts of the spine such as the neck.

Soft neural interfaces offer a compelling technological answer to the challenges of EES. Due to their low bending stiffness, soft microelectrode arrays are able to span the entire width of the spinal cord and to follow its complex topology without compressing it. Similarly, their stretchability means they can seamlessly comply with the natural motion of the spine. Finally, microfabrication technologies offer a cost-efficient way to produce implants tailor-made for specific applications or even specific subjects.

In the context of a larger study on the rehabilitation of upper-limb motor functions in rat, we therefore set out to fabricate a soft spinal cord implant for the modulation of cervical motor neurons. The hypothesis was that activity-dependent modulation of the cervical spinal cord with EES could improve upper-limb functions similarly to what was demonstrated in the lumbar portion of the spine [138]. While the theoretical benefits of a soft implant in the context of EES are significant, the spinal cord represents an extremely challenging environment to work in. Mechanically speaking, the paddle needs to be able sustain the static stresses imposed by the spine anatomy as well as the large deformation generated by bodily movements. Within the spine itself, the cervical region constitute the toughest location to operate in, due to the fact that (1) the available space between the spine cord and the vertebrae is significantly smaller and (2) the range of motion is much greater. From an engineering perspective, this application thus provided an environment to assess the functionality of the micropatterned interconnects under mechanical strains that are not replicated by standard characterization methods such as cyclic stretching [139].

## 5.2 Methods

**Device fabrication** The spinal cord implants were fabricated using the core-shell micropatterns technology presented in section 2.3.2. In contrast with the other implants presented so far, the thickness of the silicone encapsulation was reduced to 40 $\mu$ m on each side, for a total thickness of 80 $\mu$ m. The change was implemented in order to accommodate for the limited space available between the spinal cord and the vertebrae at the cervical level. The device outline was customized to target the spinal segments between T1 and C3 using 5 individually addressable electrodes of 140 by 500  $\mu$ m. The return electrode is composed of 3 contact sites shorted together and lined up to cover the center of the spinal cord. The device is wired to a standard 16-channel omnetics connector using a FlexComb connector. The flexible flat cable is designed to allow for the fixation of the omnetics connector on top of the skull of the animal. A teflon coated silver wire is soldered near the device connector in order to enable monopolar stimulation. Tests structures are implemented at various key locations in order to validate the functionality of the device over time (see fig 5.6).

**Surgical procedure** In clinical settings, electrodes paddle are typically inserted on top of the spinal cord by pushing the device into the epidural space through a single opening performed between the vertebrae (laminectomy). This strategy can unfortunately not be translated to the soft spinal cord implant due to its mechanical signature. Indeed, the low bending stiffness of the device will cause it to wrinkle and fold over when pushed from a single end. As a result, the implantation has to be performed with the help of a so-called passing elevator. In the case, this tool takes the form of a 4.0 ethilon suture wire, inserted through a first laminectomy rostral of C4 and exiting through a second

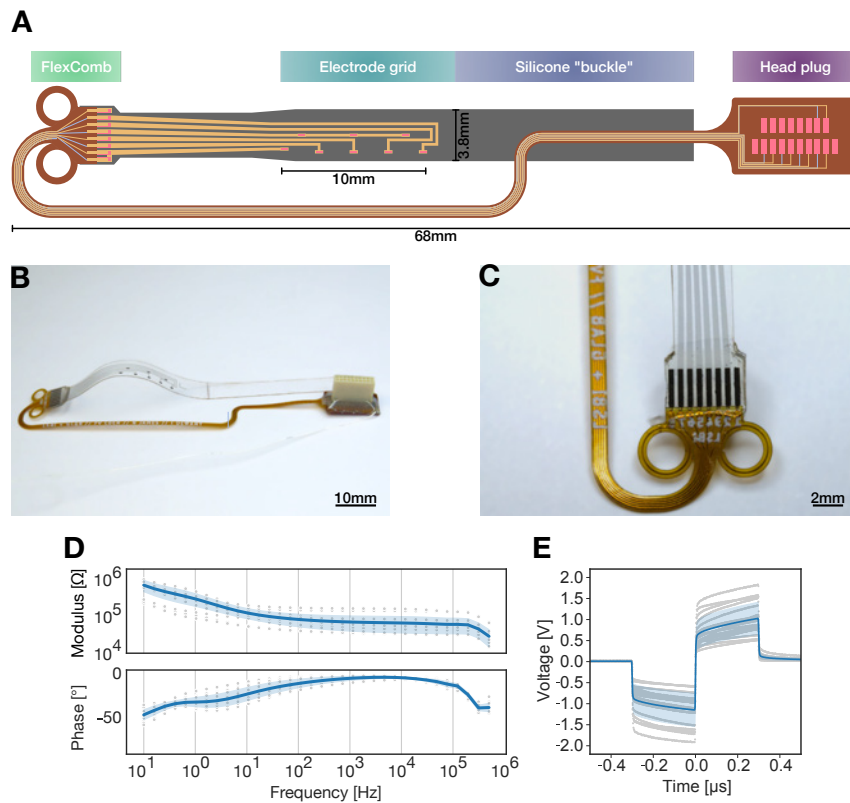


Figure 5.1: Soft spinal cord implant based on the core-shell micropatterns technology. **A** Schematic of the device. **B-C** Pictures of a fully assembled device. The FlexComb connector feature two loops (**C**) around which to fasten a suture in order to secure the array in place following implantation. In order to pull the array into the epidural space, a buckle can be formed using a strip of bare PDMS located at the distal end of the electrode grid. An commercial Omnetics connector affixed on top of the animal head allows to interface with the device. **D** Average impedance spectrum as measured in-vitro (n = 20 electrodes). The shaded area represents the standard deviation. **E** Average voltage transient upon the injection of 100μA biphasic current pulse (n = 20 electrodes). The shaded area represents the standard deviation.

one, located caudal of T1. A loop is formed at the T1 end of the suture and the soft implant is wrapped around it, as depicted in figure 5.2C-D. The ethilon can then be used to pull the array into the T1 opening, continuing until exiting the epidural space between C3 and C4 (fig. 5.2E-F). The positioning of the array is optimized based on the muscle twitch responses observed upon current stimulation at each individual electrode sites (fig. 5.2H). Once the proper placement of the device has been confirmed, the superfluous silicone buckle of the implant is cut. Two bone screws are inserted into the T2 and T3 vertebrae and used as anchoring point for the array. There, the implant is secured in place using a suture and a biocompatible silicone adhesive (Kwik-Cast, World Precision Instruments). Finally, the 16-channel ometronics connector is fixed on top of the skull using dental cement and a bone screw.

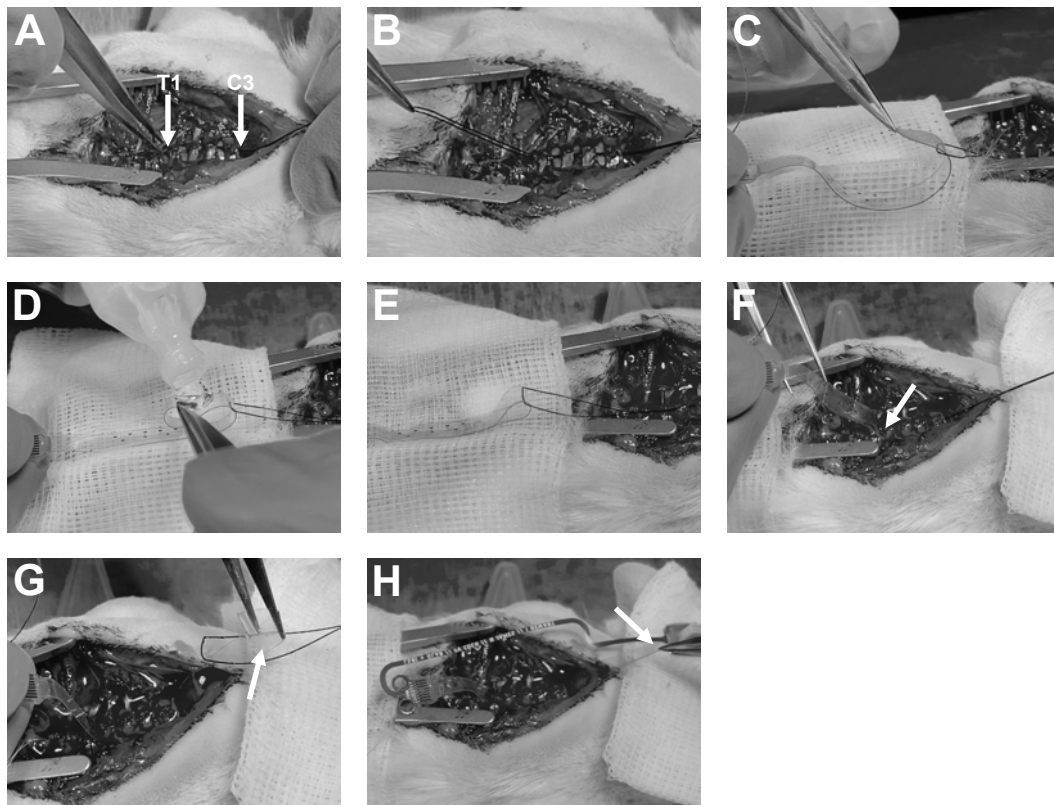


Figure 5.2: Implantation procedure of the soft spinal cord array. **A-B** First, a 4.0 ethilon suture wire is inserted between T1 and C3 to serve as a so-called passing elevator for the implant itself. **C-D** A buckle is formed around the suture wire using the strip of bare PDMS located at the distal end of the electrode grid. The application of a few saline drops is enough to create a weak adhesion between the PDMS surfaces, thus closing the buckle. **E-F** Using the suture wire, the implant can be slowly pulled in the epidural space (T1 entry pointed by the arrow). **G-H** Upon exit of the array, the buckle is unfastened (**G**) and the position of the array adjusted by pulling on the silicone strip (**H**) before cutting it off.

## Chapter 5. Application: Spinal Cord Stimulation

---

In addition to the soft spinal cord implant, a series of bipolar EMG wires are implanted chronically in order to monitor muscle response. The teflon-coated, stainless steel wires are placed on top of the spinodeltoideus, biceps brachii, the triceps brachii, the extensor carpi ulnaris, the extensor carpi radialis, and/or the extensor digitorum communis muscles and secured in place using non-dissolvable sutures. All wires are routed to a percutaneous head-plug fixed next to the omnetics connector using dental cement.

After baseline recordings, animals received a unilateral cervical spinal cord injury. A controlled hemicontusion (200kdynes) was delivered to the C5 spinal segment following partial a laminectomy over the target. The injury was performed using a IH impactor (Precision Systems and Instrumentation) on the side of the dominant forelimb, as pre-determined during training in push/pull tasks.

**Kinematic and EMG recordings** In order to characterize the effectiveness of the EES therapy, the animals are placed in a neurorobotic platform[140] combining the recording of forelimb kinematic and electromyographic activity. The forces applied during the push/pull tasks are measured using a 6-axis load cell (Nano17, ATI Industrial Automation, USA) mounted on the articulated arm of the robot. Two Hall effect position sensors (A1301, Allegro Microsystems) and a piezoelectric element are included in order to detect the extremities of the movement on the x axis and to signal to the animal the completion of each trial. In the context of this pilot experiment, two rats were trained to use the neurorobotic platform over a period of six weeks. One of these rats was trained to perform an unassisted pulling task, whilst the other rat was trained to perform an unassisted pushing task. Once training was completed, both animals received a cervical hemicontusion and were implanted with a cervical spinal cord implant and EMG electrodes. At 6, 7, 8, and 9 days post-injury, both rats performed their respective unassisted tasks under a variety of different stimulation conditions and with no stimulation. To study the specific effects of targeted stimulation on the capacity to push or pull the robot arm, the maximum force peak generated by the rat was calculated for each trial.

The EMG signals are amplified and passband filtered (10-1000Hz) through a differential AC amplifier (A-M Systems) before being recorded using a commercial data acquisition system (PowerLab 8/35, AD Instruments). The collected recordings are subsequently analyzed online using a custom MatLab script.

**Impedance spectroscopy** In-vitro EIS is performed using a potentiostat (Autolab PG-STAT128N, Metrohm) in a 3-electrode configuration. The Ag/AgCl reference electrode, platinum counter electrode and implant under test (working electrode) are immersed in PBS (1x) and the impedance spectrum is measured between 0.1Hz and 500kHz using an input signal amplitude of 100mV (root-mean-square).

In-vivo EIS data are collected using a portable potentiostat (Reference 600, Gamry Instru-



ments) in a 2-electrode configuration with the reference and counter channels shorted together and connected to the ground wire of the implant. The impedance spectrum is measured between 0.1Hz and 1MHz using an input signal amplitude of 100mV (root-mean-square). A breakout PCB connected to the Omnetics head-plug allows easy access to the individual channels.

**Chronopotentiometry** In-vitro voltage transients (VTs) are measured in PBS (1x) upon the application of symmetric, biphasic, cathodic-first, current pulses between the electrode under test and a platinum counter electrode. The pulses amplitude is set to 100 $\mu$ A and their duration to 600 $\mu$ s (300 $\mu$ s/phase), with an inter-pulse period of 10ms. The resulting VTs are collected via an oscilloscope (MDO3014, Tektronix) connected across the two poles of the current pulse generator (ISP2100, A-M Systems).

In-vivo VTs are collected using the same setup but this time with the counter electrode connected with the ground wire of the implant. A breakout PCB connected to the Omnetics head-plug allows easy access to the individual channels.

## 5.3 Results & Discussion

**Upper-limb activation** The impaired postural control resulting from severe SCI presents a significant obstacle in the assessment of EES as a neurorehabilitation tool. Indeed, rats having undergone hemicontusion at the cervical level are not able to maintain a well-balanced posture, as necessary to perform push/pull sequences. Here, the use of a state-of-the-art neurorobotic platform [140] allows to map the muscle responses to EES protocols under well-controlled conditions, with adequate postural support of the body and upper-limbs, and without confounding behavioral factors.

In order to determine the effect of each stimulating electrode, a comprehensive mapping of the relationships between the location of EES and the recruitment of upper-limb muscles is performed. To do so, 200 $\mu$ s biphasic current pulses are delivered at a frequency of 1 Hz with gradually increasing intensities up to 500 $\mu$ A. The current pulses are injected using an isolated pulse stimulator (Model 2100, AM systems, USA) and the resulting EMG responses are amplified, filtered, recorded, and visualized as previously described. During these sessions experimenter observations are made of which muscles were recruited first and which muscles seemed to be responding most at each electrode position. Offline analysis allows to calculate recruitment curves for each muscle, with data normalized to the maximal response evoked for each muscle using its optimal electrode on the array. The resulting motor neuron activation maps reveals the relationship between each electrode/EES parameters and the activation of specific muscles (fig. 5.4C). Compared to other electrodes, EES delivered through channel 1 leads to larger EMG responses from the muscles associated with the push/pull motion. Based

on this information, continuous, targeted stimulation can be applied, resulting in a larger forces compared to trials without EES or with mistargeted EES.

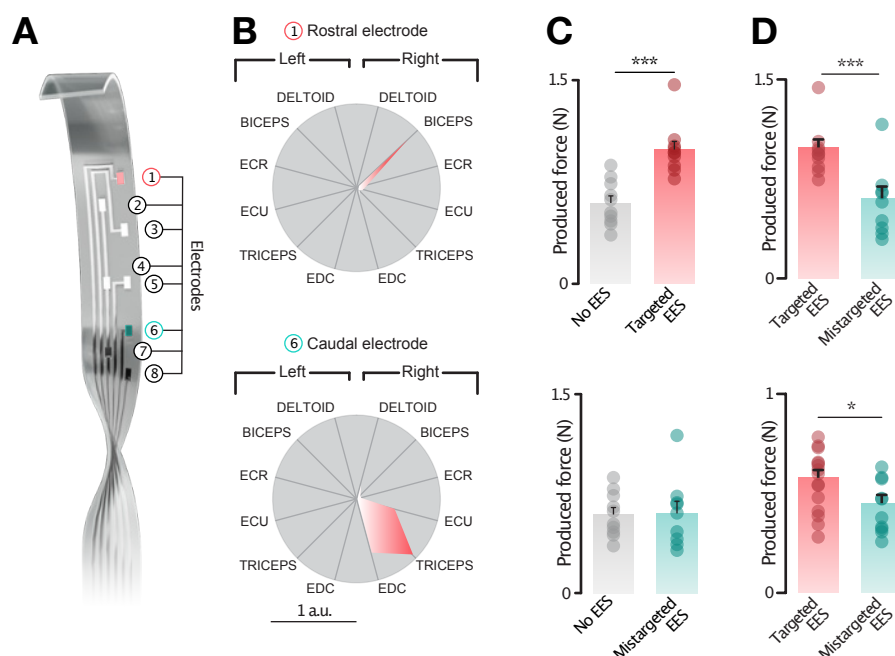


Figure 5.3: Upper-limb activation following SCI using targeted EES. Adapted from [140], courtesy of Dr. Nicholas James. **A** The custom-designed spinal cord implant allows selective targeting of specific motor neuron populations. **B** Polar plots showing the relative activation of each upper limb muscle with targeted EES (electrode 1 vs. 6). ECR, Extensor carpi radialis (wrist abduction); ECU, extensor carpi ulnaris (wrist adduction); EDC, Extensor digitorum communis. **C** Bar plot reporting the produced force without EES, with targeted EES and with mistargeted EES (electrode targeting a different muscle). Data are presented as mean  $\pm$  s.e.m. ( $n = 20$  trials); \*\*\* $p < 0.001$  (Kruskal-Wallis test). **D** Compared to mistargeted EES, EES delivered through the electrode (red) targeting the muscle involved in the movement (pulling versus pushing) leads to increase in produced force, as reported in bar plots. Data are presented as mean  $\pm$  s.e.m. ( $n = 20$  trials); \* $p < 0.05$ , \*\*\* $p < 0.001$  (Kruskal-Wallis test).

Next, a feedback loop is implemented in order to triggered EES bursts targeting tricep or biceps motor neurons based on the detection of the relevant muscle activity while the rats are attempting to perform reach or retrieval movements (fig. 5.4F). This activity-dependent stimulation protocol enables the production of significantly larger force than continuous stimulation (Fig. 8G,H). These results demonstrate that activity-dependent control of EES augments the volitional activation of motor neurons innervating upper-limb muscles, effectively allowing rats with SCI to regain the ability to produce force.

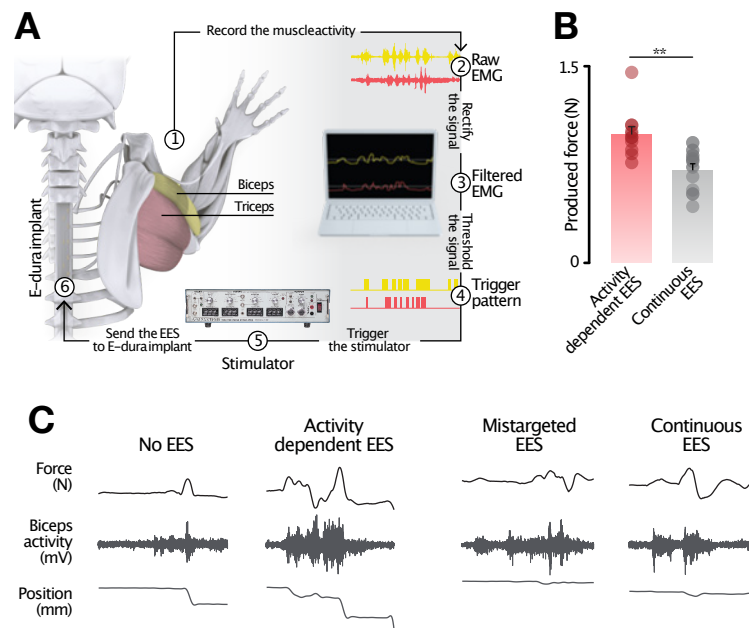


Figure 5.4: Activity-dependent stimulation of upper-limb motor neurons. Adapted from [140], courtesy of Dr. Nicholas James. **A** Schematic showing how detection of muscle activity triggers bursts of EES targeting the activated muscle. This activity-dependent stimulation protocol augments muscle activation. **B** Bar plots reporting the produced force during activity-dependent EES significantly versus continuous EES. Data are presented as mean  $\pm$  s.e.m. ( $n=20$  trials);  $**p<0.01$  (Kruskal-Wallis test). **C** Representative raw force, biceps muscle activity, and wrist position traces for each of the different stimulation protocols.

**Functionality over time** In order to assess the functionality of the soft cervical implants over time, chronopotentiometric measurements and electroimpedance spectrometry are performed at various points throughout the experimental campaign. In total, six animals were implanted with a soft spinal cord array. Figure 5.5 presents the average voltage drop over time for each of them. As expected, the required voltage to inject the same current pulse increases over time, reaching a maximum of 13.5V after 16 days. The evolution of the VTs is mostly driven by the increase in the access voltage  $V_A$ , which describes the contribution of the surrounding medium and the track. Therefore, the gradual decline in performances should be understood to originate from either: (1) the build-up of fibrotic tissue around the implant or (2) the onset of the interconnects electromechanical failure or (3) a combination of the two.

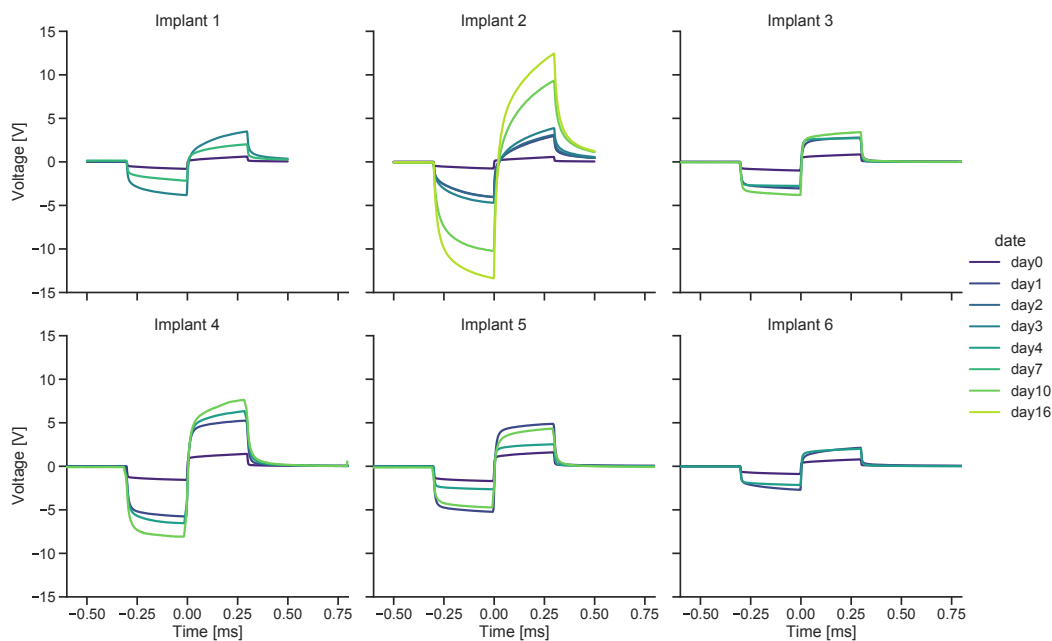


Figure 5.5: Evolution of the voltage transient for each implanted array. Day 0 corresponds to in-vitro measurements in PBS.

In addition to the electrodes, test structures were implemented on the soft cervical implant in order to help detect potential failure points. These structures consist of blind tracks terminated at a key location on the device and destined to verify the hermeticity of the FlexComb connector (fig 5.6A). The first two tracks (T1 and T2), are routed on each side of the custom-designed flexible PCB and are meant to monitor the potential delamination of the board layers. The third track (T3) stops at the level of the FlexComb "fingers" and can thus be used to check the strength of the encapsulation at this location. At each time point, a biphasic current pulse ( $100\mu\text{A}$ ,  $300\mu\text{s}$ ) is injected between the blind tracks and the ground wire. The resulting voltage drop is reported in figure 5.6B for a period of 16 days. There, it can be observed that the voltage drops of T1 and T2 remain

steady at 50V, which corresponds to the compliance of the stimulator. These values indicate that the dielectric properties of the custom flexible PCB remain stable throughout the whole implantation period. On the other hand, the voltage drop measured between T3 and the ground wire decreases steadily over time, reaching a minimum of 16V. This behavior points towards a failure of the silicone encapsulation via the diffusion of ionic species inside the material. The rapid pace of the degradation is likely a due to the fact that no silicone over-molding is performed at the back of the FlexComb connector, leaving only 40 $\mu$ m of PDMS as a moisture barrier (fig ??).

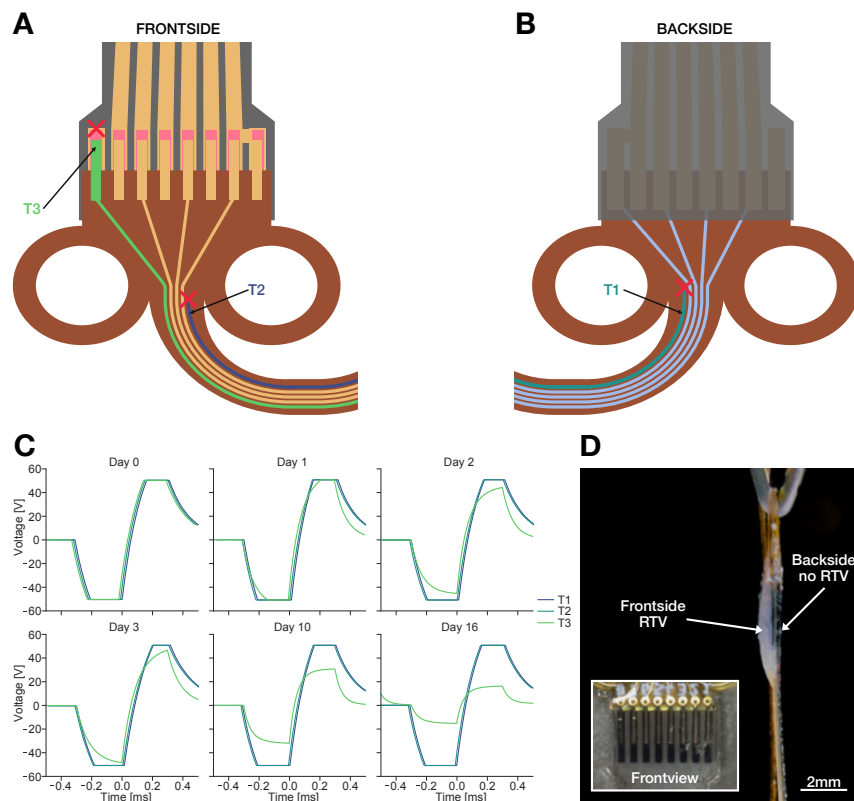


Figure 5.6: Functionality assessment based on dedicated test structures inside the device. **A-B** Schematic representation of the test structure implemented on the frontside (**A**) and backside (**B**) of the FlexComb connector. T1 and T2 are blind tracks ending inside the custom flexible PCB. T3 leads to one of the Pt-PDMS "well" used to transition from the connector to the soft electrode array. **C** Evolution of the applied voltage upon the injection of a 100 $\mu$ A current pulse between the test tracks and the ground wire. The curves for T1 and T2 overlap across the whole timeline, reaching consistently a value of 50V (stimulator compliance voltage). The voltage across T3 and ground decreases over time, an indication that the encapsulation is failing at this level. **D** Sideview of the transition area between the FlexComb connector and the soft electrode. The addition of RTV only on a single side could explain the early voltage decrease in the T3 test structure. Inset: frontview of the FlexComb connector.

The periodic measurement of impedance in-vivo proved to be more challenging than anticipated. Due to a number of external factors, including environmental electrical noise, intermittent failure of the equipment and safety concern for the animal, meaningful impedance spectrum could not always be measured. Consequently, abhorrent data had to be discarded manually by the experimenter based on the shape of the impedance spectrum, in particular the phase, and the corresponding VT measurements. The compiled impedance spectra over a period of 10 days is shown in figure 5.7. The initial jump in impedance, from in-vitro (day 0) to in-vivo (day 1), originates from the change in medium (from PBS to tissue) and from potential damages to the implant during implantation. At day 4, the impedance has decreased, which is likely a consequence of the tissue settling around the implant. At day 10, the impedance increases again. At this stage, the animal has performed 4 rounds of behavioral tasks, an activity which involves large strain at the level of the cervical spinal cord due to the animal reaching forward with its head to obtain food rewards. As a result, the increase in impedance could be understood as the onset of mechanical fatigue in the stretchable interconnects.

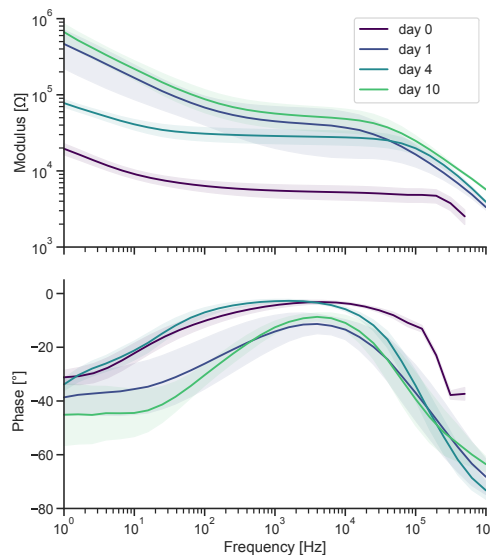


Figure 5.7: Compiled impedance spectra of the soft spinal cord implants at day 0 (in-vitro), 1 (intra-op), 4 and 10. The shaded area corresponds to half the standard deviation.

At day 12, rats implanted with array 3, 4 and 5 were terminally anesthetized in order to proceed with the histological analysis. The animals implanted with array 1 and 6 had to be sacrificed prior to that point due to infection, while the one with device 2 was kept until day 23, at which point all VTs reached the stimulator compliance and the experiment was terminated. Unfortunately, no device could be explanted in working conditions in order to compare performances before and after implantation. The techniques employed to secure to implant in place, namely dental cement on the caudal end and silicone adhesive on the rostral end, did not allow to extract the implants without destroying them.

## 5.4 Conclusion

**Summary** This chapter introduces a soft electrode paddle tailor-made for the stimulation of the cervical spinal cord of rodents. The electrical layout of the device has been optimized based on histological data in order to precisely target the dorsal root located between segments T1 and C3. Compared to the core-shell micropatterned devices presented previously, the thickness of the device has been reduced down to 80 $\mu$ m, in order to accommodate for the limited space available between the spinal cord and the vertebrae at the cervical level.

In this pilot experiment, the implant is used in conjunction with a neurorobotic platform in order to assess EES as a therapeutic tool for the restoration of upper-limb functions following SCI. A comprehensive motor neuron activation map is successfully established, revealing the relationship between each EES location and the recruitment of specific upper-limb muscles. This information is then used to perform targeted EES in rats having undergone SCI, thus demonstrating increased force production compared to control experiments without EES or with mistargeted EES. Finally, the implant is integrated in a feedback loop in order to perform stimulation based on the detection of motor intents. Using this setup, it is shown that activity-dependent EES augments the volitional activation of motor neurons innervating upper-limb muscles.

From a technological perspective, the micropatterns-based spinal cord implants were able to maintain functionality for up to 16 days in-vivo. In order to quantify the performances of the soft cervical implants over time, chronopotentiometric measurements and electroimpedance spectrometry were performed throughout the experimental campaign. The voltage required to inject a 100 $\mu$ A current pulse is found to increase from 5V intra-operatively to 13.5V after 16 days. This change is believed to originate from the formation of a fibrotic encapsulation around the implant combined with mechanical fatigue of the interconnects. Surprisingly, the in-vivo impedance spectrum is shown to decrease within the first few days following implantation before starting to increase. The initial reduction is attributed to the tissue settling around the implant post-operatively, while the subsequent augmentation is explained by the same mechanisms as for the VT increase. Finally, the injection of current through a set of blind tracks reveals a potential failure point in the silicone encapsulation at the level of the transition between the FlexComb connector and the soft electrode array.

**Outlook** This study provided another scientifically meaningful context in which to assess the core-shell micropatterns technology. The design and fabrication of soft spinal cord implant demonstrated once more the versatility of the manufacturing process. Here, the freedom of design is leveraged to seamlessly tailor the electrical layout of the device based on histological data. The implementation of a custom FlexComb connector provided the means to anchor and interface with the array with a single component.

The soft spinal cord implant was able to successfully deliver targeted electrical stimuli for up to 16 days. During that time, the implant was used to selectively activate the upper-limb muscles involved in a reach and retrieve sequences, effectively allowing rodents with SCI to regain the ability to produce force. With regard to the performances of the devices, the constraints imposed by spinal cord stimulation might still be out of reach for the current iteration of the micropattern technology. With voltages approaching 16V after two weeks, the implants had already exceeded the theoretical compliance of med-grade implantable pulse generator (10-15V). If this early trend is any indication, it is most likely that, within a month, the implants will either have exceeded the compliance of most bench-top stimulators (50V). A straightforward way to prolong the lifespan of the device would be to implement interconnects with a lower initial resistance. In that regard, the narrowness of the spinal cord anatomy does not permit to design wider tracks. An another solution would be to increase the thickness of the metallization, however in the case of the spinal cord, the mechanical constraints are such that the consequent decrease in stretchability might be unacceptable. As a result, the development of a truly chronic cervical implant is likely to require a re-optimization of the Y-shape motif.

From a technological perspective, the study was unfortunately too short to assess the long-term implications in terms of bio-integration and electromechanical performances of the technology. In particular, the limited timeframe did not allow to fully explore the potential ramifications of the silicone encapsulation failure observed at the transition between the FlexComb and the soft electrode array. While the collected data demonstrate the expected trends, the structure of the experiment did not allow to decouple the different mechanisms leading to these results. Future studies should aim to not only prolong the implantation period, but also to combine in-vivo results with data from anatomically realistic in-vitro models. The inclusion of measurements obtained from robotic ageing platform such as the one presented by Schiavone et al in ?? would provide a controlled environment with which to compare in-vivo observations. The cross-examination of the results could then be used to isolate specific failure modalities to drive technological development in a more quantitative way.



## 6 General Discussion and Outlook

### 6.1 Discussion

**Micropatterned core-shell interconnects** This thesis introduces new methods and approaches for the reliable manufacturing of soft neural interfaces for both recording and stimulation. The stretchable interconnects technology that enables the device to conform intimately with the surface of the tissue is based on a so-called kirigami approach. This fundamental idea consists of creating reversibly stretchable structures by performing periodic cuts into normally inelastic films. Here, Y-shaped motifs are etched through a multilayer stack of polyimide, platinum, polyimide in order to enable in- and out-of-plane deformations. The novelty presented in this thesis consists of patterning the conductive and dielectric layers in two separate steps with a slightly different version of the base motif. This effectively allows the conductive (core) and dielectric (shell) layers to perfectly interlock inside each other, enabling full encapsulation of the metallic layers. This new microstructuring strategy, dubbed core-shell, required several technological innovations with regard to the transfer of the Y-shaped motifs, including the transition to a new photoresist and the optimization of the pattern geometry to offset the losses in critical dimensions. These improvements allowed the manufacturing of stretchable interconnects with superior electrical properties with extended barrier lifetimes: compared to the first generation of micropatterned devices, the core-shell structure allows to decrease mechanical fatigue by a factor of 25 and to reduce the leakage current by an order of magnitude after 21 days of accelerated ageing (at 67°C). This substantial increase in performances was enabled by both the complete encapsulation of the conductive layer inside the polyimide and the extension of the elastic regime from 10% to 15% strain.

In regards to the microfabrication process, future work should focus on developing a new silicone encapsulation strategy. Indeed, the current method, based of oxygen plasma bonding, leads to the presence of air gaps between the meanders of the Y-shaped motifs. It is likely that these voids are, currently, the single greatest contributor

to the increase in leakage current over time. In that regard, an alternative process was suggested (upside-down process) which would allow the direct overmolding of the micropatterned stack. It remains to be seen however, how filling these spaces between the meanders would affect the mechanical behavior of the Y-shaped motifs. Another aspect that remained unexplored with regard to encapsulation is the integration of high-performance encapsulation materials as part of the shell layer. The most promising candidate is silicon carbide (SiC), due to its exceptional moisture barrier properties and its ability to bind with polyimide via the creation of strong carbide bonds. A potential issue is that most hermetic thin films still require to be several hundreds of nanometer thick in order to form a pin-hole free layers. Combined with the fact that these materials are often extremely stiff ( $E_{\text{SiC}} = 400\text{GPa}$ ), it is therefore likely that their integration will significantly alter the mechanical behavior of the micropatterned interconnects. To address this potential issue, the Y-shaped motif could be re-optimized in order to reduce the apparent elastic modulus and thus compensate for the integration of stiffer materials.

Similarly, the Y-shape geometry could be tuned within the device itself in order to change the local electromechanical properties of the interconnect. This principle could be leveraged to form strain gradients around rigid components ( $\mu\text{LED}$ , bare dies, etc.) in order to prevent stress concentration at the interface. Alternatively, variations in the Y-shape geometrical parameters could be used to tune the local resistivity of the device. By carefully optimizing the local elasticity vs. resistivity trade-off based on the expected strain in different part of the device, the overall resistance of the interconnects could be minimized. This level of optimization could prove critical to the development of an implant compatible with clinical IPG. Indeed, fully implantable IPG are limited to a voltage compliance of 10 to 15V which places a stringent requirements on the maximum allowable impedance for the electrode array. Since the development of a more powerful IPG would be cost prohibitive, the engineering effort has to be placed on reducing the resistance of the interconnects instead.

From a translational perspective, the deployment of the core-shell micropatterns technology in humans will require the transition to medical grade materials. In that regard, there exist numerous medical grade silicone that could serve as potential carrier (e.g. NuSil MED-6216), however extensive mechanical testing should be carried out in order to assess their potential effects on the Y-shapes mechanics as well as their ability to strongly adhere to  $\text{SiO}_2$  via oxygen plasma bonding. As of now, polyimide has found limited access to the clinical for long-term implantation with the exception of devices such as the IMS-alpha retinal implant (Reuligen, Germany) which holds the CE mark, the Aleva (Switzerland) DirectSTN DBS electrode or the NeuroOne subdural electrode (USA) among others. It is, however, the material of choice in current academic research and it is therefore only a matter of time before it get more accepted with regulatory bodies and with the broader adoption of microfabricated neural interfaces. In addition to the material constituting the device, attention should also be given to the chemical that en-

ter in contact with it. For example, it should be verified through a bioburden study that the different photoresists used in the fabrication process do not leach in or out of the implant, a phenomenon which could lead to adverse effects.

### Applications in vivo of soft implants

The core-shell micropattern technology presented in chapter 2 of this thesis was used to investigate the potential benefits of a soft auditory brainstem implant (ABI) to restore hearing in a non-human primate model. In the context of this project, two neural interfaces were built and implanted in a single animal: a 28-channel  $\mu$ ECoG to record the activity of the auditory cortex and an 11-channel ABI devised for the stimulation of the cochlear nucleus. By now, the  $\mu$ ECoG has allowed to successfully capture auditory evoked potentials with frequency-specific distribution for a period of over 3 months. From these recordings, tonotopic maps could be constructed, allowing the granular analysis of the hearing response of the animal. This level of details contrasts starkly with the auditory brainstem responses (ABR) typically used in the clinic and which only give a rough indication of the functionality of the auditory pathway. Three months after the  $\mu$ ECoG implantation, a soft ABI was successfully implanted in the lateral recess of the fourth ventricle, in close contact with the cochlear nucleus. Two weeks post ABI implantation, we were able to record electrically evoked ABRs with the ECoG by stimulating several different electrodes in both monopolar and bipolar configuration on the cochlear nucleus. This effectively demonstrates the successful establishment of a chronic ABI primate model, a world first.

In terms of future improvements, it is critical that a system be devised in order to improve the anchoring of the ABI. As it stands, the softness of the electrode paddle is both its greatest strength and weakness. While the bulky clinical array can be tucked inside the lateral recess with ease, the thinness of the soft ABI makes it a challenge to keep in place. A potential solution could be the implementation of a so-called dry tissue adhesive such as the one presented in [141]. Placed at key locations along the lengths of the electrode paddle, these anchoring points could provide mechanical stability required to ensure the soft ABI stays in place.

## 6.2 Outlook

**Next-generation long-lasting implantable interconnects** Looking ahead, the fabrication of a truly long-lasting neural interface will require the key technological development with regard to interconnects conductivity, hermeticity and system integration. As discussed above, the single greatest limitation for thin film devices is the limited voltage compliance of clinical IPGs instead of macroscopic wires as is the case in current clinical devices. Modulating the stretchability in favor of more conductivity can offset

the limited compliance of the IPG. Furthermore connecting from the thin film device to feedthroughs on the titanium case will require developments of new bonding strategies that can both connect a myriad of connections over a small area in an hermetic fashion. Solutions such as flip chip bonding, wire bonding or soldering can be adapted to this use case but will require extensive testing to guarantee long-term reliability once implanted. Other implant types using thin film technologies as cited above have tackled these challenges and can be reproduced with the conformable electrode arrays presented here.

### **Future translation of soft ABIs to the clinic**

With the primate model established in this work, several iterations of the technology and the experimental paradigm will enable the validation of the soft ABI for restoring high quality hearing sensations. In a next logical step, the device can be translated to humans. In a first step, the device could be validated in an acute setting in awake conditions during auditory nerve tumor resections or regular ABI implantations . Placing the soft ABI over the cochlear nucleus and eliciting responses from the stimulation of the brainstem will enable the tailoring of the implant geometry to optimize the hearing percepts. The only drawback to this approach is the fact that in ABI patients, the hearing perception improves over time both due to learning and neural plasticity. In a second phase when the implant is optimized and integrated with an IPG in a pilot study, comparison to clinical rigid ABI electrodes can then be made in terms of amount of side-effects, stability of the technology, anchoring stability of the array over the cochlear nucleus and ultimately the capability to restore high quality hearing.

## Bibliography

- [1] R. B. North, D. H. Kidd, M. Zahurak, C. S. James, and D. M. Long. Spinal cord stimulation for chronic, intractable pain: experience over two decades. *Neurosurgery*, 32(3):384–394; discussion 394–395, March 1993.
- [2] Joel S. Perlmutter and Jonathan W. Mink. Deep brain stimulation. *Annual Review of Neuroscience*, 29:229–257, 2006.
- [3] Fan-Gang Zeng. Trends in Cochlear Implants. *Trends in Amplification*, 8(1):1–34, December 2004. Publisher: SAGE Publications.
- [4] Aleksandra V. Rachitskaya and Alex Yuan. Argus II retinal prosthesis system: An update. *Ophthalmic Genetics*, 37(3):260–266, September 2016.
- [5] Tong Yang, Shahin Hakimian, and Theodore H. Schwartz. Intraoperative ElectroCorticoGraphy (ECog): indications, techniques, and utility in epilepsy surgery. *Epileptic Disorders*, 16(3):271–279, September 2014.
- [6] William S. Anderson, Eric H. Kossoff, Gregory K. Bergey, and George I. Jallo. Implantation of a responsive neurostimulator device in patients with refractory epilepsy. *Neurosurgical Focus*, 25(3):E12, September 2008.
- [7] Brian Lee, Muhammad N. Zubair, Yvette D. Marquez, David M. Lee, Laura A. Kalayjian, Christianne N. Heck, and Charles Y. Liu. A Single-Center Experience with the NeuroPace RNS System: A Review of Techniques and Potential Problems. *World Neurosurgery*, 84(3):719–726, September 2015.
- [8] Xi Wang, C. Alexis Gkogkidis, Olga Iljina, Lukas D. J. Fiederer, Christian Henle, Irina Mader, Jan Kaminsky, Thomas Stieglitz, Mortimer Gierthmuehlen, and Tonio Ball. Mapping the fine structure of cortical activity with different micro-ECoG electrode array geometries. *Journal of Neural Engineering*, 14(5):056004, August 2017. Publisher: IOP Publishing.
- [9] Jae-Woong Jeong, Gunchul Shin, Sung Il Park, Ki Jun Yu, Lizhi Xu, and John A. Rogers. Soft Materials in Neuroengineering for Hard Problems in Neuroscience. *Neuron*, 86(1):175–186, April 2015.

## Bibliography

---

- [10] Dimiter Prodanov and Jean Delbeke. Mechanical and Biological Interactions of Implants with the Brain and Their Impact on Implant Design. *Frontiers in Neuroscience*, 10, 2016.
- [11] Shaokoon Cheng, Elizabeth C. Clarke, and Lynne E. Bilston. Rheological properties of the tissues of the central nervous system: A review. *Medical Engineering & Physics*, 30(10):1318–1337, December 2008.
- [12] Alain Goriely, Marc G. D. Geers, Gerhard A. Holzapfel, Jayaratnam Jayamohan, Antoine Jérusalem, Sivabal Sivaloganathan, Waney Squier, Johannes A. W. van Dommelen, Sarah Waters, and Ellen Kuhl. Mechanics of the brain: perspectives, challenges, and opportunities. *Biomechanics and Modeling in Mechanobiology*, 14(5):931–965, October 2015.
- [13] Deed E. Harrison, Rene Cailliet, Donald D. Harrison, Stephan J. Troyanovich, and Sanghak O. Harrison. A review of biomechanics of the central nervous system—part III: Spinal cord stresses from postural loads and their neurologic effects. *Journal of Manipulative and Physiological Therapeutics*, 22(6):399–410, July 1999.
- [14] David E. Koser, Emad Moeendarbary, Janina Hanne, Stefanie Kuerten, and Kristian Franze. CNS Cell Distribution and Axon Orientation Determine Local Spinal Cord Mechanical Properties. *Biophysical Journal*, 108(9):2137–2147, May 2015.
- [15] Andreas F. Christ, Kristian Franze, Helene Gautier, Pouria Moshayedi, James Fawcett, Robin J. M. Franklin, Ragnhildur T. Karadottir, and Jochen Guck. Mechanical difference between white and gray matter in the rat cerebellum measured by scanning force microscopy. *Journal of Biomechanics*, 43(15):2986–2992, November 2010.
- [16] Silvia Budday, Richard Nay, Rijk de Rooij, Paul Steinmann, Thomas Wyrobek, Timothy C. Ovaert, and Ellen Kuhl. Mechanical properties of gray and white matter brain tissue by indentation. *Journal of the Mechanical Behavior of Biomedical Materials*, 46:318–330, June 2015.
- [17] Stéphanie P. Lacour, Grégoire Courtine, and Jochen Guck. Materials and technologies for soft implantable neuroprostheses. *Nature Reviews Materials*, 1(10):16063, October 2016.
- [18] L. White. Structure of the human sensorimotor system. I: Morphology and cytoarchitecture of the central sulcus. *Cerebral Cortex*, 7(1):18–30, January 1997.
- [19] Jane Bradbury. Molecular Insights into Human Brain Evolution. *PLoS Biology*, 3(3):4, 2005.
- [20] Mark E. Wagshul, Per K. Eide, and Joseph R. Madsen. The pulsating brain: A review of experimental and clinical studies of intracranial pulsatility. *Fluids and Barriers of the CNS*, 8(1):5, January 2011.

- [21] John K. Hermann and Jeffrey R. Capadona. Understanding the Role of Innate Immunity in the Response to Intracortical Microelectrodes. *Critical reviews in biomedical engineering*, 46(4):341–367, 2018.
- [22] Vadim S. Polikov, Patrick A. Tresco, and William M. Reichert. Response of brain tissue to chronically implanted neural electrodes. *Journal of Neuroscience Methods*, 148(1):1–18, October 2005.
- [23] James C. Barrese, Juan Aceros, and John P. Donoghue. Scanning electron microscopy of chronically implanted intracortical microelectrode arrays in non-human primates. *Journal of Neural Engineering*, 13(2):026003, January 2016. Publisher: IOP Publishing.
- [24] I. R. Mineev, P. Musienko, A. Hirsch, Q. Barraud, N. Wenger, E. M. Moraud, J. Gandar, M. Capogrosso, T. Milekovic, L. Asboth, R. F. Torres, N. Vachicouras, Q. Liu, N. Pavlova, S. Duis, A. Larmagnac, J. Voros, S. Micera, Z. Suo, G. Courtine, and S. P. Lacour. Electronic dura mater for long-term multimodal neural interfaces. *Science*, 347(6218):159–163, January 2015.
- [25] Seongjun Park, Hyunwoo Yuk, Ruike Zhao, Yeong Shin Yim, Eyob W. Woldeghebriel, Jeewoo Kang, Andres Canales, Yoel Fink, Gloria B. Choi, Xuanhe Zhao, and Polina Anikeeva. Adaptive and multifunctional hydrogel hybrid probes for long-term sensing and modulation of neural activity. *Nature Communications*, 12(1):3435, June 2021. Number: 1 Publisher: Nature Publishing Group.
- [26] Dongjin Seo, Ryan M. Neely, Konlin Shen, Utkarsh Singhal, Elad Alon, Jan M. Rabaey, Jose M. Carmena, and Michel M. Maharbiz. Wireless Recording in the Peripheral Nervous System with Ultrasonic Neural Dust. *Neuron*, 91(3):529–539, August 2016.
- [27] John A. Rogers, Roozbeh Ghaffari, and Dae-Hyeong Kim, editors. *Stretchable Bioelectronics for Medical Devices and Systems*. Microsystems and Nanosystems. Springer International Publishing, Cham, 2016.
- [28] Maria Francisca Porto Cruz, Maria Vomero, Elena Zucchini, Emanuela Delfino, Maria Asplund, Thomas Stieglitz, and Luciano Fadiga. Can Crosstalk Compromise the Recording of High-Frequency Neural Signals? In *2019 9th International IEEE/EMBS Conference on Neural Engineering (NER)*, pages 924–927, March 2019. ISSN: 1948-3554.
- [29] A Vanhoestenbergh and N Donaldson. Corrosion of silicon integrated circuits and lifetime predictions in implantable electronic devices. *Journal of Neural Engineering*, 10(3):031002, June 2013.
- [30] Konlin Shen and Michel M Maharbiz. Ceramic packaging in neural implants. *Journal of Neural Engineering*, 18(2):025002, April 2021.

- [31] D R Enzmann and N J Pelc. Brain motion: measurement with phase-contrast MR imaging. *Radiology*, 185(3):653–660, December 1992. Publisher: Radiological Society of North America.
- [32] D.A. Robinson. The electrical properties of metal microelectrodes. *Proceedings of the IEEE*, 56(6):1065–1071, June 1968.
- [33] Qianru Yang, Bingchen Wu, James R. Eles, Alberto L. Vazquez, Takashi D. Y. Kozai, and X. Tracy Cui. Zwitterionic Polymer Coating Suppresses Microglial Encapsulation to Neural Implants In Vitro and In Vivo. *Advanced Biosystems*, 4(6):1900287, 2020. \_eprint: <https://onlinelibrary.wiley.com/doi/pdf/10.1002/adbi.201900287>.
- [34] Adrian Onken, Helmut Schütte, Anika Wulff, Heidi Lenz-Strauch, Michaela Kreienmeyer, Sabine Hild, Thomas Stieglitz, Stefan Gassmann, Thomas Lenarz, and Theodor Doll. Predicting Corrosion Delamination Failure in Active Implantable Medical Devices: Analytical Model and Validation Strategy. *Bioengineering*, 9(1):10, January 2022. Number: 1 Publisher: Multidisciplinary Digital Publishing Institute.
- [35] Paul Čvančara, Tim Boretius, Víctor M. López-Álvarez, Pawel Maciejasz, David Andreu, Stanisa Raspopovic, Francesco Maria Petrini, Silvestro Micera, Giuseppe Granata, Eduardo Fernandez, Paolo Maria Rossini, Ken Yoshida, Winnie Jensen, Jean-Louis Divoux, David Guiraud, Xavier Navarro, and Thomas Stieglitz. Stability of flexible thin-film metallization stimulation electrodes: analysis of explants after first-in-human study and improvement of *in vivo* performance. *Journal of Neural Engineering*, June 2020.
- [36] Moritz Doering, Jochen Kieninger, Gerald A Urban, and Andreas Weltin. Electrochemical microelectrode degradation monitoring: in situ investigation of platinum corrosion at neutral pH. *Journal of Neural Engineering*, 19(1):016005, February 2022.
- [37] Suji Choi, Hyunjae Lee, Roozbeh Ghaffari, Taeghwan Hyeon, and Dae-Hyeong Kim. Recent Advances in Flexible and Stretchable Bio-Electronic Devices Integrated with Nanomaterials. *Advanced Materials*, 28(22):4203–4218, 2016. \_eprint: <https://onlinelibrary.wiley.com/doi/pdf/10.1002/adma.201504150>.
- [38] Thomas Stieglitz, Tim Boretius, Juan Ordonez, Christina Hassler, Christian Henle, Wolfgang Meier, Dennis T. T. Plachta, and Martin Schuettler. Miniaturized neural interfaces and implants. In *Microfluidics, BioMEMS, and Medical Microsystems X*, volume 8251, pages 77–88. SPIE, February 2012.
- [39] Daniel R. Kramer, Morgan B. Lee, Michael F. Barbaro, Angad S. Gogia, Terrance Peng, Charles Y. Liu, Spencer Kellis, and Brian Lee. Mapping of primary somatosensory cortex of the hand area using a high-density electrocorticography grid for closed-loop brain computer interface. *Journal of Neural Engineering*, 18(3):036009, March 2021. Publisher: IOP Publishing.



- [40] Guillaume Petit-Pierre, Philippe Colin, Estelle Laurer, Julien Déglon, Arnaud Bertsch, Aurélien Thomas, Bernard L. Schneider, and Philippe Renaud. In vivo neurochemical measurements in cerebral tissues using a droplet-based monitoring system. *Nature Communications*, 8(1):1239, November 2017. Number: 1 Publisher: Nature Publishing Group.
- [41] Jokubas Ausra, Mingzheng Wu, Xin Zhang, Abraham Vázquez-Guardado, Patrick Skelton, Roberto Peralta, Raudel Avila, Thomas Murickan, Chad R. Haney, Yonggang Huang, John A. Rogers, Yevgenia Kozorovitskiy, and Philipp Gutruf. Wireless, battery-free, subdermally implantable platforms for transcranial and long-range optogenetics in freely moving animals. *Proceedings of the National Academy of Sciences*, 118(30):e2025775118, July 2021. Publisher: Proceedings of the National Academy of Sciences.
- [42] Luyao Lu, Philipp Gutruf, Li Xia, Dionnet L. Bhatti, Xinying Wang, Abraham Vazquez-Guardado, Xin Ning, Xinru Shen, Tian Sang, Rongxue Ma, Grace Pakeltis, Gabriel Sobczak, Hao Zhang, Dong-oh Seo, Mantian Xue, Lan Yin, Debashis Chanda, Xing Sheng, Michael R. Bruchas, and John A. Rogers. Wireless optoelectronic photometers for monitoring neuronal dynamics in the deep brain. *Proceedings of the National Academy of Sciences*, 115(7):E1374–E1383, February 2018. Publisher: Proceedings of the National Academy of Sciences.
- [43] Nikita Obidin, Farita Tasnim, and Canan Dagdeviren. The Future of Neuroimplantable Devices: A Materials Science and Regulatory Perspective. *Advanced Materials*, page 1901482, June 2019.
- [44] M. M. Swindle, A. Makin, A. J. Herron, F. J. Clubb, and K. S. Frazier. Swine as Models in Biomedical Research and Toxicology Testing. *Veterinary Pathology*, 49(2):344–356, March 2012. Publisher: SAGE Publications Inc.
- [45] Sandrine Camus, Wai Kin D. Ko, Elsa Pioli, and Erwan Bezard. Why bother using non-human primate models of cognitive disorders in translational research? *Neurobiology of Learning and Memory*, 124:123–129, October 2015.
- [46] Bert A. 't Hart, David H. Abbott, Katsuki Nakamura, and Eberhard Fuchs. The marmoset monkey: a multi-purpose preclinical and translational model of human biology and disease. *Drug Discovery Today*, 17(21):1160–1165, November 2012.
- [47] Julia Koch, Martin Schuettler, Cristian Pasluosta, and Thomas Stieglitz. Electrical connectors for neural implants: design, state of the art and future challenges of an underestimated component. *Journal of Neural Engineering*, July 2019.
- [48] Aaron K. Compton, Binit Shah, and Salim M. Hayek. Spinal Cord Stimulation: A Review. *Current Pain and Headache Reports*, 16(1):35–42, February 2012.

## Bibliography

---

- [49] J. L. Gbur and J. J. Lewandowski. Fatigue and fracture of wires and cables for biomedical applications. *International Materials Reviews*, 61(4):231–314, May 2016. Publisher: Taylor & Francis \_eprint: <https://doi.org/10.1080/09506608.2016.1152347>.
- [50] Sigurd Wagner and Siegfried Bauer. Materials for stretchable electronics. *MRS Bulletin*, 37(3):207–213, March 2012. Publisher: Cambridge University Press.
- [51] John A. Rogers, Takao Someya, and Yonggang Huang. Materials and Mechanics for Stretchable Electronics. *Science*, 327(5973):1603–1607, March 2010. Publisher: American Association for the Advancement of Science.
- [52] Dae-Hyeong Kim and John A. Rogers. Stretchable Electronics: Materials Strategies and Devices. *Advanced Materials*, 20(24):4887–4892, 2008. \_eprint: <https://onlinelibrary.wiley.com/doi/pdf/10.1002/adma.200801788>.
- [53] Chunyu Li, Erik T. Thostenson, and Tsu-Wei Chou. Dominant role of tunneling resistance in the electrical conductivity of carbon nanotube–based composites. *Applied Physics Letters*, 91(22):223114, November 2007. Publisher: American Institute of Physics.
- [54] Zongping Chen, Wencai Ren, Libo Gao, Bilu Liu, Songfeng Pei, and Hui-Ming Cheng. Three-dimensional flexible and conductive interconnected graphene networks grown by chemical vapour deposition. *Nature Materials*, 10(6):424–428, June 2011. Number: 6 Publisher: Nature Publishing Group.
- [55] Le Cai, Jinzhu Li, Pingshan Luan, Haibo Dong, Duan Zhao, Qiang Zhang, Xiao Zhang, Min Tu, Qingsheng Zeng, Weiya Zhou, and Sishen Xie. Highly Transparent and Conductive Stretchable Conductors Based on Hierarchical Reticulate Single-Walled Carbon Nanotube Architecture. *Advanced Functional Materials*, 22(24):5238–5244, 2012. \_eprint: <https://onlinelibrary.wiley.com/doi/pdf/10.1002/adfm.201201013>.
- [56] Alexandre Larmagnac, Samuel Eggenberger, Hanna Janossy, and Janos Vörös. Stretchable electronics based on Ag-PDMS composites. *Scientific Reports*, 4(1):7254, December 2014. Number: 1 Publisher: Nature Publishing Group.
- [57] Benjamin C.-K. Tee, Chao Wang, Ranulfo Allen, and Zhenan Bao. An electrically and mechanically self-healing composite with pressure- and flexion-sensitive properties for electronic skin applications. *Nature Nanotechnology*, 7(12):825–832, December 2012. Number: 12 Publisher: Nature Publishing Group.
- [58] T. S. Hansen, K. West, O. Hassager, and N. B. Larsen. Highly Stretchable and Conductive Polymer Material Made from Poly(3,4-ethylenedioxythiophene) and Polyurethane Elastomers. *Advanced Functional Materials*, 17(16):3069–3073, 2007. \_eprint: <https://onlinelibrary.wiley.com/doi/pdf/10.1002/adfm.200601243>.

- [59] Samuel Rosset, Muhamed Niklaus, Philippe Dubois, and Herbert R. Shea. Metal Ion Implantation for the Fabrication of Stretchable Electrodes on Elastomers. *Advanced Functional Materials*, 19(3):470–478, 2009. \_eprint: <https://onlinelibrary.wiley.com/doi/pdf/10.1002/adfm.200801218>.
- [60] Oliver Graudejus, Patrick Görrn, and Sigurd Wagner. Controlling the Morphology of Gold Films on Poly(dimethylsiloxane). *ACS Applied Materials & Interfaces*, 2(7):1927–1933, July 2010. Publisher: American Chemical Society.
- [61] St  phanie P  richon Lacour, Sigurd Wagner, Zhenyu Huang, and Z. Suo. Stretchable gold conductors on elastomeric substrates. *Applied Physics Letters*, 82(15):2404–2406, April 2003. Publisher: American Institute of Physics.
- [62] Ingrid M. Graz, Darryl P. J. Cotton, and St  phanie P. Lacour. Extended cyclic uniaxial loading of stretchable gold thin-films on elastomeric substrates. *Applied Physics Letters*, 94(7):071902, February 2009. Publisher: American Institute of Physics.
- [63] Yue Cao, Timothy G. Morrissey, Eric Acome, Sarah I. Allec, Bryan M. Wong, Christoph Keplinger, and Chao Wang. A Transparent, Self-Healing, Highly Stretchable Ionic Conductor. *Advanced Materials*, 29(10):1605099, 2017. \_eprint: <https://onlinelibrary.wiley.com/doi/pdf/10.1002/adma.201605099>.
- [64] Christoph Keplinger, Jeong-Yun Sun, Choon Chiang Foo, Philipp Rothmund, George M. Whitesides, and Zhiqiang Suo. Stretchable, Transparent, Ionic Conductors. *Science*, 341(6149):984–987, August 2013. Publisher: American Association for the Advancement of Science.
- [65] Ju-Hee So, Jacob Thelen, Amit Qusba, Gerard J. Hayes, Gianluca Lazzi, and Michael D. Dickey. Reversibly Deformable and Mechanically Tunable Fluidic Antennas. *Advanced Functional Materials*, 19(22):3632–3637, 2009. \_eprint: <https://onlinelibrary.wiley.com/doi/pdf/10.1002/adfm.200900604>.
- [66] Michael D. Dickey. Stretchable and Soft Electronics using Liquid Metals. *Advanced Materials*, 29(27):1606425, 2017. \_eprint: <https://onlinelibrary.wiley.com/doi/pdf/10.1002/adma.201606425>.
- [67] Hyunwoo Yuk, Baoyang Lu, Shen Lin, Kai Qu, Jingkun Xu, Jianhong Luo, and Xuanhe Zhao. 3D printing of conducting polymers. *Nature Communications*, 11:1604, March 2020.
- [68] Klas Tybrandt, Dion Khodagholy, Bernd Dielacher, Flurin Stauffer, Aline F. Renz, Gy  rgy Buzs  ki, and J  nos V  r  s. High-Density Stretchable Electrode Grids for Chronic Neural Recording. *Advanced Materials (Deerfield Beach, Fla.)*, 30(15):e1706520, April 2018.

- [69] Arthur Hirsch, Hadrien O. Michaud, Aaron P. Gerratt, Séverine de Mulatier, and Stéphanie P. Lacour. Intrinsically Stretchable Biphase (Solid–Liquid) Thin Metal Films. *Advanced Materials*, 28(22):4507–4512, 2016. \_eprint: <https://onlinelibrary.wiley.com/doi/pdf/10.1002/adma.201506234>.
- [70] Steven Nagels and Wim Deferme. Fabrication Approaches to Interconnect Based Devices for Stretchable Electronics: A Review. *Materials*, 11(3):375, March 2018. Number: 3 Publisher: Multidisciplinary Digital Publishing Institute.
- [71] Ned Bowden, Scott Brittain, Anthony G. Evans, John W. Hutchinson, and George M. Whitesides. Spontaneous formation of ordered structures in thin films of metals supported on an elastomeric polymer. *Nature*, 393(6681):146–149, May 1998. Number: 6681 Publisher: Nature Publishing Group.
- [72] S.P. Lacour, J. Jones, Z. Suo, and S. Wagner. Design and performance of thin metal film interconnects for skin-like electronic circuits. *IEEE Electron Device Letters*, 25(4):179–181, April 2004. Conference Name: IEEE Electron Device Letters.
- [73] Michael Drack, Ingrid Graz, Tsuyoshi Sekitani, Takao Someya, Martin Kaltenbrunner, and Siegfried Bauer. An Imperceptible Plastic Electronic Wrap. *Advanced Materials*, 27(1):34–40, 2015. \_eprint: <https://onlinelibrary.wiley.com/doi/pdf/10.1002/adma.201403093>.
- [74] D. S. Gray, J. Tien, and C. S. Chen. High-Conductivity Elastomeric Electronics. *Advanced Materials*, 16(5):393–397, 2004. \_eprint: <https://onlinelibrary.wiley.com/doi/pdf/10.1002/adma.200306107>.
- [75] Mario Gonzalez, Fabrice Axisa, Mathieu Vanden Bulcke, Dominique Brosteaux, Bart Vandevelde, and Jan Vanfleteren. Design of Metal Interconnects for Stretchable Electronic Circuits using Finite Element Analysis. In *2007 International Conference on Thermal, Mechanical and Multi-Physics Simulation Experiments in Microelectronics and Micro-Systems. EuroSime 2007*, pages 1–6, April 2007.
- [76] Fabrice Axisa, Frederick Bossuyt, Thomas Vervust, and Jan Vanfleteren. Laser based fast prototyping methodology of producing stretchable and conformable electronic systems. In *2008 2nd Electronics System-Integration Technology Conference*, pages 1387–1390, September 2008.
- [77] R. Carta, P. Jourand, B. Hermans, J. Thoné, D. Brosteaux, T. Vervust, F. Bossuyt, F. Axisa, J. Vanfleteren, and R. Puers. Design and implementation of advanced systems in a flexible-stretchable technology for biomedical applications. *Sensors and Actuators A: Physical*, 156(1):79–87, November 2009.
- [78] Qiang Ma and Yihui Zhang. Mechanics of Fractal-Inspired Horseshoe Microstructures for Applications in Stretchable Electronics. *Journal of Applied Mechanics*, 83(11):111008, November 2016.

- [79] Xin Ning, Xueju Wang, Yi Zhang, Xinge Yu, Dongwhi Choi, Ning Zheng, Dong Sung Kim, Yonggang Huang, Yihui Zhang, and John A. Rogers. Assembly of Advanced Materials into 3D Functional Structures by Methods Inspired by Origami and Kirigami: A Review. *Advanced Materials Interfaces*, 5(13):1800284, 2018. \_eprint: <https://onlinelibrary.wiley.com/doi/pdf/10.1002/admi.201800284>.
- [80] Lizhi Xu, Terry C. Shyu, and Nicholas A. Kotov. Origami and Kirigami Nanocomposites. *ACS Nano*, 11(8):7587–7599, August 2017. Publisher: American Chemical Society.
- [81] Terry C. Shyu, Pablo F. Damasceno, Paul M. Dodd, Aaron Lamoureux, Lizhi Xu, Matthew Shlian, Max Shtein, Sharon C. Glotzer, and Nicholas A. Kotov. A kirigami approach to engineering elasticity in nanocomposites through patterned defects. *Nature Materials*, 14(8):785–789, August 2015. Number: 8 Publisher: Nature Publishing Group.
- [82] Nicolas Vachicouras, Christina M. Tringides, Philippe B. Campiche, and Stéphanie P. Lacour. Engineering reversible elasticity in ductile and brittle thin films supported by a plastic foil. *Extreme Mechanics Letters*, 15:63–69, September 2017.
- [83] H. Jiang, D.-Y. Khang, J. Song, Y. Sun, Y. Huang, and J. A. Rogers. Finite deformation mechanics in buckled thin films on compliant supports. *Proceedings of the National Academy of Sciences*, 104(40):15607–15612, October 2007.
- [84] Jonathan A. Fan, Woon-Hong Yeo, Yewang Su, Yoshiaki Hattori, Woosik Lee, Sung-Young Jung, Yihui Zhang, Zhuangjian Liu, Huanyu Cheng, Leo Falgout, Mike Bajema, Todd Coleman, Dan Gregoire, Ryan J. Larsen, Yonggang Huang, and John A. Rogers. Fractal design concepts for stretchable electronics. *Nature Communications*, 5(1):3266, February 2014. Number: 1 Publisher: Nature Publishing Group.
- [85] Nicolas Vachicouras, Osama Tarabichi, Vivek V. Kanumuri, Christina M. Tringides, Jennifer Macron, Florian Fallegger, Yohann Thenaisie, Lorenz Epprecht, Stephen McInturff, Ahad A. Qureshi, Valentina Paggi, Martin W. Kuklinski, M. Christian Brown, Daniel J. Lee, and Stéphanie P. Lacour. Microstructured thin-film electrode technology enables proof of concept of scalable, soft auditory brainstem implants. *Science Translational Medicine*, 11(514), October 2019. Publisher: American Association for the Advancement of Science Section: Research Article.
- [86] Paul Le Floch, Nicola Molinari, Kewang Nan, Shuwen Zhang, Boris Kozinsky, Zhigang Suo, and Jia Liu. Fundamental Limits to the Electrochemical Impedance Stability of Dielectric Elastomers in Bioelectronics. *Nano Letters*, 20(1):224–233, January 2020.

## Bibliography

---

- [87] S. Zeitler, E. Wendler-Kalsch, W. Preidel, and V. Tegeder. Corrosion of platinum electrodes in phosphate buffered saline solution. *Materials and Corrosion/Werkstoffe und Korrosion*, 48(5):303–310, May 1997.
- [88] J. W. Osenbach. Water-Induced Corrosion of Materials Used for Semiconductor Passivation. *Journal of The Electrochemical Society*, 140(12):3667–3675, December 1993.
- [89] Eckardt Bihler and Marc Hauer. Miniaturized Electronic Modules for Aggressive Environments. In *Smart Systems Integration; 13th International Conference and Exhibition on Integration Issues of Miniaturized Systems*, pages 1–7, April 2019.
- [90] C A Diaz-Botia, L E Luna, R M Neely, M Chamanzar, C Carraro, J M Carmena, P N Sabes, R Maboudian, and M M Maharbiz. A silicon carbide array for electrocorticography and peripheral nerve recording. *Journal of Neural Engineering*, 14(5):056006, October 2017.
- [91] Frederick Bossuyt, Thomas Vervust, and Jan Vanfleteren. Stretchable Electronics Technology for Large Area Applications: Fabrication and Mechanical Characterization. *IEEE Transactions on Components, Packaging and Manufacturing Technology*, 3(2):229–235, February 2013. Conference Name: IEEE Transactions on Components, Packaging and Manufacturing Technology.
- [92] Terrence J. Sejnowski, Patricia S. Churchland, and J. Anthony Movshon. Putting big data to good use in neuroscience. *Nature Neuroscience*, 17(11):1440–1441, November 2014. Number: 11 Publisher: Nature Publishing Group.
- [93] Edward S Boyden, Feng Zhang, Ernst Bamberg, Georg Nagel, and Karl Deisseroth. Millisecond-timescale, genetically targeted optical control of neural activity. *Nature Neuroscience*, 8(9):1263–1268, September 2005.
- [94] Georg Nagel, Martin Brauner, Jana F. Liewald, Nona Adeishvili, Ernst Bamberg, and Alexander Gottschalk. Light Activation of Channelrhodopsin-2 in Excitable Cells of *Caenorhabditis elegans* Triggers Rapid Behavioral Responses. *Current Biology*, 15(24):2279–2284, December 2005.
- [95] Anding Bi, Jinjuan Cui, Yu-Ping Ma, Elena Olshevskaya, Mingliang Pu, Alexander M. Dizhoor, and Zhuo-Hua Pan. Ectopic Expression of a Microbial-Type Rhodopsin Restores Visual Responses in Mice with Photoreceptor Degeneration. *Neuron*, 50(1):23–33, April 2006.
- [96] Toru Ishizuka, Masaaki Kakuda, Rikita Araki, and Hiromu Yawo. Kinetic evaluation of photosensitivity in genetically engineered neurons expressing green algae light-gated channels. *Neuroscience Research*, 54(2):85–94, February 2006.
- [97] Jessica Ortigoza-Diaz, Kee Scholten, Christopher Larson, Angelica Cobo, Trevor Hudson, James Yoo, Alex Baldwin, Ahuva Weltman Hirschberg, and Ellis Meng.

- Techniques and Considerations in the Microfabrication of Parylene C Microelectromechanical Systems. *Micromachines*, 9(9):422, September 2018.
- [98] Dong-Wook Park, Amelia A. Schendel, Solomon Mikael, Sarah K. Brodnick, Thomas J. Richner, Jared P. Ness, Mohammed R. Hayat, Farid Atry, Seth T. Frye, Ramin Pashaie, Sanitta Thongpang, Zhenqiang Ma, and Justin C. Williams. Graphene-based carbon-layered electrode array technology for neural imaging and optogenetic applications. *Nature Communications*, 5(1):5258, December 2014.
- [99] Peter Ledochowitsch, Elisa Olivero, Tim Blanche, and Michel M. Maharbiz. A transparent  $\mu$ ECoG array for simultaneous recording and optogenetic stimulation. In *2011 Annual International Conference of the IEEE Engineering in Medicine and Biology Society*, pages 2937–2940, August 2011. ISSN: 1558-4615, 1094-687X, 1557-170X, 1557-170X.
- [100] Teppei Araki, Fumiaki Yoshida, Takafumi Uemura, Yuki Noda, Shusuke Yoshimoto, Taro Kaiju, Takafumi Suzuki, Hiroki Hamanaka, Kousuke Baba, Hideki Hayakawa, Taiki Yabumoto, Hideki Mochizuki, Shingo Kobayashi, Masaru Tanaka, Masayuki Hirata, and Tsuyoshi Sekitani. Long-Term Implantable, Flexible, and Transparent Neural Interface Based on Ag/Au Core–Shell Nanowires. *Advanced Healthcare Materials*, 8(10):1900130, 2019. \_eprint: <https://onlinelibrary.wiley.com/doi/pdf/10.1002/adhm.201900130>.
- [101] Weiyang Yang, Yan Gong, Cheng-You Yao, Maheshwar Shrestha, Yaoyao Jia, Zhen Qiu, Qi Hua Fan, Arthur Weber, and Wen Li. A fully transparent, flexible PEDOT:PSS–ITO–Ag–ITO based microelectrode array for ECoG recording. *Lab on a Chip*, 21(6):1096–1108, March 2021. Publisher: The Royal Society of Chemistry.
- [102] Ahuva W. Hirschberg, Huijing Xu, Kee Scholien, Theodore W. Berger, Dong Song, and Ellis Meng. Development of an anatomically conformal parylene neural probe array for multi-region hippocampal recordings. In *2017 IEEE 30th International Conference on Micro Electro Mechanical Systems (MEMS)*, pages 129–132, January 2017.
- [103] Dion Khodagholy, Thomas Doublet, Moshe Gurfinkel, Pascale Quilichini, Esma Ismailova, Pierre Leleux, Thierry Herve, Sébastien Sanaur, Christophe Bernard, and George G. Malliaras. Highly Conformable Conducting Polymer Electrodes for In Vivo Recordings. *Advanced Materials*, 23(36):H268–H272, 2011. \_eprint: <https://onlinelibrary.wiley.com/doi/pdf/10.1002/adma.201102378>.
- [104] D Rodger, A Fong, W Li, H Ameri, A Ahuja, C Gutierrez, I Lavrov, H Zhong, P Menon, and E Meng. Flexible parylene-based multielectrode array technology for high-density neural stimulation and recording. *Sensors and Actuators B: Chemical*, 132(2):449–460, June 2008.

- [105] Yu Chong Tai. Parylene BioMEMS. In *2005 IEEE International Conference on Robotics and Biomimetics - ROBIO*, pages xxxvii–xxxvii, July 2005.
- [106] Sofian N. Obaid, Rose T. Yin, Jinbi Tian, Zhiyuan Chen, Sheena W. Chen, K. Benjamin Lee, Nicolas Boyajian, Alana N. Miniovich, Igor R. Efimov, and Luyao Lu. Multifunctional Flexible Biointerfaces for Simultaneous Colocalized Optophysiology and Electrophysiology. *Advanced Functional Materials*, 30(24):1910027, 2020. \_eprint: <https://onlinelibrary.wiley.com/doi/pdf/10.1002/adfm.201910027>.
- [107] Nobuo Kunori and Ichiro Takashima. A transparent epidural electrode array for use in conjunction with optical imaging. *Journal of Neuroscience Methods*, 251:130–137, August 2015.
- [108] Aline F. Renz, Jihyun Lee, Klas Tybrandt, Maciej Brzezinski, Dayra A. Lorenzo, Mouna Cerra Cheraka, Jaehong Lee, Fritjof Helmchen, Janos Vörös, and Christopher M. Lewis. Opto-E-Dura: A Soft, Stretchable ECoG Array for Multimodal, Multi-scale Neuroscience. *Advanced Healthcare Materials*, 9(17):2000814, 2020. \_eprint: <https://onlinelibrary.wiley.com/doi/pdf/10.1002/adhm.202000814>.
- [109] Yue Wang, Chenxin Zhu, Raphael Pfattner, Hongping Yan, Lihua Jin, Shucheng Chen, Francisco Molina-Lopez, Franziska Lissel, Jia Liu, Noelle I. Rabiah, Zheng Chen, Jong Won Chung, Christian Linder, Michael F. Toney, Boris Murmann, and Zhenan Bao. A highly stretchable, transparent, and conductive polymer. *Science Advances*, 3(3):e1602076, 2011. Publisher: American Association for the Advancement of Science.
- [110] Eui Dae Jung, Yun Seok Nam, Houn Seo, Bo Ram Lee, Jae Choul Yu, Sang Yun Lee, Ju-Young Kim, Jang-Ung Park, and Myoung Hoon Song. Highly efficient flexible optoelectronic devices using metal nanowire-conducting polymer composite transparent electrode. *Electronic Materials Letters*, 11(5):906–914, September 2015.
- [111] Jing Zhang, Xiaojun Liu, Wenjing Xu, Wenhan Luo, Ming Li, Fangbing Chu, Lu Xu, Anyuan Cao, Jisong Guan, Shiming Tang, and Xiaojie Duan. Stretchable Transparent Electrode Arrays for Simultaneous Electrical and Optical Interrogation of Neural Circuits in Vivo. *Nano Letters*, 18(5):2903–2911, May 2018.
- [112] Dong-Ho Kim, Mi-Rang Park, Hak-Jun Lee, and Gun-Hwan Lee. Thickness dependence of electrical properties of ITO film deposited on a plastic substrate by RF magnetron sputtering. *Applied Surface Science*, 253(2):409–411, November 2006.
- [113] Rene Patrick von Metzen and Thomas Stieglitz. The effects of annealing on mechanical, chemical, and physical properties and structural stability of Parylene C. *Biomedical Microdevices*, 15(5):727–735, October 2013.
- [114] L Kerkache, A Layadi, E Dogheche, and D Rémiens. Physical properties of RF sputtered ITO thin films and annealing effect. *Journal of Physics D: Applied Physics*, 39(1):184–189, January 2006.



- [115] Yutaka Ohmori, Akihiko Fujii, Masao Uchida, Chikayoshi Morishima, and Katsumi Yoshino. Observation of spectral narrowing and emission energy shift in organic electroluminescent diode utilizing 8-hydroxyquinoline aluminum/aromatic diamine multilayer structure. *Applied Physics Letters*, 63(14):1871–1873, October 1993.
- [116] Josef Parvizi and Sabine Kastner. Promises and limitations of human intracranial electroencephalography. *Nature Neuroscience*, 21(4):474–483, April 2018. Number: 4 Publisher: Nature Publishing Group.
- [117] Patrick Kwan, Steven C. Schachter, and Martin J. Brodie. Drug-Resistant Epilepsy. *New England Journal of Medicine*, 365(10):919–926, September 2011. Publisher: Massachusetts Medical Society.
- [118] Stefan S. Kim, Ian E. McCutcheon, Dima Suki, Jeffrey S. Weinberg, Raymond Sawaya, Frederick F. Lang, David Ferson, Amy B. Heimberger, Franco DeMonte, and Sujit S. Prabhu. Awake craniotomy for brain tumors near eloquent cortex: correlation of intraoperative cortical mapping with neurological outcomes in 309 consecutive patients. *Neurosurgery*, 64(5):836–845; discussion 345–346, May 2009.
- [119] Leigh R. Hochberg, Mijail D. Serruya, Gerhard M. Friehs, Jon A. Mukand, Maryam Saleh, Abraham H. Caplan, Almut Branner, David Chen, Richard D. Penn, and John P. Donoghue. Neuronal ensemble control of prosthetic devices by a human with tetraplegia. *Nature*, 442(7099):164–171, July 2006. Number: 7099 Publisher: Nature Publishing Group.
- [120] Florian Fallegger, Giuseppe Schiavone, and Stéphanie P. Lacour. Conformable Hybrid Systems for Implantable Bioelectronic Interfaces. *Advanced Materials*, 32(15):1903904, 2020. \_eprint: <https://onlinelibrary.wiley.com/doi/pdf/10.1002/adma.201903904>.
- [121] Dion Khodagholy, Jennifer N. Gelinas, Thomas Thesen, Werner Doyle, Orrin Devinsky, George G. Malliaras, and György Buzsáki. NeuroGrid: recording action potentials from the surface of the brain. *Nature neuroscience*, 18(2):310–315, February 2015.
- [122] Florian Fallegger, Giuseppe Schiavone, Elvira Pirondini, Fabien B. Wagner, Nicolas Vachicouras, Ludovic Serex, Gregory Zegarek, Adrien May, Paul Constanthin, Marie Palma, Mehrdad Khoshnevis, Dirk Van Roost, Blaise Yvert, Grégoire Courtine, Karl Schaller, Jocelyne Bloch, and Stéphanie P. Lacour. MRI-Compatible and Conformal Electrocorticography Grids for Translational Research. *Advanced Science*, 8(9):2003761, 2021. \_eprint: <https://onlinelibrary.wiley.com/doi/pdf/10.1002/advs.202003761>.

## Bibliography

---

- [123] Alan D. Degenhart, James Eles, Richard Dum, Jessica L. Mischel, Ivan Smalianchuk, Bridget Endler, Robin C. Ashmore, Elizabeth C. Tyler-Kabara, Nicholas G. Hatsopoulos, Wei Wang, Aaron P. Batista, and X. Tracy Cui. Histological evaluation of a chronically-implanted electrocorticographic electrode grid in a non-human primate. *Journal of Neural Engineering*, 13(4):046019, June 2016. Publisher: IOP Publishing.
- [124] Frank G. Shellock and Alberto Spinazzi. MRI Safety Update 2008: Part 2, Screening Patients for MRI. *American Journal of Roentgenology*, 191(4):1140–1149, October 2008. Publisher: American Roentgen Ray Society.
- [125] Johannes B. Erhardt, Erwin Fuhrer, Oliver G. Gruschke, Jochen Leupold, Matthias C. Wapler, Jürgen Hennig, Thomas Stieglitz, and Jan G. Korvink. Should patients with brain implants undergo MRI? *Journal of Neural Engineering*, 15(4):041002, May 2018. Publisher: IOP Publishing.
- [126] Peter Serano, Leonardo M. Angelone, Husam Katnani, Emad Eskandar, and Giorgio Bonmassar. A Novel Brain Stimulation Technology Provides Compatibility with MRI. *Scientific Reports*, 5(1):9805, April 2015. Number: 1 Publisher: Nature Publishing Group.
- [127] Christian Boehler, Stefano Carli, Luciano Fadiga, Thomas Stieglitz, and Maria Asplund. Tutorial: guidelines for standardized performance tests for electrodes intended for neural interfaces and bioelectronics. *Nature Protocols*, 15(11):3557–3578, November 2020.
- [128] Marc S. Schwartz, Steven R. Otto, Robert V. Shannon, William E. Hitselberger, and Derald E. Brackmann. Auditory brainstem implants. *Neurotherapeutics: The Journal of the American Society for Experimental NeuroTherapeutics*, 5(1):128–136, January 2008.
- [129] Levent Sennaroğlu, Vittorio Colletti, Thomas Lenarz, Manuel Manrique, Roland Laszig, Helge Rask-Andersen, Nebil Göksu, Erwin Offeciers, Shakeel Saeed, Robert Behr, Yıldırım Bayazıt, Jan Casselman, Simon Freeman, Paul Kileny, Daniel J. Lee, Robert V. Shannon, Mohan Kameswaran, Abdulrahman Hagr, Andrzej Zarowski, Mark S. Schwartz, Burçak Bilginer, Ameet Kishore, Gonca Sennaroğlu, Esra Yücel, Sarp Saraç, Ahmet Ataş, Lilian Colletti, Martin O’Driscoll, In Seok Moon, Lutz Gärtner, Alicia Huarte, Gunnar Nyberg, Burçe Özgen Mocan, Gamze Atay, Münir Demir Bajin, Betül Çicek Çınar, Merve Özbal Batuk, Mehmet Yaralı, Fatma Esen Aydın, Filiz Aslan, Meltem Cigdem Kirazlı, Hilal Burcu Özkan, J. M. Hans, Julie Kosaner, and Marek Polak. Consensus statement: Long-term results of ABI in children with complex inner ear malformations and decision making between CI and ABI. *Cochlear Implants International*, 17(4):163–171, July 2016. Publisher: Taylor & Francis \_eprint: <https://doi.org/10.1080/14670100.2016.1208396>.

- [130] Samuel R. Barber, Elliott D. Kozin, Aaron K. Remenschneider, Sidharth V. Puram, Max Smith, Barbara S. Herrmann, Mary E. Cunnane, M. Christian Brown, and Daniel J. Lee. Auditory Brainstem Implant Array Position Varies Widely Among Adult and Pediatric Patients and is Associated with Perception. *Ear and hearing*, 38(6):e343–e351, 2017.
- [131] Vittorio Colletti. Auditory outcomes in tumor vs. nontumor patients fitted with auditory brainstem implants. *Advances in Oto-Rhino-Laryngology*, 64:167–185, 2006.
- [132] Jeon Mi Lee, Jin Woo Chang, Jae Young Choi, Won Seok Chang, and In Seok Moon. Hearing Restoration in Neurofibromatosis Type II Patients. *Yonsei Medical Journal*, 57(4):817, 2016.
- [133] Shruti N. Deshpande, Lisa Houston, and Robert W. Keith. Hearing Testing, Auditory Brainstem Response (ABR). In Stilianos E. Kountakis, editor, *Encyclopedia of Otolaryngology, Head and Neck Surgery*, pages 1151–1158. Springer Berlin Heidelberg, Berlin, Heidelberg, 2013.
- [134] S. M. Kurtz and J. N. Devine. PEEK Biomaterials in Trauma, Orthopedic, and Spinal Implants. *Biomaterials*, 28(32):4845–4869, November 2007.
- [135] Krishna Kumar, Rod S. Taylor, Line Jacques, Sam Eldabe, Mario Meglio, Joan Molet, Simon Thomson, Jim O’Callaghan, Elon Eisenberg, Germain Milbouw, Eric Buchser, Gianpaolo Fortini, Jonathan Richardson, and Richard B. North. Spinal cord stimulation versus conventional medical management for neuropathic pain: a multicentre randomised controlled trial in patients with failed back surgery syndrome. *Pain*, 132(1-2):179–188, November 2007.
- [136] Rubia van den Brand, Janine Heutschi, Quentin Barraud, Jack DiGiovanna, Kay Bartholdi, Michèle Huerlimann, Lucia Friedli, Isabel Vollenweider, Eduardo Martin Moraud, Simone Duis, Nadia Dominici, Silvestro Micera, Pavel Musienko, and Grégoire Courtine. Restoring Voluntary Control of Locomotion after Paralyzing Spinal Cord Injury. *Science*, 336(6085):1182–1185, June 2012. Publisher: American Association for the Advancement of Science.
- [137] Marco Capogrosso, Tomislav Milekovic, David Borton, Fabien Wagner, Eduardo Martin Moraud, Jean-Baptiste Mignardot, Nicolas Buse, Jerome Gandar, Quentin Barraud, David Xing, Elodie Rey, Simone Duis, Yang Jianzhong, Wai Kin D. Ko, Qin Li, Peter Detemple, Tim Denison, Silvestro Micera, Erwan Bezard, Jocelyne Bloch, and Grégoire Courtine. A brain–spine interface alleviating gait deficits after spinal cord injury in primates. *Nature*, 539(7628):284–288, November 2016. Number: 7628 Publisher: Nature Publishing Group.
- [138] Fabien B. Wagner, Jean-Baptiste Mignardot, Camille G. Le Goff-Mignardot, Robin Demesmaeker, Salif Komi, Marco Capogrosso, Andreas Rowald, Ismael Seáñez,

- Miroslav Caban, Elvira Pirondini, Molywan Vat, Laura A. McCracken, Roman Heimgartner, Isabelle Fodor, Anne Watrin, Perrine Seguin, Edoardo Paoles, Katrien Van Den Keybus, Grégoire Eberle, Brigitte Schurch, Etienne Pralong, Fabio Becce, John Prior, Nicholas Buse, Rik Buschman, Esra Neufeld, Niels Kuster, Stefano Carda, Joachim von Zitzewitz, Vincent Delattre, Tim Denison, Hendrik Lambert, Karen Minassian, Jocelyne Bloch, and Grégoire Courtine. Targeted neurotechnology restores walking in humans with spinal cord injury. *Nature*, 563(7729):65–71, November 2018. Number: 7729 Publisher: Nature Publishing Group.
- [139] Giuseppe Schiavone, Florian Fallegger, Xiaoyang Kang, Beatrice Barra, Nicolas Vachicouras, Evgenia Roussinova, Ivan Furfaro, Sébastien Jiguet, Ismael Seáñez, Simon Borgognon, Andreas Rowald, Qin Li, Chuan Qin, Erwan Bézard, Jocelyne Bloch, Grégoire Courtine, Marco Capogrosso, and Stéphanie P. Lacour. Soft, Implantable Bioelectronic Interfaces for Translational Research. *Advanced Materials*, 32(17):1906512, 2020. \_eprint: <https://onlinelibrary.wiley.com/doi/pdf/10.1002/adma.201906512>.
- [140] Maria Pasquini, Nicholas D. James, Inssia Dewany, Florent-Valéry Coen, Newton Cho, Stefano Lai, Selin Anil, Jacopo Carpaneto, Quentin Barraud, Stéphanie P. Lacour, Silvestro Micera, and Grégoire Courtine. Preclinical upper limb neurobotic platform to assess, rehabilitate, and develop therapies. *Science Robotics*, 7(64):eabk2378, March 2022.
- [141] Hyunwoo Yuk, Claudia E. Varela, Christoph S. Nabzdyk, Xinyu Mao, Robert F. Padera, Ellen T. Roche, and Xuanhe Zhao. Dry double-sided tape for adhesion of wet tissues and devices. *Nature*, 575(7781):169–174, November 2019. Number: 7781 Publisher: Nature Publishing Group.

# Florent-Valéry Coen

Avenue de Cour 105, 1007 Lausanne, Switzerland

☎ (+41) 79 286 68 08 | ✉ florent.coen@protonmail.com | 📅 May 20th, 1991

## Education

### École Polytechnique Fédérale de Lausanne (EPFL)

PHD IN MICROSYSTEMS AND MICROELECTRONICS

- Collaboration with Harvard Medical School, MA, USA

Lausanne, Switzerland

2017 - 2022

### École Polytechnique Fédérale de Lausanne (EPFL)

M.Sc. IN MICROSYSTEMS ENGINEERING

- Master thesis at Stanford University, CA, USA
- Major in Robotics and Autonomous Systems
- Minor in Management, Technology and Entrepreneurship

Lausanne, Switzerland

2014 - 2017

### École Polytechnique Fédérale de Lausanne (EPFL)

B.Sc. IN MICROSYSTEMS ENGINEERING

- 1 year exchange at the Royal Institute of Technology (KTH) in Stockholm, Sweden

Lausanne, Switzerland

2011 - 2014

## Experience

### Laboratory for Soft Bioelectronic Interfaces (Prof. S. Lacour), EPFL

PHD THESIS

- Developed innovative soft neural interfaces targeted at the recording and stimulation of the central nervous system.
- Employed advanced microfabrication techniques to manufacture implants with improved electromechanical performances.
- Performed a variety of characterization techniques to assess the implants properties, incl. electroimpedance spectroscopy (EIS), voltage transient (VT), cyclic voltametry (CV), tensile test and cyclic stretching.
- Deployed and tested the resulting devices in various animal models incl. rats and non-human primates.

Geneva, Switzerland

2017 - 2022

### Jeffrey Laboratory (Prof. S. Jeffrey), Stanford University - School of Medicine

MASTER THESIS

- Designed and fabricated a digital microfluidic chip for the analysis of circulating tumor cells (CTCs)
- Implemented a novel dielectric material leading to a 100-fold reduction in powering voltage over similar systems
- Assessed the suitability of a commercially-available digital microfluidic platform for cell-based experiments

Stanford, USA

Aug. 2016 - Mar. 2017

## Skills

### Microfabrication

Processing on stiff/flexible/stretchable substrates (Silicon, glass, Polyimide, Parylene, PDMS), photolithography incl. direct-write system and mask aligner, dry etching, thin film sputtering and evaporation, hybrid integration of components incl. connectors and microLEDs

### CAD

AutoCAD, KLayout, SolidWorks, L-Edit

### Programming

Python, C/C++, Objective-C, MatLab, Mathematica

### Languages

French (native), English (C2, Cambridge English Advanced (CAE) certificate), German (B2)

## Honors & Awards

2020 **Best Poster Award** at the annual doctor school symposium

Lausanne, Switzerland

2020 **2nd Place** at START Lausanne an elevator pitch and business plan writing team contest

Lausanne, Switzerland

## Publications

### Preclinical upper limb neurobotic platform to assess, rehabilitate, and develop therapies

Pasquini M\*, James ND\*, Dewany I\*, **Coen FV**, Cho N, Lai S, Anil S, Carpaneto J, Barraud Q, Lacour SP, Micera S, Courtine G

*Science Robotics* 7.64 (2022)

### Comparison of Responses to DCN vs. VCN Stimulation in a Mouse Model of the Auditory Brainstem Implant

McInturff S, **Coen FV**, Hight AE, Tarabichi O, Kanumuri VV, Vachicouras N, Lacour SP, Lee DJ, Brown MC

*Journal of the Association for Research in Otolaryngology* 23.3 (2022)